

ACOUSTIC TRANSDUCTION – MATERIALS AND DEVICES

Period 31 July 1996 to 31 December 1997

Annual Report

VOLUME IV

**OFFICE OF NAVAL RESEARCH
Contract No: N00014-96-1-1173**

**APPROVED FOR PUBLIC RELEASE –
DISTRIBUTION UNLIMITED**

**Reproduction in whole or in part is permitted for any
purpose of the United States Government**

Kenji Uchino

PENNSTATE



**THE MATERIALS RESEARCH LABORATORY
UNIVERSITY PARK, PA**

19980910 004

REPORT DOCUMENTATION PAGE

Form Approved
OMB No. 0704-0188

Public reporting burden for this collection of information is estimated to average 1 hour per response, including the time for reviewing instructions, searching existing data sources, gathering and maintaining the data needed, and completing and reviewing the collection of information. Send comments regarding this burden estimate or any other aspect of this collection of information, including suggestions for reducing this burden, to Washington Headquarters Services, Directorate for Information Operations and Reports, 1215 Jefferson Davis Highway, Suite 1204, Arlington, VA 22202-4302, and to the Office of Management and Budget, Paperwork Reduction Project (0704-0188), Washington, DC 20503.

1. AGENCY USE ONLY (Leave blank)

2. REPORT DATE

05/01/98

3. REPORT TYPE AND DATES COVERED

ANNUAL REPORT 07/31/96-12/31/97

4. TITLE AND SUBTITLE

ACOUSTIC TRANSDUCTION -- MATERIALS AND DEVICES

5. FUNDING NUMBERS

ONR CONTRACT NO:
N00014-96-1-1173

6. AUTHOR(S)

KENJI UCHINO

7. PERFORMING ORGANIZATION NAME(S) AND ADDRESS(ES)

Materials Research Laboratory
The Pennsylvania State University
University Park, PA 16802

8. PERFORMING ORGANIZATION
REPORT NUMBER

9. SPONSORING/MONITORING AGENCY NAME(S) AND ADDRESS(ES)

Office of Naval Research Office of Naval Research
ONR 321SS Regional Office Chicago
Ballston Centre Tower One 536 S Clark Str., Rm 208
800 N Quincy Street Chicago IL 60605-1588
Arlington, VA 22217-5660

10. SPONSORING/MONITORING
AGENCY REPORT NUMBER

11. SUPPLEMENTARY NOTES

12a. DISTRIBUTION / AVAILABILITY STATEMENT

12b. DISTRIBUTION CODE

13. ABSTRACT (Maximum 200 words)

SEE FOLLOW PAGE

14. SUBJECT TERMS

15. NUMBER OF PAGES

16. PRICE CODE

17. SECURITY CLASSIFICATION
OF REPORT

18. SECURITY CLASSIFICATION
OF THIS PAGE

19. SECURITY CLASSIFICATION
OF ABSTRACT

20. LIMITATION OF ABSTRACT

GENERAL INSTRUCTIONS FOR COMPLETING SF 298

The Report Documentation Page (RDP) is used in announcing and cataloging reports. It is important that this information be consistent with the rest of the report, particularly the cover and title page. Instructions for filling in each block of the form follow. It is important to *stay within the lines* to meet optical scanning requirements.

Block 1. Agency Use Only (Leave blank).

Block 2. Report Date. Full publication date including day, month, and year, if available (e.g. 1 Jan 88). Must cite at least the year.

Block 3. Type of Report and Dates Covered. State whether report is interim, final, etc. If applicable, enter inclusive report dates (e.g. 10 Jun 87 - 30 Jun 88).

Block 4. Title and Subtitle. A title is taken from the part of the report that provides the most meaningful and complete information. When a report is prepared in more than one volume, repeat the primary title, add volume number, and include subtitle for the specific volume. On classified documents enter the title classification in parentheses.

Block 5. Funding Numbers. To include contract and grant numbers; may include program element number(s), project number(s), task number(s), and work unit number(s). Use the following labels:

C - Contract	PE - Project
G - Grant	TA - Task
PE - Program Element	WU - Work Unit Accession No.

Block 6. Author(s). Name(s) of person(s) responsible for writing the report, performing the research, or credited with the content of the report. If editor or compiler, this should follow the name(s).

Block 7. Performing Organization Name(s) and Address(es). Self-explanatory

Block 8. Performing Organization Report Number. Enter the unique alphanumeric report number(s) assigned by the organization performing the report.

Block 9. Sponsoring/Monitoring Agency Name(s) and Address(es). Self-explanatory

Block 10. Sponsoring/Monitoring Agency Report Number. (If known)

Block 11. Supplementary Notes. Enter information not included elsewhere such as: Prepared in cooperation with...; Trans. of...; To be published in.... When a report is revised, include a statement whether the new report supersedes or supplements the older report.

Block 12a. Distribution/Availability Statement. Denotes public availability or limitations. Cite any availability to the public. Enter additional limitations or special markings in all capitals (e.g. NOFORN, REL, ITAR).

DOD - See DoDD 5230.24, "Distribution Statements on Technical Documents."

DOE - See authorities.

NASA - See Handbook NHB 2200.2.

NTIS - Leave blank.

Block 12b. Distribution Code.

DOD - Leave blank.

DOE - Enter DOE distribution categories from the Standard Distribution for Unclassified Scientific and Technical Reports.

NASA - Leave blank

NTIS - Leave blank

Block 13. Abstract. Include a brief (Maximum 200 words) factual summary of the most significant information contained in the report.

Block 14. Subject Terms. Keywords or phrases identifying major subjects in the report.

Block 15. Number of Pages. Enter the total number of pages.

Block 16. Price Code. Enter appropriate price code (NTIS only)

Blocks 17. - 19. Security Classifications. Self-explanatory. Enter U.S. Security Classification in accordance with U.S. Security Regulations (i.e., UNCLASSIFIED). If form contains classified information, stamp classification on the top and bottom of the page.

Block 20. Limitation of Abstract. This block must be completed to assign a limitation to the abstract. Enter either UL (unlimited) or SAR (same as report). An entry in this block is necessary if the abstract is to be limited. If blank, the abstract is assumed to be unlimited.

ABSTRACT

The report documents work carried out over the period 31 July 1996 to 31 December 1997 on a Multi-University Research Initiative (MURI) program under Office of Naval Research (ONR) sponsorship. The program couples transducer materials research in the Materials Research Laboratory (MRL), design and testing studies in the Applied Research Laboratory (ARL) and vibration and flow noise control in the Center for Acoustics and Vibration (CAV) at Penn State.

The overarching project objective is the development of acoustic transduction materials and devices of direct relevance to Navy needs and with application in commercial products. The initial focus of studies is upon high performance sensors and high authority high strain actuators. This objective also carries the need for new materials, new device designs, improved drive and control strategies and a continuing emphasis upon reliability under a wide range of operating conditions.

In *Material Studies*, undoubtedly major breakthroughs have occurred in the ultra-high strain relaxor ferroelectric systems. Earlier reports of unusual piezoelectric activity in single crystal perovskite relaxors have been amply confirmed in the lead zinc niobate : lead titanate, and lead magnesium niobate : lead titanate systems for compositions of rhombohedral symmetry close to the Morphotropic Phase Boundary (MPB) in these solid solutions. Analysis of the unique properties of 001 field poled rhombohedral ferroelectric crystals suggests new intrinsic mechanisms for high strain and carries the first hints of how to move from lead based compositions. A major discovery of comparable importance is a new mode of processing to convert PVDF:TrFE copolymer piezoelectric into a relaxor ferroelectric in which electrostrictive strains of 4% have been demonstrated at high fields. Both single crystal and polymer relaxors appear to offer energy densities almost order of magnitude larger than in earlier polycrystal ceramic actuators.

Transducer Studies have continued to exploit the excellent sensitivity and remarkable versatility of the cymbal type flextensional element. Initial studies of a small cymbal arrays show excellent promise in both send and receive modes, and larger arrays are now under construction for tests at ARL. New studies in constrained layer vibration damping and in flow noise reduction are yielding exciting new results.

In *Actuator Studies*, an important advance in piezoelectric generated noise control now permits wider use of acoustic emission as a reliability diagnostic technique. Joint studies with NRL, Washington have developed a completely new d_{15} driven torsional actuator and the CAV program element has designed an exciting high strain high force inchworm.

Finite element analysis continues to be an important tool for understanding the more complex composite structures and their beam forming capability in water. *Thin and Thick Thin Film Studies* are gearing up to provide the material base for micro-tonpils arrays. New exploitation of ultra sensitive strain and permittivity measurements is providing the first reliable data of electrostriction in simple solids, and suggesting new modes for separating the polarizability contributors in dielectrics and electrostrictors.

APPENDICES

VOLUME I

GENERAL SUMMARY PAPERS

1. Ito, Y. and K. Uchino, Wiley Encyclopedia of Electrical and Electronics Engineering, J. G. Webster, Edit., (Partial Charge "Piezoelectricity"), John Wiley & Sons (1998). [in press].
2. Newnham, R.E., "Molecular Mechanisms in Smart Materials," MRS Bulletin (May 1997).
3. Swartz, S.L., T.R. Shrout, and T. Takenaka, "Electronic Ceramics R&D in the U.S., Japan, Part I: Patent History," The American Ceramic Society Bulletin 76 (8) (1997).

2.0 MATERIALS STUDIES

2.1 Polycrystal Perovskite Ceramics

4. Alberta, E.F., and A.S. Bhalla, "Piezoelectric Properties of $\text{Pb}(\text{InNb})_{1/2}\text{O}_3$ - PbTiO_3 Solid Solution Ceramics," J. Korean Phys. Soc. 32, S1265-S1267 (February 1998).
5. Alberta, E.F. and A.S. Bhalla, "High Strain and Low Mechanical Quality Factor Piezoelectric $\text{Pb}[\text{Sc}_{1/2}\text{Nb}_{1/2}]_{0.575}\text{Ti}_{0.425}\text{O}_3$ Ceramics" (1997).
6. Zhang, Q.M. and J. Zhao, "Polarization Responses in Lead Magnesium Niobate Based Relaxor Ferroelectrics," Appl. Phys. Lett. 71 (12, 1649-1651 (1997).
7. Glazounov, A.E., J. Zhao, and Q.M. Zhang, "Effect of Nanopolar Regions on Electrostrictive Coefficients of a Relaxor Ferroelectric," Proceedings Williamsburg Meeting, Williamsburg, Virginia (1998).
8. Zhao, J. A.E. Glazounov, Q.M. Zhang, and B. Toby, "Neutron Diffraction Study of Electrostrictive Coefficients of Prototype Cubic Phase of Relaxor Ferroelectric $\text{PbMg}_{1/3}\text{Nb}_{2/3}\text{O}_3$," Appl. Phys. Lett. 72 (9), 1-3 (1998).
9. Park, S.-E., T.R. Shrout, P. Bridenbaugh, J. Rottenberg, and G.M. Loiacono, "Electric Field Induced Anisotropy in Electrostrictive $\text{Pb}(\text{Mg}_{1/3}\text{Nb}_{2/3})\text{O}_3$ - PbTiO_3 Crystals," Ferroelectrics (1997).
10. You, H. and Q.M. Zhang, "Diffuse X-Ray Scattering Study of Lead Magnesium Niobate Single Crystals," Phys. Rev. Lett. 79 (20), 3950-3953 (1997).
11. Zhao, J., V. Mueller, and Q.M. Zhang, "The Influence of the External Stress on the Electromechanical Response of Electrostrictive $0.9\text{Pb}(\text{Mg}_{1/3}\text{Nb}_{2/3})\text{O}_3$ - 0.1PbTiO_3 in the DC Electrical Field Biased State," J. Mat. Res. (1998).

VOLUME II

12. Yoon, S.-J., A. Joshi, and K. Uchino, "Effect of Additives on the Electromechanical Properties of $\text{Pb}(\text{Zr,Ti})\text{O}_3$ - $\text{Pb}(\text{Y}_{2/3}\text{W}_{1/3})\text{O}_3$ Ceramics," J. Am. Ceram. Soc 80 (4), 1035-39 (1997).
13. Hackenberger, W., M.-J. Pan, V. Vedula, P. Pertsch, W. Cao, C. Randall, and T. Shrout, "Effect of Grain Size on Actuator Properties of Piezoelectric Ceramics," Proceedings of the SPIE's 5th International Symposium on Smart Structures and Materials, San Diego, CA (March 1-5, 1998).

Materials Studies—continued

14. Mueller, V. and Q.M. Zhang, "Shear Response of Lead Zirconate Titanate Piezoceramics," *J. Appl. Phys.* (1998).
15. Park, S.-E., M.-J. Pan, K. Markowski, S. Yoshikawa, and L.E. Cross, "Electric Field Induced Phase Transition of Antiferroelectric Lead Lanthanum Zirconate Titanate Stannate Ceramics," *J. Appl. Phys.* **82** (4), 1798-1803 (1997).
16. Yoshikawa, S., K. Markowski, S.-E. Park, M.-J. Pan, and L.E. Cross, "Antiferroelectric-to-Ferroelectric Phase Switching Lead Lanthanum Zirconate Stannate Titanate (PLZST) Ceramics," Proceedings of SPIE's 4th Annual Symposium on Smart Structures and Materials, San Diego, CA (March 3-6, 1997).
17. Pan, M.-J., S.-E. Park, K.A. Markowski, W.S. Hackenberger, S. Yoshikawa, and L.E. Cross, "Electric Field Induced Phase Transition in Lead Lanthanum Stannate Zirconate Titanate (PLSnZT) Antiferroelectrics: Tailoring Properties through Compositional Modification" (1997).
18. Pan, M.-J., P. Pertsch, S. Yoshikawa, T.R. Shrout, and V. Vedula, "Electroactive Actuator Materials: Investigations on Stress and Temperature Characteristics," Proceedings of the SPIE's 5th International Symposium on Smart Structures and Materials, San Diego, CA (March 1-5, 1998).
19. Pan, M.-J. and S. Yoshikawa, "Effect of Grain Size on the Electromechanical Properties of Antiferroelectric-to-Ferroelectric Phase Switching PLSnZT Ceramics" (1997).

2.2 Relaxor Ferroelectric Single Crystal Systems

20. Service, R.F., "Shape-Changing Crystals Get Shiftier," *Science* **275**, 1878 (28 March 1997).
21. Shrout, T.R., S.-E. Park, C.A. Randall, J.P. Shepard, L.B. Hackenberger, "Recent Advances in Piezoelectric Materials" (1997).
22. Park, S.-E. and T.R. Shrout, "Ultrahigh Strain and Piezoelectric Behavior in Relaxor Based Ferroelectric Single Crystals," *J. Appl. Phys.* **82** (4), 1804-1811 (1997).
23. Park, S.-E. and T. R. Shrout, "Characteristics of Relaxor-Based Piezoelectric Single Crystals for Ultrasonic Transducers," *IEEE Transactions, Ferroelectrics, and Frequency Control* **44** (5), 1140-1147 (1997).
24. Park, S.-E. and T.R. Shrout, "Relaxor Based Ferroelectric Single Crystals for Electro-Mechanical Actuators," *Mat. Res. Innov.* **1**, 20-25 (1997).
25. Park, S.-E., M.L. Mulvihill, G. Risch, and T.R. Shrout, "The Effect of Growth Conditions on the Dielectric Properties of $\text{Pb}(\text{Zn}_{1/3}\text{Nb}_{2/3})\text{O}_3$ Single Crystals," *Jpn. J. Appl. Phys.* **36**, 1154-1158 (1997).
26. Mulvihill, M.L., L.E. Cross, W. Cao, and K. Uchino, "Domain-Related Phase Transitionlike Behavior in Lead Zinc Niobate Relaxor Ferroelectric Single Crystals," *J. Am. Ceram. Soc.* **80** (6), 1462-68 (1997).
27. Park, S.-E., P.D. Lopath, K.K. Shung, and T.R. Shrout, "Relaxor-Based Single Crystal materials for Ultrasonic Transducer Applications" (1997).
28. Lopath, P.D., S.-E. Park, K.K. Shung, and T.R. Shrout, " $\text{Pb}(\text{Zn}_{1/3}\text{Nb}_{2/3})\text{O}_3/\text{PbTiO}_3$ Single Crystal Piezoelectrics for Ultrasonic Transducers" (1997).
29. Lopath, P.D., S.-E. Park, K.K. Shung, and T.R. Shrout, "Single Crystal $\text{Pb}(\text{Zn}_{1/3}\text{Nb}_{2/3})\text{O}_3/\text{PbTiO}_3$ (PZN/PT) in Medical Ultrasonic Transducers" (1997).

Materials Studies—continued

2.3 New High Strain Polymer Materials

30. Su, J., Q.M. Zhang, C.H. Kim, R.Y. Ting, and R. Capps, "Effect of Transitional Phenomena on the Electric Field Induced Strain-Electrostrictive Response of a Segmented Polyurethane Elastomer" (1997).
31. Su, J., Q.M. Zhang, and R.Y. Ting, "Space-Charge-Enhanced Electromechanical Response in Thin-Film Polyurethane Elastomers," *Appl. Phys. Lett* **71** (3), 386-388 (1997).

VOLUME III

32. Su, J., Q.M. Zhang, P.-C. Wang, A.G. MacDiarmid, K.J. Wynne, "Preparation and Characterization of an Electrostrictive Polyurethane Elastomer with Conductive Polymer Electrodes," *Polymers for Adv. Tech.* (1998).
33. Zhang, Q.M., V. Bharti, and X. Zhao, "Giant Electrostriction and Relaxor Ferroelectric Behavior in Electron Irradiated Poly(vinylidene Fluoride-Trifluoroethylene) Copolymer," *Science* (1998).

3.0 TRANSDUCER STUDIES

3.1 Cymbal : Moonie : BB Composites

34. Newnham, R.E., "Composite Sensors and Actuators" (1997).
35. Steele, B.CH., R.E. Newnham, and A.G. Evans, "Ceramics, Composites, and Intergrowth," *Current Opinion in Solid State & Materials Science* **2**, 563-565 (1997).
36. Tressler, J.F. S. Alkoy, and R.E. Newnham, "Piezoelectric Sensors and Sensor Materials" (1997).
37. Tressler, J.F., S. Alko, A. Dogan, and R.E. Newnham, "Functional Composites for Sensors, Actuators, and Transducers" (1997).
38. Dogan, A., K. Uchino, R.E. Newnham, "Composite Piezoelectric Transducer with Truncated Conical Endcaps 'Cymbal'," *IEEE Transactions on Ultrasonics, Ferroelectrics, and Frequency Control* **44** (3), 597-605 (1997).
39. Dogan, A., J.F. Fernandez, K. Uchino, and R.E. Newnham, "The 'Cymbal' Electromechanical Actuator" (1997).
40. Tressler, J.F., W. Cao, K. Uchino, and R.E. Newnham, "Ceramic-Metal Composite Transducers for Underwater Acoustic Applications" (1997).
41. Tressler, J.F. and R.E. Newnham, "Doubly Resonant Cymbal-Type Transducers," *IEEE Transactions on Ultrasonics, Ferroelectrics, and Frequency Control* **44** (5), 1175-1177 (1997).
42. Tressler, J.F., W. Cao, K. Uchino, and R.E. Newnham, "Finite Element Analysis of The Cymbal-Type Transducer" (1997).
43. Tressler, J.F., W.J. Hughes, W. Cao, K. Uchino, and R.E. Newnham, "Capped Ceramic Underwater Sound Projector" (1997).

VOLUME IV

44. Alkoy, S., P.D. Lopath, R.E. Newnham, A.-C. Hladky-Hennion, and J.K. Cochran, "Focused Spherical Transducers for Ultrasonic Imaging" (1997).
45. Alkoy, S., A. Dogan, A.-C. Hladky, P. Langlet, J.K. Cochran, and R.E. Newnham, "Miniature Piezoelectric Hollow Sphere Transducers (BBs)" (1997).
46. Zipparo, M.J., K.K. Shung, and T.R. Shrout, "Piezoceramics for High-Frequency (20 to 100 MHz) Single-Element Imaging Transducers," IEEE Transactions on Ultrasonics, Ferroelectrics, and Frequency Control **44** (5), 1038-1048 (1997).

3.2 Frequency Agile Transducers

47. Davis, C. and G.A. Lesieutre, "An Actively-Tuned Solid State Piezoelectric Vibration Absorber" (1997).
48. Davis, C.L., G.A. Lesieutre, and J. Dosch, "A Tunable Electrically Shunted Piezoceramic Vibration Absorber" (1997).
49. Lesieutre, G.A. and U. Lee, "A Finite Element for Beams Having Segmented Active Constrained Layers with Frequency-Dependent Viscoelastic Material Properties" (1997).
50. Hebert, C.A. and G.A. Lesieutre, "Rotocraft Blade Lag Damping Using Highly Distributed Tuned Vibration Absorbers," American Institute of Aeronautics and Astronautics (AIAA 98-2001).
51. Lesieutre, G.A. and C.L. Davis, "Can a Coupling Coefficient of a Piezoelectric Device be Higher than Those of its Active Material?," SPIE 4th Annual Symposium on Smart Structures and Materials, San Diego, CA (March 1997).

3.3 3-D Acoustic Intensity Probes

52. Lauchle, G.C., J.R. MacGillivray, and D.C. Swanson, "Active Control of Axial-flow Fan Noise," J. Acoust. Soc. Am **101** (1), 341-349 (1997).
53. McGuinn, R.S., G.C. Lauchle, and D.C. Swanson, "Low Flow-Noise Microphone for Active Noise Control Applications," AIAA Journal **35** (1), 29-34 (1997).
54. McGuinn, R.S., G.C. Lauchle, and D.C. Swanson, "Low Flow-Noise Pressure Measurements Using a "Hot-Mic," AIAA -97-1665-CP.
55. Capone, D.E., and G.C. Lauchle, "Designing a Virtual Sound-Level Meter in LabVIEW," Education/Acoustics, LabVIEW, National Instruments.

VOLUME V

4.0 ACTUATOR STUDIES

4.1 Materials : Designs : Reliability

56. Uchino, K., "Piezoelectric Actuators" (1997).
57. Uchino, K., "Overview: Materials Issues in Design and Performance of Piezoelectric Actuators," SPIE Mtg. (1997).
58. Uchino, K., "Shape Memory Ceramics," Chapter 8 (1997).

Actuator Studies—continued

59. Aburatani, H., S. Yoshikawa, K. Uchino, and J.W.C. deVries, "A Study of Acoustic Emission in Piezoelectric Multilayer Ceramic Actuator," *Jpn. J. Appl. Phys.* **37**, 204-209 (1998).
60. Aburatani, H. and K. Uchino, "Acoustic Emission (AE) Measurement in Piezoelectric Ceramics" (1997).
61. Aburatani, H. and K. Uchino, "The Application of Acoustic Emission (AE) Method for Ferroelectric Devices and Materials," 8th US-Japan Seminar (1997).
62. Uchino, K., "Reliability of Ceramic Actuators" (1997).

4.2 Photostrictive Actuators

63. Tonooka, K. P. Poosanaas, and K. Uchino, "Mechanism of the Bulk Photovoltaic Effect in Ferroelectrics," Proceedings of the 5th SPIE Mtg., San Diego, CA (1998).
64. Poosanaas, P. A. Dogan, S. Thakoor, and K. Uchino, "Dependence of Photostriction on Sample Thickness and Surface Roughness for PLZT Ceramics," Proceedings of the 1997 IEEE Ultrasonics Symposium, Toronto, Ontario, Canada (October 1997).
65. Poosanaas, P. A. Dogan, A.V. Prasadaraao, S. Komarneni, and K. Uchino, "Photostriction of Sol-Gel Processed PLZT Ceramics," *J. Electroceramics* **1** (1), 105-111 (1997).

VOLUME VI

66. Poosanaas, P., A. Dogan, A.V. Prasadaraao, S. Komarneni, and K. Uchino, "Effect of Ceramic Processing Methods on Photostrictive Ceramics," *J. Adv. Perf. Mat.* (1997).
67. Thakoor, S., P. Poosanaas, J.M. Morookian, A. Yavrovian, L. Lowry, N. Marzwell, J. Nelson, R.R. Neurgaonkar, and K. Uchino, "Optical Microactuation in Piezoceramics" (1997).

4.3 New Torsional Amplifier/Actuators

68. Glazounov, A.E., Q.M. Zhang, and C. Kim, "Piezoelectric Actuator Generating Torsional Displacement from Piezoelectric d_{15} Shear Response," *Appl. Phys. Lett.* (1997).
69. Glazounov, A.E., Q.M. Zhang, and C. Kim, "A New Torsional Actuator Based on Shear Piezoelectric Response," Proceedings of SPIE Smart Materials, San Diego, CA (March 1998).

4.4 High Force Amplifiers and Inchworms

70. Uchino, K., J. Zheng, A. Joshi, S. Yoshikawa, S. Hirose, S. Takahashi, and J.W.C. deVries, "High Power Characterization of Piezoelectric Materials" (1997).
71. Uchino, K., "High Electromechanical Coupling Piezoelectrics - How High Energy Conversion Rate is Possible," *Mat. Res. Soc. Symp. Proc.* **459**, 3-14 (1997).
72. Park, S.-E., V. Vedula, M.-J. Pan, W.S. Hackenberger, P. Pertsch, and T.R. Shrout, "Relaxor Based Ferroelectric Single Crystals for Electromechanical Actuators," Proceedings of the SPIE's 5th International Symposium on Smart Structures and Materials, San Diego, CA (March 1998).

Actuator Studies—continued

73. Koopmann, G.H. G.A. Lesieutre, B.R. Dershem, W. Chen, and S. Yoshikawa, "Embeddable Induced Strain Actuators Using Framed 3-3 Piezoceramic Stacks: Modeling and Characterization," Proceedings of the SPIE's 4th Annual International Symposium on Smart Structures and Materials, San Diego, CA (March 1997).
74. Driesch, P.L., G.H. Koopmann, J. Dosch, and H. Iwata, "Development of a Surface Intensity Probe for Active Control Applications," IMECE, Dallas, Texas (November 1997).
75. Galante, T., J. Frank, J. Bernard, W. Chen, G.A. Lesieutre, and G.H. Koopmann, "Design, Modeling, and Performance of a High Force Piezoelectric Inchworm Motor" (1997).
76. Galante, T.P., "Design and Fabrication of a High Authority Linear Piezoceramic Actuator: The PSU H3 Inchworm," Master of Science Thesis, The Pennsylvania State University (August 1997).
77. Lesyna, M.W., "Shape Optimization of a Mechanical Amplifier for Use in a Piezoceramic Actuator," Master of Science Thesis, The Pennsylvania State University (May 1998).

VOLUME VII

78. Uchino, K., "Piezoelectric Ultrasonic Motors: Overview," J. Smart Materials and Structures—Special Issue (1997).
79. Uchino, K., "Compact Piezoelectric Ultrasonic Motors," J. Medical Ultrasonics 24 (9), 1191-92 (1997).

5.0 MODELING and CHARACTERIZATION

5.1 Finite Element Methods

80. Qi, W. and W. Cao, "Finite Element Analysis and Experimental Studies on the Thickness Resonance of Piezocomposite Transducer," Ultrasonic Imaging 18, 1-9 (1996).
81. Qi, W. and W. Cao, "Finite Element Study on Random Design of 2-2 Composite Transducer," SPIE 3037, 176-180 (1997).
82. Geng, X. and Q.M. Zhang, "Evaluation of Piezocomposites of Ultrasonic Transducer Applications—Influence of the Unit Cell Dimensions and the Properties of Constituents on the Performance of 2-2 Piezocomposites," IEEE Transactions on Ultrasonics, Ferroelectrics, and Frequency Control 44 (4), 857-872 (1997).
83. Zhang, Q. and X. Geng, "Acoustic Properties of the Interface of a Uniform Medium-2-2 Piezocomposite and the Field Distributions in the Composite," Jpn. J. Appl. Phys. 36, 6853-6861 (1997).
84. Geng, X. and Q.M. Zhang, "Analysis of the Resonance Modes and Losses in 1-3 Composites for Ultrasonic Transducer Applications," IEEE UFFC (1997).

APPENDIX 44

Focused Spherical Transducers for Ultrasonic Imaging

Sedat Alkoy, *Member, IEEE*, Patrick D. Lopath, Robert E. Newnham, *Member, IEEE*,
The Pennsylvania State University, 254 MRL, University Park, PA 16802, USA

Anne-Christine Hladky-Hennion
IEMN, Departement ISEN, 59046, Lille, France

Joe K. Cochran
Georgia Institute of Technology, School of Mater. Sci. & Eng., Atlanta, GA 30332, USA

Abstract – Spherically focused transducers were prepared from miniature thin-wall lead zirconate titanate hollow spheres (BBs). The spheres were prepared from slurries of soft PZT powders using a coaxial nozzle process, and had diameters ranging from 1 to 6 mm and wall thickness from 12 to 150 μm . Two main vibrations modes, namely radial and thickness modes, were obtained around 1 MHz and 30-40 MHz, respectively. Focused transducers were prepared by machining sections of the hollow spheres. The transducers were characterized in pulse echo mode and by using finite element analysis (FEA). The results obtained from experiments were confirmed by FEA. The transducers were found to have a center frequency of ~ 48 MHz with a bandwidth of 22 % and a minimum insertion loss of ~ 44 dB.

INTRODUCTION

In clinical applications of ultrasonic transducers, higher axial and lateral resolution requires operation frequencies greater than 20 MHz. In recent years transducers operating in this range have been prepared from polymers [1] as well as from ceramics [2]. Polymer based transducers have good beam properties, broad bandwidth, and can be fabricated easily into various shapes, but they are also associated with high losses and low electromechanical coupling coefficients. Therefore, ceramic transducers with their high coupling coefficients and low losses lead to improved image qualities. However, obtaining a focused beam from these transducers suggests a spherical shape, and machining a focused transducer (wall thickness < 100 μm) using conventional techniques is not feasible.

Lockwood et al. [3] developed a bending technique to obtain a spherical shape from very thin ceramic plates. In this technique, a ceramic plate is bonded to a malleable material, an epoxy. This layered composite structure is shaped into a shallow spherical shell by gently pressing it with a ball bearing at 65°C . While this approach works fairly well for high f -number transducers with very high frequencies, it is difficult to apply for transducers that operate below 40 MHz, where ceramic thickness hinders the bending process. Also Zipparo et al. [4] reported a decrease in electromechanical coupling, dielectric constant, mechanical compliance, and an increase in mechanical losses of the ceramic, along with microcracks, resulting from this bending process.

In this paper, preliminary results of our study on the fabrication of focused spherical transducers from miniature piezoelectric hollow spheres (BBs) are reported. Hollow sphere transducers can be readily made with center frequencies of 20 MHz and above. It is also possible to fabricate transducers with f -numbers down to 1. The fabrication of green hollow spheres, and construction of focused transducers from those, are described. Results obtained from impedance and pulse-echo measurements are compared with results of the finite element analysis.

FABRICATION OF THE TRANSDUCERS

Processing of the hollow spheres

Millimeter size thin-wall piezoelectric hollow spheres are produced using a coaxial nozzle slurry process. The process was originally developed by Torobin [5] to mass produce ceramic and metallic hollow spheres. Fabrication of green hollow spheres includes preparation of a slurry of fine-grained PZT-5 powder (grade C5500, Channel Industries, Inc.) along with PMMA (poly methyl-methacrylate) and acetone. This slurry is then injected through a coaxial nozzle with air passing through the center tube. The slurry forms a hollow cylindrical form as it leaves the nozzle. The bottom of the cylinder later closes with surface tension, and air pressure creates a bubble. At a certain inner pressure the bubble breaks free from the rest of the slurry closing the upper end and forming a hollow sphere. This process has been shown to be a flexible technique for the fabrication of hollow spheres of different ceramic compositions with fairly uniform diameters from 1 to 6 mm, and wall thickness from 12 to 150 μm . The green piezoelectric hollow spheres used in this study are produced in the Georgia Institute of Technology with diameters from 3-4 mm and thickness from 40-100 μm .

These green spheres are then fired at 550°C for 30 minutes for binder burnout, and sintered at 1285°C for 90 minutes. Although Fielding et al. [6] reported microcracks, porosity and larger than expected wall thickness variations for PZT hollow spheres, improvements in the fabrication process are being undertaken to minimize these defects as well as wall thickness non-uniformity.

Construction of the focused BB transducers

Following the sintering step spheres are then encased in Crystal Bond™ and ground down to a spherical shell, followed by sputter coating of both surfaces with gold electrodes. Radial poling of the samples is performed in a silicone oil bath at 120°C by applying an electric field of 80 kV/cm. After poling a conductive backing of highly attenuative silver loaded epoxy (Ablebond 16-1 LV, Ablestik Lab., Rancho Dominguez, CA) is centrifuged onto the convex surface. A high speed lathe is used to turn the rear surface of the element back to prevent contact with the ground electrode and a true circle is formed. The self-focused elements are then mounted in a SMA connector for testing using Lockwood's method [3]. A schematic drawing of the finished transducer is shown in figure 1.

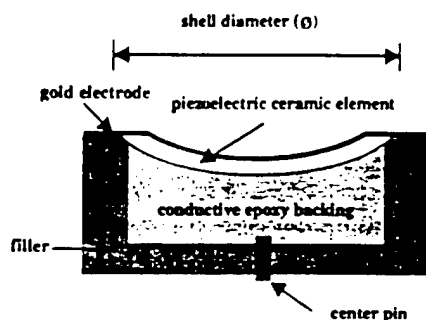


Figure 1. Cross-section of a spherically focused BB transducer

TRANSDUCER CHARACTERIZATION

Transducer characteristics and the performance of the machined and poled ceramics are evaluated by dielectric measurements using an HP Multifrequency LCR meter at 1.0 volt and 1.0 kHz, and by impedance measurements using a HP Impedance-Gain Phase Analyzer up to 100 MHz.

Transducers are also tested in water bath by reflecting off a smooth metal target placed at the transducer's focal point. Excitation was achieved using a Panametrics model 5900 PR computer controlled pulser receiver. Due to the thin composite structure, 6 dB of attenuation is included in the line before the transducer to protect against breakdown of the transducer element. The reflected waveform is received at 50 ohms and digitized on a 500 MHz Lecroy oscilloscope. A limiter / expander setup similar to that used by Zipparo et al. [4] is used to account for the transmission line effects seen in the coaxial cable at these elevated frequencies. The waveform is then downloaded to a PC via GPIB for later processing. Bandwidth and insertion loss measurements are made from frequency domain data calculated from the downloaded time domain data using the MathCad software package.

Evaluation of the transducer performance is also done with finite element analysis computations using the ATILA code. The ATILA was developed by the Acoustics Department at the Institut Supérieur d'Electronique du Nord (ISEN) for modeling of transducers. A static analysis can be performed with ATILA, which provides information concerning

prestresses and the behavior under hydrostatic pressure. Modal analysis can be carried out to identify the vibration modes and determine their resonance frequencies and associated coupling factors. Finally, in-air or in-water impedance and displacement field, transmit voltage response, and sonar directivity patterns can be modeled using a harmonic analysis procedure [7]. The ATILA code proved to be very effective in the modeling of full hollow sphere transducers in a previous study [8]. In this study, it is used to identify the modes of vibration and their frequencies, to determine the effect of backing layer thickness on these vibrations, and evaluation of the acoustic pressure field created by a focused transducer.

RESULTS AND DISCUSSION

Modes of vibration of focused transducers

Results of the finite element analysis of the in-air focused transducers suggest two main modes of vibration for the radial poling configuration: (1) a radial mode around 1 MHz utilizing the d_{11} coefficient where the spherical shell vibrates similar to a disk, and (2) a wall thickness mode around 30 MHz utilizing the d_{33} coefficient. The dimensions and materials properties used in these computation are as follows: a shell diameter (ϕ) of 1.69 mm which was machined from a full sphere with 1.75 mm radius (r) and with a wall thickness of 65 μm . $s_{11}^E = 16.4 \times 10^{-12} \text{ m}^2/\text{N}$, $s_{12}^E = -5.74 \times 10^{-12} \text{ m}^2/\text{N}$, $\rho = 7.75 \text{ g/cm}^3$. Finite element analysis results suggest that harmonics of the radial vibration mode and several radial modes coupled to the thickness mode vibration are also expected from a shell. Normally, the frequency range of these vibrations can be shifted to higher or lower frequencies by changing the sphere size, shell diameter or wall thickness of the spheres. An experimentally obtained impedance-frequency spectrum is shown in figure 2. From the measurements the thickness mode electromechanical coupling coefficient, $k_t = 0.51$ is calculated. A similar response is observed in both the FEA and measurements, but with different resonance frequencies. This is due to the fact that FEA analysis assumes a transducer with certain uniform dimensions, but dimensions vary from sample to sample accompanied with non-uniformity in their wall thickness.

FEA analysis of a focused BB after backing it with conductive epoxy indicates that backing damps the spurious harmonics and coupled modes, and causes a shift in thickness mode resonance frequency towards lower frequencies. The results of the analysis are given in table 1 along with the measured frequencies obtained from the figure 2.

Transducer characteristics

Transducer characteristics are measured in a water bath using the set-up explained in the "Transducer Characterization" section. The transducer was excited with a 16 V monocycle pulse, and the pulse echo response was obtained by recording the reflection from a smooth metal target placed at the transducer's focal point. The focal distance

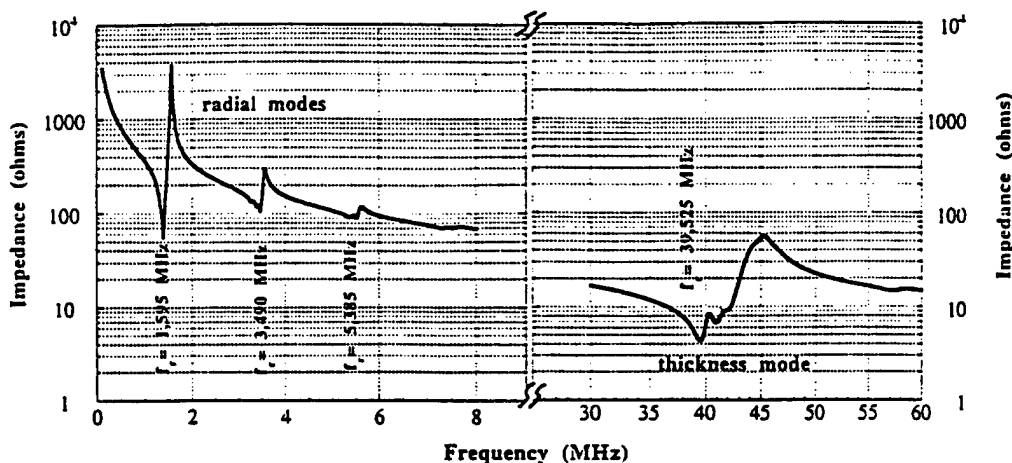


Figure 2. Impedance spectrum of a focused spherical BB transducer

Table 1. Resonance frequencies of main vibration modes

Backing thickness (mm)	Radial Modes (MHz)		Thickness Mode (MHz)	
	FEA	Exp.	FEA	Exp.
0.0	1.148	1.595	29,850	39,525
	2.816	3,490		
	4,436	5,385		
1.22	-	-	28,200	
2.22	-	-	27,000	
3.22	-	-	26,700	

was set by adjusting the transducer-reflector separation until a maximum amplitude of returned signal is obtained. The pulse echo response of the transducer is given in figure 3. Bandwidth and insertion loss of the transducer is calculated from frequency domain data using MathCad from the measured time domain data. The results of these calculations are plotted in figure 4. The pulse is centered at 47.7 MHz with a 6 dB bandwidth of 22%. A minimum insertion loss of -44 dB was obtained from the samples. At this preliminary stage, the bandwidth of the focused BBs is low and insertion loss is high compared to commercially available transducers. However, improvements are possible through decreasing size of the shells and designing proper backing and quarter wave matching layers. According to Zipparo et al. [4] single element high frequency transducers made from PZT materials with areas larger than 1 mm^2 can have an electrical impedance substantially lower than 50Ω which is that of the operation electronics. This results in higher insertion losses and longer pulse length. This problem can be alleviated by either using a piezoelectric material with a lower dielectric constant such as lead titanate (PbTiO_3) or by decreasing the area of the element, both of which result in decreasing the capacitance and thereby increasing the impedance.

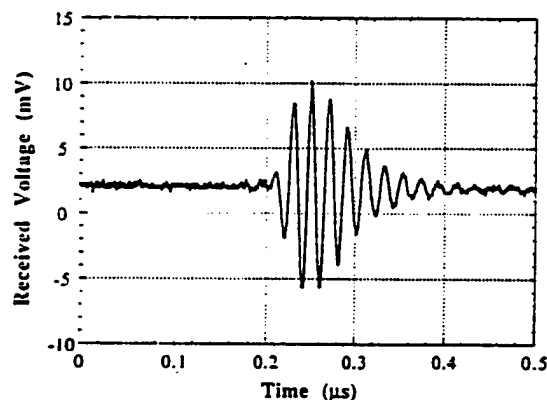


Figure 3. Pulse echo response of the focused transducer

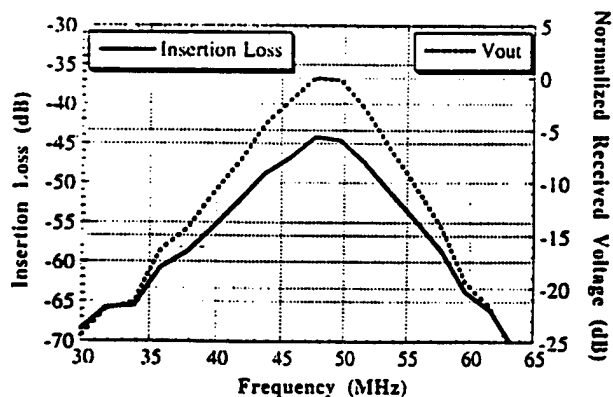


Figure 4. Pulse spectrum and insertion loss of the transducer. The center frequency is calculated to be 47.7 MHz with a 6 dB bandwidth of 22. A minimum insertion loss of -44 dB is obtained.

As a part of evaluation of the design, the acoustic pressure field created by the focused BB is computed as a function of distance in two dimensions (x and y) at different instants in an interval of 0 – 3 μ s using ATILA. The finite element mesh used for this computation is shown in figure 5. The computation of variation of acoustic pressure at point A on the transducer surface as a function of time indicates that the first

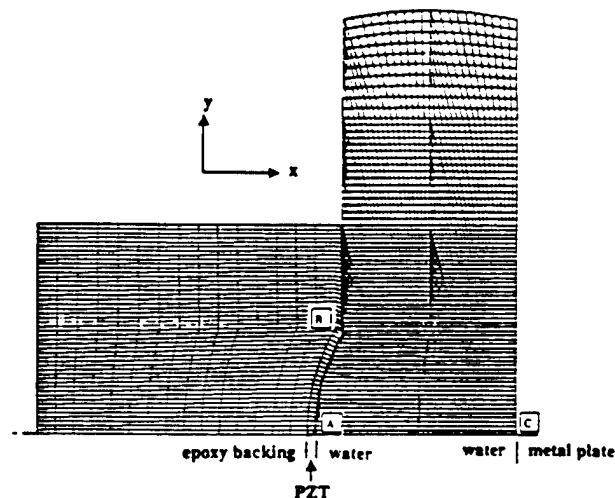


Figure 5. The finite element mesh used in the computation of the in-water performance of focused transducers

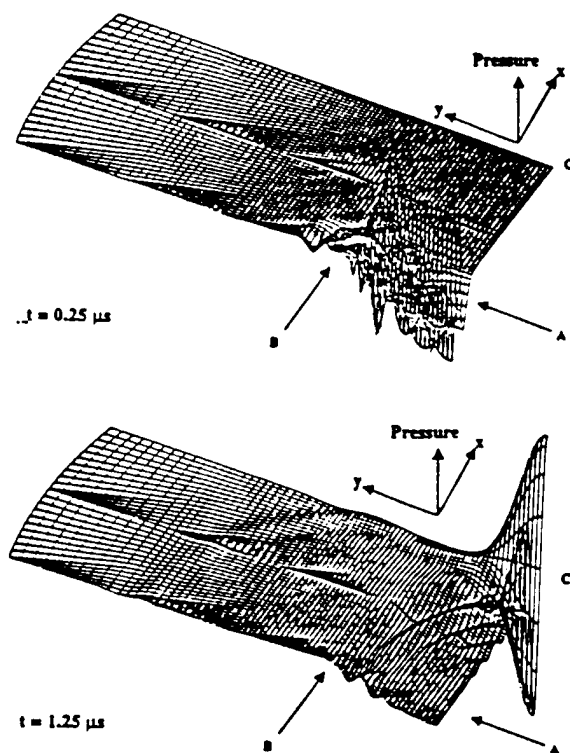


Figure 6. Acoustic pressure created by the focused transducer represented in 3-D at different instants

maximum appears at 2.32×10^{-4} seconds. Taking the velocity of sound in water to be 1489 m/s, this first peak corresponds to a focal distance of 1.727 mm. The plots of the acoustic pressure in three dimensions at different instants given in figure 6 clearly show the focusing action.

SUMMARY AND CONCLUSIONS

High frequency biomedical applications require transducers with high sensitivity, broad bandwidth and a focused ultrasound beam for increased resolution. In this paper, preliminary results from the characterization of a focused ceramic transducer operating in high frequencies (> 20 MHz) fabricated from piezoelectric hollow spheres are discussed. Hollow spheres have an inherent focus, and the process used in fabricating them allows for the dimensions of the spheres to be tailored to specific requirements. Hence, the resonance frequencies of the available vibration modes can also be tailored. Initial results do not present an improvement over polymer based transducers in terms of bandwidth and insertion loss. However, the results do warrant further studies of spherically focused transducers from hollow spheres in order to improve their characteristics, with a view to ultimately applying them in medical ultrasound applications.

REFERENCES

- [1] M. S. Shearer and F. S. Foster, "The design and fabrication of high frequency poly (vinylidene fluoride) transducers," *Ultrasonic Imaging*, vol. 11, pp. 75-94, 1989.
- [2] F. S. Foster, L. K. Ryan and D. H. Turnbull, "Characterization of lead zirconate titanate ceramics for use in miniature high-frequency (20-80 MHz) Transducers," *IEEE Trans. Ultrason. Ferroelec. Freq. Contr.*, vol. 38, no.5, pp. 446-453, 1991.
- [3] G. R. Lockwood, D. H. Turnbull and F. S. Foster, "Fabrication of high frequency spherically shaped ceramic transducers," *IEEE Trans. Ultrason. Ferroelec. Freq. Contr.*, vol. 41, no. 2, pp. 231-235, 1994.
- [4] M. J. Zipparo, K. K. Shung and T. R. Shrout, "Piezoceramics for high-frequency (20 to 100 MHz) single-element imaging transducers," *IEEE Trans. Ultrason. Ferroelec. Freq. Contr.*, vol. 44, no. 5, pp. 1038-1048, 1997.
- [5] L. B. Torobin, "Methods of making hollow, porous microspheres," *U.S. Patent 4,671,909*, 1987.
- [6] J. T. Fielding, Jr., D. Smith, R. Meyer, Jr., S. Troler-McKinstry and R. E. Newnham, *IEEE Int. Symp. Appl. Ferroelec.*, pp. 202-5, 1994.
- [7] A. C. Hladky-Hennion and J. N. Decarpigny, "Finite element modeling of active periodic structures: application to 1-3 piezocomposites," *J. Acoust. Soc. Amer.*, vol. 94, pp. 621-635, 1993.
- [8] S. Alkoy, A. Dogan, A. C. Hladky, P. Langlet, J. K. Cochran and R. E. Newnham, "Miniature piezoelectric hollow sphere transducers (BBs)," *IEEE Trans. Ultrason. Ferroelec. Freq. Contr.*, vol. 44, no.5, pp. 1067-1076, 1997.

APPENDIX 45

MINIATURE PIEZOELECTRIC HOLLOW SPHERE TRANSDUCERS (BBs)

Sedat ALKOY, Aydin DOGAN, Anne-Christine HLADKY*, Philippe LANGLET*,
Joe. K. COCHRAN**, and Robert E. NEWNHAM,

IMRL, The Pennsylvania State University, University Park, PA 16802, USA

*IEMN-Departement ISEN, 41 Boulevard Vauban, 59046 LILLE Cedex, France

**Georgia Institute of Technology, Atlanta, GA 30332, USA

Abstract - Miniature piezoelectric transducers were prepared from millimeter size hollow spheres which have been formed from PZT-5A powder slurries using a coaxial nozzle process. After sintering, the spheres were poled in two ways: radially and tangentially. Principal modes of vibration were found to be a breathing mode near 700 kHz and a thickness mode near 13 MHz for the radially poled spheres, and an ellipsoidal, a circumferential, and a breathing mode near 230 kHz, 350 kHz, and 700 kHz, respectively for tangentially poled spheres. Coupled modes were also observed at higher frequencies. These same modes with similar frequencies were obtained from finite element analysis using the ATILA FEM code, and experimental results were shown to be consistent with the modeling study. Hydrostatic d_h coefficients ranged between 700 - 1,800 pC/N which is considerably higher than the d_h of bulk PZT. The hydrophone figure of merits ($d_h * g_h$) were calculated to be between 68,000 - 325,000 * $10^{-15} \text{ m}^2/\text{N}$ for various types of poled spheres. These values are three orders of magnitude higher than the bulk PZT figure of merit. Potential applications include ultrasonic imaging, non-destructive testing, and hydrophones.

I. INTRODUCTION

Lead zirconate titanate (PZT) based ceramics have been the leading piezoelectric materials for electromechanical transducers for the last 40 years [1]. However, for both underwater hydrophones and biomedical ultrasound applications, bulk PZT is a poor material for several reasons. The hydrostatic piezoelectric charge coefficient, $d_h (=d_{33}+2d_{31})$ of PZT is very low due to the opposing signs of d_{33} and d_{31} . The hydrostatic piezoelectric voltage coefficient, $g_h (=d_h/\epsilon_r \cdot \epsilon_0)$ is also low because of the high dielectric constant, ϵ_r , of PZT. In addition to those drawbacks, the acoustic impedance matching of PZT with water and the human body (density $\approx 1.0 \text{ g/cm}^3$) is poor due to the high density (7.75 g/cm^3) of bulk PZT.

Since the 1980's attempts have been made to overcome those problems by coupling the ceramic material with polymers [2,3] and metals [4,5], and introducing hollow spaces into the transducer structure. These studies succeeded in improving the hydrostatic piezoelectric properties by decreasing the density of the transducer, and by amplifying the sensing and actuating characteristics of the ceramic by redesigning the transducer.

In developing new transducers, the biological world has often been used as the inspiration for innovative ideas and new designs. Sharks, fish and the other inhabitants of the underwater world - the way they talk and listen - can be imitated in piezoelectric transducer designs. The piezoelectric hollow sphere transducers described in this paper and elsewhere [6] are modeled after the inner ear of a fish. The inner ear is made up of inertia-sensing chambers resembling accelerometers. Within each chamber is a dense ear stone (otolith) which vibrates in a near field sound wave. The inertia of the ear stone causes it to lag behind the motion of the fish, and to push against the hair cells lining the chamber (sacculus). On bending, the hair cell membranes deform, stimulating neural transmissions to the brain. Connections to swim bladder of the fish further improve the sensitivity to far-field sound. [7]

Directional characteristics are important in designing a transducer for underwater and biomedical applications. Several novel transducers based on a spherical design have been

introduced by researchers in order to exploit symmetry to achieve omnidirectional transmit and receive responses. In the area of underwater acoustics, these designs include hollow ceramic spheres with various electrode and poling patterns [8-11], spherical arrays of small, planar hydrophones [12], magnetostrictive diaphragms with spherical forms [13], and fiber optic windings wrapped around a resilient ball to form a spherical, omnidirectional acoustic sensor [14]. A similar trend towards spherically shaped transducers is also evident in high frequency biomedical ultrasonic transducers. Recently, a quasi-omnidirectional polymer based transducer was developed by Vilkomersan et al.[15] for ultrasonic guidance of catheters. Another study on focused transducers for biomedical ultrasonic imaging proposed a spherical ceramic shell structure with an inherent focal length as a solution.[16]. In addition to omnidirectionality, smaller sizes are necessary in some applications. For example, smaller transducers can be used to achieve improved resolution and higher power densities in intravascular image catheters in biomedical ultrasound. Smaller transducers can also be used in embedded sensors for nondestructive evaluation, or in flow noise studies of complex surface structures in underwater ultrasound. In comparison with other spherical transducers, the millimeter size, thin wall piezoelectric hollow sphere transducers (BBs) are much smaller in size, and possess a higher radius to thickness ratio (r/t). BBs are omnidirectional and have a low density ($\sim 1.3 \text{ g/cm}^3$), both of which are inherent to the unique structure and design of the transducer. As discussed in the proceeding section, they are produced by a simple, inexpensive process in large numbers, which makes it possible to mass produce throw-away transducers.

In this paper, several poling and electroding configurations for the hollow sphere transducers are introduced. Results of the dielectric and hydrostatic piezoelectric charge coefficient measurements are presented. Vibration modes and their resonance frequencies are identified by the ATILA finite element analysis code and the results of the modeling study are compared with the experimentally obtained admittance spectra.

II. FABRICATION OF PZT HOLLOW SPHERE TRANSDUCERS

Green PZT spheres are prepared using a fabrication technique, which was developed by Torobin [17] to produce large numbers of ceramic and metallic hollow spheres. A fine-grained slurry of PZT-501A (Ultrasonic Powders, Inc.) is prepared and injected through a coaxial nozzle with air passing through the center tube. The slurry exits the nozzle in a hollow cylindrical form, but the bottom later closes because of surface tension and hydrostatic pressure. The closed cylinder is inflated into a bubble by the inner air pressure until the pressure equals that of the cylinder. At this critical pressure the bubble closes, and the sphere breaks free. The Torobin process has been shown to be a flexible fabrication technique for hollow spheres of various compositions [18,19]. It also allows us to tailor the size (1 to 6 mm in diameter) and the wall thickness (12 to 150 μm) of the spheres by changing the viscosity and air jet velocity.

The green PZT spheres are fired at 550°C for 30 minutes for binder burnout, followed by sintering at 1285°C for 90 minutes. Sintering is performed in a closed alumina crucible in a bed of PZT powder to minimize lead loss from the spheres. A physical characterization study by Fielding et.al. [20] concluded that spheres with a sintered diameter of ~ 2.76 mm and a mean wall thickness of 80 μm contain microcracks and substantial porosity. The results reported in this paper are obtained from the same batch of spheres. Density measurements using the Archimedes method gave an average bulk sphere wall density of ~ 7.2 g/cm³. Although this value is close to the theoretical density of PZT ceramics (~ 7.75 g/cm³), the measurement technique is not very sensitive to open pores and microcracks, such as those reported by Fielding et al. [20]. The wall thickness variation was also found to be larger than expected, ranging from 40 to 100 μm . Improvements in the fabrication process are being undertaken to minimize these defects and wall thickness variations, since they degrade the dielectric and electromechanical properties and disturb the vibration modes of the transducer.

Two poling configurations have been studied: radial poling with inside and outside electrodes, and top-to-bottom poling with two external cap electrodes, (see Fig.1). For top-to-bottom poling, three symmetric electrode configurations, with electrode gap dimensions (d) of $d = 0.79$ mm (Type-1), $d = 1.38$ mm (Type-2) and $d = 1.71$ mm (Type-3) were investigated. The effect of increasing the poled regions on the capacitance, vibration modes and hydrostatic sensitivity of the transducer was examined.

For radial poling Conductive Silver 200 (Demetron GmbH) was used as the inner electrode after drilling an electrode hole with a diameter of about $450\text{ }\mu\text{m}$ prior to the binder burnout step. Silver electrical lead wires were attached and the electrode hole was sealed using E-solder # 3021 (Insulating Materials, Inc.) silver epoxy adhesive. A thin layer of gold was deposited as the external electrode for both the radial and top-to-bottom configurations. Poling was carried out with an electric field of 20 kV/cm at 120°C in a silicone oil bath. Prior to the hydrostatic measurements, a soft polyurethane (Dexter Hysol us-0089) coating, with an average thickness of less than $50\text{ }\mu\text{m}$, was applied for insulation and to provide extra strength under hydrostatic pressure. The dielectric and piezoelectric measurements reported here were performed on spheres with no protective coating, and the hydrostatic piezoelectric measurements were performed on spheres with the coating.

Three samples for each electrode configuration were prepared and evaluated in order to assess the reproducibility of the results. The results reported in this paper are average values, and fall within a $\pm 15\%$ range.

III. "ATILA" FINITE ELEMENT CODE

ATILA is a finite element code developed by the Acoustics Department at ISEN for the modeling of sonar transducers. It can provide information concerning prestresses, and the behavior under hydrostatic pressure (static analysis), together with the resonant frequencies

of various modes and the associated coupling factors (modal analysis), the in-air or in-water impedance and displacement field, the Transmitting Voltage Response and the directivity patterns (harmonic analysis). [21-23]

In our study, ATILA was used to identify the modes of vibration and to determine the resonance and antiresonance frequencies of these modes for different electrode configurations. The frequency step used in the finite elements computation was 10kHz in all cases, except for the thickness mode of radially poled spheres. In the computation of the thickness mode, the frequency step was 100 kHz, since the frequency range under investigation was in the MHz. The resultant calculated admittance vs. frequency spectra are compared with the experimental measurements obtained using an HP 4194-A Impedance/Gain Phase Analyzer. The polyurethane coating was not taken into consideration in the modeling study, since the dielectric and piezoelectric measurements reported here were performed on spheres with no protective coating. The mass of the electrode was assumed to be negligible.

IV. RESULTS AND DISCUSSION

A. Dielectric Characterization

Dielectric properties of the transducers were measured using a HP 4275-A Multi-frequency LCR Meter at 1.0 kHz and 1.0 Volt. For radially poled spheres the capacitance was 2.900 pF and the dielectric loss was 0.020. The relative dielectric constant (ϵ_r) of about 1,000 was calculated from the capacitance using the following equation for a spherical capacitor [6] :

$$C = 4\pi\epsilon_r\epsilon_o\left(\frac{r_i r_o}{r_o - r_i}\right) \quad (1)$$

Compared to the relative dielectric constant of UPI 501A ceramics ($\epsilon_r=1,850$), this lower than expected dielectric constant can be attributed to wall thickness variations, incomplete inner electrode, and the defects observed in the sphere wall [20]. In the case of top-to-bottom poled spheres, capacitance values ranging from 3 to 7 pF is measured, (see Table 1). Those values are also low compared with the calculated values of 9 to 11 pF computed using a cylindrical tube approximation [6] :

$$C = \epsilon_r \epsilon_o \frac{\pi t (r_i + r_o)}{d} \quad (2)$$

As expected, the capacitance of top-to-bottom poled spheres is highly dependent on the electrode size and uniformity.

B. Modes of vibration of radially poled transducers :

Finite Element Analysis (FEA) of a radially poled hollow sphere suggests two principal modes of vibration as shown in the calculated admittance spectra (Fig.2a). The first mode is a volumetric expansion and contraction of the sphere, the so-called breathing mode utilizing d_{31} . The resonance and antiresonance frequencies of this mode are calculated as 620 kHz and 780 kHz, respectively. Materials properties used in these calculations are as follows: $s_{11}^E = 16.4 \cdot 10^{-12} \text{ m}^2/\text{N}$, $s_{12}^E = -5.74 \cdot 10^{-12} \text{ m}^2/\text{N}$, $\rho = 7.75 \text{ g/cm}^3$. Using the relation [24]

$$k_p^2 = 1 - \frac{f_r^2}{f_a^2} \quad (3)$$

the planar coupling factor (k_p) is calculated as 0.61 from the FEA results. The second vibration mode is identified as the wall thickness mode of the sphere, and the predicted frequencies are $f_r = 21.5 \text{ MHz}$ and $f_a = 24.0 \text{ MHz}$.

In comparison to the FEA results, the experimental admittance spectra obtained from a radially poled sphere transducer with a $\sim 450 \mu\text{m}$ diameter electrode hole, and with an inner radius (r_i) = 1.30 mm, outer radius (r_o) = 1.38 mm, and an average wall thickness (t) = 80 μm is shown in Fig.2b. The experimental measurements agree well with the FEA results. For the breathing mode the resonance and antiresonance frequencies are 633 kHz and 686 kHz, respectively. Since the breathing mode frequency is mainly controlled by the diameter of the sphere [6], the close agreement between the calculated and measured values indicates a fairly uniform diameter for the spheres. The planar coupling factor is calculated as 0.38 from these measurements. The difference between the calculated and observed values of k_p is attributed to the electroding problems of the inner sphere surface. However, the resonance and antiresonance frequencies of 13.4 MHz and 13.8 MHz, respectively, for the thickness mode vibration - which is determined from the sample given in Fig.2b - is quite different from the values suggested by FEA. The thickness mode itself has only been detected in a few of the samples, and the samples which possess a detectable thickness mode reveal this response as a smooth, broad peak in the admittance spectra. This discrepancy between the calculated and observed values is due to the large variations in wall thickness, as reported previously [20].

C. *Modes of vibration of top-to-bottom poled transducers*

A static analysis of the top-to-bottom poling configuration using ATILA to determine the polarization direction gives the electrical potential isocontours shown in Fig.3. The results of the analysis indicate that only the unelectroded region between the electrode caps is tangentially poled, and the regions under the electrodes are unpoled and therefore inactive. The electrode gap is expected to control the dielectric and acoustic properties of the transducer. Three types of top-to-bottom poled spheres with increasing electrode gap dimensions were studied. The principal mode of vibration under investigation for top-to-

bottom poling configuration is the ellipsoidal distortion of the sphere. However, FEA results indicate the presence of two other modes as well: a higher order circumferential mode and a breathing mode, together with higher frequency coupled modes. The admittance spectra obtained from FEA for a sphere with type-3 electrode configuration, i.e. with the largest electrode gap, is compared with the experimentally obtained spectra in Fig.4. Each major peak in the spectra was studied by FEA and the displacement fields of these vibrations are shown in Fig.5.

The calculated and experimental resonance and antiresonance frequencies of all three types of transducers are listed in Table 2 . It is clear from these values that there is a close match between the modeling and the measurements for the three main vibration modes. However, in the case of the coupled vibration modes, the measured frequencies differ significantly from the values calculated by FEA. This is attributed to the non-uniform wall thickness of the spheres, since these vibrations result from coupling between the ellipsoidal and thickness modes, or between the circumferential and thickness modes.

Another result obtained from the experiments and confirmed by the FEA is the introduction of new higher order circumferential-thickness coupled modes created by decreasing the electrode separation (see Table 2).

D. Effect of Polymer Coating

Prior to the hydrostatic measurements the spheres were dip-coated with polyurethane. Admittance spectra of a radially poled sphere recorded before and after the polymer coating are shown in Fig.6. It is found that the polymer coating has a clamping effect on the spheres, causing a decrease in the peak amplitude of the breathing mode, and a smoothing of the spectrum. A similar effect is observed for the top-to-bottom poled spheres leading to a slight shift of the ellipsoidal and breathing modes to lower frequencies. This shift is about 10 kHz for the ellipsoidal mode, and 20-40 kHz for the breathing mode.

E. Hydrostatic sensitivity measurements

As part of the transducer characterization, hydrostatic measurements were carried out on poled and coated hollow spheres for possible application as underwater hydrophones. The hydrostatic piezoelectric charge coefficient (d_h) was measured in an oil bath at hydrostatic pressures from 100 to 1,000 psi with a 30 Hz stimulus. A PZT disc was used to calibrate the measurements. The d_h results are plotted in Fig.7a as a function of hydrostatic pressure.

The hydrostatic piezoelectric voltage coefficient (g_h), and hydrophone figure of merit of the spheres are defined and calculated from the measured d_h values:

$$g_h = \frac{d_h}{\epsilon_{33}} \quad (4)$$

$$figure\ of\ merit = d_h * g_h \quad (5)$$

The results are plotted in Fig.7b for the hydrophone figure of merit vs. hydrostatic pressure. The measured and calculated values for both d_h and figure of merit are presented in Table 1. From these plots, the d_h values of the BBs are found to be one to two orders of magnitude higher than the d_h of bulk PZT, with the radially poled BBs displaying the highest d_h of all. Similarly the hydrophone figure of merit is three orders of magnitude higher than that of bulk PZT. Finally, evaluation of the results indicates that increasing the electrode separation for top-to-bottom poled spheres results in an increase in the hydrostatic sensitivity.

The amplification of the d_h and figure of merit results from the geometry of the spherical BBs. A simplified explanation can be derived using Timoshenko's [25] argument for the transformation of an applied hydrostatic pressure on a spherical shell into a radial stress (σ_r) and two tangential stresses (σ_t). This is schematically shown in figure-8. These stresses can be calculated using the following relations

$$\sigma_r = \frac{p_o r_o^3 (r^3 - r_i^3)}{r^3 (r_i^3 - r_o^3)} - \frac{p_i r_i^3 (r_o^3 - r^3)}{r^3 (r_i^3 - r_o^3)} \quad (6)$$

$$\sigma_t = \frac{p_o r_o^3 (2r^3 + r_i^3)}{2r^3 (r_i^3 - r_o^3)} - \frac{p_i r_i^3 (2r^3 - r_o^3)}{2r^3 (r_i^3 - r_o^3)} \quad (7)$$

where P_o is the outer hydrostatic pressure, P_i is the inner hydrostatic pressure, and r is the radius at which the stress is evaluated. For a thin-walled shell with the wall thickness ($t = r_o - r_i$), assuming $P_i = 0$, the above equations are simplified to give average stresses of:

$$\sigma_t = -8.89 * P_o \approx -0.50 * P_o * (r/t) \quad (8)$$

$$\sigma_r = -0.50 * P_o \quad (9)$$

The ratio (r/t) is the stress amplification factor which makes hollow spheres important as a sensor. From the known relation between polarization (P) and stress (σ)

$$P_3 = d_{31} * \sigma_1 + d_{32} * \sigma_2 + d_{33} * \sigma_3 = -P_o * d_h \quad (10)$$

Using the stress configuration in figure-8, and combining equation (10) with equations (8) and (9), we obtain the following relations :

$$\text{radial poling} \quad d_h = 0.5 * d_{33} + 17.8 * d_{31} \quad (11)$$

$$\text{top-to-bottom poling} \quad d_h = 8.89 * d_{33} + 9.39 * d_{31} \quad (12)$$

From equation (11) a d_h of about 2,600 pC/N is calculated for radial poling assuming that

90 % of the sphere surface is electroded and poled effectively. This is somewhat larger than the average measured value d_h of 1800 pC/N. The difference is attributed to the defects in the sphere wall and the imperfect inner electrode. For top-to-bottom poling the model holds better, and equation (12) gives d_h values ranging from 550 pC/N to 1,190 pC/N for poled regions of 28.6 % for type-1 to 62 % for type-3. Experimental d_h values of 743 pC/N to 870 pC/N were recorded.

Comparison of the BBs with the commercially available hollow sphere transducers for underwater hydrophones indicates that the BBs have an advantage in size, stress amplification factor (r/t) and cost. Currently, in the market the smallest sphere available has a radius of ~2.8 mm and a wall thickness of ~800 μ m. The r/t ratio is ~ 3.5, whereas BBs have a r/t ratio of 17. Although there are no available data on the d_h of the conventional spheres, the higher stress amplification factor of BBs suggests a much higher d_h and figure of merit.

V. CONCLUSIONS

Small, hollow-sphere piezoelectric transducers can be prepared with an inexpensive and flexible manufacturing process. The main modes of vibration for radially poled PZT spheres are the breathing and thickness modes, which can be tailored over a frequency range of 200 kHz to 20 MHz by changing the diameter and the wall thickness. The principal modes of vibration for top-to-bottom poled spheres are ellipsoidal, higher order circumferential and breathing modes. Higher frequency ellipsoidal and higher order circumferential modes coupled to a thickness mode are also observed. Compared to bulk PZT, much higher d_h and $d_h \cdot g_h$ values are obtained with the BB transducer design.

ACKNOWLEDGMENTS

This study is partly funded by ONR through contract # N0001492J1510, and by the Gebze Institute of Technology - Turkey. We thank the Georgia Institute of Technology - USA and IEMN, Department ISEN - France for letting us use their facilities.

REFERENCES

- [1] B. Jaffe, W.R. Cooke & H. Jaffe, *Piezoelectric Ceramics*, Academic Press, 1971, pp.135-83
- [2] K.A. Klicker, J.V. Biggers & R.E. Newnham, " Composites of PZT and epoxy for hydrostatic transducer applications", *J. Amer. Ceram. Soc.*, 64, pp.5-9, 1981
- [3] T.R. Gururaja, R.E. Newnham, K.A. Klicker, S.Y. Lynn, W.A. Schulze, T.R. Shrout & L.J. Bowen, "Composite piezoelectric transducers" in *Proc. IEEE Ultrason.Symp.*, 1980, 2, pp 576-581
- [4] Q.C. Xu, S. Yoshikawa, J. Belsick & R.E. Newnham, " Piezoelectric composites with high sensitivity and high capacitance for use at high pressures". *IEEE Trans. Ultrason. Ferroelec. Freq. Cont.*, 38, 6, pp.634-639, 1991
- [5] A. Dogan, "Flextensional moonie and cymbal actuators", *Ph.D. Thesis*, The Pennsylvania State University, University Park, 1994
- [6] R. Meyer, Jr., H. Weitzing, Q. Xu, Q. Zhang & R.E. Newnham. " Lead Zirconate Titanate hollow sphere transducers", *J. Amer. Ceram. Soc.*, 77, (6), pp. 1669-1672, 1994
- [7] C.E. Bond, in *Biology of Fishes*, Saunders College Publishing Co., Philadelphia, PA, 1979
- [8] S. Hanish. "Theory of a very thin piezoceramic hollow sphere underwater sound radiator", *NRL Report 5267*, 1959, Naval Research Laboratory, Washington, D.C.

- [9] L. E. Ivey, "NRL-USRD Series F42 Omnidirectional Standard Transducers", *Underwater Sound Reference Detachment*. 1979, Naval Research Laboratory, Orlando, FL
- [10] J.W. Holloway, "Omnidirectional high sensitivity hydrophone". *U.S. Patent* No. 3,805,226 , 1974
- [11] S.L. Ehrlich, " Spherical acoustic transducer", *U.S. Patent* No. 3,732,535 , 1973
- [12] W.L. Clearwaters, L.T. Einstein. P.F. Radics. Jr. & J.W. Soderberg, "Electrically steerable spherical hydrophone array", *U.S. Patent* No. 4,203,162 , 1980
- [13] S. Klein, "Omnidirectional transducer of elastic waves with a wide pass band and production process", *U.S. Patent* No. 4,782,471 , 1988
- [14] S.A. Fisher, "Omni-directional hydrophone". *U.S. Patent* No. 5,155,707 , 1992
- [15] D. Vilkomerson & D. Lyons, "A system for ultrasonic beacon-guidance of catheters and other minimally-invasive medical devices", *IEEE Trans. Ultrason., Ferroelec., Freq. Contr.*, vol. 44, no 1, pp. 27-35, 1997
- [16] G.R. Lockwood, D.H. Turnbull & F.S. Foster. "Fabrication of high frequency spherically shaped ceramic transducers", *IEEE Trans. Ultrason., Ferroelec., Freq. Contr.*, vol. 41, no 2, pp. 231-235. 1994
- [17] L.B. Torobin. " Methods of making hollow, porous microspheres". *U.S. Patent* No. 4,671,909 , 1987
- [18] R.B. Clancy, T.H. Sanders, Jr. & J.K. Cochran, "Fabrication of hollow nickel spheres and low density syntatic foams", in *Light Weight Alloys for Aerospace Applications II*. Edited by E.W. Lee & N.J. Kim. The Minerals. Metals and Materials Society, Warrendale.PA,1991. pp.477-85
- [19] A.T. Chapman, J.K.Cochran, Jr., J.M. Britt & T.J. Hwang, " Thin-wall hollow spheres, from slurries", DOE-ECUT Program. ORNL Subcontent 86X-22043C, *Annual reports*. 1987,1988, 1989. Department of Energy, Washington. D.C
- [20] J.T. Fielding, Jr., D. Smith. R. Meyer, Jr., S. Trolrier-McKinstry & R.E.

- Newnham, "Characterization of PZT hollow sphere transducers", *IEEE Int. Symp. Appl. Ferroelec.*, 1994, pp.202-205
- [21] A.C. Hladky-Hennion & J.N. Decarpigny, "Finite element modelling of active periodic structures: application to 1-3 piezocomposites", *J. Acous. Soc. Am.*, 94, pp.621-635, 1993
- [22] B. Hamonic, J.C. Debus, J.N. Decarpigny, D. Boucher & B. Tocquet, "Analysis of a radiating thin-shell sonar transducer using the finite element method", *J. Acous. Soc. Am.*, 86, (4), pp.1245-1253, Oct. 1989
- [23] A.C. Hladky-Hennion & J.N. Decarpigny, "Application of the finite element method to the modeling of 2D and 3D passive or active structures", *Ultrason. Int. Conf. Proc.*, 1991, pp.415-418
- [24] D.A. Berlincourt, D.R. Curran & H. Jaffe, "Piezoelectric and piezomagnetic materials and their function in transducers" in *Physical Acoustics*, Vol. 1, Part A, Edited by W.P. Mason, Academic Press, New York, 1964, pp.169-257
- [25] S. Timoshenko and J.N. Goodier, in *Theory of Elasticity*, McGraw Hill Book Company Inc. , New York, 1951

LIST OF FIGURES

Figure-1 Poling Configurations

- (a) Radial poling configuration
- (b) Top-to-bottom poling configuration

Figure-2. Admittance spectra of a radially poled PZT hollow sphere transducer

- (a) calculated
- (b) observed

Figure-3. Polarized region of a top-to-bottom poled sphere

Figure-4. Admittance spectra of a top-to-bottom poled PZT hollow sphere transducer

- (a) calculated
- (b) observed

Figure-5. Modes of vibration of a top-to-bottom poled piezoelectric hollow sphere

- (a) Ellipsoidal mode ($f_r \sim 240$ kHz)
- (b) Higher order circumferential mode ($f_r = 300 - 400$ kHz)
- (c) Breathing mode ($f_r \sim 600$ kHz)
- (d) Ellipsoidal + thickness coupled mode ($f_r \sim 1.0$ MHz)
- (e) Higher order circumferential + thickness coupled mode ($f_r > 1.0$ MHz)

Figure-6. Effect of polymer coating

- (a) before coating
- (b) after coating

Figure-7. Comparison of the hydrostatic sensitivity of the hollow spheres with bulk PZT

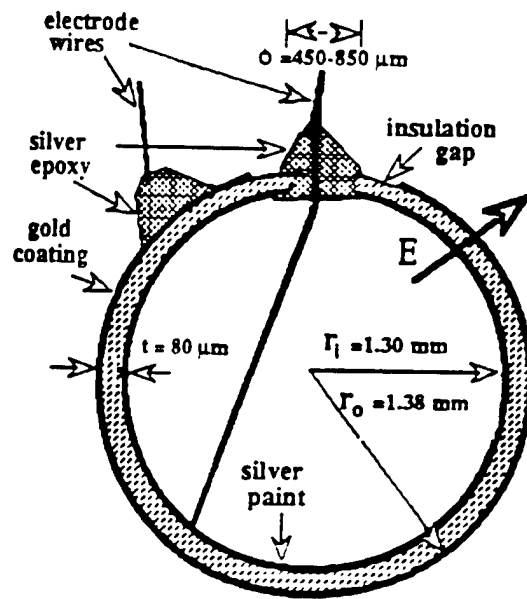
- (a) effective hydrostatic piezoelectric charge coefficient (d_h) vs. hydrostatic pressure
- (b) hydrophone figure of merit ($d_h \times g_h$) vs. hydrostatic pressure

Figure-8. Transformation of an applied hydrostatic pressure into radial and tangential stresses

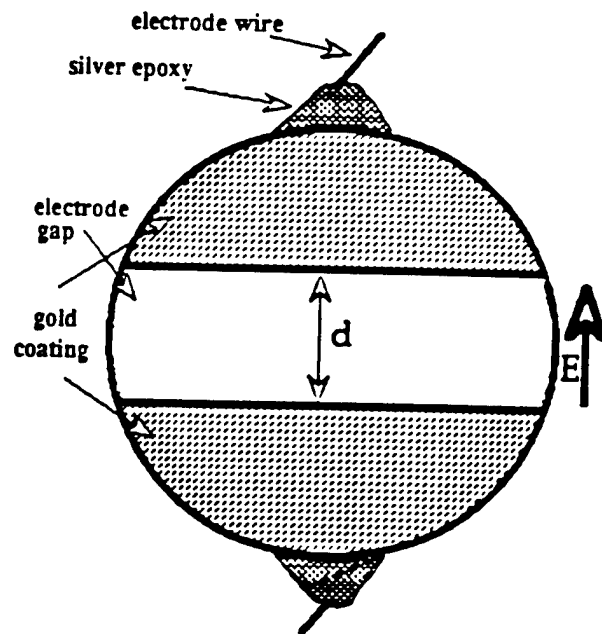
- (a) radial poling case
- (b) top-to-bottom poling case

LIST OF TABLES

- Table-1. Comparison of the dielectric and piezoelectric properties
- Table-2. Comparison of the calculated and measured resonance frequencies

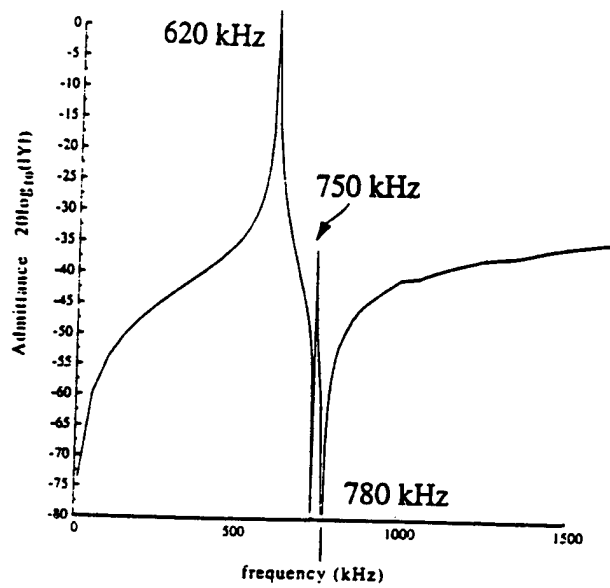


(a) Radial poling configuration

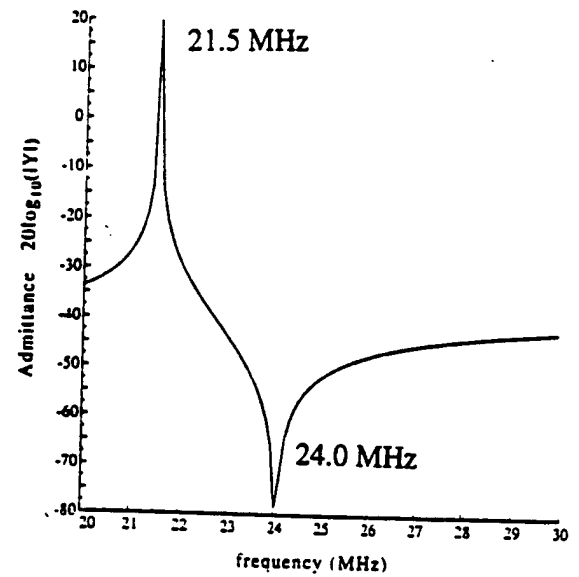


(b) Top-to-bottom poling configuration

Figure-1 Poling Configurations

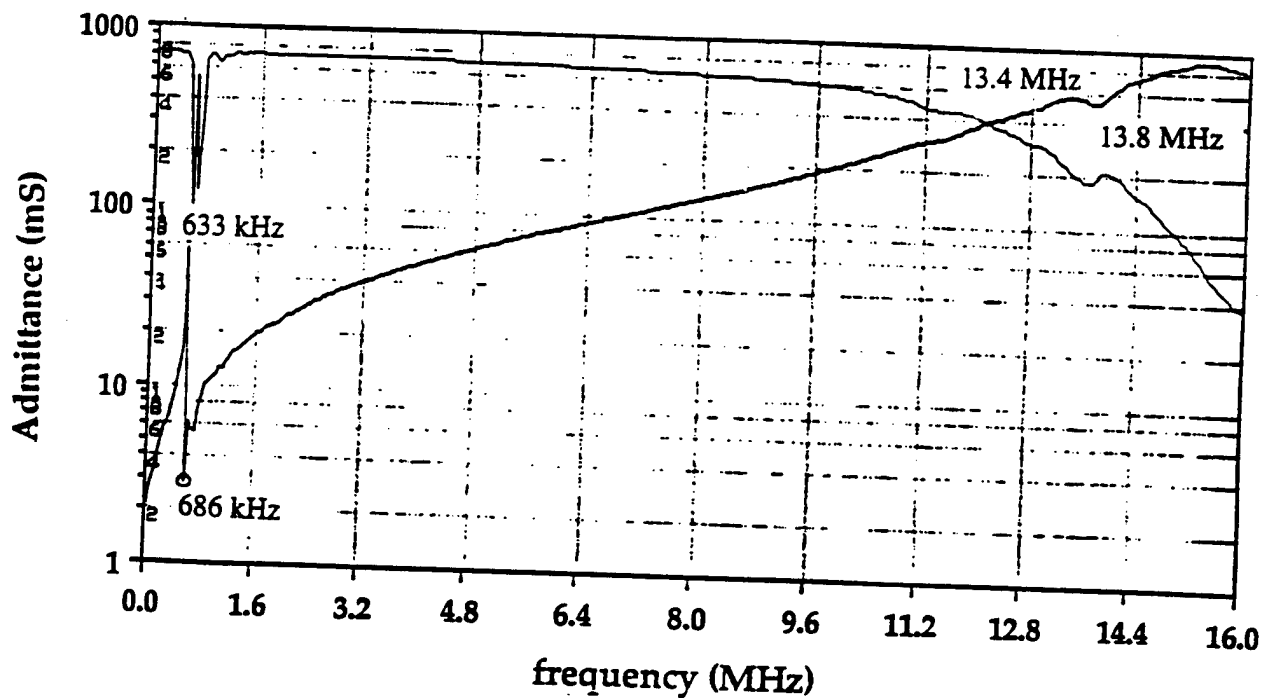


breathing mode (for a sphere with a hole)



thickness mode

(a) Calculated



(b) observed

Figure-2. Admittance spectra of a radially poled PZT hollow sphere transducer

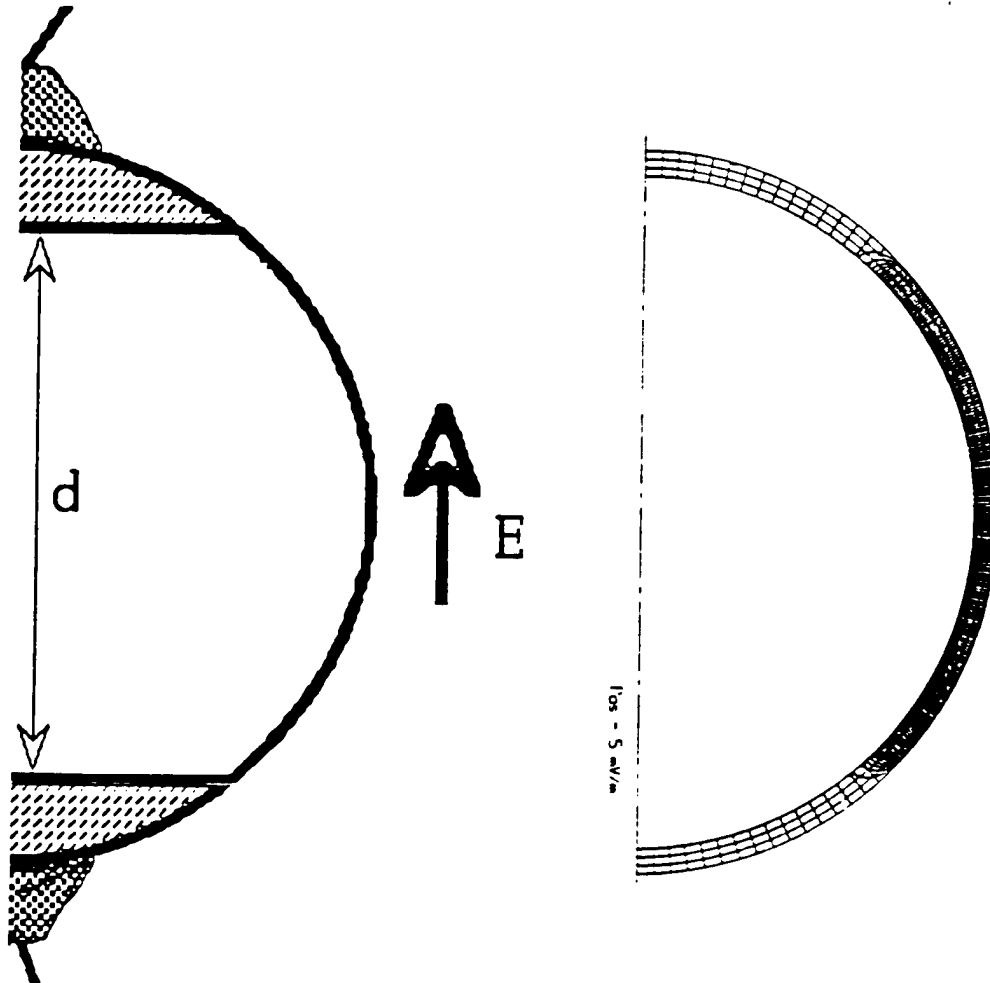
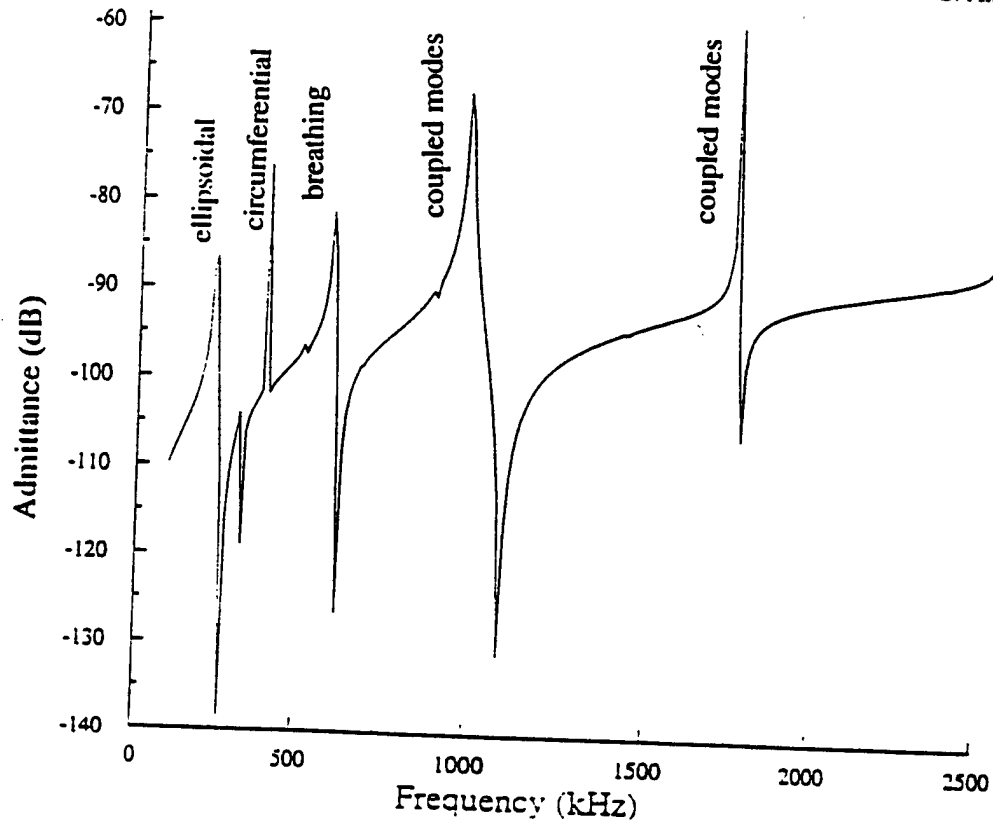
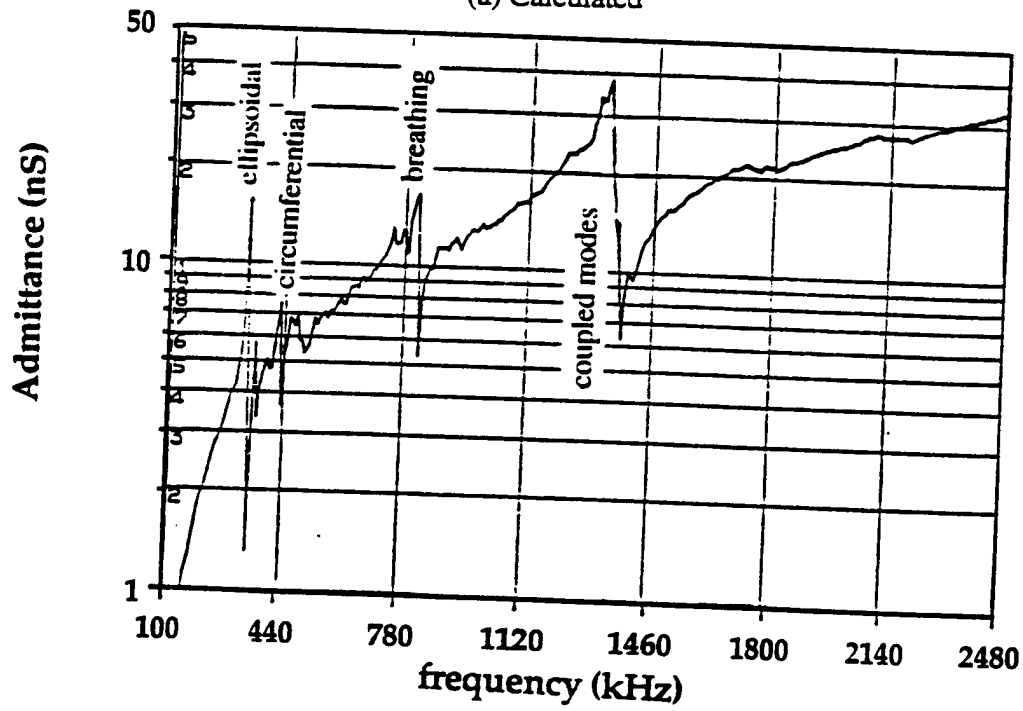


Figure-3. Polarized region of a top-to-bottom poled sphere

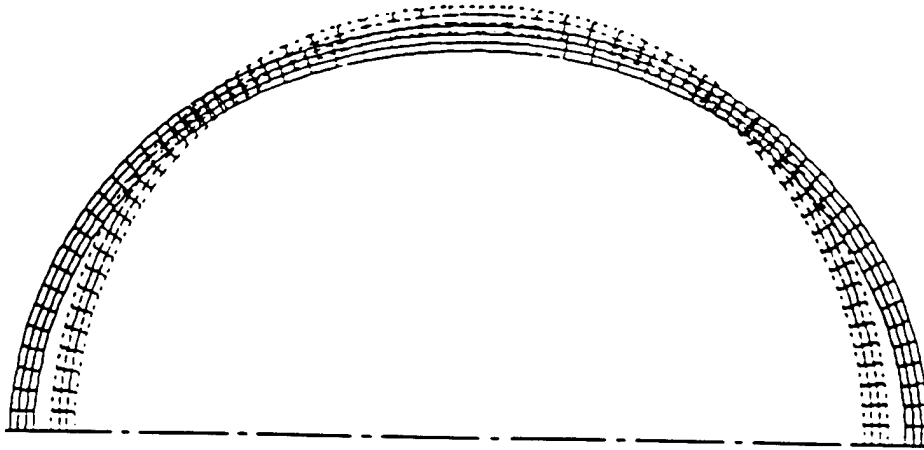


(a) Calculated

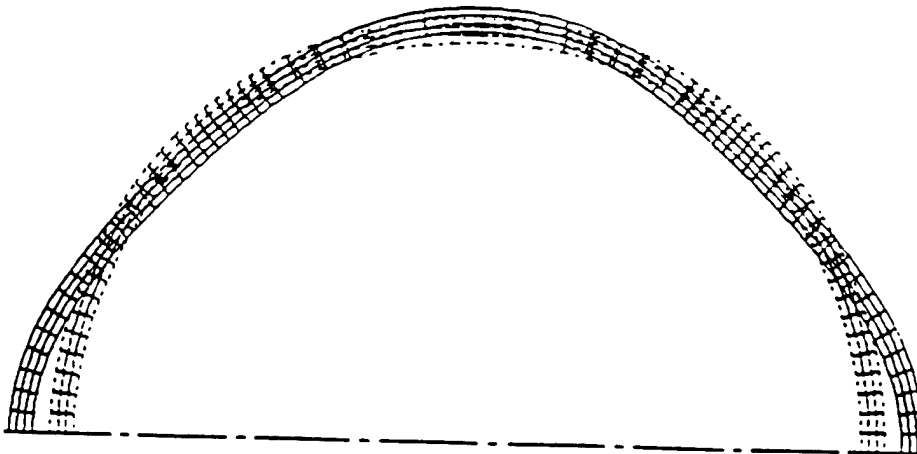


(b) observed

Figure-4. Admittance spectra of a top-to-bottom poled PZT hollow sphere transducer

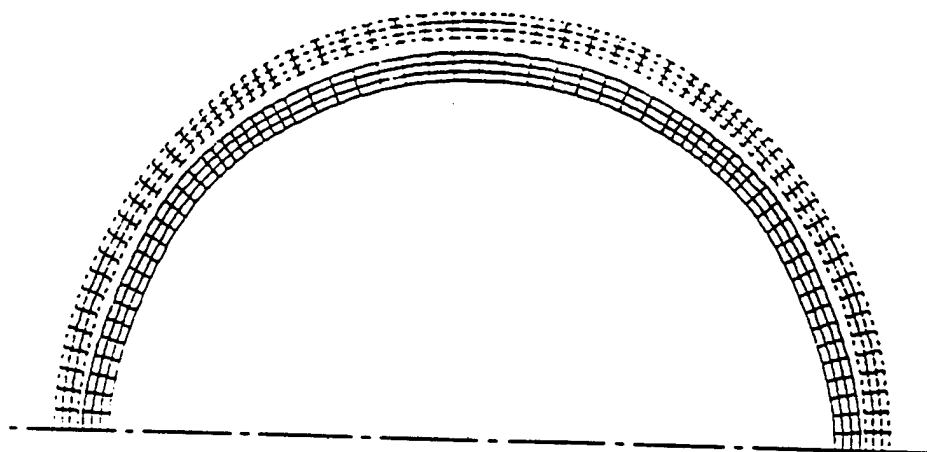


(a) Ellipsoidal mode ($f_r \sim 240$ kHz)

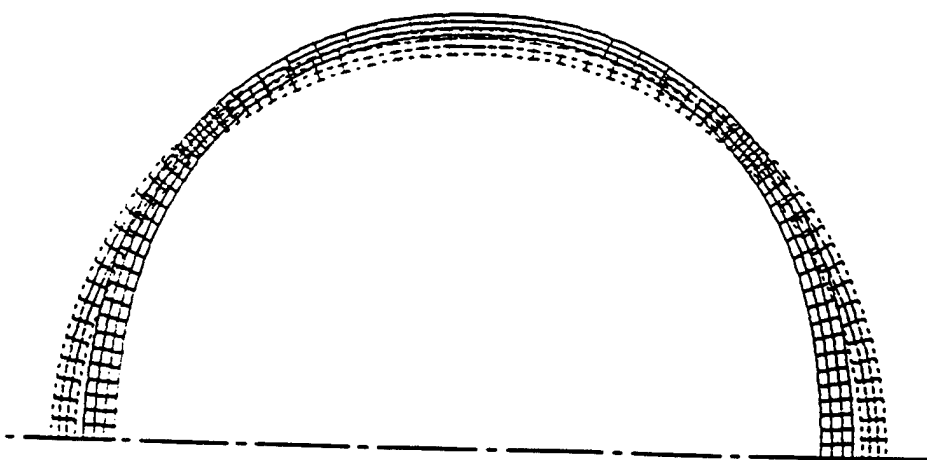


(b) Higher order circumferential mode ($f_r = 300$ - 400 kHz)

Figure-5. Modes of vibration of a top-to-bottom poled piezoelectric hollow sphere.
Dashed lines corresponds to rest position

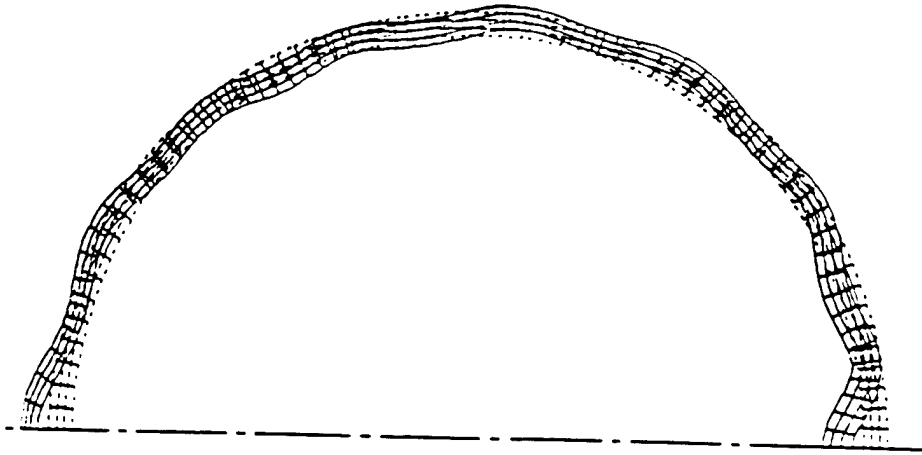


(c) Breathing mode ($f_r \sim 600$ kHz)



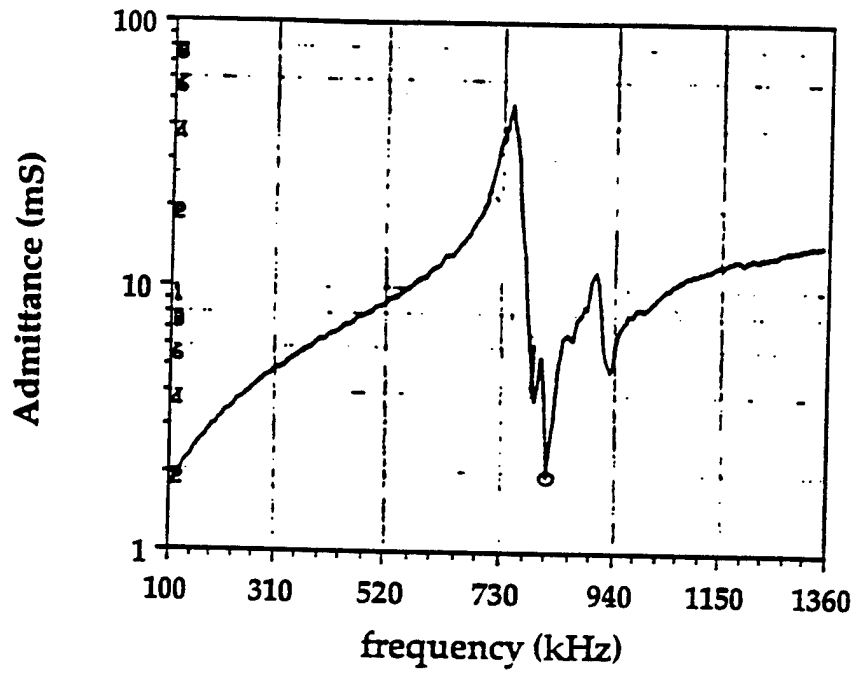
(d) Ellipsoidal+thickness coupled mode ($f_r \sim 1.0$ MHz)

Figure-5.(cont.) Modes of vibration of a top-to-bottom poled piezoelectric hollow sphere. Dashed lines corresponds to rest position

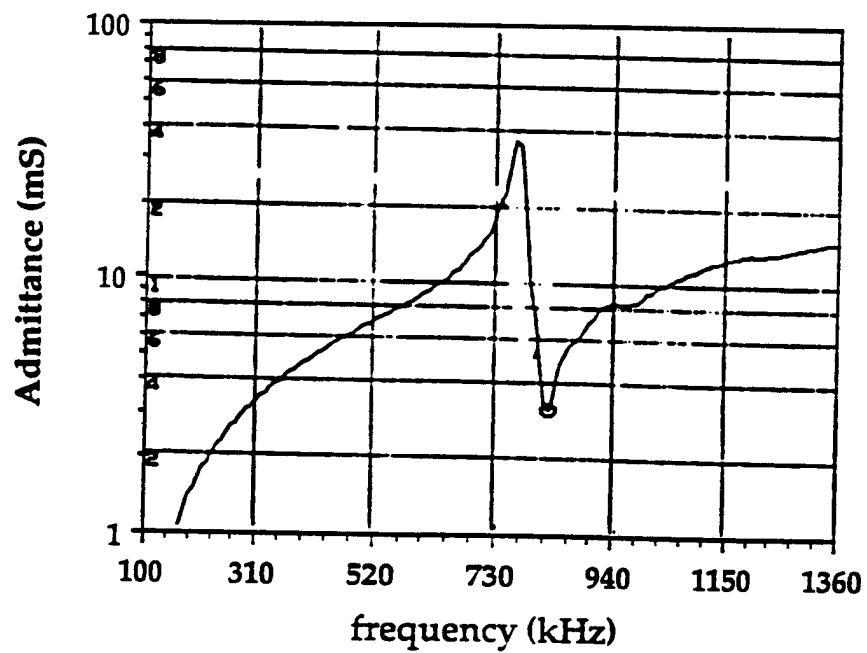


(e) Higher order circumferential+thickness coupled mode ($f_r > 1.0$ MHz)

Figure-5.(cont.) Modes of vibration of a top-to-bottom poled piezoelectric hollow sphere. Dashed lines corresponds to rest position

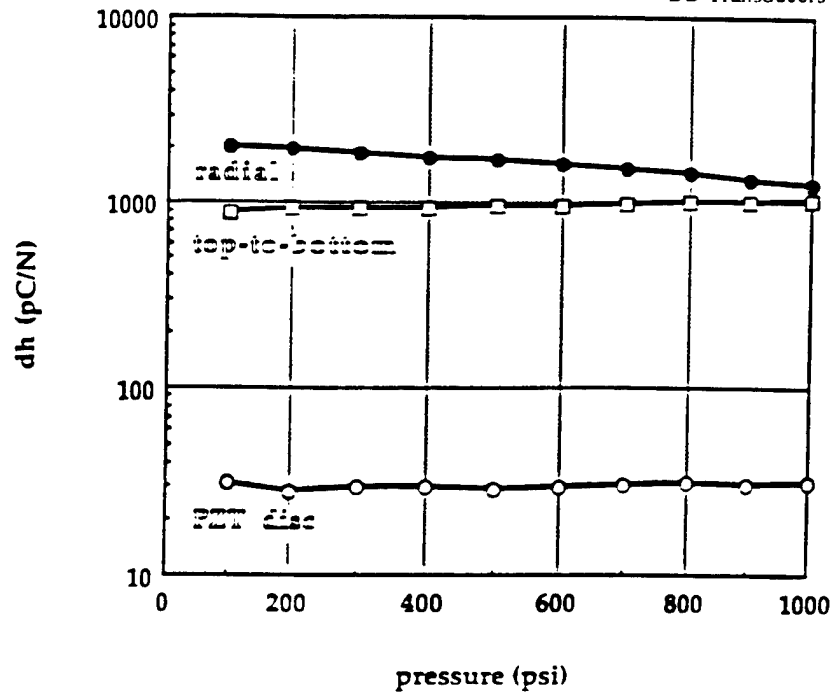


(a) before coating

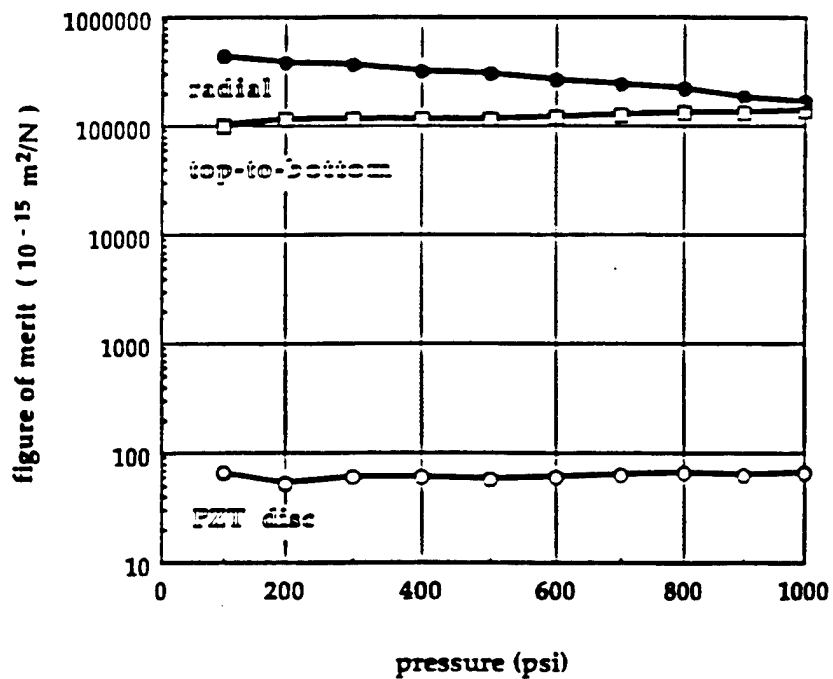


(b) after coating

Figure-6. Effect of polymer coating



(a) effective hydrostatic piezoelectric charge coefficient (d_h) vs. hydrostatic pressure



(b) hydrophone figure of merit ($d_h \times g_h$) vs. hydrostatic pressure

Figure-7. Comparison of the hydrostatic sensitivity of the hollow spheres with bulk PZT

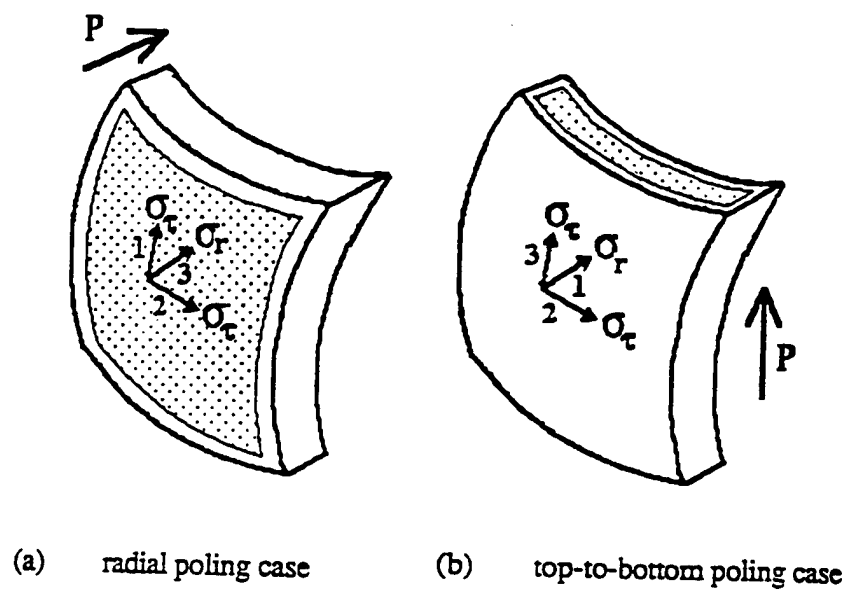


Figure-8. Transformation of an applied hydrostatic pressure into radial and tangential stresses

Table-1. Comparison of the dielectric and piezoelectric properties

Property	Type PZT-5A	Top-to-bottom poled			radially poled
		type-1	type-2	type-3	
electrode gap [#] , d (mm)	n/a	0.790 0.985	1.380 0.690	1.710 0.525	n/a n/a
Capacitance, C (pF)	131.0	6.9	3.7	3.0	2.900
Dielectric loss, tan δ	0.017	0.027	0.071	0.026	0.020
Dielectric constant, ϵ_r	1.622	909	861	869	1,000
Hydrostatic piezoelectric charge coefficient *, d _h (pC/N)	30	743	788	870	1,800
Figure of merit d _h × g _h , (10 ⁻¹⁵ m ² /N)	60	68.677	81,659	98,610	324,000

* valid only for top-to-bottom poled transducers

* determined at 100 psi and 30 Hz

Table-2. Comparison of the calculated and measured resonance frequencies

Type Vibration mode & resonance freq.(kHz)	Type-1		Type-2		Type-3		Radial	
	FEA	Exp.	FEA	Exp.	FEA	Exp.	FEA	Exp.
Ellipsoidal mode	240	235	240	221	240	233	n/a	n/a
Higher order circumferential mode	390	380	320	308	400	358	n/a	n/a
Breathing mode	590	712	590	701	590	708	620	633
Ellipsoidal + thickness coupled mode	980	1,272	980	1,226	980	1,280	n/a	n/a
Higher order circumferential + thickness coupled mode	1,630 2,330	2,005 2,866 3,751	1,680 2,480	1,987	1,750	not found	n/a	n/a

APPENDIX 46

Piezoceramics for High-Frequency (20 to 100 MHz) Single-Element Imaging Transducers

Michael J. Zipparo, K. Kirk Shung, *Fellow, IEEE*, and Thomas R. Shrout

Abstract—The performance of transducers operating at high frequencies is greatly influenced by the properties of the piezoelectric materials used in their fabrication. Selection of an appropriate material for a transducer is based on many factors, including material properties, transducer area, and operating frequency. The properties of a number of piezoceramic materials have been experimentally determined by measuring the electrical impedance of air-loaded resonators whose thickness corresponds to resonance frequencies from 10 to 100 MHz. Materials measured include commercially available compositions of lead zirconate titanate (PZT) with relatively high dielectric constants and a modified lead titanate (PT) composition with a much lower dielectric constant. In addition, materials which have been designed or modified to result in improved properties at high frequencies are studied. Conclusions concerning the influence of the microstructure and composition on the frequency dependence of the material properties are made from the calculated properties and microstructural analysis of each material. Issues which affect transducer performance are discussed in relation to the properties. For transducers larger than about 1 mm in diameter, the use of a lower dielectric constant material is shown to result in a better electrical match between the transducer and a standard 50 Ω termination. For transducers whose impedance is close to that of the connecting cables and electrical termination, equivalent circuit model simulations show improved performance without the need for electrical matching networks. Measurements of fabricated transducers show close agreement with the simulations, validating the measurements and showing the performance benefits of electrically matched transducers.

I. INTRODUCTION

THE USE of ultrasonic transducers operating at frequencies greater than 20 MHz has been demonstrated to provide higher resolution in both the axial and lateral directions, resulting in improved diagnosis of many diseases. Ultrasound backscatter microscopy (UBM) has been shown to have many clinical applications in the 20 to 100 MHz range [1]. The design of high frequency transducers, between 50 and 100 MHz, has remained an engineering challenge. A knowledge of the properties of transducer materials is crucial at the design stage. Foster *et al.* [2] described the characterization of commercially available PZT materials in the 20 to 80 MHz range, useful for

the design of miniature transducers for applications such as intravascular imaging. Results show a marked decrease in the material properties of commercial PZT as the operating frequency is increased. Even with reduced properties, however, the ceramic materials have been shown to still have higher electromechanical coupling coefficients than polymer materials. Lockwood *et al.* [3] described a technique for fabricating high frequency focused transducers, allowing mechanically focused transducers operating at 20 MHz and higher to be constructed. Recent work [4] was focused on electrical matching using transmission line stubs, while treating the rest of the transducer as a "black box" whose properties were unknown and to an extent uncontrollable.

At frequencies above 20 MHz, the scale of the devices approaches the microstructural scale of conventional materials. There have been very few studies exploring the relationships between the microstructure and composition and the frequency dependence of piezoelectric properties for ceramic materials. Results obtained by Foster *et al.* [2] suggested that the microstructure may influence the properties at very high frequencies. However, the materials examined were limited to commercial PZT with a similar composition and with a grain size of roughly 3 μm .

In this paper, measured properties are reported for an expanded number of commercially available materials, including several lead zirconate titanate (PZT) and one modified lead titanate (PT) ceramics. In addition, fine grain materials fabricated using a process described by Kim [5] which results in a submicron grain size are also studied. Also, commercial materials post-processed to alter the microstructure are characterized to determine their high frequency properties.

With a precise knowledge of the transducer material properties, it is possible to select the best material by considering design requirements such as transducer area, operating frequency, and electrical impedance matching. Certain characteristics are desirable for transducers used for medical imaging. For instance, a high k_t favors a wide bandwidth and a low insertion loss, both of which can contribute to improved image quality. Low mechanical losses can also lead to improved sensitivity, an important consideration for high frequency applications because of the increased attenuation in the tissue at these frequencies. For larger high-frequency single-element transducers, a lower dielectric constant can be used to obtain an electrical operating impedance closer

Manuscript received July 1, 1996; accepted April 19, 1997. The authors would like to acknowledge the financial support of The Office of Naval Research and The Whitaker Foundation.

The authors are with the Pennsylvania State University, University Park, PA 16802.

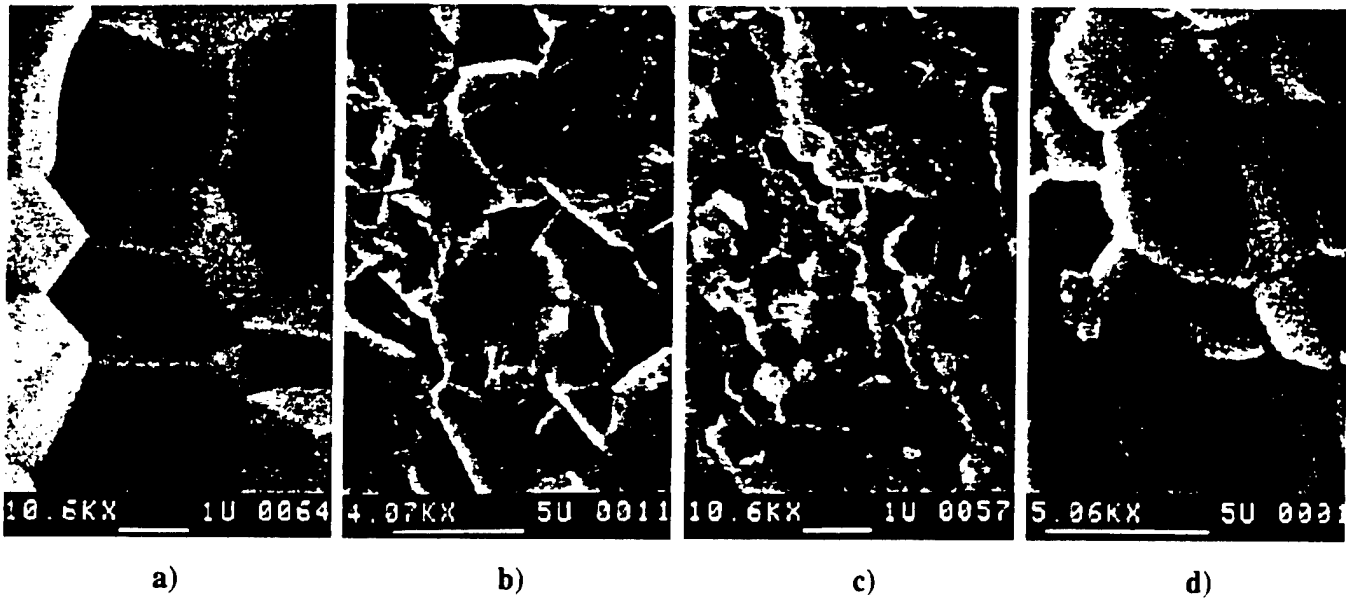


Fig. 1. SEM micrographs of polycrystalline piezoceramic materials: (a) Motorola 3203HD, (b) EDO EC97, (c) 0.5 μm AGS fine grain PZT, (d) post-processed EDO EC97-HIP.

to that of the pulsing and receiving electronics, resulting in lower insertion loss and shorter pulse length. Simulated results showing the effects of material properties on transducer performance were obtained using an equivalent circuit model. Criteria for material selection based on the properties and transducer dimensions are discussed. An example is given comparing a 2 mm diameter 45 MHz transducer designed using both PZT and PT ceramics. Modeled waveforms are compared to waveforms measured for fabricated transducers, showing the performance improvement of electrically matched transducers.

II. MATERIAL PREPARATION AND MEASUREMENT METHOD

Observation of the microstructure of a variety of materials was carried out using a scanning electron microscope (SEM) to give an indication of the average grain size (AGS) and the level of porosity for each material. Thickness mode resonators were prepared by lapping and polishing plates to the desired thickness. The materials tested include two commercially available high density PZT compositions, Motorola 3203HD and 3195HD (Motorola Ceramic Products, Albuquerque, NM) [Fig. 1(a)]; a high dielectric constant PZT composition, Ferroperm PZ21 (rep. Seacor Piezoceramics, Branford, CT); and a commercial modified lead titanate, EC97 (EDO Western, Ltd., Salt Lake City, UT) [Fig. 1(b)]. These materials all have an AGS in the 3 to 6 μm range. In addition, two PZT compositions designed to have fine grain size were also tested, FG-0.9 and FG-0.5 [Fig. 1(c)], the numbers referring to the AGS in micrometers. A group of the modified PT samples was post processed by hot isostatic pressing or HIPing. This changed the microstructure by reducing the amount of porosity [Fig. 1(d)].

For each material tested, multiple samples were prepared to resonate at frequencies between 10 and 100 MHz. Not all of the materials resulted in satisfactory resonators for frequencies above 80 MHz, as sample toughness and porosity contributed to some of the materials having inadequate mechanical integrity. For each material, between three and six different sample thicknesses (and, therefore, operating frequencies) were tested, with typically two to six samples at each frequency. A gold electrode approximately 1000 Å thick was sputter deposited on each side of the samples.

KLM model simulations were run to ensure that this thickness would not load the high frequency samples mechanically and result in inaccurate measurements. Fig. 2 shows a schematic of the equivalent circuit used in the model [6], which includes the addition of a term, expressed as a quality factor, which represents mechanical losses within the piezoelectric material. The value for the electromechanical transformer turns ratio is:

$$o = \left[k_t \cdot \sqrt{\frac{1}{2 \cdot f_p \cdot C^S \cdot Z_m}} \cdot \text{sinc} \left(\frac{f}{2 \cdot f_p} \right) \right]^{-1} \quad (1)$$

and that of the series reactance C' is:

$$C' = \frac{C_0}{k_t^2 \cdot \text{sinc} \left(\frac{\omega}{\omega_p} \right)}, \quad (2)$$

where k_t is the thickness mode electromechanical coupling coefficient and ω_p is the radian parallel resonance frequency. C_0 represents the complex clamped capacitance and has a value of:

$$C_0 = \frac{\epsilon_{33r}^S \cdot \epsilon_0 \cdot A}{t} \cdot [1 - j \cdot \tan(\delta)] \quad (3)$$

where ϵ_{33r}^S and ϵ_0 are the relative clamped and free space dielectric permittivities. A is the transducer area. t is the

transducer thickness, and $\tan(\delta)$ is the dielectric loss tangent. The transmission line components include the complex mechanical impedance, Z_m (kg/s), which is related to the acoustic impedance, Z_a (MRayl), by the relation

$$Z_m = Z_a \cdot A \cdot \left(1 + \frac{j}{2 \cdot Q_m}\right), \quad (4)$$

where Q_m is the mechanical quality factor. The wave velocity, v (m/s), is also included. An algorithm based on the transfer matrix approach described by Selfridge and Gehlbach [7] was implemented on a personal computer.

Simulations were run comparing an ideal infinitely thin electrode to the actual 1000 Å thick electrode for free air resonators of a typical PZT piezoceramic material operating at 40 and 100 MHz. Results showed a shift of the parallel resonance frequency of less than 1% for the 40 MHz resonator and approximately 2% for the 100 MHz resonator. This was judged to be within the measurement accuracy so as to have a minimal effect on the measured material properties for measurements made up to 100 MHz. An electrode thickness of 10,000 Å (1 μm) showed almost a 10% reduction for the 40 MHz resonator and an 18% reduction for the 100 MHz resonator, indicating that such thick electrodes at high frequencies can cause significant mass loading.

The material properties of thickness mode plates were experimentally evaluated to determine their suitability for single element transducers operating at frequencies from 20 to 100 MHz. Materials evaluated included commercially available PZT with an average grain size in the 2.5 to 5.0 μm range, and fine grain PZT materials designed to exhibit a grain size up to an order of magnitude smaller. The fine grain materials were studied to determine whether grain size has a dominant effect on the properties at high frequencies. Also, conventional ceramic materials are of limited use at frequencies approaching 100 MHz because the dimensions of the samples approach the grain size, resulting in not only reduced properties but also reduced structural integrity. Because of the increased number of grains across the controlling dimension, the fine grain materials provide increased toughness for very high frequency samples.

Transducers with a larger radiating aperture have better lateral resolution due to a narrower beamwidth [1]. High frequency transducers made from PZT materials can have an electrical impedance which is substantially lower than 50 Ω if the area is larger than about 1 mm². A commercial modified PT material was selected for evaluation based on its lower dielectric constant ($\epsilon_{33r}^S = 200$), 5 to 10 times lower than for typical soft PZT materials ($\epsilon_{33r}^S = 1100$), which results in less capacitance and hence a higher impedance for a transducer with a larger area.

Measurements of the electrical impedance of air-loaded plate resonators were used to calculate the properties using the resonance technique whereby an air-loaded piezoelectric sample is made to resonate at a frequency determined by its mode of vibration and dimensions. The mode which is excited is determined by its particular shape, such as

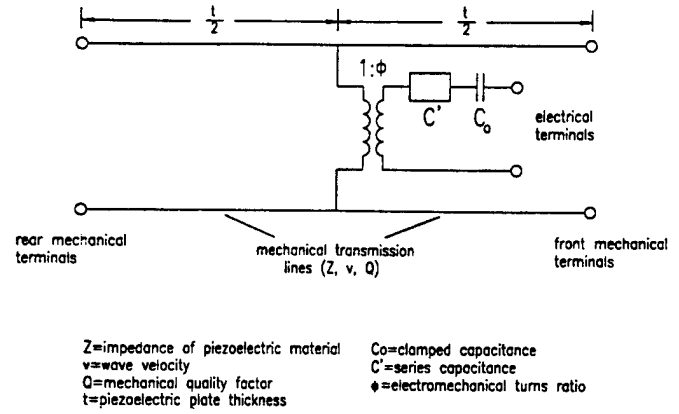


Fig. 2. KLM model equivalent circuit.

a long bar or thin plate. The shape of the test specimen should be the same as that used in a working transducer.

In this work thickness mode resonators are studied since the transducers of interest use thin plates with a large area relative to the thickness. The method of the IEEE Standards [8] was used to calculate the electromechanical coupling coefficient, k_t , based on measurement of the series and parallel resonance frequencies, f_s and f_p ,

$$k_t = \sqrt{\frac{\pi}{2} \cdot \frac{f_s}{f_p} \cdot \tan\left(\frac{\pi}{2} \cdot \frac{f_p - f_s}{f_p}\right)}. \quad (5)$$

Several different methods of measuring mechanical losses within the plate, expressed as a mechanical quality factor, Q_m , were evaluated, including the method used by Foster *et al.* [2], which is based on an analysis of the KLM model and requires measurement of electrical impedance over a span of frequencies. The method of Ih and Lse [9] was also used to calculate mechanical loss. Unlike the previous method, this one requires measurement of impedance only at a single frequency. This method uses an intermediate coefficient D which is calculated as

$$D = \frac{\pi^2 \cdot R_{\max} \cdot C^S \cdot f_p}{k_t^2}, \quad (6)$$

where R_{\max} is the maximum of the real part of the measured impedance, C^S is the measured clamped capacitance, f_p is the parallel resonance frequency (i.e., frequency of R_{\max}), and k_t is calculated as described above. From D the attenuation coefficient, α (Np/m), is calculated as:

$$\alpha = \frac{1}{t} \cdot \ln\left(\frac{D+1}{D-1}\right) \quad (7)$$

where t is the thickness of the sample. From α it is possible to calculate Q_m as [2]:

$$Q_m = \frac{\pi \cdot f_p}{\alpha \cdot v} \quad (8)$$

where v is the wave velocity.

The calculated values were found to be similar between the two methods for samples tested around 25 MHz. Table I shows the values of Q_m measured for two thickness

TABLE I
 Q_m MEASURED USING TWO METHODS.

Thickness	f_p	measured Q_m		
(μm)	(MHz)	Foster	Ih and Lee	% difference
92	26.0	41.4	42.5	2.6
96	23.6	36.6	36.9	0.8

mode resonators using Foster's method [2] and the method of Ih and Lee [9]. The variation between the two methods is at most only a few percent. Because of its accuracy and simplicity, the Ih and Lee method [9] was used to measure the mechanical losses presented in this paper. Fig. 3 shows a comparison of the measured and modeled electrical input impedance for an air-loaded 98 MHz thickness mode resonator of hot-pressed lead titanate ceramic. The modeled spectrum was calculated using the KLM model with the measured parameters as inputs. The excellent agreement between the two curves confirms the accuracy of the measurements, even at the upper limit of the measurement range.

III. EXPERIMENTAL RESULTS

The properties calculated from impedance measurements are shown in Table II. These properties are sufficient to model the performance of transducers using the one-dimensional KLM model. The calculated properties are summarized in Table III for each material. Physical properties such as transition temperature, T_c , and density, ρ , were also measured. T_c was measured as the temperature where a peak in the dielectric constant was observed as the operating temperature increased. The density was measured for each material using bulk samples to determine mass and volume. Measurements were not made using high frequency samples because of the inherent measurement inaccuracy. Properties of thickness mode plates operating at 20 MHz are shown, as well as the slopes calculated from linear regression analysis of the higher frequency properties. The values of the slopes can be compared between the different materials and conclusions drawn relating the microstructure and composition to the frequency dependence of the properties.

A. Commercial Lead Zirconate Titanate (PZT) Materials

PZT materials of the type tested here (i.e., PZT5 type materials) are piezoelectrically soft materials. That means that the internal dipoles or domains are easily reoriented by an applied electric field. This fact can contribute to higher coupling coefficients and dielectric constants, since domain wall motion contributes to the piezoelectric response. At high frequencies the finite activation energy and inertial mass associated with domain wall motion [10] may lower these extrinsic contributions. A reduction in the domain wall motion contribution could cause lower piezoelectric properties at high frequencies.

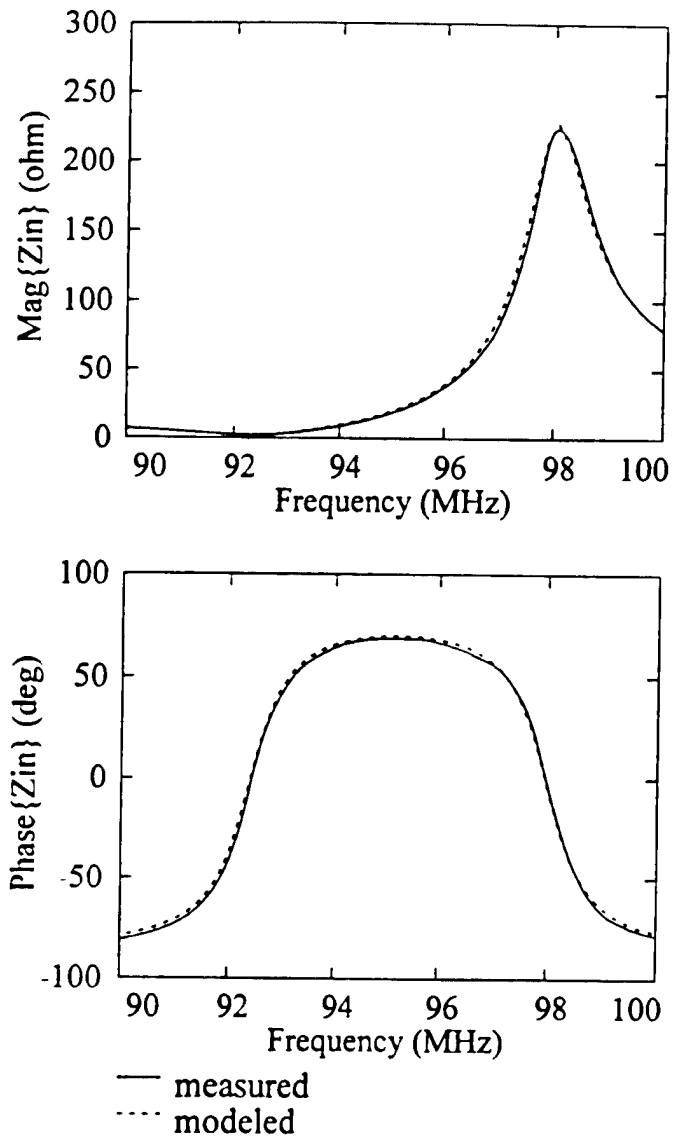


Fig. 3 Comparison of measured and modeled Z_{in} for air-loaded 98 MHz EC97-HIP thickness mode resonator.

The data for the two high density PZT materials, both with an AGS of approximately $2.5 \mu\text{m}$, confirm the frequency dependence of k_t previously reported by Foster *et al.* [2], where a slope of approximately $-1.0 \times 10^{-3}/\text{MHz}$ was reported. The measured frequency dependence of Q_m also agrees with that previously reported.

SEM analysis of the high dielectric constant material, Ferroperm PZ21, revealed an AGS of $5 \mu\text{m}$, slightly larger than for the Motorola materials. Also apparent was a higher level of porosity. The frequency dependence of k_t was very close to the Motorola materials, indicating that a small amount of porosity does not significantly affect k_t at high frequencies. The strong frequency dependence of Q_m for PZ21 leads to high losses at high operating frequencies, similar to other commercial PZTs.

The microstructure and measurements for the commercial PZT materials show that porosity does not significantly contribute to lower piezoelectric properties at high

TABLE II
MATERIAL PROPERTIES OF THICKNESS MODE RESONATORS
WHICH ARE CALCULATED FROM IMPEDANCE MEASUREMENTS.

Symbol	Description	Units
k_t	thickness electromechanical coupling coefficient	
Q_m	mechanical quality factor	
v	longitudinal plane wave velocity	mm/ μ s
N_t	thickness frequency constant	MHz mm
ρ	density	g/cm ³
Z_a	characteristic impedance	MRayl
ϵ_{33r}^S	relative clamped dielectric permittivity	
$\tan(\delta^S)$	clamped dielectric loss tangent	
ϵ_{33r}^T	relative free dielectric permittivity	
$\tan(\delta^T)$	free dielectric loss tangent	

TABLE III
MEASURED PROPERTIES OF PIEZOCERAMIC MATERIALS.

Material	Type	T_c (deg. C)	AGS (mm)	ρ (g/cm ³)	20 MHz measurements				Linear regressions	
					k_t	Q_m	ϵ_{33r}^S	N_t (MHz mm)	slope of k_t (-10^{-3} /MHz)	slope of Q_m (-1 /MHz)
3203HD	VI	210	3.5	7.8	0.53	50	1100	2.4	1.03	0.74
3195HD	II	330	3.5	7.8	0.48	90	750	2.4	0.93	1.06
PZ21	VI	150	5.0	7.8	0.48	40	1500	2.3	1.02	0.55
FG-0.9	II	350	0.9	7.8	0.49	50	600	2.3	0.67	0.55
FG-0.5	II	350	0.5	7.8	0.46	40	1050	2.3	0.68	0.25
EC97	n/a	260	6.0	6.7	0.48	120	220	2.6	0.32	1.88
EC97-HIP	n/a	260	6.0	6.9	0.52	120	200	2.7	0.37	0.63

frequencies. The frequency dependence was similar for Motorola 3203HD and Ferroperm PZ21. materials which had different levels of porosity. The frequency-dependent behavior, therefore, must be explained by other factors.

The relative clamped permittivity of 1500, highest of the materials tested, is achieved by compositionally lowering T_c to 150°C. This results in a higher permittivity at room temperature, an important consideration for small area array elements which benefit from the higher capacitance which can lower the electrical impedance and more closely match the transducer to the electrical terminations. For high frequency single element transducers, which are typically large in area relative to their thickness, the high permittivity results in an impedance which is substantially lower than 50 Ω .

B. Fine Grain Lead Zirconate Titanate (PZT) Materials

The fine grain PZT materials showed a similar decrease in both k_t and Q_m at high frequencies. However, the slope of k_t vs. frequency is considerably lower than for the conventional PZT materials, as shown in Fig. 4(a). The AGS 0.9 and 0.5 μ m materials both showed the same slope of 0.67×10^{-3} /MHz. Thus the frequency dependence of k_t does not seem to be improved by reducing the grain size appreciably below 1 μ m. The change in Q_m with frequency, however, does show additional improvement for the FG-0.5 material which showed a slope of -0.25 /MHz, lowest of all

materials tested. Therefore, grain size does seem to greatly influence the frequency dependence of Q_m , even for grain sizes less than 1 μ m.

The size of the domains has previously been shown to decrease with decreasing grain size [10]. A possible explanation for the lower frequency dependence of k_t and Q_m for the fine grain materials is that the dependence is moved to higher frequencies. In other words, the effect of grain and domain size is reduced in the frequency range from 20 to 80 MHz. Thus conventional materials show reduced properties at high frequencies owing to their larger grain and domain size, while fine grain PZT materials show less-reduced properties due to the shifting of these losses to frequencies greater than 100 MHz.

The properties of the fine grain materials at frequencies less than 20 MHz are slightly lower but comparable to the commercially available materials. This is consistent with previous conclusions [10] which explained the decrease in terms of a reduced domain wall mobility due to clamping at the grain boundaries and a reduced number of domain orientations within an individual grain. Overall, the reduced frequency dependence results in better properties at high frequencies compared to commercial PZT. Another important advantage of the fine grain materials is their ability to be formed into very thin resonators. The minimum plate thickness achievable for the conventional materials was about 24 μ m, while by using the same technique for the fine grain materials plates as thin as 13 μ m were made, corresponding to a projected thickness mode

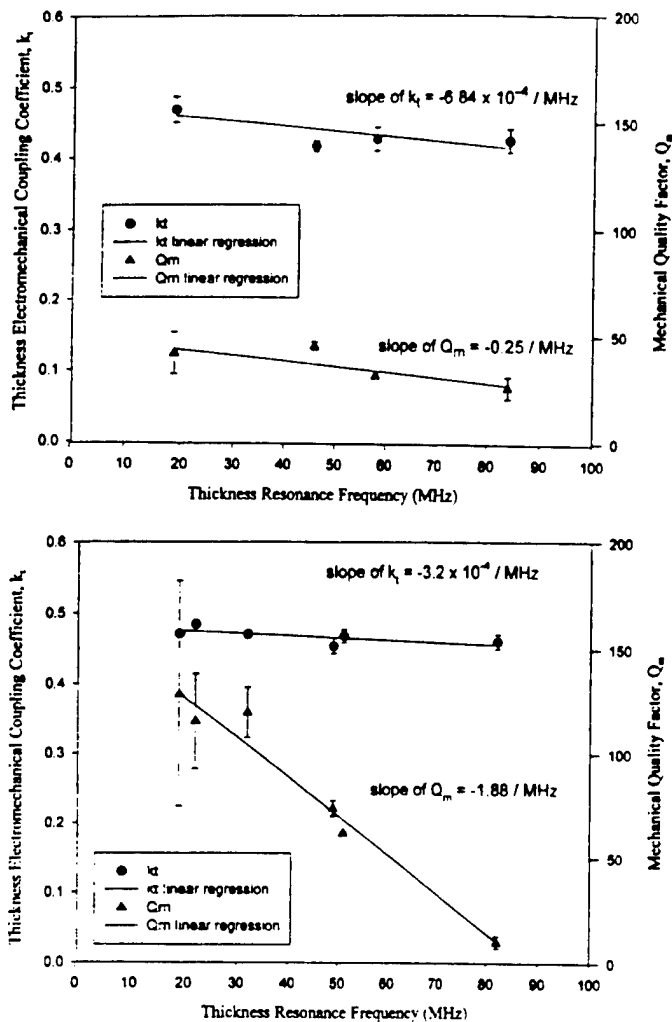


Fig. 4. Frequency dependence of k_t and Q_m for: (a) $0.5\ \mu\text{m}$ AGS fine grain PZT. (b) EDO EC97.

resonance at 150 MHz. These samples were able to be handled but were not electroded and polarized because of the 100 MHz measurement limit of the impedance analyzer.

C. Lead Titanate (PT) Materials

A material from the lead titanate class, EC97, was tested. The grain size of this material was the largest of all the materials tested, with an average of approximately $6\ \mu\text{m}$ and some grains approaching $10\ \mu\text{m}$. Also evident from the SEM analysis was a fairly high level of porosity. The size of the domains was also quite large, being visible at magnifications where the domains of PZT are not apparent. Despite its large grain size, the material was fairly easy to process into very thin plates. The minimum plate thickness achieved for a 1 cm diameter disk was $24\ \mu\text{m}$.

The measured k_t at low frequencies was found to be approximately 0.5, comparable to the PZT materials. Considering the relatively large grain size, it is interesting to note the very low slope of k_t vs. frequency ($-0.32 \times 10^{-3}/\text{MHz}$) which can be seen in Fig. 4(b) to result in an

extrapolated k_t of 0.45 at 100 MHz. This slope was the lowest of all materials tested despite the grain size being the highest, indicating that grain size is not the dominant contributor to reduced properties at high frequencies. The low slope of k_t vs. frequency can be attributed to a lower contribution of the properties from extrinsic effects which tend to be reduced at high operating frequencies. Domain wall motion in particular appears to be an important factor in determining the frequency dependence of k_t . Since PT materials in general have a reduced domain wall mobility relative to PZT materials, it is not surprising that the frequency dependence of k_t is reduced. Thus even though both the grain and domain sizes are larger than for the PZT materials tested, the lower contribution from extrinsic effects makes the frequency dependence less for the PT materials.

The Q_m at low frequencies for the PT material was highest among all of the materials evaluated, although there was a large variation in the measured results from sample to sample at low frequencies. It is believed that the inconsistency in the results are linked to incomplete mixing or some other processing deficiency which leads to regions of inhomogeneous properties within the samples. In fact, areas of varying opacity were evident in the very thin samples, indicating that the composition varies spatially through the samples. The high value of Q_m at low frequencies can again be ascribed to the low degree of domain wall mobility which is present in PT materials, as domain losses dominate internal loss in PZT materials [11, p. 32]. The slope of Q_m vs. frequency for EC97 was highest of all materials tested, resulting in a low Q_m of about 10 at 80 MHz. This is believed to be a result of porosity present in the material. Due to the large impedance mismatch at the ceramic-pore boundary, the scattering of sound from a pore will be high, leading to significant attenuation within the material and thus a lower Q_m . The effect is most severe when the wavelength in the material approaches the size of the pores, as is the case at frequencies approaching 100 MHz.

The EC97 material was post processed with a heat treatment in order to improve the properties for high frequency transducers. The resulting material is referred to as EC97-HIP. The process referred to above is hot isostatic pressing, or HIP, and consists of heating the samples to a high temperature such as 1000°C at a high isostatic pressure such as 13.8 MPa (2000 psi). The result of the pressure and heat is a reduction in pore size and an increase in the density [12]. Both 6.0 and 0.6 mm thick samples were processed to determine if sample thickness influenced the results. All HIP samples were poled at 110°C with a field of 50 kV/cm applied for 10 minutes in a fluorinert (FC-40, Sigma Chemical Co., St. Louis, MO) bath.

From an SEM analysis of the EC97-HIP material, it was evident that porosity had been reduced significantly. For the samples tested, the density increased $\sim 4\%$ relative to the nontreated samples. The k_t increased slightly to a value of 0.52 measured at 50 MHz, higher than for the PZT

materials and the standard EC97. This increase can probably be attributed to the decrease in porosity. The HIP treatment and the associated decrease in porosity had an even more profound effect on Q_m , with a value of about 100 being measured at 98 MHz. This is significantly higher than the best PZT which showed a Q_m of about 20 in this range. This is also convincing evidence that losses due to domain wall motion do contribute to a lower Q_m for PZT materials, and that PT materials, owing to reduced extrinsic contributions, are inherently less lossy at high frequencies. The difference between EC97 and EC97-HIP also seems to suggest that porosity is a significant contributor to mechanical loss for PT type materials.

IV. TRANSDUCER DESIGN BASED ON PROPERTIES

The relative clamped dielectric permittivity, ϵ_{33r}^S , of the fine grain PZT materials was similar to the conventional PZT materials. Thus, while the high-frequency properties are slightly better, the high dielectric constant effectively limits the fine grain materials to miniature single element and array applications where the small element area dictates the use of a higher dielectric material for electrical impedance matching. Fine grain PZT materials offer great promise for high-frequency array applications in particular because the element width and spacing are necessarily close to the grain size of conventional materials, making processing into arrays difficult because of the reduced mechanical integrity.

For the PT material ϵ_{33r}^S was 220, typical for this type of material. This is an advantage for some high frequency single element transducers in terms of electrical impedance matching, particularly for transducers more than a few square millimeters in area. The reduced dielectric constant results in a higher electrical impedance and better matching to standard 50 Ω electronics for larger area transducers.

The influence of the material properties on the response of single element transducers was determined by using the KLM model, as described earlier. The measured material properties shown in Table III, in addition to the front and rear acoustic loading conditions and the transducer dimensions, are sufficient to model transducer operation. The connecting cable impedance and length can also strongly influence the transducer response. Selection of the best material can be made based on the modeled performance characteristics, such as the pulse-echo waveform amplitude and pulse length and the frequency spectrum. The electrical impedance of the transducer is particularly important in determining transducer performance, especially in situations where the electrical terminations are fixed [13]–[15].

Simulations of electrical impedance, Z_{in} , were obtained using the measured 45 MHz properties for PZ21 and EC97-HIP. A 2 mm diameter transducer was loaded with water on the front and a 5.4 MRayl material on the back. For a transducer operating at 45 MHz, a diameter larger than 1 mm can result in improved lateral resolution while maintaining a reasonable depth of field [1]. The larger area

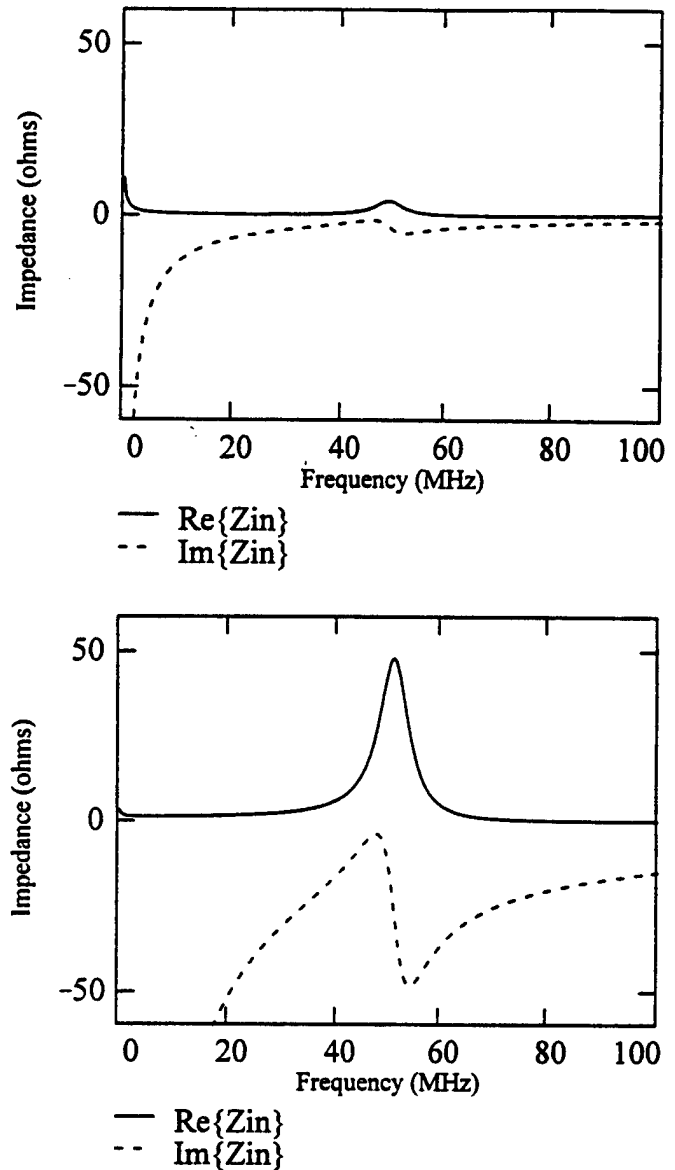


Fig. 5. Modeled electrical impedance for a backed 2 mm diameter 50 MHz resonator: (a) PZT material (Ferroperm PZ21), (b) PT material (EDO EC97). Note the closer match to 50 Ω for the PT material due to the lower dielectric constant.

relative to thickness dictates the use of a lower dielectric constant piezoelectric material so that the electrical impedance, Z_{in} , is closer to 50 Ω . Results for the real and imaginary parts of Z_{in} are shown in Fig. 5(a) for PZ21. The peak in the real part is less than 10 Ω , considerably lower than standard 50 Ω terminations. Results are shown in Fig. 5(b) for EC97-HIP, with a much lower dielectric constant. The peak, at 56 Ω , is higher and much closer to 50 Ω than the PZT transducer. In addition to a lower dielectric constant, the PT material has a higher coupling coefficient, k_t , and a higher mechanical Q , Q_m , both of which favor an improved transducer response.

Simulated waveforms for the two transducers were generated using the KLM model with the test configuration shown in Fig. 6. The electrical excitation signal was a neg-

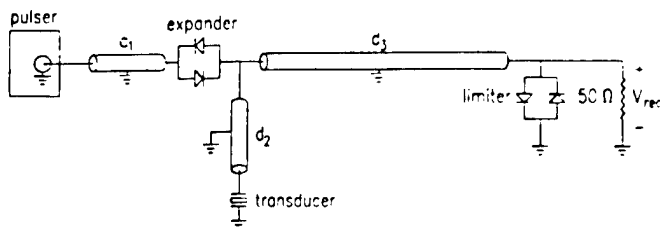


Fig. 6. Circuit configuration for simulation and measurement of pulse echo response. The received signal was measured directly across the $50\ \Omega$ termination. The limiter is designed to prevent receiver overload on transmit; the expander prevents the pulser impedance from loading the transducer on receive; and the lengths of cables d_1 and d_2 are made much less than a wavelength, while cable d_3 is made a quarter wavelength at the transducer center frequency; all described by Lockwood *et al.* [15].

active impulse with an amplitude of 32 V peak from a $50\ \Omega$ source impedance. The PZT transducer waveform, shown in Fig. 7(a), can be seen to have a long pulse length. The PT transducer response, shown in Fig. 7(b), can be seen to have a higher signal amplitude and a shorter pulse length, both of which contribute to improved image quality. These results are similar to those obtained by Lockwood and Foster [4] for a PZT transducer with an electrical matching network. The matched electrical impedance of the PT transducer facilitates energy transfer between the transducer and the electronics without the need for a matching network, resulting in improved system performance.

Focused transducers which operate at 45 MHz were constructed from PZT (PZ21) and PT (EC97-HIP) materials for comparison with the simulations. The 2 mm diameter was the same as that used in the simulations. A cross section of the transducers is shown in Fig. 8. The transducers were built into an SMA connector with a conductive epoxy backing ($Z = 5.4\ \text{MRayl}$) and focused using the technique described by Lockwood *et al.* [3]. The piezoceramic was focused while supported with a slug of backing approximately 1 mm thick. This alleviated the need to focus the transducer and then apply additional backing material, as the Lockwood method [3] requires. Also, the volume around the backing was completely potted with epoxy (EP30: Master Bond, Hackensack, NJ). The electrical resistance of the backing material was found to have a minimal influence on the transducer response, being measured less than $100\ \text{m}\Omega$ for a backing piece of the thickness and diameter used in the transducers. The front electrode was a layer of sputtered gold approximately $1000\ \text{\AA}$ thick which covered the front of the ceramic and made a connection to the outer connector housing which served as the ground.

The transducers were spherically focused, also using the technique described by Lockwood *et al.* [3], except that the operation was done at 65°C . An experiment was performed to investigate the result of the focusing operation on the properties of a backed resonator. Table IV shows the properties measured using the technique described in Section II for a free air resonator and for a backed res-

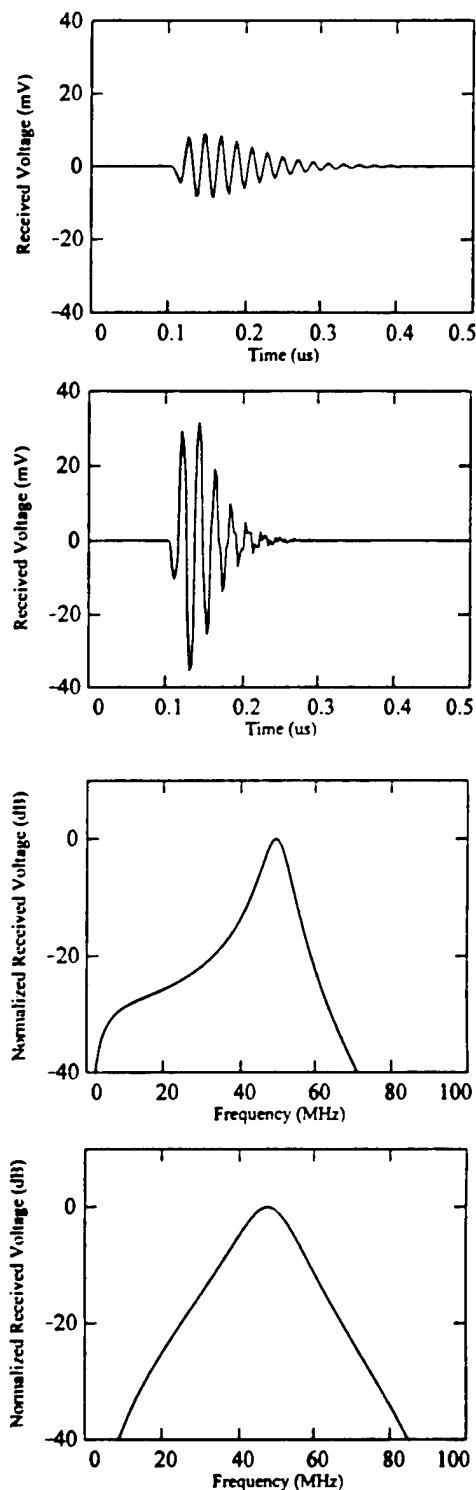


Fig. 7. Simulated pulse echo waveform for 2 mm diameter 45 MHz transducers: (a) PZT material (Ferroperm PZ21), (b) PT material (EDO EC97). Note the higher signal level and shorter pulse length of the PT transducer.

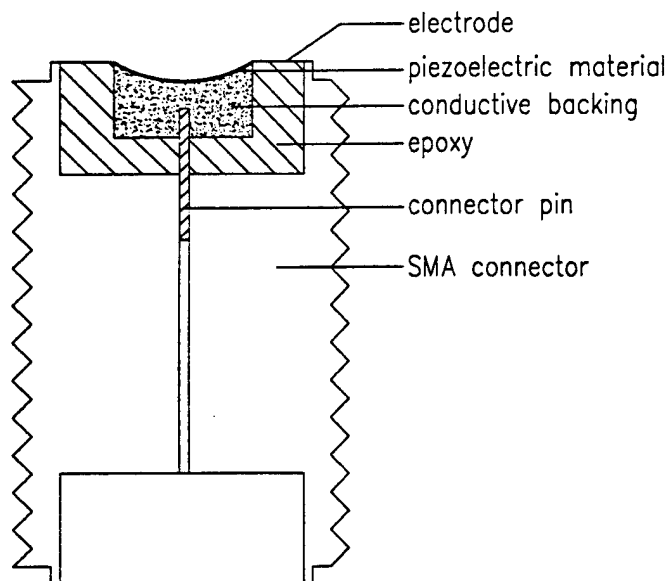


Fig. 8. Cross-section of single element transducer built into an SMA connector (after Lockwood [3]). Note the simplified construction of the ceramic-backing composite which was formed in one step and the one step potting of the connector with epoxy.

TABLE IV
MEASURED PROPERTIES OF THICKNESS MODE RESONATORS
UNDER DIFFERENT LOADING CONDITIONS.

	Free plate	Backed	Backed and focused
k_t	0.470	0.418	0.416
Q_m	71.0	9.1	7.7
ϵ_{33r}^S	156	168	166
N_t	2.60	2.36	2.35

onator both before and after the focusing operation. The free air resonator can be seen to have a higher coupling coefficient and significantly lower mechanical losses. This shows that the effect of the damping from the backing is principally to increase mechanical losses, in the form of energy transferred to and absorbed by the backing, while the dielectric constant and mechanical stiffness remains essentially constant. The focusing operation can be seen to slightly lower the electromechanical coupling, dielectric constant, and mechanical compliance, and to increase mechanical losses by about 15%. Considering the degree of mechanical alteration of the composite structure, resulting in additional small cracks which are visible as a mosaic pattern on the surface of the transducer when viewed under 30 power magnification, this modest change in the measured properties is somewhat surprising. A possible explanation is that enough of the ceramic structure remains intact that the inter-granular coupling remains largely unchanged over most of the sample.

The transducers were tested with the same setup shown in Fig. 6 and excited with a 32 V negative impulse. A flat steel plate reflector was placed at the focal distance of 5.2 mm. The result for the PZT transducer, depicted in Fig. 9(a), shows a lower signal level than the PT transducer

[Fig. 9(b)]. The pulse length and frequency spectrum of the PT transducer closely match the modeled response for a transducer with the same diameter and thickness. The ringdown characteristics are nearly the same, while the measured frequency spectrum shows a slight decrease in bandwidth relative to the modeled spectrum. An insertion loss of 30 dB for the PT transducer was measured at the center frequency, as compared with a loss of over 40 dB for the PZT transducer.

These results demonstrate that an improvement in performance can be achieved by choosing a material with a dielectric constant that results in a transducer impedance which closely matches the electrical termination conditions. Also, the excellent correlation between the modeled and measured waveforms shows that it is possible to accurately predict transducer performance by carefully measuring the material properties at the frequency of interest.

V. CONCLUSIONS

As has been generally recognized for years, the piezoelectric properties of ceramic transducer materials operated at high frequencies can be significantly different from those at low frequencies. An experimental investigation determined the properties of a number of ceramic materials operated as thickness-mode resonators at frequencies between 10 and 100 MHz. Results showed that conventional PZT materials have significantly reduced k_t and increased losses at high frequencies, most likely as a result of decreased domain wall motion contributions to the piezoelectric response. New fine grain PZT materials have been demonstrated to have less frequency-dependent properties, particularly the mechanical loss. This behavior is believed to be due to a shifting of the extrinsic reduction phenomenon to a higher frequency.

The PT class of materials was found to have properties which behaved markedly different from PZT materials at high frequencies. The frequency dependence of k_t was found to be less for EC97 than for even the fine grain PZT, despite the order of magnitude larger average grain size, AGS. Coupling coefficients close to 0.5 were measured at 80 MHz. This shows that composition plays a more significant role than grain size in determining the frequency dependence of k_t . While the EC97 showed high losses at frequencies close to 100 MHz, the same material after undergoing a hot isostatic press or HIP treatment showed much lower losses as a result of the decreased porosity. Thus it appears that the frequency dependence of Q_m is affected by not only grain size and porosity, but also by composition. PT materials, due to reduced extrinsic contributions, suffer less of a decrease at high frequencies than do PZT materials, despite a larger grain size. Mechanical losses are considerably lower for the PT materials in the 50 to 100 MHz range, with a Q_m of nearly 100 being measured at 98 MHz for densified PT.

The properties of the piezoelectric material greatly influence the response of the transducer. A larger diameter

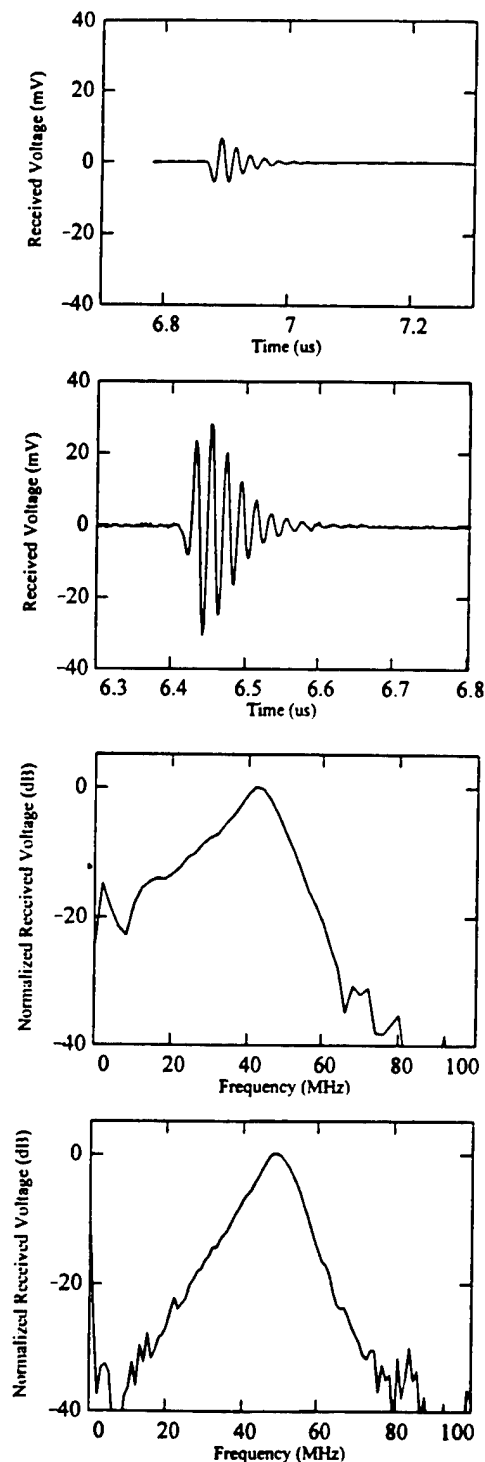


Fig. 9. Measured pulse echo waveform for 2 mm diameter 45 MHz transducers: (a) PZT material (Ferroperm PZ21), (b) PT material (EDO EC97). Note the lower signal level for the PZT transducer. The measured waveform for the PT transducer shows excellent correlation with that predicted by the KLM model using the measured properties.

is permitted for high frequency transducers used for external scanning than for those used for applications such as intravascular imaging where the transducer diameter is severely limited by space constraints. This larger radiating area results in better lateral resolution than for a smaller transducer operating at the same frequency. For transducers greater than 50 MHz with a diameter greater than 1 mm, the larger area relative to the thickness dictates the use of a lower dielectric constant material for a transducer impedance, Z_{in} , which closely matches 50 Ω . Simulations using the measured properties showed that the lower dielectric constant of the PT material can result in a Z_{in} close to 50 Ω for a 2 mm diameter 45 MHz transducer. The simulated waveform showed higher amplitude and shorter pulse length than for a PZT transducer with the same dimensions. The improved high frequency properties of PT materials, due to their different composition and microstructure, also contribute to improved transducer response.

Measurements on transducers which were fabricated show good agreement with the modeled waveforms in both the time and frequency domains. This indicates that it is possible to accurately predict transducer performance based on material property measurements made at high frequencies.

ACKNOWLEDGMENTS

The authors would like to thank a number of people at Penn State for their technical assistance: Beth Jones for processing the fine grain PZT ceramics, Gaylord Shawzer and Tom Gingher for helping to prepare the thickness mode plates, and Gene Gerber for helping to build the transducers.

REFERENCES

- [1] F. S. Foster, C. J. Pavlin, G. R. Lockwood, L. K. Ryan, K. A. Harasiewicz, L. Berube, and A. M. Rauth, "Principles and applications of ultrasound backscatter microscopy," *IEEE Trans. Ultrason., Ferroelect., Freq. Contr.*, vol. UFFC-40, pp. 608-616, Sept. 1993.
- [2] F. S. Foster, L. K. Ryan, and D. H. Turnbull, "Characterization of lead zirconate titanate ceramics for use in miniature high-frequency (20-80 MHz) transducers," *IEEE Trans. Ultrason., Ferroelect., Freq. Contr.*, vol. UFFC-38, pp. 446-453, Sept. 1991.
- [3] G. R. Lockwood, D. H. Turnbull, and F. S. Foster, "Fabrication of high-frequency spherically shaped ceramic transducers," *IEEE Trans. Ultrason., Ferroelect., Freq. Contr.*, vol. UFFC-41, pp. 231-235, Mar. 1994.
- [4] G. R. Lockwood and F. S. Foster, "Modeling and optimization of high-frequency ultrasound transducers," *IEEE Trans. Ultrason., Ferroelect., Freq. Contr.*, vol. UFFC-41, pp. 225-230, Mar. 1994.
- [5] N. Kim, "Grain size effect of dielectric and piezoelectric properties in compositions which are near the morphotropic phase boundary of lead zirconate-titanate based ceramics," Ph.D. dissertation, Penn State Univ., May 1994.
- [6] R. Krimholtz, D. A. Leedom, and D. L. Matthaei, "New equivalent circuits for elementary piezoelectric transducers," *Electron. Lett.*, vol. 6, pp. 398-399, July 1971.
- [7] A. R. Selfridge and S. Gehlbach, "KLM transducer model implementation using transfer matrices," *Proc. IEEE Ultrason. Symp.*, 1985, pp. 875-877.

- [8] ANSI/IEEE Standard on piezoelectricity, Std. 176-1987, IEEE, New York, 1987.
- [9] J.-H. Ih and B.-H. Lee, "Attenuation coefficient of a piezoelectric resonator operating in a thickness mode," *Electron. Lett.*, vol. 22, pp. 357-358, Mar. 1986.
- [10] W. Cao and C. A. Randall, "Grain size and domain size relations in bulk ceramic ferroelectric materials," *J. Phys. Chem. Solids*, vol. 57, no. 10, pp. 1499-1505, 1996.
- [11] B. Jaffe, W. R. Cook, Jr., and H. Jaffe, *Piezoelectric Ceramics*. New York: Academic, 1971.
- [12] C. E. Millar, B. Anderson, E. Ringgard, W. Wolny, J. Ricote, and L. Pardo, "Fabrication of high-density, fine-grained PZT ceramics using a post sinter HIP treatment," *Proc. 1994 IEEE Int. Symp. Applications Ferroelect.*, pp. 118-121.
- [13] C. S. Desilets, J. D. Fraser, and G. S. Kino, "The design of efficient broad-band piezoelectric transducers," *IEEE Trans. Sonics Ultrason.*, vol. SU-25, pp. 115-25, May 1978.
- [14] M. Sherar and F. S. Foster, "The design and fabrication of high frequency poly(vinylidene fluoride) transducers," *Ultrason. Imaging*, vol. 111, pp. 75-94, 1989.
- [15] G. R. Lockwood, J. W. Hunt, and F. S. Foster, "Design of protection circuitry for high frequency ultrasound systems," *IEEE Trans. Ultrason., Ferroelect., Freq. Contr.*, vol. UFFC-38, pp. 48-55, Jan. 1991.



Michael J. Zipparo was born in Pittsburgh, PA, on October 25, 1968. He received the B.Sc. degree in electrical engineering in May 1991, the M.Sc. degree in acoustics in December 1993, and the Ph.D. degree in bioengineering in December 1996, all from The Pennsylvania State University, University Park, PA.

From 1991 to 1993 he was employed as a transducer engineer at Blatek, Inc. in State College, Pennsylvania where he worked on the development of single element ultrasonic transducers for medical and NDT applica-

tions. In January 1994 he joined The Whitaker Center for Medical Ultrasonic Transducer Engineering as one of its founding graduate students. In June 1995 he initiated a student internship at Sound Technology, Inc. in State College where he developed a modeling and optimization method for the acoustic design of curved linear array transducers for medical imaging applications. Since January 1997 he has been employed by Advanced Coronary Intervention, Inc. where he is working on the development of an intravascular ultrasonic imaging system. His current research interests include material characterization, optimization, and manufacturing methods for high frequency medical imaging transducers and arrays.



K. Kirk Shung (S'73-M'75-SM'89-F'93) was born on June 2, 1945. He received a B.S. degree in electrical engineering from Cheng-Kung University in Taiwan in 1968, and M.S. and Ph.D. degrees in electrical engineering, respectively, from the University of Missouri, Columbia, MO, in 1970 and the University of Washington, Seattle, WA, in 1975. Following postdoctoral work, he was employed as a research engineer at Providence Medical Center, Seattle, WA, while holding a position of research scientist at the Institute of Applied Physiology and Medicine, Seattle, WA. In 1979, he moved to the Pennsylvania State University as an Assistant Professor of Bioengineering and became a Professor in 1989. He was appointed Director of the Whitaker Center for Medical Ultrasonic Transducer Engineering at Penn State in 1994.

Dr. Shung is a fellow of the IEEE, of the American Institute of Ultrasound in Medicine and of the Acoustical Society of America. He is a founding fellow of the American Institute of Medical and Biological Engineering. He served as a member on National Institutes of Health Diagnostic Radiology Study Section from 1985 to 1989. He was the recipient of the IEEE Engineering in Medicine and Biology Society early career achievement award in 1985. Dr. Shung has published more than 100 papers and is the author of a textbook, *Principles of Medical Imaging*, published by Academic Press in 1992 and the co-editor of a book, *Ultrasonic Scattering by Biological Tissues*, published by CRC Press in 1993.

His research interest is in ultrasonic imaging and tissue characterization, ultrasonic transducers and arrays, and contrast agents.



Thomas R. Shrout is Professor of Materials and Senior Scientist at the Pennsylvania State University. He received a B.S. and Ph.D. in ceramic science from Pennsylvania State University in 1976 and 1981, respectively.

Prior to joining the faculty at Penn State, Dr. Shrout was with Sprague Electric Co. and AVX Co. He holds five patents and has co-authored more than 100 papers in the area of electronic ceramics with an emphasis on processing property relationship.

Frequency Agile Transducers

APPENDIX 47

An actively-tuned solid state piezoelectric vibration absorber

Christopher L. Davis^a, George A. Lesieutre^b

^aSmart Structures Technology, The Boeing Company, Seattle, WA 98032

^bDepartment of Aerospace Engineering, The Pennsylvania State University, University Park, PA 16802

ABSTRACT

A tunable solid state piezoelectric vibration absorber and an active tuning method were developed and demonstrated. A passive vibration absorber generally acts to minimize structural vibration at a specific frequency associated with either a tonal disturbance or the response of a lightly damped structural vibration mode. Because this frequency is rarely stationary in real applications, damping is usually added to ensure some level of effectiveness over a range of frequencies. Maximum response reductions, however, are achieved only if the absorber is lightly damped and accurately tuned to the frequency of concern. Thus, an actively-tuned vibration absorber should perform better than a passive one and, furthermore, could be made lighter. In its simplest form, a vibration absorber consists of a spring-mass combination. A key feature of the tunable vibration absorber described herein is the use of piezoelectric ceramic elements as part of the device stiffness. The effective stiffnesses of these elements was adjusted electrically, using a passive capacitive shunt circuit, to tune the resonance frequency of the device. The tuning range of the absorber is thus bounded by its short-circuit and open-circuit resonance frequencies. An alternative tuning approach might employ resistive shunting, but this would introduce undesirable damping. Another feature of the device is the ability to use the piezoelectric elements as sensors. A control scheme was developed to estimate the desired tuning frequency from the sensor signals, to determine the appropriate shunt capacitance, and then to provide it. The shunt circuit itself was implemented in ten discrete steps over the tuning range, using a relay-driven parallel capacitor ladder circuit. Experimental results showed a maximum 20 dB, and a 10 dB average improvement in vibration reduction across the tuning range, as compared to a pure passive absorber tuned to the center frequency, with additional benefit extending beyond the tuning range.

Keywords: passive vibration absorber, semi-active tuning, piezoelectric ceramic, capacitive shunting

1. INTRODUCTION

Vibration is an important aspect of many engineering systems, from machine tools to structure-borne noise in aircraft¹. In most cases, such vibration is undesirable and requires attenuation. Attenuation techniques range in complexity from relatively simple narrow-band passive elastomeric vibration absorbers to fully active broad-band vibration control systems.

Passive attenuation methods represent an important class of approaches to the control unwanted structural vibrations². One particular method of passive vibration suppression involves the use of passive vibration absorbers (PVAs). Passive vibration absorbers are conceptually simple devices consisting of a mass attached to a structure via a spring or via a parallel spring-damper combination. PVAs are commonly constructed of an elastomeric material sandwiched between the structure and an inertial (or proof) mass. The primary function of these devices is to increase the effective dynamic stiffness of a structure over a relatively narrow frequency band. Increasing the dynamic stiffness of a structure reduces its dynamic displacement (assuming the forcing level remains constant). In practice, PVAs are typically used to minimize vibration at a specific frequency associated with either a lightly damped structural mode or a tonal disturbance. The advantages of using vibration absorbers are low cost, low weight, and ease of attachment. The fact that a PVA may only be used effectively at a single frequency, however, can sometimes be a significant drawback.

Further author information:

G.A.L. (correspondence): Email: g-lesieutre@psu.edu; Telephone: 814-863-0103. Associate Professor.

C.L.D.: Email: christopher.l.davis@boeing.com; Telephone: 253-773-2036. Research Engineer.

While a common use of PVAs is to reduce vibration in tall buildings or towers³, they have also been successfully used in the aviation industry for some time. For example, the DC-9 for many years used a set of four PVAs attached to each engine pylon⁴ to reduce aft cabin noise associated with the operating spool frequency of the engines. Similarly, both the Fokker F27 and the Saab 340⁵ aircraft use PVAs attached directly to the fuselage frame to lower interior cabin noise levels.

In these applications, the absorbers provide considerable vibration attenuation at specific frequencies. Performance can be seriously degraded, however, if the disturbance source changes frequency. If this occurs, the PVA must be physically re-tuned to maintain optimal performance. Physically re-tuning the absorber is generally impractical. Thus, there is a need for vibration absorbers with tunable variable properties.

Active vibration absorbers (AVAs) are passive vibration absorbers with variable stiffness, mass, or damping properties. The advantage of using an AVA over a PVA is the tunability of the resonance frequency of the device. AVAs are commonly used to track frequency-varying disturbances or to increase the bandwidth of a vibration attenuation method. Recently, Northwest Airlines initiated plans to upgrade 173 of its DC-9s with active tuned mass absorbers built by Barry Controls^{6,7}. Due to the increased weight and complexity of using AVAs, however, they have not generally found widespread use.

The goal of this research was to extend AVA technology by developing a tunable piezoceramic vibration absorber. The key aspects of a tunable vibration absorber are the method by which the stiffness or mass of the device is altered and the magnitude of the resulting change in frequency. Because it is generally more difficult to vary the mass of a device, focusing on how to incorporate a variable stiffness into the absorber is appropriate. Precisely how the stiffness may be changed is an important issue.

Piezoceramic materials offer an attractive solution to the variable stiffness problem, because these materials exhibit relatively strong coupling between electrical and mechanical behavior. Recently, the Center for Acoustics and Vibration at Penn State and PCB Piezotronics, Inc. were involved in the development of a piezoceramic inertial actuator (PIA)⁸. Part of the development research conducted by Penn State showed that a PIA, used passively, behaves like a passive vibration absorber⁹. The research presented here focused on developing a method for using such a PIA as an active vibration absorber.

2. BACKGROUND

A model was developed to improve insight into the effects of shunting a piezoceramic inertial actuator. First, a single degree-of-freedom (DOF) structure and absorber model were created. Next, the absorber model was modified to incorporate the effects of the piezoceramic forcing element of the inertial actuator. Finally, the electro-mechanical dynamics of the passively shunted piezoceramic were added to the model to capture the desired frequency dependent effects.

2.1 Vibration absorber/structure interaction

Consider a damped vibration absorber attached to a single DOF system, as shown in Figure 1. Let m_s , k_s , and b_s represent the effective mass, stiffness, and damping of the structure respectively, and m_a , k_a , and b_a represent the mass, stiffness, and damping of the absorber respectively.

First, consider the response of the structure only (*i.e.*, no absorber, just the base structure). The following linear equation of motion is readily found. (Note: unless otherwise stated, the damping terms b_s and b_a are considered small and ignored, to simplify analysis.)

$$m_s \ddot{x}_s = -k_s(x_s - x_{in}) \quad (1)$$

Assuming zero initial conditions, Eq. 1 may be transformed into the Laplace domain and expressed in transfer function form. Eq. 2 represents the ratio of the structural displacement, X_s , to the base disturbance displacement, X_{in} , or

$$\frac{X_s(s)}{X_{in}(s)} = \frac{k_s}{m_s s^2 + k_s} \quad (2)$$

The positive root of the denominator of Eq. 2 may be used to calculate natural frequency of the structure, ω_s , namely

$$\omega_s = \sqrt{\frac{k_s}{m_s}} \quad (3)$$

Thus, when the structure is excited harmonically at a frequency ω_s , it will resonate (*i.e.*, X_s will be large compared to X_{in}).

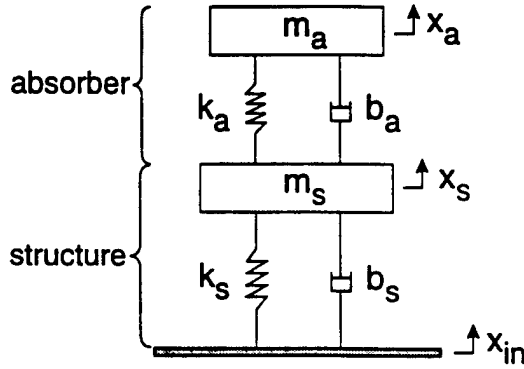


Figure 1. Passive vibration absorber attached to a single-DOF structure lumped parameter model

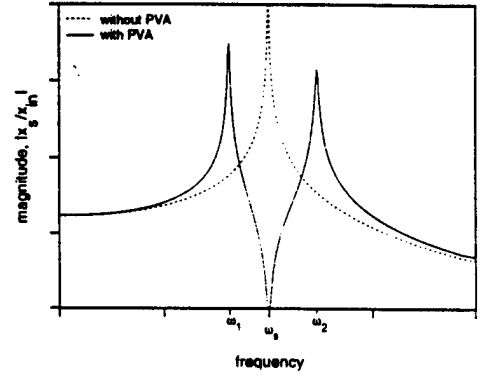


Figure 2. Sample frequency response functions for the single-DOF structure and the single-DOF structure with attached PVA

Next, consider the equations of motion for the coupled structure/absorber system shown in Figure 1, namely

$$m_a \ddot{x}_a = -k_a(x_a - x_s) \quad \text{and} \quad m_s \ddot{x}_s = -k_s(x_s - x_{in}) - k_a(x_s - x_a) \quad (4a, b)$$

Transforming Eqs. 4a and 4b into the Laplace domain and combining the results yields an expression for the structural displacement, X_s , in terms of the input disturbance displacement, X_{in} , or

$$\frac{X_s(s)}{X_{in}(s)} = \frac{k_s(m_a s^2 + k_a)}{m_s m_a s^4 + (m_a(k_s + k_a) + m_s k_a)s^2 + k_s k_a} \quad (5)$$

Eq. 5 describes the coupled dynamics of the structure/absorber system. Note that as with Eq. 2, the roots of the denominator of Eq. 5 are the poles of the coupled system and the roots of the numerator of Eq. 5 are the zeros of the coupled system. The frequencies of the poles (ω_1 and ω_2) and zero (ω_{abs}) of the coupled structure/absorber system are

$$\omega_{1,2} = \frac{\sqrt{2}}{2} \sqrt{\frac{m_a(k_a + k_s) + m_s k_a \pm \sqrt{m_a k_a (m_a(k_a + 2k_s) + 2m_s k_a) + (m_a k_s + m_s k_a)^2}}{m_a m_s}} \quad \text{and} \quad \omega_{abs} = \sqrt{\frac{k_a}{m_a}} \quad (6a, b)$$

Note that ω_{abs} defines the frequency of minimum response of the coupled structure/absorber system, and is equal to the natural frequency of the (undamped) vibration absorber itself.

Consider now the structural frequency response function, both with and without an attached vibration absorber, due to an input displacement disturbance (see Figure 2). The response of the structure only (*i.e.*, the magnitude of Eq. 2) is denoted by the dashed line in Figure 2. Notice the large structural response at the frequency ω_s .

The solid line in Figure 2 shows the response of the structure with an attached vibration absorber that has a natural frequency, ω_{abs} , equal to the natural frequency of the original structural mode, ω_1 . The response is reduced dramatically at the frequency of the original structural mode, ω_1 , and increased at frequencies both above and below the frequency of the original structural mode (i.e., at the frequencies of the poles of the coupled system, ω_1 and ω_2).

From Eq. 5 and Figure 2, it is clear that the natural frequency of the absorber defines the frequency at which minimum structural response will occur. Upon closer inspection of the numerator of Eq. 5, it is also evident that the frequency of minimum structural response is solely a function of the absorber mass and stiffness. Thus it is possible in principle to reduce structural response at any disturbance frequency, provided the natural frequency of the absorber is equal to the disturbance frequency and the absorber is lightly damped. This idea will be used later when developing a tuning control strategy to maintain optimum absorber performance when subjected to a tonal disturbance frequency.

2.2 Vibration absorber frequency tuning via passive electrical shunting

With the knowledge that the natural frequency of the absorber defines the frequency of minimum structural response, the next step was to develop a method for changing the stiffness of the absorber in real-time to make the absorber tunable. Electrically shunting the actuator has the effect of changing the effective stiffness (and thus the natural frequency) of the device. A full description of the theory behind the shunting method for frequency tuning is presented in the conference paper by Davis, *et al.*¹⁰ as well as the thesis by Davis¹¹ and is summarized here for completeness.

As mentioned previously, a vibration absorber may be modeled using lumped parameters such as a spring, k_a , and mass, m_a (Figure 3a). Similarly, an inertial actuator may be modeled as a spring-mass system with a forcing element, F_p , in parallel with the spring element, k_a , of the absorber (Figure 3b). Placing the forcing element of the inertial actuator (which has an associated effective stiffness) in parallel with the inherent structural stiffness of the absorber (Figure 3c) results in a net device stiffness that is the sum of the two stiffnesses.

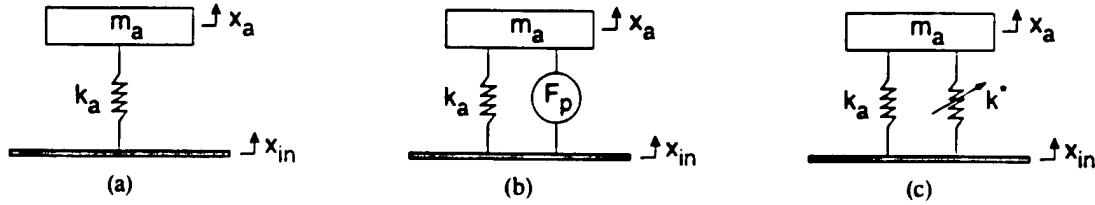


Figure 3. (a) Passive vibration absorber lumped parameter model, (b) Inertial actuator lumped parameter model, (c) Passively shunted inertial actuator lumped parameter model

Electrically shunting the piezoceramic forcing elements within a piezoceramic inertial actuator changes the effective stiffness of the piezoceramics. An expression was developed¹¹ for the effective stiffness, k^* , of the piezoceramic forcing element within the piezoceramic inertial actuator, namely

$$k^* = k^E \left(1 + \frac{k_p^2}{1 - k_p^2 + \alpha(s)} \right) \quad (7)$$

where k^E is the effective short circuit piezoceramic stiffness, k_p is the piezoceramic planar electromechanical coupling coefficient, $\alpha(s)$ is the nondimensional ratio of the electrical impedance of the piezoceramic (i.e., $1/sC_p^T$, where C_p^T is the capacitance of the piezoceramic measured under constant stress) to the electrical impedance of the shunt circuit, and s is the Laplace parameter (i.e., $s=i\omega$ where ω is radian frequency).

Regardless of the type of simple electrical shunt circuit (e.g., resistor, capacitor, inductor), there are limits on the range of values k^* can take on. These limits are conveniently defined in terms of shunt circuit short- and open-circuit electrical impedances. When short circuited, the shunt impedance is effectively zero and Eq. 7 reduces to $k^* = k^E$. At open circuit, the

shunt impedance is effectively infinite and $k^* = k^E (k_p^2 / (1 - k_p^2))$. Thus the tunable range of k' is limited by the value of the piezoceramic planar electromechanical coupling coefficient, k_p .

In the application described here, the value of k_p was approximately 0.6. For a device made solely of this type of piezoceramic material, the change in stiffness from short to open circuit could be as high as 56%, resulting in an almost 25% change in natural frequency. In practice, however, the stiffness of the piezoceramic is in parallel with the inherent mechanical stiffness of the actuator, and only some fraction of the net device stiffness may be changed due to electrical shunting.

Note that Eq. 7 may be complex depending upon the type of shunt circuit used (e.g., if a resistor is used as the shunt circuit). A complex stiffness would indicate that the device has mechanical properties similar to those of an anelastic material and therefore will add hysteretic damping effects to the system. In terms of vibration absorber performance, adding damping has the effect of increasing the response magnitude at the natural frequency of the absorber. Because the goal of this research was to maintain minimum structural response at ω_{abs} , shunt circuits which added damping to the system were not considered.

An ideal capacitor is a purely reactive element (i.e., capacitors do not dissipate energy and thus provide no damping). The ratio of the effective tunable piezoceramic stiffness of a capacitively shunted piezoceramic element to the short circuit stiffness of the element is shown in Figure 4. Notice that for this case, the tuning ratio is the ratio of the shunt capacitance, C_{sh} , to the clamped capacitance of the piezoceramic. As illustrated in Figure 4, the tunable piezoceramic stiffness varies smoothly with increasing shunt capacitance. Also note that roughly a four-order-of-magnitude change in shunt capacitance is necessary to effectively change from open to short circuit (or vice versa).

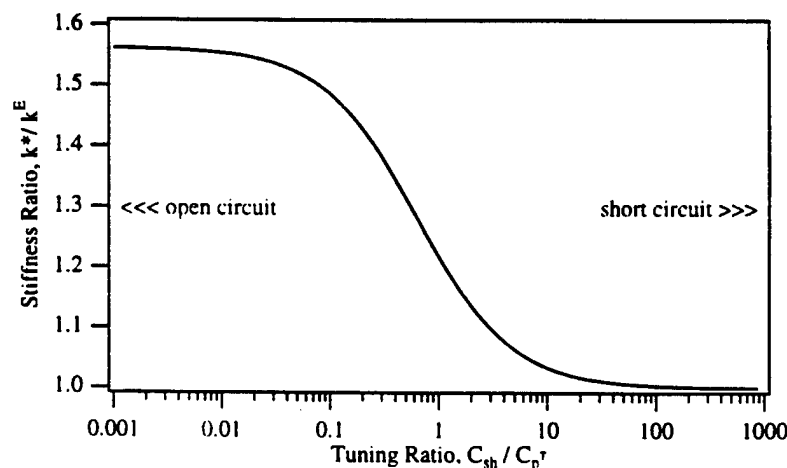


Figure 4. Effect of shunt capacitance on effective piezoceramic stiffness

As mentioned previously, the total stiffness of a piezoceramic vibration absorber is the sum of the effective tunable piezoceramic stiffness and the inherent stiffness of the device. The relative magnitudes of the two stiffnesses determines the net frequency change possible via electrical shunting. An experiment was conducted using a commercially available piezoceramic inertial actuator as a passive, electrically shunted vibration absorber. A schematic of the piezoceramic inertial actuator used for the experiments, PCB Model X712A02, is shown in Figure 5. The actuator (the lower flat cylinder in Figure 5) is approximately 2 inches in diameter and approximately 3/8 of an inch thick. The reaction mass is attached to the top of the actuator by a standard 10-32 threaded stud, making it relatively easy to coarsely tune the device by changing the mass. The base of the inertial actuator (hidden in Figure 5) also has a 10-32 threaded stud used for attaching the actuator to a structure.

The purpose of the experiment was to measure the natural frequency and modal damping ratio of the actuator under a variety of capacitive shunt conditions ranging between short and open circuit. In the experiment, the inertial actuator was attached to a shaker and accelerometers were used to measure both the input (i.e., the shaker) acceleration and the reaction mass acceleration. The ratio of the two acceleration measurements formed a frequency response function which was then curve fit to approximate the natural frequency and modal damping ratio of the actuator for a given shunt condition. The electrodes of

the inertial actuator were attached to a solderless breadboard where discrete values of capacitance could be used to shunt the device.

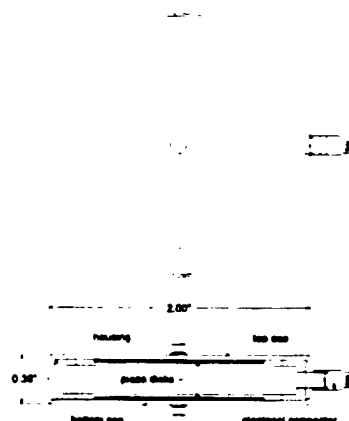


Figure 5. Schematic of the PCB Model X712A02 inertial actuator with 200g reaction mass

The results of the passive shunting experiment verified the ability to predictably tune the natural frequency of the piezoceramic vibration absorber between a short circuit natural frequency of 313 Hz and an open circuit natural frequency of 338 Hz. The resulting change in natural frequency was approximately 7.5% from short to open circuit. Next, a frequency tuning control method for the shunted piezoceramic vibration absorber was developed.

3. SEMI-ACTIVE PIEZOCERAMIC VIBRATION ABSORBER FREQUENCY TUNING CONTROLLER

The preceding section showed that it is possible to use a PIA as a passive vibration absorber and that such a PIA may be passively tuned with an external shunt circuit. In this section, the approach used to implement a semi-active tuning method is described.

3.1 Concept

Consider a flexible structure with several well-spaced structural modes of vibration subjected to a tonal disturbance. Attaching a conventional passive vibration absorber to the structure, tuned to the tonal disturbance frequency, would reduce structural response at that frequency. Thus, as long as the disturbance frequency remained constant, a high level of attenuation would be achieved (*i.e.*, structural vibration would be minimized). If, however, the tonal disturbance frequency changed, performance would decrease (*i.e.*, the vibration level would increase). Therefore it is clearly beneficial to have a tunable vibration absorber and a tuning method to track a changing disturbance frequency and appropriately re-tune the frequency of the absorber.

Developing a tuning method for the PIA involved three steps: First, an appropriate system signal was identified, from which the desired tuning frequency could be estimated. The next step was to develop a method for actually estimating the frequency of structural vibration from the signal. The final step involved formulating a control scheme to determine and provide the proper shunt capacitance.

The concept of monitoring the disturbance frequency and tuning the absorber to maintain minimum structural response is illustrated in Figure 6. The upper plot represents broadband structural response for a structure both with and without an attached PIA vibration absorber. The highlighted area of the upper plot is enlarged in the lower portion of Figure 6 to show the transfer function zeros (or minima) created by the addition of a short circuit, shunted, and open circuit PIA to the structure.

First, consider the case when the piezoceramic element within the PIA is short circuited (indicated by the dashed line in the highlighted section in the lower plot of Figure 6). If a tonal disturbance acted on the structure at a frequency equal to f_{sc} , structural response would be minimal. If the disturbance frequency were to decrease while the PIA remained short circuited,

structural response would increase. Similarly, if the disturbance frequency were to increase to the frequency f_{oc} , while the piezo element remained short circuited, structural response would again increase. However, if the absorber were "re-tuned" by adjusting the electrical shunt impedance to an open circuit condition structural response would remain minimal. In addition, if the disturbance frequency were to fall anywhere between f_{sc} and f_{oc} , there exists a shunt impedance that will deliver minimum structural response.

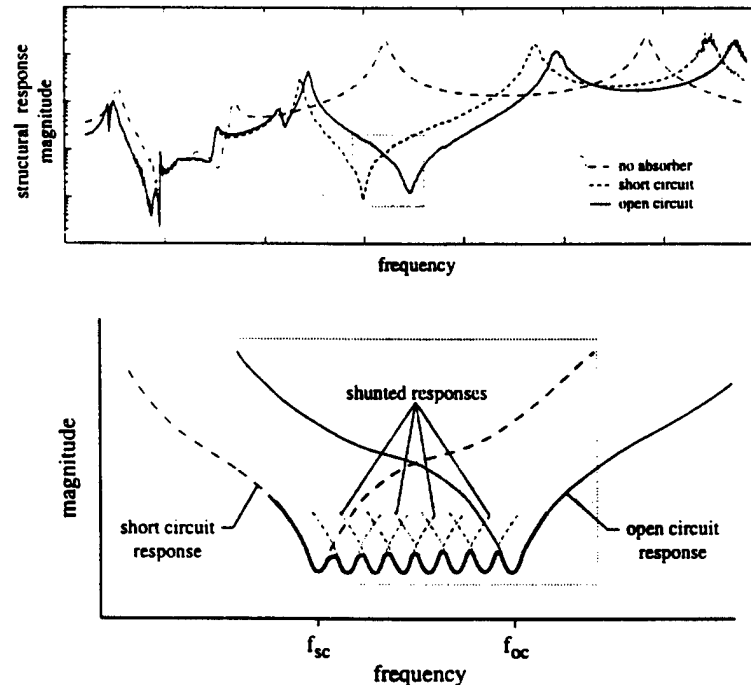


Figure 6. Conceptual tuned vibration absorber structural response

Consider the following situation: a structural mode is excited by a pure tone harmonic disturbance which varies in frequency by a few percent of some nominal frequency. In principle, a PIA-based vibration absorber could be added to the structure such that at a shunt tuning ratio of one, the natural frequency of the absorber would be equal to the nominal disturbance frequency (*i.e.*, the natural frequency of the absorber for a tuning ratio of one is half-way between f_{sc} and f_{oc}). If sensing (in the form of determining the frequency of the disturbance), control (in the form of a command signal based on the sensed frequency to alter the electric shunt impedance), and actuation (in the form of a means to alter the electrical shunt condition) were provided, then minimum structural response could be maintained within the band defined between the open and short circuit frequencies.

The heavy solid line in Figure 6 illustrates the conceptual response of a discretely tuned PVA. In this illustration, the shunt capacitance does not vary smoothly between f_{sc} and f_{oc} , but instead is discretized. Thus, determining a means to estimate the disturbance frequency, choosing the correct value of shunt impedance based on the estimated frequency, and physically changing the shunt impedance are the main subject of the next section. Two important questions to be addressed are: 1) what sensor(s) could be used; and 2) once a sensed signal is acquired, how can frequency information be extracted from it?

3.2 Implementation

It is clearly desirable to try to use the fewest number of sensors in order to reduce control system complexity, weight, and power consumption. With this in mind, a method for sensing the tonal disturbance frequency based on the voltage produced by the piezoceramic within the PIA was developed.

Assuming a linear model for the coupled structure/PIA system, the voltage produced by the piezoceramic elements within the PIA is directly proportional to the piezoceramic strain and the shunt circuit electrical impedance. Thus, for an open circuit electrical PIA being forced near resonance, the piezo elements would be under considerable strain due to the motion of the

inertial mass (and corresponding small motion of the attached structure), producing considerable voltage. If, however, the PIA were short circuited, there would be effectively no measurable voltage across the terminals of the PIA. Instead, short-circuiting the device would produce a large current (for the same forcing conditions). Thus, because shunting the PIA can vary the electrical impedance of the device from nearly short circuit to nearly open circuit, using the electrical state of the piezoceramic to estimate vibration frequency can only be effective if both voltage and current are used as sensor variables.

For the prototype system described here, a control system was used in which the A/D conversion process required voltages within a prescribed range. Thus it was necessary to convert the PIA current to a corresponding voltage. The current estimation process was realized using an op-amp as an ideal current-to-voltage converter¹².

The controller used for tuning the PIA is shown in Figure 7. The controller used two inputs and one output. The inputs were the PIA voltage, V_v , and the voltage proportional to the PIA current, V_i . The output was a voltage proportional to the tuning impedance of the shunt circuit. The main elements of the controller were: 1) the band-pass filters; 2) the frequency estimation logic; and 3) the control voltage calculation.

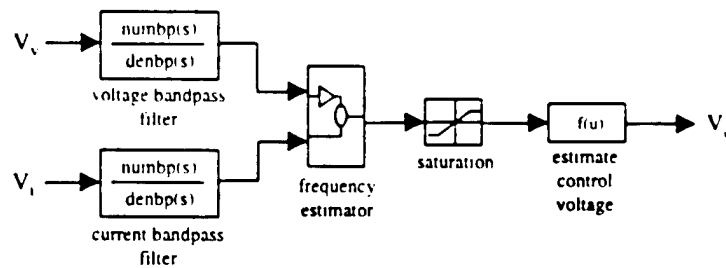


Figure 7. Control system block diagram

The band-pass filters removed any DC-component of the input signals and attenuated high frequency noise. The filters were second order with low and high cut-off frequencies of approximately 130 and 780 Hz respectively. Note that for the prototype system, the frequency range of interest (*i.e.*, the range of frequencies defined by the short and open circuit resonance frequencies of the PIA) was approximately 290 to 350 Hz. Thus the pass-band encompassed the range of interest well.

The filtered signals were next used to estimate the frequency of the tonal disturbance. For the prototype version, frequency estimation was done by the control computer. For increased performance, analog circuitry could be implemented in the form of a phase locked loop to convert the sensed voltages to a voltage proportional to frequency for use by the control system.

With a proper estimate for the frequency of vibration, the remaining task of the controller was to calculate an appropriate control voltage with which to vary the shunt impedance. Before the controller could be programmed, however, it was necessary to determine a method for physically altering the shunt capacitance. Recall that in Figure 2, the effective tuning ratio range for capacitive shunting is roughly 0.01 to 100 times the capacitance of the PIA measured at constant stress. The capacitance of the PIA measured at constant stress used in prototype system was approximately 0.072 μF . Therefore, to tune the natural frequency of the PIA between f_{sc} and f_{oc} , a shunt capacitance range of roughly 0.7 nF to 7 μF was required.

Variable capacitors do exist. However, the majority of variable capacitors have relatively small ranges (*e.g.*, even a range of 12 to 100 pF is not common) and must be tuned by physical means. Programmable capacitors also exist, but due to their added complexity and resistance, they were not considered for the prototype system. Instead, a "ladder" circuit of discrete capacitors wired in parallel was used to tune the PIA.

The effect of placing capacitors in parallel is a net capacitance equal to the sum of the individual capacitances. Figure 8 illustrates a conceptual shunt circuit with several parallel capacitors. If the frequency tuning band of the shunted PIA were discretized into a finite number of capacitive impedances, a control law could be developed to select a number of parallel capacitors whose sum would be the net electrical impedance needed to tune the actuator very close to the estimated disturbance frequency. Clearly, the number of discrete capacitance values used in a specific application will depend on the overall size of

the frequency tuning range, the intrinsic damping of the absorber, and the acceptable deviation from minimum response. Finer discretization of the tuning band will yield more uniformly low system response.

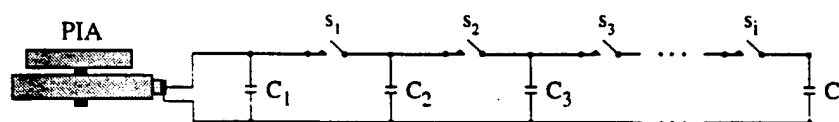


Figure 8. Conceptual "ladder" capacitive shunt circuit

Consider a discretized shunt circuit with 10 discrete capacitance levels ranging from approximately 0.7 nF to 7 μ F. Ideally, each discrete shunt capacitance will tune the PIA such that structural response will be a minimum for a prescribed frequency within the control bandwidth. Thus the tunable frequency band was divided into nine frequency bands between the short and open circuit natural frequencies of the PIA as shown in Figure 9.

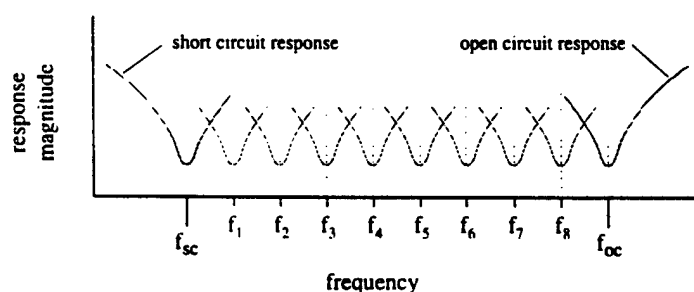


Figure 9. Frequency band shunt discretization

The frequencies at the minima of each frequency band (labeled as f_{sc} , f_1 through f_8 , and f_{oc} in Figure 8) define frequencies at which the cumulative combinations of shunt capacitance prescribe the shunted natural frequency of the PIA. First, consider the open circuit shunt case. Open circuit corresponds to a very small (or zero) shunt capacitance. Thus if capacitor C_1 in Figure 8 were very small (or removed) and all switches were open, the PIA would be in an approximately open circuit shunt condition (*i.e.*, the natural frequency of the PIA would equal f_{oc}). Next, consider closing the switch s_1 in Figure 8. The net capacitance of the shunt circuit increases to the sum of C_1 and C_2 . Conversely, the natural frequency of the PIA decreases to f_8 (assuming C_1 and C_2 are chosen correctly). Similarly, closing switches s_1 and s_2 will increase the net shunt capacitance to the sum of the C_1 , C_2 , and C_3 and the PIA natural frequency (and thus the frequency of minimum structural response) will decrease to f_7 . Closing all of the switches will increase the net shunt capacitance to the total of all of the capacitors in the ladder circuit. Thus, if C_1 through C_i are chosen correctly, the sum of all the capacitors will be large enough to approximate a short circuit shunt condition (*i.e.*, the total parallel capacitance will be greater than or equal to $100 \times C_p^T$). The question remains, however, as to how to open and close the switches in the ladder circuit.

The switches in the shunt circuit shown in Figure 8 determine the number of capacitors in parallel with the PIA. Ideally, these switches would operate in response to a prescribed signal from the control system. In doing so, however, the switches should not introduce any additional electrical impedance into the shunt circuit. A relay provides one possible solution to this problem.

The control voltage, V_c , shown in Figure 7, is used to turn the relays on in succession. Variable resistors wired between each relay driver circuit were adjusted such that for $V_c=1V$, relay #1 would turn "on" while the others would remain "off". For $V_c=2V$, relays #1 and #2 would turn "on" while the other relays would remain "off". Similarly, more relays would turn "on" while the remaining relays remained "off" for increasing integer voltage levels up to and including 9V. What remained was to program the control logic to output discrete integer voltage levels corresponding to desired shunt capacitance levels. Note that discrete voltage outputs were required to ensure the appropriate relays in the switching circuit were either "on" or "off".

Figure 10 illustrates the correlation between control voltage, V_c , PIA capacitive tuning ratio, α , and the frequency of minimum structural response. From Figure 10 it is clear that, for a control voltage of 0V, no transistors are "on" and thus the PIA is shunted with one capacitor, C_1 . As stated earlier, if C_1 is sufficiently small (say approximately $0.01 \times C_p^T$), the PIA will behave as if it were open circuited. For a control voltage of 1V, the first transistor turns "on" and the shunt capacitance is increased from C_1 to the sum of C_1 and C_2 . If C_2 equals $0.1 \times C_p^T$, the net tuning ratio would be approximately 0.11 and the natural frequency of the PIA and therefore the frequency of minimum structural response would be f_n .

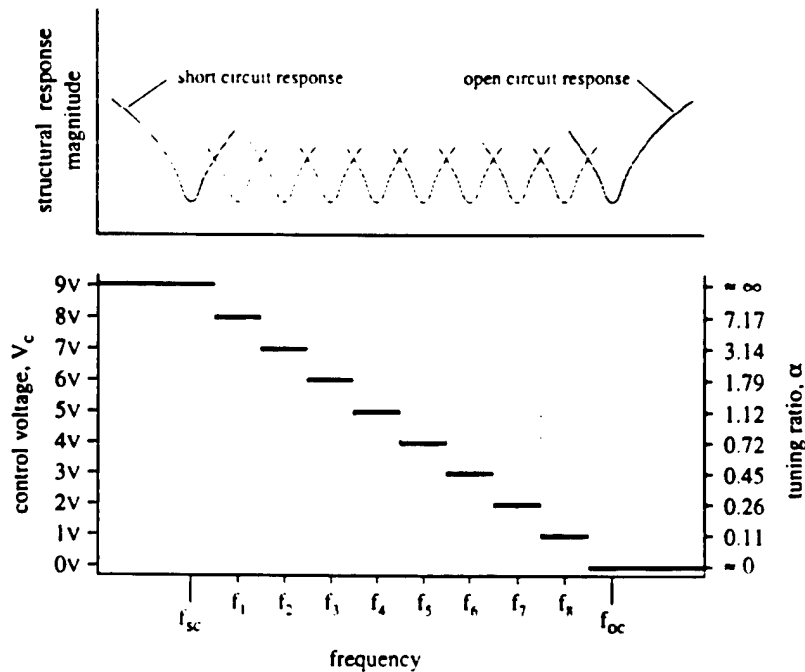


Figure 10. Control voltage to structural response correlation

As shown in Figure 10, varying the control voltage, V_c , from 0 to 9V changes the frequency of minimum structural response from approximately the open circuit natural frequency to approximately the short circuit natural frequency. Referring to the control system block diagram in Figure 6, the *estimate control voltage* block contains the code to convert the estimated disturbance frequency to an appropriate control voltage.

4. TUNING CONTROL EXPERIMENTS

Several experiments were designed to evaluate the effectiveness of the tunable piezoceramic inertial actuator. In the experiments, a representative structure (a clamped-clamped beam) was driven with a tonal force disturbance. First, structural acceleration measurements were taken both with and without the passive PIA attached to the structure. Measurements in which the PIA was both short and open circuited were used to define the effective tuning bandwidth for the shunt control system. Finally, a sine sweep was used to vary the disturbance frequency from just below the PIA short circuit natural frequency to just above the PIA open circuit natural frequency for the short circuit, open circuit, and actively tuned cases.

Figure 11 shows the experimental setup for the semi-actively tuned PIA vibration absorber experiments. The representative structure was a $0.913 \times 0.038 \times 0.006$ m aluminum beam rigidly fixed at both ends. An inertial actuator placed 10 cm from the left end of the beam was used to apply a disturbance force to the structure. The drive signal for the actuator was generated by a Hewlett Packard 3562A signal analyzer and amplified using a PCB/AVC high power charge amplifier. A dynamic force transducer placed between the actuator and the structure measured the force applied to the structure, while a high-sensitivity accelerometer located 30 cm from the right side of the beam measured the dynamic response of the beam at the location of the

PIA. Both the force transducer and the accelerometer signals were amplified via portable power units and then recorded by the HP signal analyzer. The analyzer was also used to process the force and acceleration signals to calculate acceleration FRFs.

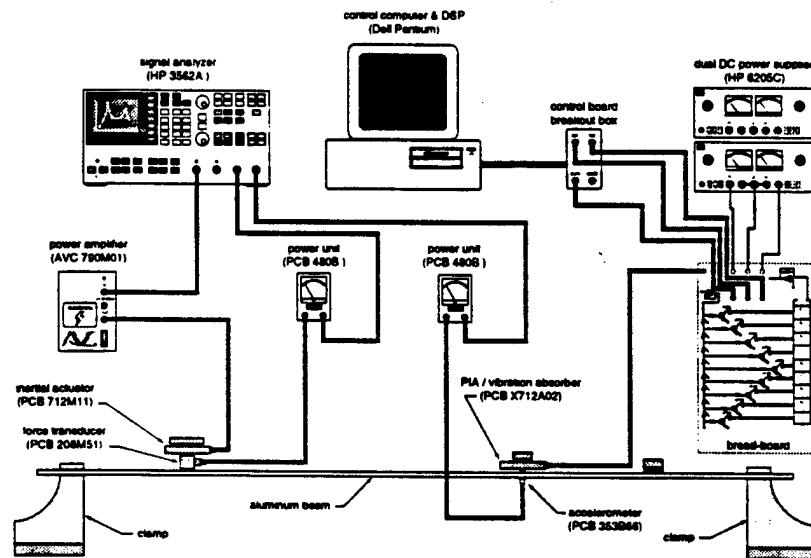


Figure 11. Semi-active tuned PIA vibration absorber experimental setup

Figure 12 shows the response of the system both with and without the PIA absorber attached to the clamped-clamped beam. The response of the system with no absorber attached has a prominent structural resonance at approximately 318 Hz. Clearly, the passive PIA significantly reduced the structural response in the neighborhood of the original structural resonance, and the frequency at which minimum structural response was obtained varied with the value of the electrical shunt.

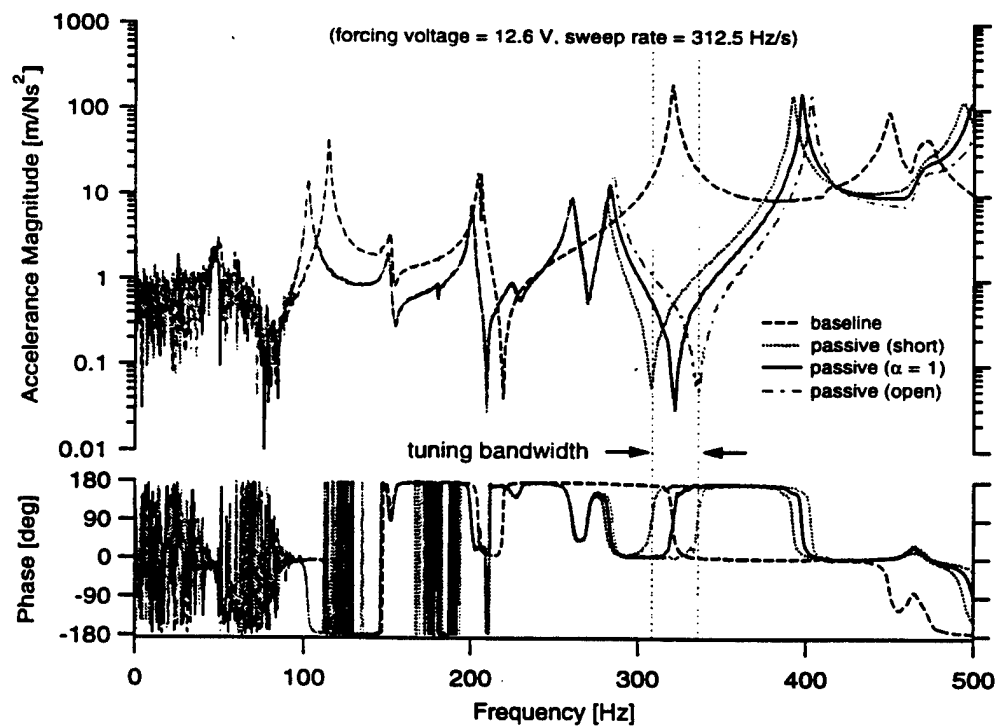


Figure 12. Structural acceleration for structure with PIA absorber

In addition to the open and short circuit measurements (i.e., measurements taken for tuning ratios of 0 and respectively), the acceleration was also measured for a tuning ratio of 1.0. The response for $\alpha = 1$ defined the nominal or "control off" condition. In practice, a nominal disturbance frequency would be identified and the mass of the PIA would be selected such that for $\alpha=1$, minimal structural response would occur at the nominal disturbance frequency.

Next, the actuator was connected to the tuning circuit, which was implemented on an electronic breadboard. The breadboard was also connected to the real-time control computer to supply PIA voltage and PIA current estimates and receive shunt control voltages. The op-amps and relays used for the switching circuit were powered with Hewlett Packard DC power supplies.

The control computer used for the experiments was a 100 MHz Dell Pentium. The Pentium housed a dSPACE DS1102 Floating-Point Controller Board with Texas Instruments TMS320P14 processor chip. The two A/D channels of the controller board had an input voltage range of $\pm 10V$ and used 16-bit converters. The D/A channel had an output voltage range of $\pm 10V$ and used a 12-bit converter. MATLAB's Real-Time Workshop was used to translate a SIMULINK block diagram into C-code, then to invoke the TI C-compiler. The compiled C-code was then downloaded to the processor on the controller board. The controller was designed and set to sample at 10 kHz which adequately accommodated the simulation of the analog linear filters.

To gain a more accurate estimate of the passive and semi-active response of the system, swept sine measurements were made between 300 Hz and 350 Hz. Note that the sweep rate for the measurements was set sufficiently low to ensure that the filters within the controller had time to settle before the analyzer moved to the next frequency in the sweep.

Figure 13 illustrates the effects of using a semi-active piezoceramic vibration absorber on structural acceleration due to a varying-frequency tonal disturbance. The dotted line in Figure 13 is the passive structural acceleration (i.e., structural response with a constant $\alpha = 1$). The solid line is the structural acceleration with the tuning controller turned on (i.e., structural response with a variable α). The changing discrete capacitances are evidently effective in increasing minimum acceleration over the previously defined tuning band. In addition, structural acceleration at frequencies below the short circuit frequency of the PIA and above the open circuit frequency of the PIA was improved.

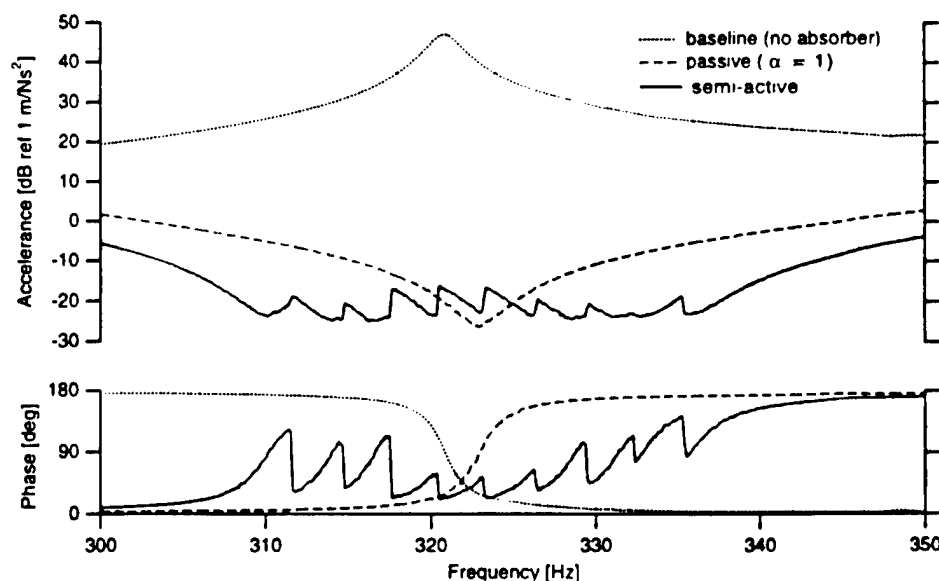


Figure 13. Actively tuned vs passive structural response

Figure 14 shows the difference (in dB) between the passive and active responses. Maximum increases in performance of about 20 dB occurred at both the short and open circuit PIA natural frequencies. On average, an approximately 10 dB increase in

performance was obtained over the frequency range shown ($\pm 7\%$ change in frequency from the center frequency of 325 Hz). A slight decrease in performance, however, was observed in a small frequency range in the center of the tuning band. This was attributed to the fact that the discretized shunt capacitance was not quite equal to the PIA capacitance measured at constant stress (*i.e.*, $\alpha = 1$) at the tuning band center frequency.

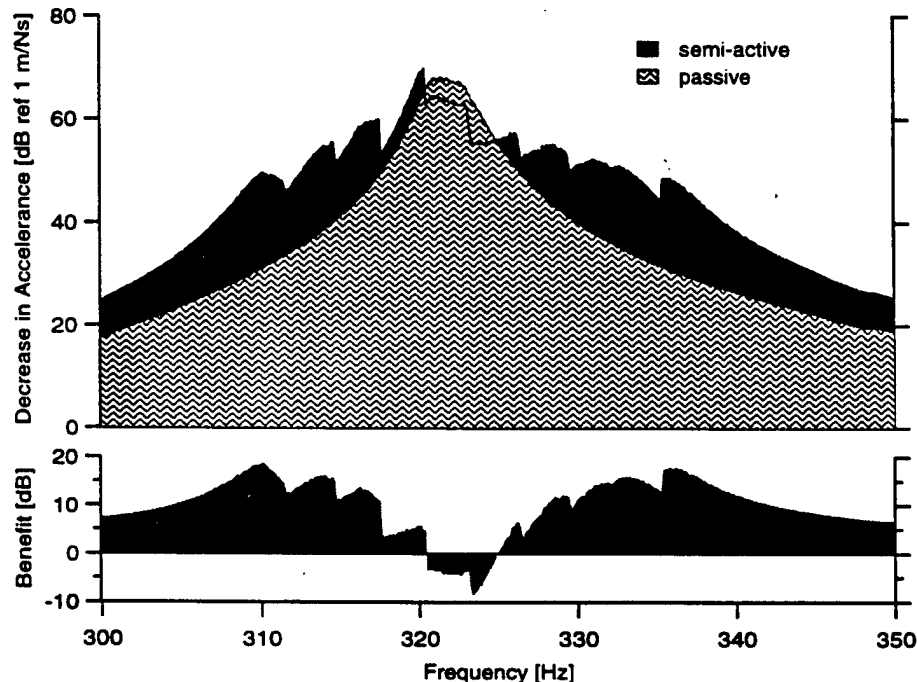


Figure 14. Active vs passive structural attenuation performance

Note that the speed of the control system was limited by the speed of the filters used in the control system. The electronics used to adjust the shunt capacitance operated very quickly compared to the filters. Thus, proper tuning was achieved as soon as the filters settled and the proper disturbance frequency was estimated. The rate of re-tuning due to a change in disturbance frequency was limited by the disturbance frequency estimation method. Small changes in disturbance frequency, less than about 11% of the tuning band, were effectively compensated in less than 60 milliseconds. Detecting, then completely switching the absorber from short to open circuit, or vice versa, required less than 250 milliseconds. A complete discussion of the effects of control speed as well as variations due to changing forcing amplitudes can be found in *A Tunable Piezoceramic Vibration Absorber*, Ph.D. thesis by Davis¹¹.

5. CONCLUSIONS

A solid-state tunable semi-active piezoceramic vibration absorber was developed. Electrically shunting a piezoelectric inertial actuator with a capacitive electrical impedance changed a fraction of the effective net stiffness of the device, thus changing the device's natural frequency. The control system used to tune the PIA monitored the voltage and current produced by the device to estimate a tonal structural vibration frequency and in turn adjust the net discrete shunt capacitance appropriately.

The semi-active PIA absorber had a $\pm 3.7\%$ tunable frequency band relative to the center frequency. Additional attenuation effects extended beyond $\pm 7\%$ of the center frequency. Within the tuning band, increases in performance beyond passive performance were as great as 20 dB. In addition, the average increase in performance across the tunable frequency band was over 10 dB.

This combination of tunable vibration absorber and active tuning method has several features that distinguish it from, and give it potential advantages over, others described in the literature. First, it is a piezoelectric-based device. Second, it uses

capacitive shunting to accomplish an effective change in stiffness. Third, it is less complex than comparable devices, because it is completely solid-state. Fourth, it requires no additional sensors, as the voltage and current signals generated in the piezoelectric elements may be used directly. Fifth, it has relatively low power consumption relative to other PVA tuning methods; the electrical power required for shunt circuit switching is far less than the power required for driving stepper-motors or heating viscoelastic materials. Furthermore, the tuning controller was novel in that it could be implemented as a completely solid-state analog system. Achieving this would require performing the frequency estimation and control voltage calculation in hardware instead of software. Frequency estimation could be accomplished using a Phase-Locked Loop (PLL) circuit^{12,13}. PLLs require little power, react quickly, and are commercially available in compact integrated circuit packages. The output of the PLL is a DC voltage directly proportional to frequency, thus making the control voltage calculation largely a matter of scaling.

ACKNOWLEDGMENTS

This work was supported by the Office of Naval Research under MURI Grant N00014-96-1173 (Acoustic Transduction).

REFERENCES

1. J.F. Unruh, "Structure-Borne Noise Control for Propeller Aircraft," *AIAA Journal of Aircraft*, Vol. 25, No. 8, pp 752-757, August 1988.
2. C.D. Johnson, "Design of Passive Damping Systems," *Journal of Vibration and Acoustics, Special 50th Anniversary Design Issue*, Vol. 117, pp 171-176, June 1995.
3. B.G. Korenev and L.M. Reznikov, *Dynamic Vibration Absorbers*, John Wiley & Sons, England, p 237-242, 1993.
4. E. Waterman, D. Kaptein, and S. Sarin, "Fokker's Activities in Cabin Noise Control for Propeller Aircraft," Proceedings of the SAE Business Aircraft Meeting & Exposition, SAE Paper No. 830736, 1983.
5. W. Halvosen and U. Emborg, "Interior Noise Control of the Saab 340 Aircraft," Proceedings of the SAE General Aviation Aircraft Meeting & Exposition, SAE Paper No. 891080, 1989.
6. M. Lavitt, "IPN International Product News: Active Absorbers Cancel Aircraft Engine Noise," *Aviation Week & Space Technology*, February 24, p. 68, 1997.
7. F. Fiorino, "Airline Outlook: DC-9 Noise Absorbers," *Aviation Week & Space Technology*, April 28, p. 15, 1997.
8. J. Dosch, G. Lesieutre, G. Koopmann, and C. Davis, "Inertial Piezoceramic Actuators for Smart Structures," Proc. of the Smart Structures and Materials 1995 Industrial and Commercial Applications of Smart Structures Technologies Conference, San Diego, CA, SPIE Vol. 2447, pp 14-25, 1995.
9. G. Lesieutre, G. Koopmann, and S. Yoshikawa, "High Power Density Piezoelectric Actuator for Noise and Vibration Reduction: Monthly Letter Status Report," NASA Contract NAS1-20205, AVC Instrumentation / PCB Piezotronics Subcontract 0001, Penn State University, July, 1995.
10. C. Davis, G. Lesieutre, and J. Dosch, "A Tunable Electrically Shunted Piezoceramic Vibration Absorber," *Proc. of the SPIE Smart Structures and Materials Passive Damping and Isolation Conference*, Vol. 3045, Paper 10, 1997.
11. C. Davis, "A Tunable Piezoceramic Vibration Absorber," Ph.D. Thesis, Department of Aerospace Engineering, The Pennsylvania State University, University Park, PA, December 1997.
12. P. Horowitz and W. Hill, *The Art of Electronics, Second Edition*, Cambridge University Press, Cambridge, U.K., p 184, 1994.
13. C. Niezrecki and H. Cudney, "Structural Control Using Analog Phase-Locked Loops," *Journal of Vibration and Acoustics*, Vol. 119, pp 104-109, January 1997.

APPENDIX 48

A tunable electrically shunted piezoceramic vibration absorber

Christopher L. Davis^a, George A. Lesieutre^a, and Jeffrey Dosch^b

^aDepartment of Aerospace Engineering, The Pennsylvania State University, University Park, PA 16802

^bAVC Instrumentation Division; PCB Piezotronics, Inc., Depew, NY 14043

ABSTRACT

A shunting method has been developed and experimentally verified for tuning the natural frequency and damping of a piezoceramic inertial actuator (PIA). Without power, a PIA behaves much like a passive vibration absorber (PVA). PVAs typically minimize vibration at a specific frequency often associated with a lightly damped structural mode. Large response reductions, however, may only be achieved if the PVA is accurately tuned to the frequency of concern. Thus, an important feature of a PVA is the ability to be accurately tuned to the possibly varying frequency of a target vibration mode. Tuning an absorber requires a change in either the mass or stiffness of the device. The electromechanical properties of the piezoceramic forcing element within a PIA in conjunction with an external passive electrical shunt circuit can be used to alter the natural frequency and damping of the device. An analytical model of a PIA was created to predict changes in natural frequency and damping due to passive electrical shunting. Capacitive shunting alters the natural frequency of the actuator only, while resistive shunting alters both the natural frequency and damping of the actuator. Experiments using both passive capacitive and passive resistive shunt circuits verified the ability to predictably shift the natural frequencies of the piezoceramic inertial actuator by more than 5%.

Keywords: vibration absorber, tuning, piezoelectric ceramic, shunting, inertial actuator

1. INTRODUCTION

Vibrations in aerospace structures create many important and difficult engineering problems. In certain aircraft and rotorcraft applications, structural vibrations may increase interior cabin noise levels and/or accelerate material fatigue. Identifying the sources of troublesome vibrations and subsequently developing strategies for reducing these vibrations has been and continues to be the focus of a large body of research.

Interior noise levels in certain propeller driven aircraft, rotorcraft, and the more advanced high-speed turboprop aircraft are, in general, higher than desirable. In these vehicles, noise is generated from both airborne and structure-borne sources. Airborne noise arises from acoustic sources such as the interaction of the propeller wake/vortex with the aircraft fuselage or the impingement of jet exhaust directed at the fuselage.^{1,2} Structure-borne noise is a result of vibrations from the engine or vibrations from the interaction of the propeller wake/vortex with the wing surface being transmitted via the aircraft structure to the main cabin.^{3,4} In addition, the flexible attachment of the rotor blades to the rotor hub and gear meshing in the main rotor gearbox of rotorcraft may also generate extremely high cabin noise levels. Thus with many of the sources of interior noise identified, the problem becomes that of reducing the resulting noise/vibration levels within the aircraft or rotorcraft cabin.

Structural acoustic control is a method for reducing the interior cabin acoustic field by reducing vibrations due to external excitation sources before they propagate to and excite the coupled interior structural acoustic modes of the aircraft fuselage. Direct airborne induced disturbances may be inhibited from propagating to the fuselage by altering the stiffness of the wing and fuselage,⁵ by adding surface damping treatments to the wing and fuselage,^{3,5} by adding blocking masses to the aircraft structure,³ by using passive and active vibration absorbers,^{3,5,6} by using resistively shunted^{7,8} and resonantly shunted^{7,9} piezoceramics, or by using active vibration control. Vibrations that propagate from the engine may be reduced by passive and active isolation, by active control, and by passive⁴ and active vibration absorbers. Of particular interest to this research is the use of passive vibration absorbers for structure-borne noise/vibration control.

Further author information -

C.L.D. (correspondence): Email: cld103@psu.edu; Telephone: 814-865-9072. Ph.D. Candidate.

G.A.L.: Email: gal4@cac.psu.edu; Telephone: 814-863-0103. Associate Professor.

Passive vibration absorbers are conceptually simple devices consisting of a mass attached to a structure via a complex spring. The primary function of these devices is to increase the dynamic stiffness of the airframe and/or engine mounts of an aircraft. PVAs are typically used to minimize vibration at a specific frequency often associated with a lightly damped structural mode. For the device to operate at the correct frequency, the mass and stiffness must be chosen correctly so as to tune the actuator to the frequency of the offending mode or disturbance. The fact that a PVA may only be used at a specific frequency, however, can sometimes be the largest drawback of using these devices.

Passive vibration absorbers have been used in the aviation industry for quite some time. For example, the DC-9 uses a set of four PVAs attached to each engine pylon⁴ to reduce the aft cabin noise associated with the operating spool frequency of the engines. Similarly, both the Fokker F27¹⁰ and the Saab 340¹¹ aircraft use PVAs attached directly to the fuselage frame to lower interior cabin noise levels. In these applications, the absorbers provide adequate vibration attenuation at specific frequencies. Performance can be seriously degraded, however, if the disturbance source changes frequency. If this occurs, the PVA(s) must be physically re-tuned. Re-tuning the absorber(s) may often be either impractical or impossible, hence there is a need for a vibration absorber with properties that are easy to alter.

The purpose of this research was to develop a straightforward method for tuning a vibration absorber. This was accomplished by electrically shunting a piezoceramic inertial actuator. In the passive sense, an inertial actuator behaves much like a PVA. This work exploits the frequency dependent properties of shunted piezoceramic forcing elements within the PIA by using them (*i.e.*, the piezo elements) as variable stiffness complex springs.

2. BACKGROUND

A model was created to gain insight into the effects of shunting a piezoceramic inertial actuator. First, a single degree-of-freedom (DOF) structure and absorber model were created. Next, the absorber model was altered to incorporate the effects of the piezoceramic forcing element of the inertial actuator. Finally, the electro-mechanical dynamics of the passively shunted piezoceramic were added to the model to create the desired frequency dependent effects.

Consider a damped vibration absorber attached to a single DOF system, as shown in Figure 1(a). Let m_s and k_s^* represent the effective mass and complex stiffness of the structure respectively and m_a and k_a^* represent the mass and complex stiffness of the absorber respectively.

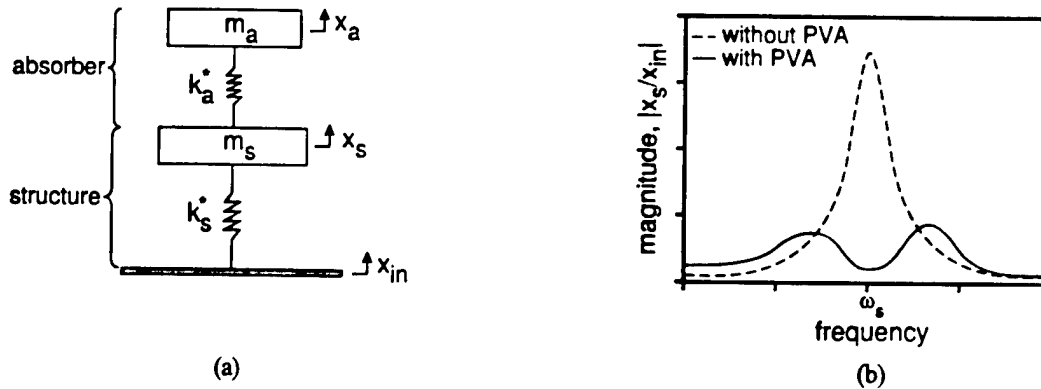


Figure 1. (a) PVA attached to single DOF system, (b) Sample frequency response function for the combined system

Equation (1) represents the ratio of the structural displacement, X_s , to the base disturbance displacement, X_{in} , in the Laplace domain (Note: the stiffness terms k_s and k_a are the real parts of the complex stiffnesses, k_s^* and k_a^* respectively; damping was assumed to be small and was removed to simplify the analysis).

$$\frac{X_s(s)}{X_{in}(s)} = \frac{k_s}{m_s s^2 + k_s} \quad (1)$$

The magnitude of the ratio of the structural displacement to the base disturbance displacement is shown by the dashed line in Figure 1(b). The natural frequency of the structure, ω_s , is directly proportional to the square root of the quantity k_s/m_s . Equation 2 represents the dynamics of combined absorber/structure system in the Laplace domain. If k_a is chosen in such a way that the natural frequency of the absorber is equal to the natural frequency of the structure and the damping is adjusted appropriately, then it is possible to obtain a system response similar to the solid line shown in Figure 1(b). Notice that it is possible to have an increase in response when the absorber is attached to the system and the input disturbance frequency deviates from ω_s .

$$\frac{X_s(s)}{X_{in}(s)} = \frac{m_a k_s s^2 + k_a k_s}{m_a m_s s^4 + (m_a(k_a + k_s) + m_s k_a) s^2 + k_a k_s} \quad (2)$$

Next consider a simple model of a piezoceramic inertial actuator, as shown in Figure 2. Like PVAs, inertial actuators consist of passive mass and complex stiffness elements. The difference between the two devices is the inclusion of a forcing element, F_p , in parallel with the complex spring of the inertial actuator. The most common form of inertial actuator, the voice-coil actuator, utilizes a coil and moving magnet for a forcing element. Recently, however, a new class of inertial actuator has been developed based on dual-unimorph displacement amplification of a piezoceramic forcing element.^{12,13}

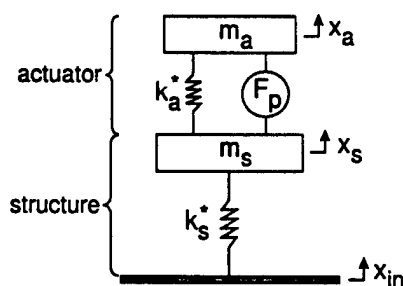


Figure 2. Inertial actuator attached to a single DOF structure model

Piezoceramic materials are capable of producing large forces but relatively small displacements (strains). The practical implementation of piezoceramics for actuation usually requires some form of piezoceramic strain amplification. Unimorph amplification is achieved by attaching one side of a piezoceramic plate or disk to a stiff cap (Figure 3(a)). The in-plane displacement of the piezoceramic causes the cap to displace in the transverse direction. The resulting transverse cap displacement is comparatively larger than the in-plane piezo displacement. Dual-unimorph amplification refers to placing two unimorphs in series in order to double the displacement amplification effect, as shown in Figure 3(b).

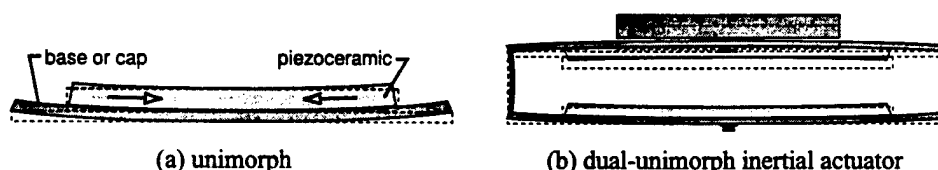


Figure 3. Unimorph actuation and the dual-unimorph inertial actuator

At this point, it is desirable to couple the electro-mechanical dynamics of the piezo elements to the mechanical dynamics of the PIA. To do this, the following forms of the piezoceramic constitutive equations were used:

$$F_p = k_{sc}(X_a - X_s) + d_{31}k_{sc}V \quad (3)$$

$$I = d_{31}k_{sc}s(X_a - X_s) - C_p^T sV \quad (4)$$

where F_p , V , and I are the force, voltage, and current respectively in the piezoceramic material. X_a and X_s are the displacements of masses m_a and m_b respectively, s is the Laplace parameter ($s=i\omega$), k_{sc} is the short circuit stiffness of the piezoceramic, d_{31} is the piezoceramic charge coefficient, and C_p^\top is the capacitance of the piezoceramic measured under constant stress conditions. Equations (3) and (4) were coupled with the equation of motion for the PIA model shown in Figure 2, namely:

$$m_a s^2 X_a = -k_s (X_a - X_s) - F_p \quad (5)$$

The result is an expression for the ratio of the absorber mass displacement, X_a , to the structural displacement, X_s , in the Laplace domain:

$$\frac{X_a(s)}{X_s(s)} = \frac{k_a + k_{sc}^*}{m_a s^2 + k_a + k_{sc}^*} \quad (6)$$

In Equation (7), k_{sc}^* is a frequency dependent (and potentially complex) stiffness of the form:

$$k_{sc}^* = k_{sc} \left[1 + k_p^2 \frac{1}{1 + \alpha(s)} \right] \quad (7)$$

where the piezo coupling coefficient is $k_p^2 = d_{31}^2 k_{sc} / C_p^\top$ and $\alpha(s)$ is the ratio of the electrical impedance of the open circuit piezo capacitance, $Z_{oc}(s)$, to the electrical impedance of the external shunt circuit, $Z_{sh}(s)$. The electrical impedance of the open circuit piezo measured under constant stress mechanical conditions, $Z_{oc}(s)$, can be expressed as:

$$Z_{oc}(s) = \frac{1}{sC_p^\top} \quad (8)$$

The $\alpha(s)$ term in Equation (7) allows the effective piezoceramic stiffness, k_{sc}^* , to be tuned by changing the electrical impedance of the external shunt circuit. In the next section, two types of shunting will be examined analytically: capacitive and resistive. In each case, the goal is to determine the effect of varying the electrical shunt condition on the natural frequency and modal damping of the passive PIA model.

3. ANALYTICAL SHUNTING ANALYSIS

Equation (6) describes the response of a single DOF piezoceramic inertial actuator due to an input structural displacement disturbance as a function of the variable piezo stiffness, k_{sc}^* . By varying the impedance of an external shunt circuit, the natural frequency and, in some cases, the modal damping of the piezoceramic inertial actuator will vary. The objective of the investigation described in this section was to gain insight into the effects of capacitive and resistive shunting on natural the frequency and modal damping of a hypothetical PIA.

First, consider capacitively shunting the piezoceramic element of the PIA. Recall the expression for the ratio of open circuit electrical impedance of the piezoceramic to the electrical shunt impedance ($\alpha(s) = Z_{oc}(s)/Z_{sh}(s)$) in Equation (7). The electrical impedance of the shunt capacitor is:

$$Z_{sh}(s) = \frac{1}{sC_{sh}} \quad (9)$$

Thus, $\alpha(s)$ is equal to:

$$\alpha(s) = \frac{C_{sh}}{C_p^T} \quad (10)$$

Equation (7) is now a purely real stiffness that varies with a change in shunt capacitance. Notice that for a very large shunt capacitance (*i.e.*, approximately a short circuit electrical shunt condition), k_{sc}^* approaches the nominal short circuit stiffness of the piezoceramic, k_{sc} . Conversely, as the shunt capacitance becomes much smaller than the capacitance of the piezoceramic (*i.e.*, approximately an open circuit electrical shunt condition), k_{sc}^* approaches a value of $k_{sc}(1+k_p^2)$. For a planar piezo coupling coefficient of 0.6, the open circuit (*i.e.*, small shunt capacitance) piezo stiffness will be approximately 36% stiffer than the short circuit case.

Figure 4 illustrates the effect of varying the shunt capacitance on the natural frequency of a representative PIA. When C_{sh} is very small compared to C_p^T (*i.e.*, approaching open circuit) the natural frequency of the device is approximately 4.5% larger than the short circuit natural frequency (*i.e.*, when C_{sh} is very large compared to C_p^T). Because the shunt capacitor is a purely reactive element, there are no loss terms and thus no change in damping.

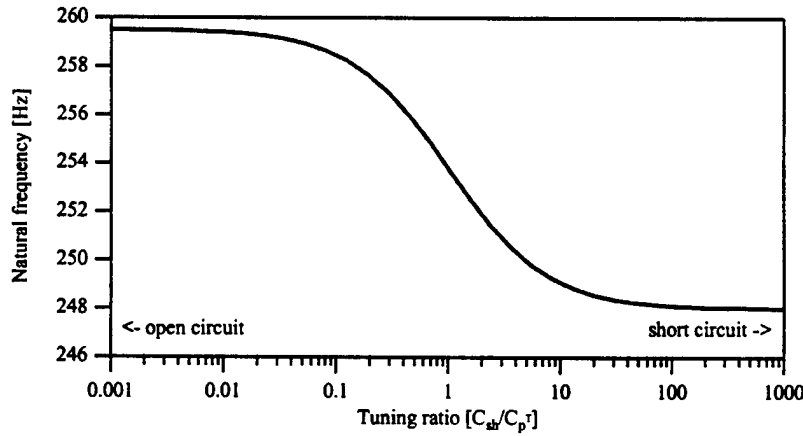


Figure 4. Capacitive shunting effect on the natural frequency of the PIA model

Next, consider resistive shunting of the piezo element of the PIA. In this case, the electrical impedance of the shunt resistor is simply:

$$Z_{sh}(s) = R_{sh} \quad (11)$$

Thus, $\alpha(s)$ is equal to:

$$\alpha(s) = \frac{1}{sR_{sh}C_p^T} \quad (12)$$

Define the natural frequency, ω_{rc} , of the RC-circuit corresponding to the combination of the shunt resistance and the piezo capacitance as:

$$\omega_{rc} = \frac{1}{R_{sh}C_p^T} \quad (13)$$

The effective piezo stiffness, k_{sc}^* may then be expressed in a complex form in terms of the ratio of shunt circuit natural frequency to input frequency (ω_{rc}/ω) as follows:

$$k_{sc}^* = k_{sc} \left[\left\{ 1 + k_p^2 \frac{1}{1 + \left(\frac{\omega_r}{\omega} \right)^2} \right\} - i \left\{ k_p^2 \frac{\left(\frac{\omega_r}{\omega} \right)}{1 + \left(\frac{\omega_r}{\omega} \right)^2} \right\} \right] \quad (14)$$

The real part of k_{sc}^* (i.e., the storage modulus) has the same dependence on the tuning ratio as k_{sc}^* has on the capacitance ratio in the capacitive shunting case. Furthermore, resistive elements also increase energy dissipation. Thus, for the resistive shunting case, additional damping may be introduced.

Figure 5 illustrates the effect of resistive shunting on the natural frequency and modal damping ratio of the PIA model. Notice that a tuning ratio of 1 corresponds to maximum system modal damping. Thus, both the natural frequency and damping of the passive PIA can be tuned using the shunt resistance.

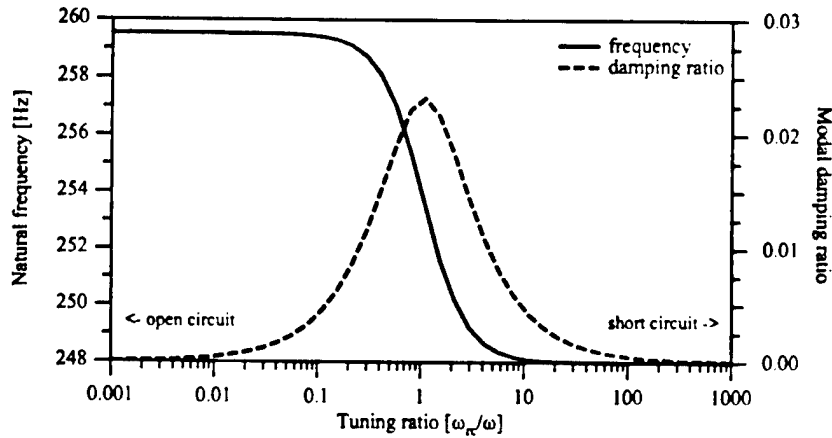


Figure 5. Resistive shunting effects on natural frequency and modal damping ratio of the PIA model

In the next section, experimental results are presented that show the effects of capacitive and resistive shunting on the natural frequency and modal damping ratios of a prototype piezoceramic inertial actuator.

4. EXPERIMENTAL SHUNTING RESULTS

A series of tests were performed to measure the natural frequency and modal damping ratio of a passive PIA. The tests conducted involved measuring the ratio of the acceleration of the actuator's reaction mass to the acceleration of the actuator's base for a variety of passive resistive and passive capacitive shunt circuits.

Figure 6 illustrates the experimental setup. A shaker was used to excite the actuator and two accelerometers were used to measure the actuator base (input) and reaction mass (output) accelerations. The acceleration of the base of the actuator could not be measured directly, but a reference accelerometer was mounted very close to the base of the actuator on a short aluminum bar also attached to the shaker. The flexibility of the aluminum bar limited the frequency range of the experiments because above approximately 2.0 kHz, the reference acceleration began to lag the mounting base acceleration.

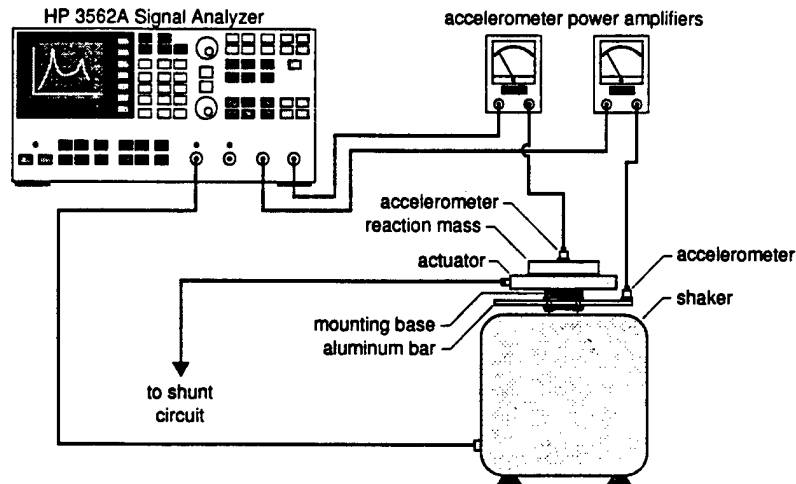


Figure 6. Experimental setup

Frequency response measurements were taken in the frequency range from 0 to 2000 Hz and averaged 30 times. Figure 7 illustrates a typical passive PIA frequency response function (FRF). The actuator was connected to a solderless breadboard where variable resistors or individual capacitors were used as shunt circuit elements. Resonant frequencies and modal damping ratios for the first mode of the actuator were calculated from s -domain curve fit estimates of the experimental FRFs.

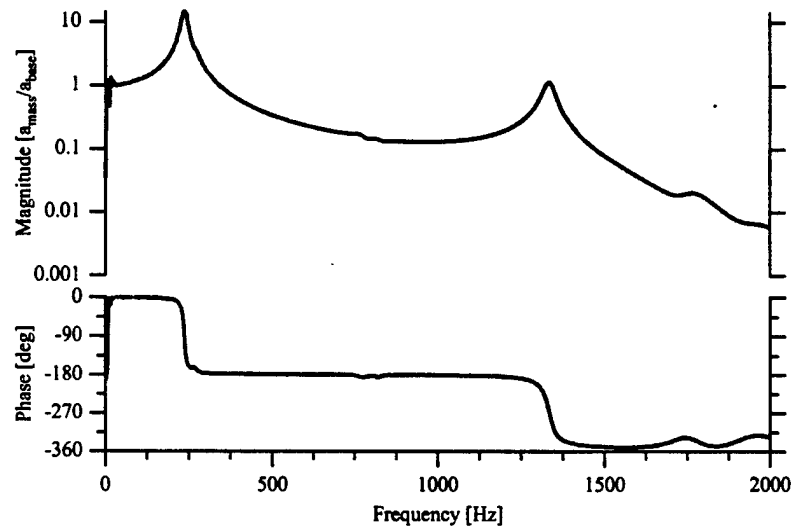


Figure 7. Sample experimental acceleration ratio frequency response function

Figure 8 illustrates the effects of capacitive shunting on both the actuator's fundamental natural frequency and the actuator's fundamental modal damping ratio. Note that the abscissa of the capacitive shunting plots represents the ratio of shunt capacitance to actuator capacitance (the actuator capacitance, C_p^T , was approximately 58 nF). In Figure 8, at very low values of capacitive shunt ratio (*i.e.*, close to open circuit electrical conditions) the fundamental natural frequency is approximately 258 Hz. As the shunt ratio increases, the fundamental natural frequency decreases, and as C_{sh}/C_p^T approaches infinity, the natural frequency asymptotically approaches a value of approximately 244 Hz (over a 5% change in natural frequency from short circuit to open circuit condition). Figure 8 also illustrates the effect of varying the shunt capacitance on the fundamental modal damping ratio. From the data, it appears that as the piezo becomes less stiff, there is a corresponding increase in modal damping ratio. Thus, the fundamental modal damping ratio ranges from roughly 3.2% for the open circuit case (C_{sh}/C_p^T very small) to approximately 4.0% for the short circuit case (C_{sh}/C_p^T very large). One explanation for the

increase in the fundamental mode's modal damping ratio from open circuit to short circuit is that as the piezo becomes less stiff with increasing shunt capacitance, a larger fraction of strain energy is imparted to the lossy material included in the actuator, thus raising the modal damping ratio.

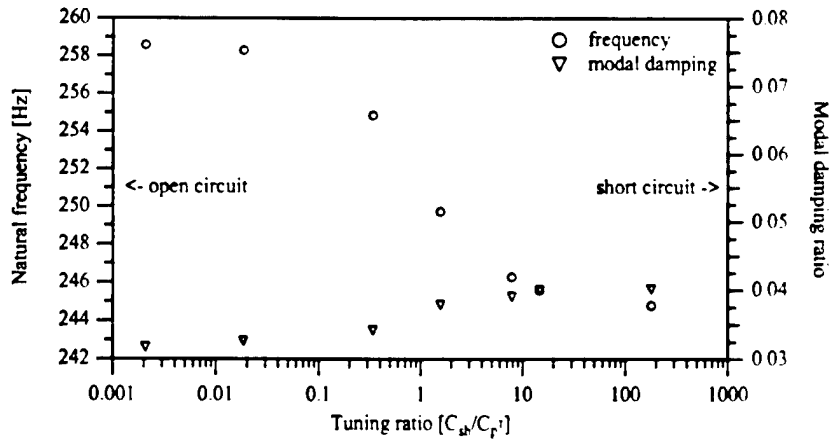


Figure 8. Experimental capacitive shunting results

Figure 9 illustrates the effects of resistive shunting on both the fundamental natural frequency and the modal damping ratio of the PIA. Note that the abscissa of the resistive shunting plots represents the ratio of the shunt circuit electrical natural frequency to the fundamental dynamic short circuit resonance frequency of the actuator. For very small tuning ratios (*i.e.*, approximately open circuit electrical conditions) the natural frequency of the fundamental mode of the actuator is approximately 257 Hz. For very large tuning ratios (*i.e.*, approximately short circuit electrical conditions) the natural frequency of the fundamental mode of the actuator is approximately 243 Hz (over a 5% change in natural frequency from short circuit to open circuit condition). A transition region exists between the open and short circuit limits. The mid-range of this transition occurs for a tuning ratio of approximately 1.0. As in the capacitive shunting case, there is a transition from the open circuit (small tuning ratio) modal damping ratio of approximately 3.2% to the short circuit (large tuning ratio) modal damping ratio of approximately 4.0%. However, for a tuning ratio of slightly greater than one, the modal damping ratio peaks at about 7%.

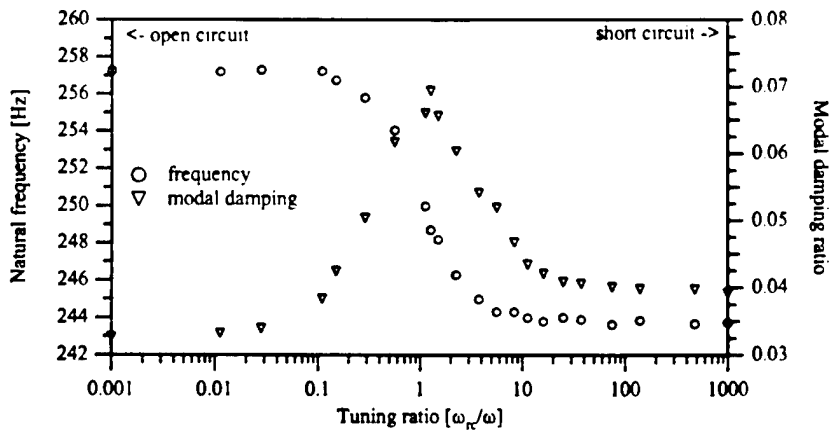


Figure 9. Experimental resistive shunting results

5. CONCLUSIONS

A shunting method for tuning the natural frequency and modal damping ratio of a piezoceramic inertial actuator has been developed. Shunting the actuator with a capacitor alters the stiffness of the piezoceramic forcing element, thus changing the

natural frequency of the device. Very large values of shunt capacitances (compared to the clamped capacitance of the piezoceramic forcing elements) correspond to a short circuit electrical boundary condition, while very small shunt capacitances correspond to an open circuit condition and have the effect of stiffening the piezo elements, in some cases, by more than a factor of 1/3. Large shunt resistances have the same effect on piezo stiffness as small shunt capacitances and, conversely, small shunt resistances have the same effect as large shunt capacitances. In addition, if the shunt resistance is chosen properly, such that the resonance frequency of the RC-circuit matches the mechanical vibration frequency of the PIA, damping may be significantly increased.

With the knowledge of the effects of capacitive and resistive shunting on both natural frequency and modal damping ratio of the passive PIA, it is conceivable to "coarse-tune" the actuator to a troublesome frequency by choosing an appropriate reaction mass and then "fine-tune" the actuator via capacitive or resistive shunting. In doing so, it may be possible to maintain a high degree of narrow-band vibration attenuation by keeping the PIA accurately tuned to the proper frequency. Because this approach is based on the use of passive electrical elements, it could also be readily used for on-line adjustment of an actuator to track a changing problem frequency.

ACKNOWLEDGEMENTS

This work was supported by the NASA Langley Research Center under a Phase II SBIR program (NAS1-20205).

REFERENCES

1. L. Pope, C. Willis, and W. Mayes, "Propeller aircraft interior noise model, part II: scale-model and flight-test comparisons," *Journal of Sound and Vibration* **118**(3), pp. 469-493, 1987.
2. H. Kuntz and R. Prydz, "Interior noise in the untreated Gulfstream II propfan test assessment aircraft," *AIAA Journal of Aircraft* **27**(7), pp. 647-652, 1990.
3. J. Unruh, "Structure-borne noise control for propeller aircraft," *AIAA Journal of Aircraft* **25**(8), pp. 752-757, 1988.
4. A. von Flotow and M. Mercadal, "The measurement of noise and vibration transmitted into aircraft," *Sound and Vibration*, pp. 16-19, November 1995.
5. M. Simpson, "Cabin noise control ground tests for ultra high bypass aircraft," *AIAA Journal of Aircraft* **27**(10), pp. 893-900, 1990.
6. J. Unruh, "Simulation of control of propeller induced structure-borne noise," *Noise Control Engineering Journal* **36**(2), pp. 91-96, 1991.
7. N. Hagood and A. von Flotow, "Damping of structural vibrations with piezoelectric materials and passive electrical networks," *Journal of Sound and Vibration* **146**(2), pp. 243-268, 1991.
8. C. Davis and G. Lesieutre, "A modal strain energy approach to the prediction of resistively shunted piezoceramic damping," *Journal of Sound and Vibration* **184**(1), pp. 129-139, 1995.
9. J. Lai and K. Wang, "Parametric control of structural vibrations via adaptable stiffness dynamic absorbers," *Journal of Vibration and Acoustics* **118**, pp. 41-47, 1996.
10. E. Waterman, D. Kaptein, and S. Sarin, "Fokker's activities in cabin noise control for propeller aircraft," *Proc. of the SAE Business Aircraft Meeting & Exposition*, SAE Paper No. 830736, 1983.
11. W. Halvosen and U. Emborg, "Interior noise control of the Saab 340 aircraft," *Proc. of the SAE General Aviation Aircraft Meeting & Exposition*, SAE Paper No. 891080, 1989.
12. G. Lesieutre, R. Rusovici, G. Koopmann, and J. Dosch, "Modeling and characterization of a piezoceramic inertial actuator," *Proc. of the 36th AIAA/ASME/ASCE/AHS Structures, Structural Dynamics & Materials Conference* **5**, pp. 3440-3449, 1995.
13. J. Dosch, G. Lesieutre, G. Koopmann, and C. Davis, "Inertial Piezoceramic Actuators for Smart Structures," *Proc. of the Smart Structures and Materials 1995 Industrial and Commercial Applications of Smart Structures Technologies Conference* **2447**, pp. 14-25, 1995.

APPENDIX 49

A finite element for beams having segmented active constrained layers with frequency-dependent viscoelastic material properties

George A. Lesieutre*, Usik Lee

The Pennsylvania State University, University Park, PA 16802

Inha University, Incheon 402-751, South Korea

ABSTRACT

A finite element for planar beams with active constrained layer damping treatments is presented. Features of this non-shear locking element include a time-domain viscoelastic material model, and the ability to readily accommodate segmented (*i.e.* non-continuous) constraining layers. These features are potentially important in active control applications: the frequency-dependent stiffness and damping of the viscoelastic material directly affects system modal frequencies and damping; the high local damping of the viscoelastic layer can result in complex vibration modes and differences in the relative phase of vibration between points; and segmentation, an effective means of increasing passive damping in long-wavelength vibration modes, affords multiple control inputs and improved performance in an active constrained layer application. The anelastic displacement fields (ADF) method is used to implement the viscoelastic material model, enabling the straightforward development of time-domain finite elements. The performance of the finite element is verified through several sample modal analyses, including proportional-derivative control based on discrete strain sensing. Because of phasing associated with mode shapes, control using a single continuous ACL can be destabilizing. A segmented ACL is more robust than the continuous treatment, in that the damping of modes at least up to the number of independent patches is increased by control action.

1. INTRODUCTION AND BACKGROUND

ACTIVE CONSTRAINED LAYER DAMPING TREATMENTS

A number of researchers have explored the potential effectiveness and optimization of active constrained layer (ACL) damping treatments. An ACL treatment parallels that of a conventional passive constrained layer treatment, consisting of a layer of high damping viscoelastic material (VEM) sandwiched between a base structure and a constraining layer. In the passive case, the constraining layer serves to develop high shear strain energy in the lossy viscoelastic layer. In the active case, the dimensions of the constraining layer can be actively modified to further enhance the shear in the viscoelastic layer.

Research efforts on active constrained layer damping treatments can be distinguished on the basis of several features, including the following:

- 1) the specific ACL configuration and materials considered;
- 2) assumptions underlying the governing equations (*e.g.*, shear, rotatory inertia);
- 3) method used to model viscoelastic material (damping) behavior;
- 4) control approach;
- 5) response solution method (*i.e.*, analytical, Galerkin, finite elements); and
- 6) optimization of ACL placement, number, and sizing.

Plump and Hubbard (1986) developed a 6th order governing PDE for an active constrained layer damper (PVDF constraining layer), using a complex modulus approach for the viscoelastic material. No analysis or experimental results were presented.

Baz and Poh (1988) investigated the effects of the bonding layer on active control effectiveness, without considering the damping properties of the bonding layer. In subsequent work, Baz (1993) and Baz and Ro (1994a) proposed an ACL with an additional piezoelectric sensor layer between the base structure and the VEM. A complex modulus approach was evidently used to model VEM behavior in this work. Using proportional control, the performance of the ACL was compared to that of a passive constrained layer (PCL) treatment. In later work, Baz and Ro (1994b) investigated, both theoretically and experimentally, combined proportional and derivative (PD) control along with a spatially-varying piezoelectric sensor, and

* G.A.L.: Email: g-lesieutre@psu.edu; Telephone: 814-863-0103. Associate Professor of Aerospace Engineering.
U.L.: Email: ulee@dragon.inha.ac.kr; Telephone: 32 860-7318. Associate Professor of Mechanical Engineering.

demonstrated good broadband vibration attenuation capability. Baz and Ro (1995a) also developed a beam finite element model, and selected PD control gains (full state feedback) based on a linear quadratic regulator (LQR) performance index. The thickness and shear modulus of the viscoelastic layer were optimized to maximize damping with minimum mass addition. A plate finite element model was developed by Baz and Ro (1995b) and theoretical and experimental results (natural frequencies and damping) were compared for PD-control and a single partial-coverage ACL treatment.

Leibowitz and Vinson (1993) presented a concept for an ACL configuration and developed the governing equations using an energy method. The viscoelastic material was modeled using a complex modulus approach. They proceeded to investigate the performance of an ACL on a beam using partial coverage, and reported the results of parametric studies, concluding that an ACL could outperform a purely passive constrained layer treatment.

Agnes and Napolitano (1993) suggested that an ACL could combine the advantages of both passive and active vibration control approaches. VanNostrand, Knowles, and Inman (1994) developed a beam finite element model, using the ATF time-domain modeling method (Lesieutre and Mingori, 1990; Lesieutre 1992) to capture the frequency-dependent behavior of the viscoelastic material. In subsequent research, VanNostrand, Knowles, and Inman (1993) experimentally investigated the effects of VEM stiffness on ACL effectiveness, as well as the implications of sensor type on control structure. Lam, Saunders, and Inman (1995) investigated the use of the GHM method (Golla and Hughes, 1985; McTavish and Hughes, 1993) to model VEM behavior.

In a series of papers, Shen (1994, 1995a, 1995b, 1996) investigated several aspects of ACL treatments, with emphasis on performance, controllability, and stability. In contrast to Baz, Shen considered the use of a point strain sensor rather than a sensing layer. Composite beam and plate models were developed, using a complex modulus approach to model VEM behavior. Numerical response results were obtained using a Galerkin discretization approach. From experiments, Shen reported that a single ACL treatment was ineffective in controlling bending and torsional vibration simultaneously, and that cracks in the PZT piezoelectric constraining layer resulted in noisy signals.

Azvine, Tomlinson, and Wynne (1995) considered an ACL concept in which the piezoelectric actuator is bonded to (not replacing) the constraining layer. They used a complex modulus approach to model the VEM, and investigated the effect of ACL location on modal damping of a cantilevered beam using a control signal proportional to the tip velocity. Veley and Rao (1995) developed a finite element model by combining a piezoelectric element and a constrained layer damping element, retaining both mechanical and electrical DOFs. They investigated optimal ACL placement using a PD control approach.

Nath and Wereley (1995) investigated the application of an ACL to rotorcraft flex beams, the goal being to enhance lag mode damping. They developed a differential equation model for a completely-treated beam, with special attention to the boundary conditions. Frequency response methods were used to study the steady-state performance of the ACL system, based on a frequency-dependent complex shear modulus model of the viscoelastic material.

Liao and Wang (1995, 1996a) considered the ACL approach in the context of active-passive hybrid structures, with the goal of preserving the advantages of fully passive (stable, fail-safe, no power) and fully active (high performance) systems. They developed a mathematical model of a beam with a partial-coverage ACL treatment, using the GHM method to model VEM behavior, Galerkin's method to discretize the governing equations, and an LQR optimal control law to obtain control gains for a specified performance index. They investigated the effects of the VEM on control authority and identified situations in which an ACL may perform better than purely passive or active systems. In recent research, Liao and Wang (1996b) suggested a way to increase active control transmissibility by using stiff "edge elements" on the perimeter of the ACL to provide a parallel load path to the base structure. Although this approach is likely to degrade passive performance, it may also increase reliability by preventing delamination.

In summary, numerous researchers are investigating the utility of active constrained layer damping treatments. Several of these researchers have used finite elements in their work, most commonly employing a complex modulus approach as a model of the behavior of the viscoelastic layer. Three research efforts report the use of time-domain methods (ATF, GHM) to model the characteristic frequency-dependent behavior of the viscoelastic damping layer; two of these used beam finite element discretizations, while the other used a Galerkin approach.

Researchers have generally addressed the use of a single active constraining layer in a particular application. Segmentation of the constraining layer is a well-known, effective means of increasing passive damping in long-wavelength vibration modes (by increasing the number of high-shear regions), but its use has not yet been explored in an ACL configuration. In addition to the potential passive benefits, segmentation provides the possibility of additional independent control inputs, a feature which is likely to improve achievable performance.

The objective of the present research was to develop an ACL beam finite element that would be useful for investigating active constrained layer treatments. To facilitate controls synthesis, this model was required to be formulated in the time-domain, preferably in state-space form, with the possibility of segmentation a desirable feature.

VISCOELASTIC DAMPING MATERIALS AND MODELS

The mechanical properties of the "damping materials" used in passive constrained layer damping treatments are often sensitive to frequency, temperature, type of deformation, and sometimes amplitude (Nashif, Jones, and Henderson, 1985). To ensure design adequacy, performance is usually analytically evaluated at a few temperatures that span the expected operating range of interest. Material properties appropriate to each temperature of interest are used in such analyses. For operation at a nearly-constant temperature, it is most important to consider the dependence of stiffness and damping properties on frequency; over a broad frequency range, damping can vary by an order of magnitude, and stiffness by several orders of magnitude.

While damping models currently available in commercial finite element software (e.g., viscous damping, proportional damping, hysteretic or structural damping, and viscous modal damping (via the modal strain energy (MSE) method (Johnson, Keinholtz, and Rogers, 1981)) do provide energy dissipation, in general they are not physically motivated and suffer from various limitations. In particular, none of these captures, in a time-domain model, the frequency-dependent behavior characteristic of real materials. Furthermore, such issues of model fidelity are especially important in control applications.

Dissatisfaction with available damping modeling techniques has motivated considerable research on the subject of time-domain methods that capture the essential frequency dependence of viscoelastic material properties and that are compatible with current structural finite element analysis techniques. This research can be broadly classified into: 1) those that use fractional time derivatives to model material relaxation behavior; and 2) those that use integer time derivatives. Both kinds of approaches have advantages and disadvantages, and none is clearly superior to others in all cases.

In a series of papers, Bagley and Torvik and their collaborators (Bagley and Torvik, 1983, 1985; Bagley and Calico, 1991) developed a fractional derivative model of viscoelastic material behavior and applied it to a number of structural problems. An important feature of their approach is the ability to capture the relatively weak frequency dependence exhibited by many materials using just a few, typically four, model parameters. This feature makes the fractional derivative model especially useful in frequency-domain analyses. Frequency-domain finite elements were initially developed to obtain structural responses for load histories which have Laplace transforms, while a time-domain version with fractional state equations was developed later. In the time domain, the presence of fractional operators makes the solution of structural equations more complicated than it is for those involving ordinary differential operators. Enelund and Olsson (1995) proposed using a different form of the time-domain equations of motion, as well as a different method for time discretization. This solution approach requires that a truncated time history be retained for use, in effect adding coordinates to the model.

Structural equations with time domain damping models involving ordinary integer differential operators are easier to solve than those involving fractional derivative operators. Several of these kinds of models have been proposed in the literature, including the ATF/ADF model (Lesieutre and Mingori, 1990; Lesieutre, 1992; Lesieutre and Bianchini, 1995) the GHM model (Golla and Hughes, 1985; McTavish and Hughes, 1993), and Yiu's model (Yiu, 1993; Yiu, 1994).

The augmenting thermodynamic fields (ATF) method is a time-domain continuum model of material damping that preserves the characteristic frequency-dependent damping and modulus of real materials—a physically-motivated model compatible with current finite element structural analysis methods. In its initial development, the ATF method introduced a single augmenting field to model the behavior of materials and structures with light damping. In subsequent work, the ability to model high-damping materials having relatively weak frequency-dependence was developed, using multiple ATFs. However, this early work was effectively limited to structural members under uniaxial stress states, such as bars and beams. Subsequently, "anelastic displacement fields" (ADF), special kinds of ATF, were introduced. Instead of addressing physical damping mechanisms directly, their effects on the displacement field were considered. The ADF method has several advantages over the initial ATF method; in particular, it has been generalized to 3-D problems, to problems involving temperature dependence (Lesieutre and Govindswamy, 1995), and to problems involving non-linear strain dependence.

The GHM model and Yiu's model are similar in several ways to the ADF model. All yield time-domain viscoelastic finite elements, and use additional coordinates to more accurately model material behavior. The ADF method differs in that it involves a direct time-domain formulation—not transform-based, and yields finite elements using conventional methods. The "dissipation coordinates" of the GHM method are internal to individual elements, while the "anelastic displacement fields" of ADF are continuous from element to element, reflecting its basis as a field theory. The "internal unobservable degrees of freedom" of Yiu's model are introduced as nodal variables using an analogy with a generalized lumped-parameter Maxwell model. Because it was developed explicitly with second-order dynamics, the GHM method is quite compatible with current structural analysis methods, and has proven to be useful in practice. Both the ADF and Yiu's models may, however, also be readily expressed in second-order form. Although the second-order form of a GHM ("mini-oscillator") model can permit unrealistic material behavior, difficulty can be avoided by proper selection of material model parameters. Yiu's model also assumes a single loss factor for all material moduli (e.g., shear and bulk for an isotropic material).

In many respects, however, finite element models yielded by the GHM method and especially Yiu's method are quite similar to those developed using ADF. In what follows, the ADF method is used as a representative time domain viscoelastic model.

2. FINITE ELEMENT DEVELOPMENT

ACTIVE CONSTRAINED LAYER CONFIGURATION AND KINEMATIC ASSUMPTIONS

ACL Configuration and Field Variables. Figure 1 illustrates the ACL beam configuration under consideration. There are three components: the base beam, the viscoelastic layer, and the piezoelectric (ceramic) constraining layer; quantities associated with each of these layers are denoted with subscripts "b," "v," and "p," respectively. Points in the cross-section are denoted using the independent coordinates "x" and "z," with the origin of the primary coordinate system located at the center of the left end of the base beam, and secondary coordinate systems located at the bottom of each of the layers.

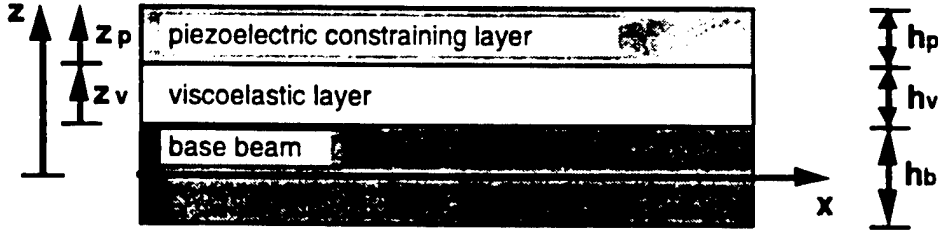


Figure 1: Active Constrained Layer Configuration

As shown in Figure 2, the motion of points in the system is described using the following dependent fields: the lateral deflection "w," the longitudinal displacement "u," the shear angle in the viscoelastic layer " β ," and, when the time-domain viscoelastic model is included, the anelastic part of the shear angle in the viscoelastic layer " β^A ".

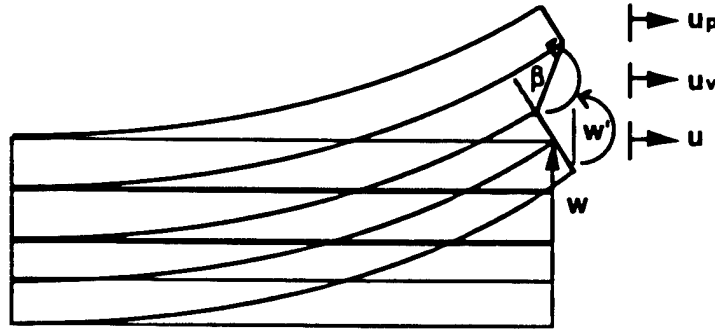


Figure 2: Displacements and Sign Conventions

Assumptions. The model is based on the following assumptions:

- 1) The base beam is elastic, and the Bernoulli-Euler bending assumptions are valid (transverse shear strain is negligible). The lateral displacement of the middle of the base beam, $w(x,t)$, is shared by all points in the cross section (transverse normal deformation is negligible, and rotations are small). The longitudinal displacement of the middle of the base beam is not required to be zero (bending extension coupling is included). Transverse and rotatory inertia are included.
- 2) The viscoelastic layer is lossy, and the Bernoulli-Euler assumptions are augmented with an additional shear angle associated with non-negligible transverse shear. An anelastic shear angle may be included to model frequency-dependent viscoelastic behavior. Longitudinal normal strain in the viscoelastic layer is included. Transverse and rotatory inertia are included.
- 3) The piezoelectric constraining layer is poled through the thickness, is elastic, and the Bernoulli-Euler bending assumptions are valid. The rotations of constraining layer cross-sections are the same as the rotations of the base beam at the same x-coordinate. The layer has both extensional and bending stiffness. Transverse and rotatory inertia are included.

Kinematics. Figure 3 illustrates the nodal degrees of freedom (DOF) of the finite element to be developed. The element has length "L." The lateral deflection, $w(x,t)$ is interpolated using a cubic polynomial in x, allowing element-to-element continuity of deflection (w) and slope (w' , or longitudinal displacement u).

$$w = w(x, z, t) = w(x, t) = [N_w] \{\bar{w}\} \quad (1)$$

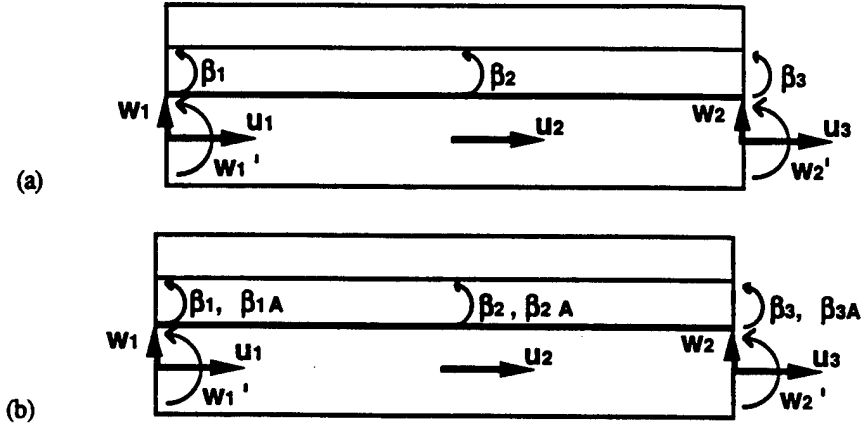


Figure 3: Nodal Degrees of Freedom of (a) Elastic and (b) Damped ACL Finite Element

where $[N_w] = [N_w(x)] = \begin{bmatrix} \left(1 - 3\left(\frac{x}{L}\right)^2 + 2\left(\frac{x}{L}\right)^3\right) & \left(\left(\frac{x}{L}\right) - 2\left(\frac{x}{L}\right)^2 + \left(\frac{x}{L}\right)^3\right) & \left(3\left(\frac{x}{L}\right)^2 - 2\left(\frac{x}{L}\right)^3\right) & \left(-\left(\frac{x}{L}\right)^2 + \left(\frac{x}{L}\right)^3\right) \end{bmatrix}$

and $\{\bar{w}\} = \{\bar{w}(t)\} = \begin{Bmatrix} w_1(t) \\ w_1'(t) \\ w_2(t) \\ w_2'(t) \end{Bmatrix}$

The longitudinal displacement at the reference axis, $u_0(x, t)$ is interpolated with a quadratic polynomial, and an internal node.

$$u_0(x, t) = [N_u] \{\bar{u}\} \quad (2)$$

where $[N_u] = [N_u(x)] = \begin{bmatrix} \left(1 - 3\left(\frac{x}{L}\right) + 2\left(\frac{x}{L}\right)^2\right) & \left(4\left(\frac{x}{L}\right) - 4\left(\frac{x}{L}\right)^2\right) & \left(-\left(\frac{x}{L}\right) + 2\left(\frac{x}{L}\right)^2\right) \end{bmatrix}$

and $\{\bar{u}\} = \{\bar{u}(t)\} = \begin{Bmatrix} u_1(t) \\ u_2(t) \\ u_3(t) \end{Bmatrix}$

Because slope (w') and longitudinal displacement (u) are interpolated consistently, the element will not shear lock. The shear angle(s) in the viscoelastic (β , β^A) is/are interpolated consistent with u and w' .

$$\beta(x, t) = [N_u] \{\bar{\beta}\} \quad (3)$$

where $\{\bar{\beta}\} = \{\bar{\beta}(t)\} = \begin{Bmatrix} \beta_1(t) \\ \beta_2(t) \\ \beta_3(t) \end{Bmatrix}$

Now, the model displacements may be explicitly stated in terms of these nodal quantities and interpolation functions.

Base Beam. The lateral deflection of a point in the base beam, or anywhere on the cross-section, is given by:

$$w = w(x, z, t) = w(x, t) = [N_w] \{\bar{w}\} \quad (4)$$

The longitudinal displacement of a point in the base beam is given by:

$$u_b = u_b(x, z, t) = u_0(x, t) - z w'(x, t) = [N_u] \{\bar{u}\} - z [N_w'] \{\bar{w}\} \quad (5)$$

Viscoelastic Layer. The longitudinal displacement of a point in the viscoelastic layer is given by the following (note that β is positive in the same direction as w).

$$u_v = u_v(x, z, t) = u_0(x, t) - z w'(x, t) - z_v \beta(x, t) = [N_u] \{\bar{u}\} - \left(\frac{h_b}{2} + z_v\right) [N'_w] \{\bar{w}\} - z_v [N_u] \{\bar{\beta}\} \quad (6)$$

Piezoelectric Constraining Layer. The longitudinal displacement of a point in the constraining layer is given as follows. Note that constraining layer may be segmented by not enforcing element-to-element continuity of β .

$$u_p = u_p(x, z, t) = u_0(x, t) - z w'(x, t) - h_v \beta(x, t) = [N_u] \{\bar{u}\} - \left(\frac{h_b}{2} + h_v + z_p\right) [N'_w] \{\bar{w}\} - h_v [N_u] \{\bar{\beta}\} \quad (7)$$

Strains. Now that the displacements of any point in the ACL system have been defined, the longitudinal normal and transverse shear strains may be determined. These are needed in strain energy expressions to develop the element stiffness matrix. Longitudinal normal strain is found from:

$$\epsilon_{xx} = \frac{\partial u}{\partial x} \quad (8)$$

And transverse shear strain is found from:

$$\epsilon_{xz} = \left(\frac{\partial u}{\partial z} + \frac{\partial w}{\partial x} \right) \quad (9)$$

Base Beam. The longitudinal normal strain at a point in the base beam is given by the following. The transverse shear strain in the base beam is negligible, by assumption.

$$(\epsilon_{xx})_b = (\epsilon_{xx}(x, z, t))_b = \begin{bmatrix} [N'_u] & -z [N''_w] & [0] \end{bmatrix} \begin{Bmatrix} \{\bar{u}\} \\ \{\bar{w}\} \\ \{\bar{\beta}\} \end{Bmatrix} \quad (10)$$

Viscoelastic Layer. The longitudinal normal strain at a point in the viscoelastic layer is given by:

$$(\epsilon_{xx})_v = (\epsilon_{xx}(x, z, t))_v = \begin{bmatrix} [N'_u] & -\left(\frac{h_b}{2} + z_v\right) [N''_w] & -z_v [N'_u] \end{bmatrix} \begin{Bmatrix} \{\bar{u}\} \\ \{\bar{w}\} \\ \{\bar{\beta}\} \end{Bmatrix} \quad (11)$$

The transverse shear strain in the viscoelastic layer is related to the shear angle:

$$(\epsilon_{xz})_v = (\epsilon_{xz}(x, z, t))_v = \begin{bmatrix} [0] & [0] & -[N_u] \end{bmatrix} \begin{Bmatrix} \{\bar{u}\} \\ \{\bar{w}\} \\ \{\bar{\beta}\} \end{Bmatrix} \quad (12)$$

Piezoelectric Constraining Layer. The longitudinal normal strain at a point in the piezoelectric constraining layer is given by the following. The transverse shear strain is negligible, by assumption.

$$(\epsilon_{xx})_p = (\epsilon_{xx}(x, z, t))_p = \begin{bmatrix} [N'_u] & -\left(\frac{h_b}{2} + h_v + z_p\right) [N''_w] & -h_v [N'_u] \end{bmatrix} \begin{Bmatrix} \{\bar{u}\} \\ \{\bar{w}\} \\ \{\bar{\beta}\} \end{Bmatrix} \quad (13)$$

STIFFNESS, MASS, AND DAMPING MATRICES; LOAD VECTOR

The stiffness and mass matrices are to be developed using energy methods, so expressions for strain and kinetic energy are required. The load vector associated with piezoelectric forcing is to be developed by considering virtual work. The damping matrix is to be developed using the ADF method. Note that the energy expressions developed could also be used to derive governing PDEs and boundary conditions using Hamilton's Principle.

Strain Energy, Stiffness Matrix. The strain energy stored in a deformed ACL beam of width "b" and length "L" is given by:

$$\begin{aligned} U = U(t) &= \frac{1}{2} b \int_0^L \int_z \left(E(x, z) (\epsilon_{xx}(x, z, t))^2 + G(x, z) (\epsilon_{xz}(x, z, t))^2 \right) dz dx \\ &= U_E + U_G \\ &= (U_{Eb} + U_{Ev} + U_{Ep}) + U_{Gv} \end{aligned} \quad (14)$$

noting that the energy can be divided into parts associated with longitudinal normal deformation (extension and bending) and shear deformation and, further, into parts associated with each component of the ACL system. The strain energy associated with longitudinal normal deformation of the base beam is given by:

$$U_{Eb} = \frac{1}{2} \begin{Bmatrix} \{\bar{u}\} \\ \{\bar{w}\} \\ \{\bar{\beta}\} \end{Bmatrix}^T b E_b \int_0^L \int_{-h_b/2}^{+h_b/2} \begin{bmatrix} [N'_u]^T [N'_u] & -z [N'_u]^T [N''_w] & [0] \\ -z [N''_w]^T [N'_u] & z^2 [N''_w]^T [N''_w] & [0] \\ [0] & [0] & [0] \end{bmatrix} dz dx \begin{Bmatrix} \{\bar{u}\} \\ \{\bar{w}\} \\ \{\bar{\beta}\} \end{Bmatrix} \quad (15)$$

The strain energy associated with longitudinal normal deformation of the viscoelastic layer is given by the following. Note that this part of the strain energy is often neglected.

$$U_{Ev} = \frac{1}{2} \begin{Bmatrix} \{\bar{u}\} \\ \{\bar{w}\} \\ \{\bar{\beta}\} \end{Bmatrix}^T b E_v \int_0^L \int_0^{h_v} \begin{bmatrix} [N'_u]^T [N'_u] & -\left(\frac{h_b}{2} + z_v\right) [N'_u]^T [N''_w] & -z_v [N'_u]^T [N'_u] \\ -\left(\frac{h_b}{2} + z_v\right) [N''_w]^T [N'_u] & \left(\frac{h_b}{2} + z_v\right)^2 [N''_w]^T [N''_w] & \left(\frac{h_b}{2} + z_v\right) z_v [N''_w]^T [N'_u] \\ -z_v [N'_u]^T [N'_u] & \left(\frac{h_b}{2} + z_v\right) z_v [N'_u]^T [N''_w] & z_v^2 [N'_u]^T [N'_u] \end{bmatrix} dz_v dx \begin{Bmatrix} \{\bar{u}\} \\ \{\bar{w}\} \\ \{\bar{\beta}\} \end{Bmatrix} \quad (16)$$

The strain energy associated with longitudinal normal deformation of the piezoelectric constraining layer is given by:

$$U_{Ep} = \frac{1}{2} \begin{Bmatrix} \{\bar{u}\} \\ \{\bar{w}\} \\ \{\bar{\beta}\} \end{Bmatrix}^T b E_p \int_0^L \int_0^{h_p} \begin{bmatrix} [N'_u]^T [N'_u] & -\left(\frac{h_b}{2} + h_v + z_p\right) [N'_u]^T [N''_w] & -h_v [N'_u]^T [N'_u] \\ -\left(\frac{h_b}{2} + h_v + z_p\right) [N''_w]^T [N'_u] & \left(\frac{h_b}{2} + h_v + z_p\right)^2 [N''_w]^T [N''_w] & \left(\frac{h_b}{2} + h_v + z_p\right) h_v [N''_w]^T [N'_u] \\ -h_v [N'_u]^T [N'_u] & \left(\frac{h_b}{2} + h_v + z_p\right) h_v [N'_u]^T [N''_w] & h_v^2 [N'_u]^T [N'_u] \end{bmatrix} dz_p dx \begin{Bmatrix} \{\bar{u}\} \\ \{\bar{w}\} \\ \{\bar{\beta}\} \end{Bmatrix} \quad (17)$$

And, finally, the strain energy associated with shear deformation of the viscoelastic layer is given by:

$$U_{Gv} = \frac{1}{2} \begin{Bmatrix} \{\bar{u}\} \\ \{\bar{w}\} \\ \{\bar{\beta}\} \end{Bmatrix}^T b G_v \int_0^L \int_0^{h_v} \begin{bmatrix} [0] & [0] & [0] \\ [0] & [0] & [0] \\ [0] & [0] & [N'_u]^T [N'_u] \end{bmatrix} dz_v dx \begin{Bmatrix} \{\bar{u}\} \\ \{\bar{w}\} \\ \{\bar{\beta}\} \end{Bmatrix} \quad (18)$$

Each of these strain energy expressions clearly shows the contributions of each to the elastic element stiffness matrix.

$$[K] = [K_E] + [K_G] = ([K_{Eb}] + [K_{Ev}] + [K_{Ep}]) + [K_{Gv}] \quad (19)$$

Kinetic Energy, Mass Matrix. The kinetic energy of a moving ACL beam of width "b" and length "L" is given by:

$$\begin{aligned} T = T(t) &= \frac{1}{2} b \int_0^L \int_z \rho(x, z) \left((\dot{w}(x, z, t))^2 + (\dot{u}(x, z, t))^2 \right) dz dx \\ &= T_w + T_u \\ &= T_w + (T_{ub} + T_{uv} + T_{up}) \end{aligned} \quad (20)$$

noting that the energy can be divided into parts associated with transverse motion and longitudinal motion and, further, into parts associated with each component of the ACL system. Note that longitudinal motion includes motion often associated

with “rotatory inertia”. The kinetic energy associated with transverse motion of the entire ACL system is given by the following, where the density and thickness have been assumed uniform over the length of the element.

$$T_w = \frac{1}{2} \begin{Bmatrix} \dot{\bar{u}} \\ \dot{\bar{w}} \\ \dot{\bar{\beta}} \end{Bmatrix}^T b (\rho_b h_b + \rho_v h_v + \rho_p h_p) \int_0^L \begin{bmatrix} 0 & 0 & 0 \\ 0 & [N_w]^T [N_w] & 0 \\ 0 & 0 & 0 \end{bmatrix} dx \begin{Bmatrix} \dot{\bar{u}} \\ \dot{\bar{w}} \\ \dot{\bar{\beta}} \end{Bmatrix} \quad (21)$$

The kinetic energy associated with longitudinal motion of the base beam is given by:

$$T_{ub} = \frac{1}{2} \begin{Bmatrix} \dot{\bar{u}} \\ \dot{\bar{w}} \\ \dot{\bar{\beta}} \end{Bmatrix}^T b \rho_b \int_0^L \int_{-h_b/2}^{+h_b/2} \begin{bmatrix} [N_u]^T [N_u] & -z [N'_w]^T [N_u] & 0 \\ -z [N'_w]^T [N_u] & z^2 [N'_w]^T [N'_w] & 0 \\ 0 & 0 & 0 \end{bmatrix} dz dx \begin{Bmatrix} \dot{\bar{u}} \\ \dot{\bar{w}} \\ \dot{\bar{\beta}} \end{Bmatrix} \quad (22)$$

The kinetic energy associated with longitudinal motion of the viscoelastic layer is given by:

$$T_{uv} = \frac{1}{2} \begin{Bmatrix} \dot{\bar{u}} \\ \dot{\bar{w}} \\ \dot{\bar{\beta}} \end{Bmatrix}^T b \rho_v \int_0^L \int_0^{+h_v} \begin{bmatrix} [N_u]^T [N_u] & -\left(\frac{h_b}{2} + z_v\right) [N_u]^T [N'_w] & -z_v [N_u]^T [N_u] \\ -\left(\frac{h_b}{2} + z_v\right) [N'_w]^T [N_u] & \left(\frac{h_b}{2} + z_v\right)^2 [N'_w]^T [N'_w] & \left(\frac{h_b}{2} + z_v\right) z_v [N'_w]^T [N_u] \\ -z_v [N_u]^T [N_u] & \left(\frac{h_b}{2} + z_v\right) z_v [N_u]^T [N'_w] & z_v^2 [N_u]^T [N_u] \end{bmatrix} dz_v dx \begin{Bmatrix} \dot{\bar{u}} \\ \dot{\bar{w}} \\ \dot{\bar{\beta}} \end{Bmatrix} \quad (23)$$

And, finally, the kinetic energy associated with longitudinal motion of the piezoelectric constraining layer is given by:

$$T_{up} = \frac{1}{2} \begin{Bmatrix} \dot{\bar{u}} \\ \dot{\bar{w}} \\ \dot{\bar{\beta}} \end{Bmatrix}^T b \rho_p \int_0^L \int_0^{h_p} \begin{bmatrix} [N_u]^T [N_u] & -\left(\frac{h_b}{2} + h_v + z_p\right) [N_u]^T [N'_w] & -h_v [N_u]^T [N_u] \\ -\left(\frac{h_b}{2} + h_v + z_p\right) [N'_w]^T [N_u] & \left(\frac{h_b}{2} + h_v + z_p\right)^2 [N'_w]^T [N'_w] & \left(\frac{h_b}{2} + h_v + z_p\right) h_v [N'_w]^T [N_u] \\ -h_v [N_u]^T [N_u] & \left(\frac{h_b}{2} + h_v + z_p\right) h_v [N_u]^T [N'_w] & h_v^2 [N_u]^T [N_u] \end{bmatrix} dz_p dx \begin{Bmatrix} \dot{\bar{u}} \\ \dot{\bar{w}} \\ \dot{\bar{\beta}} \end{Bmatrix} \quad (24)$$

Each of these kinetic energy expressions clearly shows the contributions of each to the element mass matrix.

$$[M] = [M_w] + [M_u] = [M_w] + ([M_{ub}] + [M_{uv}] + [M_{up}]) \quad (25)$$

Piezoelectric Forcing, Load Vector. The contributions of the piezoelectric forcing to the element load vector are found by considering the virtual work done by the blocked stresses moving through a virtual displacement of the ACL system. The blocked (zero strain) longitudinal normal stress in a piezoceramic, poled through the thickness, is given by:

$$(\sigma_{xx})_p = (\sigma_{xx}(x, z, t))_p = -e^t E_3 \quad (26)$$

where e^t is a piezoelectric coefficient, and E_3 is the electric field in the z -direction. Note that the electric field can be expressed in terms of the drive voltage and the thickness of the piezoelectric constraining layer as

$$E_3 = E_3(x, z, t) = E_3(t) = -\frac{V(t)}{h_p} \quad (27)$$

so that the blocked stresses may be expressed as:

$$(\sigma_{xx})_p = +\frac{e^t}{h_p} V(t) \quad (28)$$

Finally, the virtual work of the blocked stress is given by:

$$\begin{aligned}\delta W_p = \delta W_p(t) &= \frac{1}{2} b \int_0^L \int_0^{h_p} (\sigma_{xx}(x, z, t))_p (\delta \epsilon_{xx}(x, z, t))_p dz_p dx \\ &= \left\{ \begin{Bmatrix} \delta \bar{u} \\ \delta \bar{w} \\ \delta \bar{\beta} \end{Bmatrix} \right\}^T b \frac{e^t}{h_p} \int_0^L \int_{-h_b/2}^{+h_b/2} \begin{bmatrix} [N'_u]^T \\ -\left(\frac{h_b}{2} + h_v + z_p\right) [N''_w]^T \\ -h_v [N'_u]^T \end{bmatrix} dz_p dx V(t)\end{aligned}\quad (29)$$

This work expression clearly shows the contribution of piezoelectric forcing to the element load vector.

$$\{f\} = \left\{ \begin{Bmatrix} f_{pu} \\ f_{pw} \\ f_{p\beta} \end{Bmatrix} \right\} V(t) = \{F\} V(t) \quad (30)$$

Damping, Additional ADF DOF and ADF Evolution Equations. The frequency- or time-dependent behavior of the viscoelastic material can be captured by using a time-domain model such as the ADF method. In this approach, the total deformation (shear angle) of the material is considered to be the sum of two parts: 1) an elastic part, in which the strain is instantaneously proportional to the stress; and 2) an anelastic part, which captures the characteristic relaxation behavior.

$$\{\bar{\beta}\}_{Total} = \{\bar{\beta}\}_{Elastic} + \{\bar{\beta}\}_{Anelastic} \quad \text{or} \quad \{\bar{\beta}\} = \{\bar{\beta}^E\} + \{\bar{\beta}^A\} \quad (31)$$

Note that the entire anelastic displacement field itself may be comprised of several individual fields. This possibility is useful in modeling the behavior of materials that exhibit relatively weak frequency-dependence. In a finite element context, the total and anelastic fields are interpolated identically, introducing additional DOF for the anelastic displacements. Since the kinetic energy is expressed in terms of the total motion, it is unchanged. The elastic displacements that appear in strain energy expressions, however, are replaced by the difference between the total and anelastic displacements.

$$\{\bar{\beta}^E\} = \{\bar{\beta}\} - \{\bar{\beta}^A\} \quad (32)$$

Finally, an additional set of ordinary differential equations (ODE) that describe the time evolution of the anelastic displacement fields must be developed. They have the following general form:

$$\frac{c}{\Omega} [K_\beta] \{\dot{\bar{\beta}}^A\} - [K_\beta] \{\bar{\beta}\} + c [K_\beta] \{\bar{\beta}^A\} = \{0\} \quad (33)$$

where "[K_β]" is a stiffness matrix that appears in the elastic equations, "c" is a material constitutive coupling parameter, and "Ω" is a characteristic relaxation time at constant strain.

Because the ADF cannot be directly affected through the action of external forces, but only through coupling with the total displacement field, they are effectively internal fields. Consequently, there are no geometric boundary conditions for the ADF analogous to those for the total displacement field. There are, however, force-type boundary conditions: the anelastic stress is proportional to the anelastic strain rate (Lesieutre, 1996).

Discretized Equations of Motion. The final discretized equations of motion for a single element may be expressed in the following standard second order form with evident mass, damping and stiffness matrices:

$$[M]\{\ddot{q}\} + [C]\{\dot{q}\} + [K]\{q\} = \{f\} \quad (34)$$

where the nodal DOF vector is ordered as:

$$\{q\} = \left\{ \begin{Bmatrix} \bar{u} \\ \bar{w} \\ \bar{\beta} \\ \bar{\beta}^A \end{Bmatrix} \right\} = \begin{bmatrix} u_1 & u_2 & u_3 & | & w_1 & w'_1 & w_2 & w'_2 & | & \beta_1 & \beta_2 & \beta_3 & | & \beta_1^A & \beta_2^A & \beta_3^A \end{bmatrix}^T \quad (35)$$

Some details of the structure of this matrix equation are evident in the following form, particularly the presence of submatrices that are multiples of elastic stiffness submatrices. Once the mass and elastic stiffness matrices have been determined, the submatrices associated with ADF degrees of freedom may be readily determined without additional calculation.

$$\begin{bmatrix} M_{uu} & M_{uw} & M_{u\beta} & 0 \\ M_{uw}^T & M_{ww} & M_{w\beta} & 0 \\ M_{u\beta}^T & M_{w\beta}^T & M_{\beta\beta} & 0 \\ 0 & 0 & 0 & 0 \end{bmatrix} \begin{Bmatrix} \ddot{u} \\ \ddot{w} \\ \ddot{\beta} \\ \ddot{\beta}^A \end{Bmatrix} + \begin{bmatrix} 0 & 0 & 0 & 0 \\ 0 & 0 & 0 & 0 \\ 0 & 0 & 0 & 0 \\ 0 & 0 & 0 & \frac{c}{\Omega} K_{\beta\beta} \end{bmatrix} \begin{Bmatrix} \dot{u} \\ \dot{w} \\ \dot{\beta} \\ \dot{\beta}^A \end{Bmatrix} + \begin{bmatrix} K_{uu} & K_{uw} & K_{u\beta} & -K_{u\beta} \\ K_{uw}^T & K_{ww} & K_{w\beta} & -K_{w\beta} \\ K_{u\beta}^T & K_{w\beta}^T & K_{\beta\beta} & -K_{\beta\beta} \\ -K_{u\beta}^T & -K_{w\beta}^T & -K_{\beta\beta} & c K_{\beta\beta} \end{bmatrix} \begin{Bmatrix} \bar{u} \\ \bar{w} \\ \bar{\beta} \\ \bar{\beta}^A \end{Bmatrix} = \begin{Bmatrix} f_{pu} \\ f_{pw} \\ f_{pb} \\ 0 \end{Bmatrix} \quad (36)$$

Note that the matrix $[K_{\beta\beta}]$ is symmetric. If desired, these equations may be combined in first order form:

$$\begin{bmatrix} M_{uu} & M_{uw} & M_{u\beta} & 0 & 0 & 0 & 0 \\ M_{uw}^T & M_{ww} & M_{w\beta} & 0 & 0 & 0 & 0 \\ M_{u\beta}^T & M_{w\beta}^T & M_{\beta\beta} & 0 & 0 & 0 & 0 \\ 0 & 0 & 0 & I & 0 & 0 & 0 \\ 0 & 0 & 0 & 0 & I & 0 & 0 \\ 0 & 0 & 0 & 0 & 0 & I & 0 \\ 0 & 0 & 0 & 0 & 0 & 0 & \frac{c}{\Omega} K_{\beta\beta} \end{bmatrix} \begin{Bmatrix} \ddot{u} \\ \ddot{w} \\ \ddot{\beta} \\ \dot{u} \\ \dot{w} \\ \dot{\beta} \\ \dot{\beta}^A \end{Bmatrix} + \begin{bmatrix} 0 & 0 & 0 & K_{uu} & K_{uw} & K_{u\beta} & -K_{u\beta} \\ 0 & 0 & 0 & K_{uw}^T & K_{ww} & K_{w\beta} & -K_{w\beta} \\ 0 & 0 & 0 & K_{u\beta}^T & K_{w\beta}^T & K_{\beta\beta} & -K_{\beta\beta} \\ -I & 0 & 0 & 0 & 0 & 0 & 0 \\ 0 & -I & 0 & 0 & 0 & 0 & 0 \\ 0 & 0 & -I & 0 & 0 & 0 & 0 \\ 0 & 0 & 0 & -K_{u\beta}^T & -K_{w\beta}^T & -K_{\beta\beta} & c K_{\beta\beta} \end{bmatrix} \begin{Bmatrix} \dot{u} \\ \dot{w} \\ \dot{\beta} \\ \bar{u} \\ \bar{w} \\ \bar{\beta} \\ \bar{\beta}^A \end{Bmatrix} = \begin{Bmatrix} f_{pu} \\ f_{pw} \\ f_{pb} \\ 0 \\ 0 \\ 0 \\ 0 \end{Bmatrix} \quad (37)$$

The equations of motion for a complete ACL system or structure can be found using standard finite element assembly procedures. In such an approach, the total energy is just the sum of the energies of the individual elements, and common nodal DOF are eliminated when continuity is to be enforced.

3. ACL PERFORMANCE

To verify the correct performance of the subject ACL beam finite element, several numerical experiments were performed. First, passive performance was studied, for both continuous and segmented constrained layer treatments. Next, performance with a simple active proportional-derivative (PD) control law was investigated. The following subsections describe these numerical experiments and the results. In all cases, the ACL finite element and the modeled system performed as expected.

PASSIVE PERFORMANCE

The dynamic behavior of a cantilevered beam with ACL treatments were investigated. In the initial cases of interest, the ACL operated in a passive mode, *i.e.*, as a conventional constrained layer damping treatment. As shown in Figure 4, the first case of interest involved complete coverage with a continuous treatment, while the second case of interest involved complete coverage with a segmented treatment. Table 1 summarizes some of the parameter values used.

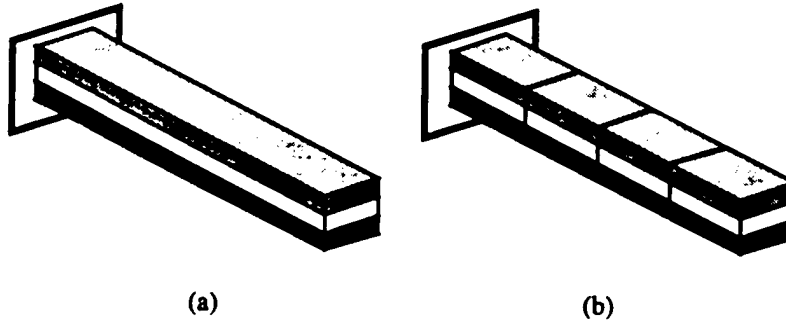


Figure 4. Beam and ACL Configurations Considered

Initial calculations were made using an elastic version of the finite element (without ADF DOFs, $\bar{\beta}^A$) and verified that modal frequencies were calculated correctly. Figure 5 shows modal damping ratios and modal frequencies for the first 5 modes of a finite element model constructed using 5 equal-length elements. The apparent frequency-dependence of modal damping is

due to a combination of two effects: the inherent variation of viscoelastic material loss factor with frequency, and the effect of different mode shapes on the fraction of strain energy stored in the viscoelastic. In addition, segmentation evidently makes the damping treatment considerably more effective in the lower modes, as expected, but slightly worse in higher modes.

Table 1. Configuration Parameter Values

Beam length (m)	0.200	Number of elements (typical)	5-25
Beam width (m)	0.010		
Base beam		Viscoelastic Layer	
Thickness (m)	0.00100	Thickness (m)	0.00025
Young's modulus (GPa)	70	Young's modulus (MPa)	25
Density (kg/m ³)	2700	Shear modulus (MPa)	10
Piezoelectric Constraining Layer		Density (kg/m ³)	1600
Thickness (m)	0.00025	ADF 'c'	1.2
Young's modulus (GPa)	50	ADF 'Ω' (rad/sec)	1500
Density (kg/m ³)	7500		
Piezoelectric constant (N/m-V)	-5.40		

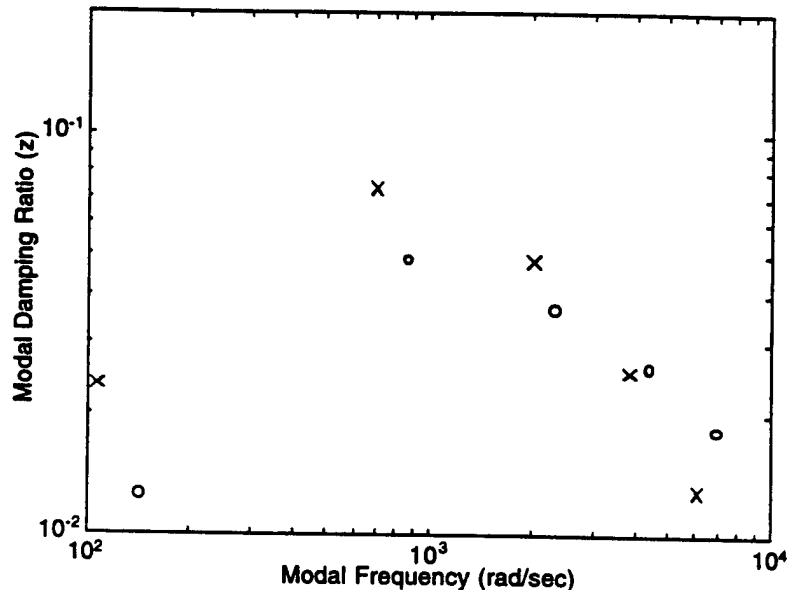


Figure 5. Passive Performance of ACL Treatments ('o' continuous; 'x' segmented)

ACTIVE PERFORMANCE

Performance of an ACL with a simple active proportional-derivative (PD) control law was subsequently investigated. In these cases, the control voltage for a particular ACL 'patch' was based on a discrete strain in the base beam, at the center of the patch, as shown in Figure 6.

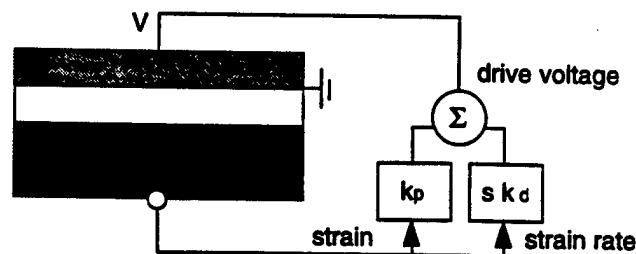


Figure 6. General Local Control Strategy for a Single ACL "Patch"

The drive voltage was taken as the sum of two terms, one proportional to strain, the other to the strain rate, as follows:

$$V_i = -k_p \varepsilon_{xxi} - k_d \dot{\varepsilon}_{xxi} \quad (38)$$

Eq. 10 may be used to obtain the strain at the desired location for element "i" as:

$$\left(\varepsilon_{xx} \left(x = \frac{L_i}{2}, z = -\frac{h_b}{2}, t \right) \right)_{b_i} = \begin{bmatrix} N'_u \left(\frac{L_i}{2} \right) & \frac{h_b}{2} N''_w \left(\frac{L_i}{2} \right) & [0] & [0] \end{bmatrix} \begin{Bmatrix} \{\bar{u}\} \\ \{\bar{w}\} \\ \{\bar{\beta}\} \\ \{\bar{\beta}^A\} \end{Bmatrix}_i \quad (39)$$

$$= [E]_i \{q\}_i$$

The elemental piezoelectric forcing then may be expressed in terms of the nodal DOF as (Eq. 30):

$$\{f\}_i = -k_p \{F\}_i [E]_i \{q\}_i - k_d \{F\}_i [E]_i \{\dot{q}\}_i \quad (40)$$

In this form, the piezoelectric forcing terms may be moved to the left hand side of the governing equations and treated as modifications to the stiffness and damping matrices. Table 2 summarizes the control gains used for validation purposes.

Table 2. Control Gains

Proportional gain, k_p	3,000,000 V	Derivative gain, k_d	60 V-s
--------------------------	-------------	------------------------	--------

Figure 7 shows the modal damping ratios and modal frequencies for the first 5 modes of a finite element model constructed using 5 equal-length elements, with control active. Relative to passive operation (Fig. 5), active control clearly increases the damping of the fundamental mode in for both continuous and segmented ACLs. In the case of the single continuous ACL, control is less effective in the higher modes. In fact, because of phasing associated with mode shapes, control using a single continuous ACL can be destabilizing: the frequency and damping of mode 3 are both decreased. The segmented ACL is more robust than the continuous treatment, in that the damping of modes at least up to the number of independent patches is increased by control action.

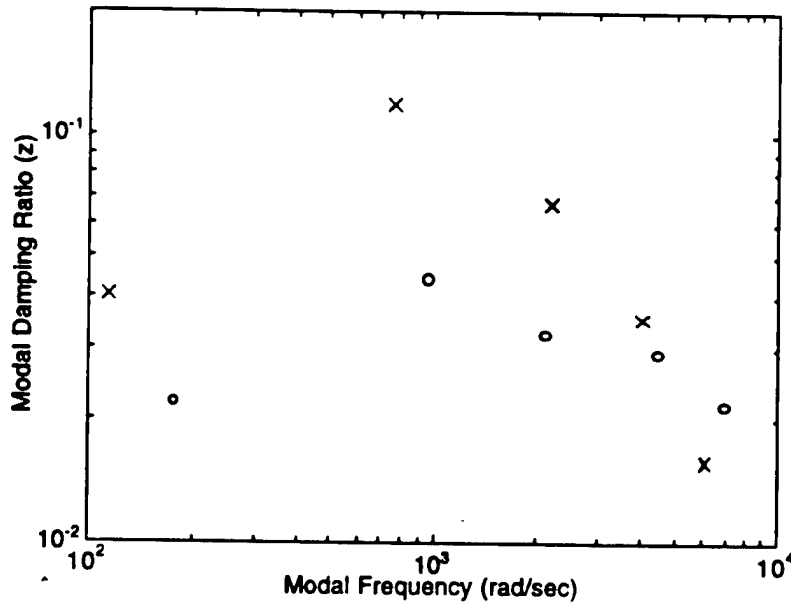


Figure 7. Active Performance of ACL Treatments ('o' continuous; 'x' segmented)

4. SUMMARY AND CONCLUSIONS

A finite element for planar beams with active constrained layer damping treatments was developed using an energy method in combination with the ADF viscoelastic modeling method. Features of this element that are potentially important in active control applications include the following: immunity to shear locking for accuracy; use of a time-domain viscoelastic material model to capture the frequency-dependent stiffness and damping of the viscoelastic material; and the ability to readily accommodate segmented constraining layers with partial coverage, permitting multiple control inputs. Future modifications could include the explicit addition of electrical degrees of freedom for current and power considerations.

The performance of the finite element was verified through several sample modal analyses, including purely passive performance in both continuous and segmented configurations, as well as corresponding active performance using a PD control strategy based on discrete strain sensing. Because of phasing associated with mode shapes, control using a single continuous ACL can be destabilizing. A segmented ACL is more robust than a continuous treatment, in that the damping of modes at least up to the number of independent patches is increased by control action.

REFERENCES

- Agnes, G. and K. Napolitano, "Active Constrained Layer Viscoelastic Damping," *Proceedings of the 34th AIAA/ASME/ASCE/AHS/ASC Structures, Structural Dynamics, and Materials Conference*, LaJolla, CA, April 19-22, 1993, pp. 3499-3506.
- Azvine, B., Tomlinson, G.R., and Wynne, R.J., "Use of Active Constrained-Layer Damping for Controlling Resonant Vibration," *Journal of Smart Materials and Structures*, Vol. 4, 1995, pp. 1-6.
- Bagley, R.L., and P.J. Torvik, "Fractional Calculus - A Different Approach to Analysis of Viscoelastically Damped Structures," *AIAA Journal*, Vol. 21, No. 5, 1983, pp. 741-748.
- Bagley, R.L., and P.J. Torvik, "Fractional Calculus in the Transient Analysis of Viscoelastically Damped Structures," *AIAA Journal*, Vol. 23, No. 3, 1985, pp. 201-210.
- Bagley, R.L., and R.A. Calico, "Fractional Order State Equations for the Control of Viscoelastically Damped Structures," *Journal of Guidance, Control, and Dynamics*, Vol. 14, No. 2, 1991, pp. 304-311.
- Baz, A. and Ro, J-J., "Optimum Design and Control of Active Constrained Layer Damping," *Transactions of the ASME, Special 50th Anniversary Design Issue*, Vol. 117, 1995, pp. 135-144.
- Baz, A. and Ro, J-J., "Performance Characteristics of Active Constrained Layer Damping," *Proceedings of Conference on Smart Structures and Materials: Passive Damping*, ed. C.D. Johnson, Orlando, FL, Feb. 14-16, 1994, SPIE Vol. 2193, pp. 98-114.
- Baz, A. and Ro, J-J., "The Concept and Performance of Active Constrained Layer Damping Treatments," *Journal of Sound and Vibration*, March, 1994, pp. 18-21.
- Baz, A. and Ro, J-J., "Vibration Control of Plates with Active Constrained Layer Damping," *Proceedings of Conference on Smart Structures and Materials: Passive Damping*, ed. C.D. Johnson, San Diego, CA, March, 1995, SPIE Vol. 2445, pp. 393-409.
- Baz, A., 1993, "Active Constrained Layer Damping," *Proceedings of Damping '93*, San Francisco, CA, November, 1993, pp. IBB 1-23.
- Baz, A., and Poh, S., "Performance of an Active Control System with Piezoelectric Actuators," *Journal of Sound and Vibration*, Vol. 126, No. 2, 1988, pp. 327-343.
- Enelund, M. and P. Olsson, "Damping Described by Fading Memory Models," *Proceedings of the 36th AIAA/ASME/ASCE/AHS Structures, Structural Dynamics & Materials Conference*, April 10-13, 1995, New Orleans, LA, Vol. 1, pp. 207-220.
- Golla, D.F., and Hughes, P.C., "Dynamics of Viscoelastic Structures - A Time-Domain, Finite Element Formulation," *Journal of Applied Mechanics*, Vol. 52, 1985, pp. 897-906.
- Johnson, C.D., Keinholz, D.A., and Rogers, L.C., "The Modal Strain Energy Finite Element Method and its Application to Damped Laminated Beams," *Shock and Vibration Bulletin*, Vol. 51, 1981, pp. 71-81.
- Lam, M.J., Saunders, W.R. and Inman, D.J., "Modeling Active Constrained Layer Damping using Golla-Hughes-McTavish Approach," *Proceedings of Conference on Smart Structures and Materials: Passive Damping*, ed. C.D. Johnson, San Diego, CA, March, 1995, SPIE Vol. 2445, pp. 86-97.
- Leibowitz, M.M., and Vinson, J.R., "On Active (Piezoelectric) Constrained Layer Damping in Composite Sandwich Structures," *Proceedings of the 4th International Conference on Adaptive Structures*, eds. Breitbach, E.J., Wada, B.K., and Natori, M.C., Cologne, Germany, November 2-4, 1993, pp. 530-541.

- Lesieutre, G.A., and E. Bianchini, "Time-Domain Modeling of Linear Viscoelasticity using Anelastic Displacement Fields," *Journal of Vibration and Acoustics*, Vol. 117, No. 4, 1995, pp. 424-430.
- Lesieutre, G.A., and Govindswamy, K.M., "Finite Element Modeling of Frequency-Dependent and Temperature-Dependent Dynamic Behavior of Viscoelastic Materials in Simple Shear," *International Journal of Solids and Structures*, Vol. 33, No. 3, 1995, pp. 419-432.
- Lesieutre, G.A., and Mingori, D.L., "Finite Element Modeling of Frequency-Dependent Material Damping Using Augmenting Thermodynamic Fields", *Journal of Guidance Control and Dynamics*, Vol. 13, No. 6, 1990, pp. 1040-1050.
- Lesieutre, G.A., "Finite Elements for Dynamic Modeling of Uniaxial Rods with Frequency Dependent Material Properties", *International Journal of Solids and Structures*, Vol. 29, 1992, pp. 1567-1579.
- Liao, W.H. and K.W. Wang, "Analysis and Design of Viscoelastic Materials for Active Constrained Layer Damping Treatments," *Proceedings of Conference on Smart Structures and Materials: Passive Damping*, ed. C.D. Johnson, San Diego, CA, March, 1996, SPIE Vol. 2720, pp. 212-223.
- Liao, W.H. and K.W. Wang, "On the Active-Passive Hybrid Vibration Control Actions of Structures with Active Constrained Layer Treatments," *Proceedings of the ASME 15th Biennial Conference on Mechanical Vibration and Noise*, ASME DE-Vol. 84-3, 1995, pp. 125-141.
- Liao, W.H. and K.W. Wang, "Synthesis and Control of Active Constrained Layers with Enhanced Boundary Actions," *Proceedings of Conference on Smart Structures and Materials: Mathematics and Control in Smart Structures*, ed. V.V. Varadan, San Diego, CA, March, 1996, SPIE Vol. 2715, paper no. 27.
- McTavish, D.J., and Hughes, P.C., "Modeling of Linear Viscoelastic Space Structures," *Journal of Vibration and Acoustics*, Vol. 115, No. 1, 1993, pp. 103-113.
- Nashif, A. D., Jones, D. I.G., and Henderson, J. P., *Vibration Damping*, New York, Wiley, 1985, Chapter 1.
- Nath, Subhobroto, and Wereley, N.M., "Active Constrained Layer Damping for Rotorcraft Flex Beams," *Proceedings of the 34th AIAA/ASME/ASCE/AHS/ASC Structures, Structural Dynamics, and Materials Conference*, New Orleans, LA, April 10-13, 1995, pp. 2867-2875.
- Plump, J.M. and Hubbard, J.E. Jr., "Modeling of an Active Constrained Layer Damper," *Proceedings of the 12th International Congress on Acoustics*, Toronto, Canada, July 24-31, 1986, Paper No. D4-1.
- Shen, I.Y., "Bending and Torsional Vibration Control of Composite Beams Through Intelligent Constrained Layer Treatments," *Proceedings of Conference on Smart Structures and Materials: Passive Damping*, ed. C.D. Johnson, San Diego, CA, March, 1995, SPIE Vol. 2445, pp. 110-122.
- Shen, I.Y., "Bending-Vibration Control of Composite and Isotropic Plates Through Intelligent Constrained Layer Treatments," *Journal of Smart Materials and Structures*, Vol. 4, 1995, pp. 59-70.
- Shen, I.Y., "Hybrid Damping Through Intelligent Constrained Layer Treatments," *Journal of Vibration and Acoustics*, Vol. 116, July, 1994, pp. 341-349.
- Shen, I.Y., "Stability and Controllability of Euler-Bernoulli Beams with Intelligent Constrained Layer Treatments," *Journal of Vibration and Acoustics*, Vol. 118, January, 1996, pp. 70-77.
- VanNostrand, W.C., Knowles, G., and Inman, D.J., "Active Constrained Layer Damping for Micro-Satellites," *Proceedings of the 2nd International Conference on Dynamics and Control of Structures in Space*, eds. Kirk, C.L. and Hughes, P.C., Cranfield Institute of Technology, OK, September 6-10, 1993, pp. 667-681.
- VanNostrand, W.C., Knowles, G., and Inman, D.J., "Finite Element Model for Active Constrained-Layer Damping," *Proceedings of Conference on Smart Structures and Materials: Passive Damping*, Orlando, FL, February 14-16, 1994, SPIE Vol. 2193, pp. 126-137.
- Veley, Duane E. and Rao, S.S., "Optimal Design of Structures with Active Constrained Layer Damping," *Proceedings of Conference on Smart Structures and Materials: Passive Damping*, ed. C.D. Johnson, San Diego, CA, March, 1995, SPIE Vol. 2445, pp. 98-109.
- Yiu, Y.C., "Finite Element Analysis of Structures with Classical Viscoelastic Materials," *Proceedings of the 34th Structures, Structural Dynamics, and Materials Conference*, La Jolla, CA, April, 1993, pp. 2110-2119.
- Yiu, Y.C., "Substructure and finite element formulation for linear viscoelastic materials," *Proceedings of the 35th AIAA/ASME/ASCE/AHS/ASC Structures, Structural Dynamics, and Materials Conference*, Hilton Head, SC, April, 1994, Vol. 3, pp. 1585-1594.

APPENDIX 50

ROTORCRAFT BLADE LAG DAMPING USING HIGHLY DISTRIBUTED TUNED VIBRATION ABSORBERS

Chad A. Hébert
Graduate Research Assistant

George A. Lesieutre
Associate Professor

Department of Aerospace Engineering
The Pennsylvania State University

Abstract

Damping of the rotor blade lag mode is especially critical in soft in-plane rotors. Lag damping is typically provided by hydraulic or elastomeric dampers. An alternative approach to providing damping over a broadband frequency range is presented. This is accomplished with multiple individual vibration absorbers which are highly distributed, both in space and in frequency. The mass for the absorbers could perhaps come from a portion of the mass of the leading edge weight structure already incorporated into the blade. The absorber system is modeled as frequency dependent mass which is distributed continuously along an elastic blade. The amount of damping can be controlled by varying the number of discrete tuning frequencies, the mass per unit length of the absorber system, the loss factor of the spring material and the frequency range of the absorbers. Through careful selection of these design parameters, substantial damping over a broad frequency range may be obtained. In an initial concept, these absorbers are embedded inside the blade leading edge weight structure, which reduces total rotor weight, complexity and drag. In addition, future research issues critical to the effective implementation of this concept are addressed.

Introduction

Lag dampers are integral parts of helicopter rotor systems. They are necessary especially for soft in-plane rotors where the problems of ground and air resonance instabilities emerge. Many approaches to

providing lag damping are being used or considered. Tarzanin and Panda¹ investigated the use of elastomeric and hydraulic lag dampers. However, elastomeric dampers are difficult to model because of their complex behavior with respect to varying operating conditions (amplitude, frequency and temperature)². Hydraulic dampers require increased maintenance as well as adding more weight and drag to the rotor system. Nath and Wereley³ developed a model using active constrained layer damping on flexbeams for lag damping. The use of electrorheological fluids in lag damping has been investigated by Kamath and Wereley⁴.

Some previous work addressed the use of absorbers attached to the blade for vibration control. The use of pendulum absorbers to reduce helicopter vibration was investigated by Taylor and Teare⁵ as well as by Pierce and Hamouda⁶. Taylor and Teare used a pendulum absorber attached to the rotor blade to control 4/rev vibrations and loads. This was done with a pendulum absorber optimally tuned to a specific frequency. Pierce and Hamouda looked at a pendulum absorber installed on a hingeless rotor to suppress hub reactions. This also required the pendulum to be tuned to a single optimal frequency.

The concept presented herein provides an alternative method to provide the damping needed in the lag modes. The basic feature of the approach is the use of highly distributed tuned vibration absorbers. The mass for these absorbers comes from a portion of the leading edge weights that are already incorporated into the blade. Current approaches to lag damping increase total rotor weight, complexity, and hub drag since components are added to the rotor blade structure. By using mass and structure already incorporated into the blade, the total rotor weight, complexity and drag can be reduced.

Highly Distributed Tuned Vibration Absorbers

Copyright © 1998 by Chad A. Hébert. Published by the American Institute of Aeronautics and Astronautics, Inc., with permission. Presented at the 39th AIAA/ASME/ASCE/AHS/ASC Structures, Structural Dynamics and Materials Conference, Long Beach, CA, April 20-23, 1998.

This method of vibration control uses a system of highly distributed vibration absorbers to provide damping in the first lag mode for the rotor blades. The absorber system consists of multiple individual vibration absorbers, highly distributed both in space and frequency to provide broadband energy dissipation. This system is similar in concept to a frequency dependent elastic foundation as shown in Figure 1, and can be represented equivalently as distributed damping or distributed mass.

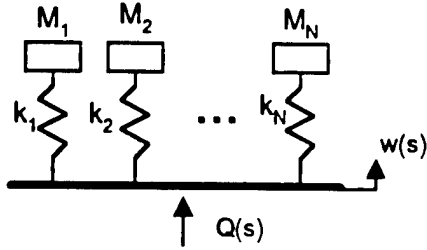


Figure 1 -- Distributed Absorbers Attached to a Common Base⁷

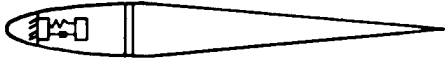


Figure 2 -- Schematic of Absorber Embedded in Blade Cross-Section

The frequency dependent distributed mass method is the modeling approach used in this paper. In order for this concept to be viable, the distributed tuned vibration absorbers must be embedded in the cross-section of the blade as seen in Figure 2. The mass for the absorbers could perhaps be provided by a portion of the leading edge weights that are already incorporated into the rotor blades. The leading edge weights in current blades account for approximately 15-20% of the weight in metal blades and up to 30% in composite blades. This concept would take these previously inert masses and use a portion of them to damp the lag mode.

The model for a system of distributed tuned vibration absorbers comes from previous research done by Zapfe and Lesieutre⁸. The absorber system may be treated as having frequency dependent complex mass per unit length as shown in Equation 1.

$$\rho A_d(\omega) = \sum_{i=1}^N \frac{\rho A_i \omega_i^2 (1 + j\eta_i)}{\omega_i^2 (1 + j\eta_i) - \omega^2} \quad (1)$$

The sum in Equation 1 is over a finite number (N) of discrete frequencies to which portions of the absorber system are tuned. In Equation 1, ω_i is the natural frequency of the i^{th} portion of the absorber system, ρA_i is the corresponding mass per unit length, and η_i is the loss factor of the spring material. The equation for this frequency dependent mass has two distinct features: First, at a given driving frequency the effective mass is complex, having magnitude and phase. Secondly, if considered within an eigenvalue problem, $\rho A_d(\omega)$ must be evaluated at the modal frequency of the system, ω , which requires that the eigenproblem be solved iteratively. In Figure 3, the characteristics of the distributed frequency dependent mass in relation to that for an individual absorber is shown through a frequency response function for a constant total absorber system mass. By examining the magnitude and phase of the effective mass of the absorber system, it is clear that a single absorber can only provide effective system damping over a small frequency range. However, the use of the multiple absorber system can provide damping over a larger range of frequencies.

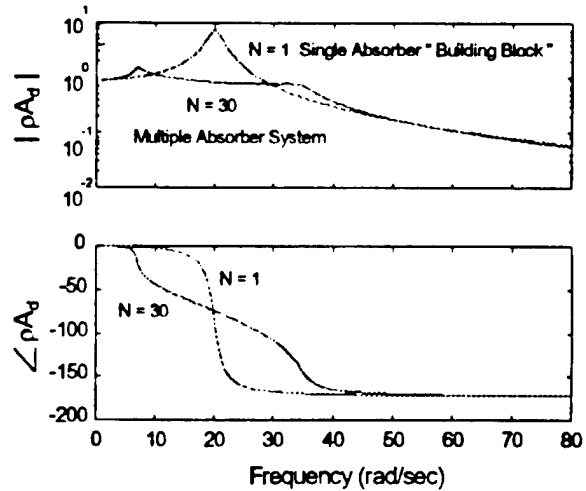


Figure 3 -- Frequency Dependent Mass Characteristics

Blade and Absorber System Model

A hingeless blade was modeled as a cantilevered elastic beam with a soft flexure (1/25th of blade flexural rigidity from 5-20% of span location) to approximate a hingeless blade with $v_{\zeta} \approx .62/\text{rev}$. The parameters used to model the blade were similar to those of a UH-60 Blackhawk. Only the lag motion

was investigated and the governing PDE given by Equation 2⁹ was discretized using the finite element method to yield Equation 3. In Equation 2, the variable P is the tensile axial load due to the centrifugal force acting on a blade cross-section.

$$\rho A \ddot{v} + EI_x (v'')'' - (Pv')' - \rho A \Omega^2 v = P_y(x, t) \quad (2)$$

$$\text{where } P = \int_x^L \rho A \Omega^2 x_1 dx_1$$

$$[M]\{\ddot{q}\} + [K]\{q\} + \Omega^2([K_G] - [M])\{q\} = \{F(q, t)\} \quad (3)$$

The equations of motion were then modified to include the frequency dependent mass of the absorber system, which was treated as a continuous system outboard of the blade flexure to 85% radius as depicted in Figure 4. In Equation 3, the frequency dependent mass is included in those terms where the mass matrix $[M]$ is present. The section mass center of the absorber system and the rest of the blade section are initially collocated on the centerline. This resulted in a blade and absorber system model with complex mass and stiffness that was used to study the dynamic behavior of the blade with the absorber system

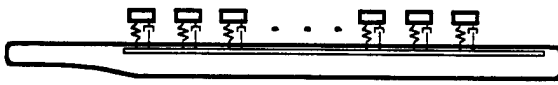


Figure 4 -- Absorber System Distribution

Absorber System Design Parameters

This numerical model was then used to simulate blade lag dynamic behavior. Some of the key design parameters investigated were the following: mass per unit length of the absorber system (ρA_d), frequency range of the absorbers, loss factor of spring material (η_i) and number (N) of tuning frequencies (ω_i). With the proper selection of appropriate values of these parameters, the absorber system can provide substantial lag mode damping.

Absorber Tuning Frequency Range

The natural frequency of the fundamental blade lag mode increases with increasing rotor speed. The range of absorber tuning frequencies should include both the range of natural vibration frequencies as well

as the frequencies involved in ground or air resonance as shown in Figure 5, including the progressive low frequency lag mode. Based on this information an initial range of absorber system tuning frequencies can be chosen.

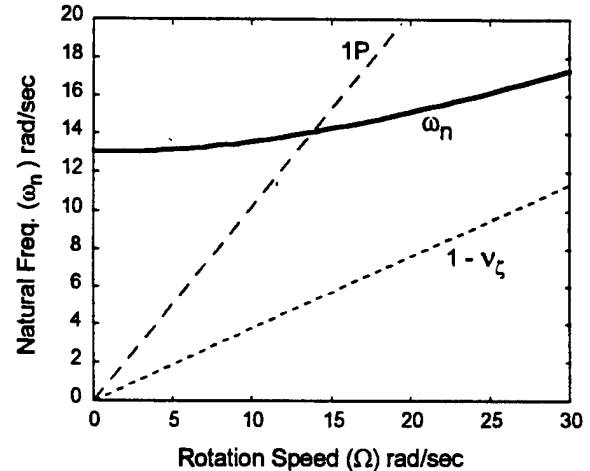


Figure 5 -- Absorber Tuning Frequency Range

Loss Factor and Number of Tuning Frequencies

The number of tuning frequencies is related to the absorber system loss factor as shown in Figure 6.

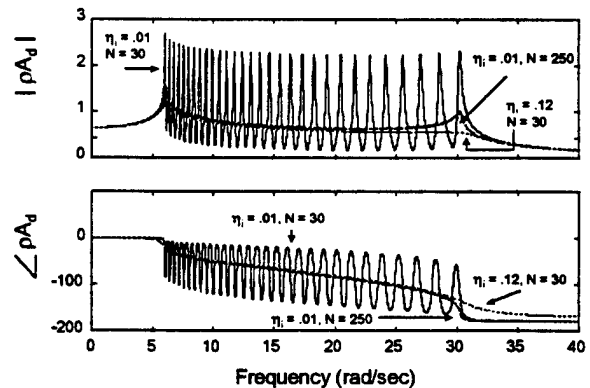


Figure 6 -- Relationship Between N and η_i

By using a small number of tuning frequencies in combination with a low loss factor the large response of at each tuning frequency can be clearly seen. There are two possible methods to accomplish a smoothly varying response over a range of frequencies. The first is to use a low loss factor in combination with a large number of tuning frequencies. The second method (which was used in further analysis) is to use a higher loss factor with a relatively small number of tuning frequencies. This is

justified by considering that production would be more efficient if only a small number of differently tuned absorbers needed to be used.

In Figure 7 the variation of damping ratio versus loss factor for different rotation speeds is shown. There is an optimal loss factor that varies with rotation speed for a fixed number of tuning frequencies and absorber mass fraction. As the loss factor increases, the damping ratio of the lag mode approaches a maximum value and then steadily decreases. This will cause a loss in performance of the absorber system if too high a loss factor is chosen. Also, note that the loss factor of the material chosen may depend on other factors such as temperature and frequency, depending on the material chosen to implement this part of the absorber.

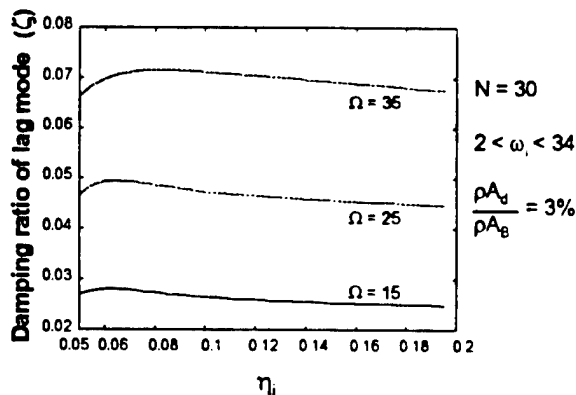


Figure 7 -- Selecting Loss Factor of Absorbers

Simulation Results

Simulation results illustrate the effects of the key parameters on absorber system performance. Using the values for loss factor and number of tuning frequencies determined previously, the relationship between the fundamental lag mode damping ratio and absorber mass fraction ratio is shown in Figure 8. Different absorber mass fractions were considered, ranging from 3% to 5% of the total blade mass. For each case, the range of absorber tuning frequencies was held constant at 2-34 rad/sec. For an increase in absorber mass ratio an increase in critical damping ratio is evidenced. The results show that, even for low rotation speeds with small mass fractions associated with the absorber system, it is capable of providing substantial effective damping over a broadband frequency range.

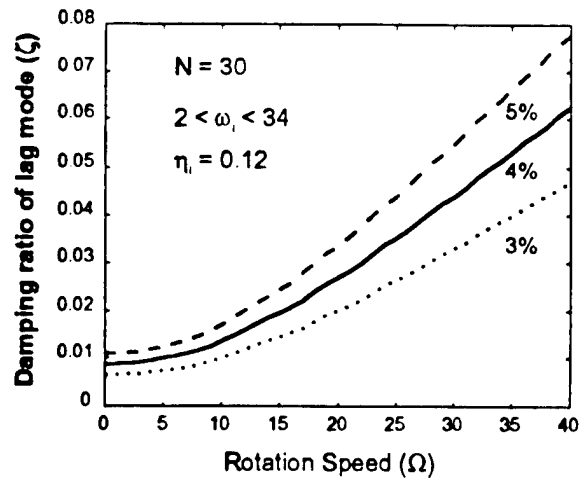


Figure 8 -- Effect of Changing Absorber Mass Ratio

The other variable that can be easily altered is the frequency bandwidth of the absorber tuning frequencies. Figure 9 shows that by decreasing the absorber frequency bandwidth, the amount of damping provided can be significantly increased for a constant absorber mass ratio of 4%. The solid curve has a absorber tuning frequency range of 2-34 rad/sec, while the dashed curve has a range of 6-30 rad/sec. Also the effects of having just a single tuning frequency of 18 rad/s is shown. Decreasing the tuning frequency range of the absorber system such that it no longer spans the frequency range of interest causes a peak in the damping, but not the broadband energy dissipation desired. Narrowing the absorber system frequency band has the same effect as increasing the absorber mass ratio and can be used accordingly to achieve the damping required by the application.

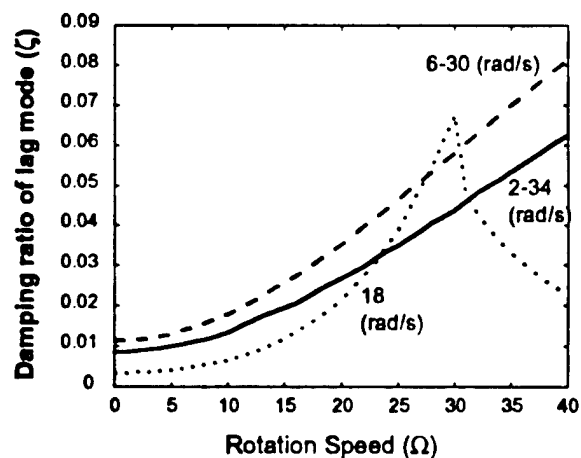


Figure 9 -- Effect of Tuning Frequency Bandwidth

In order to better understand the complete effects of the frequency dependent mass, rotation speeds above the range of normal operating speeds are investigated in Figure 10.

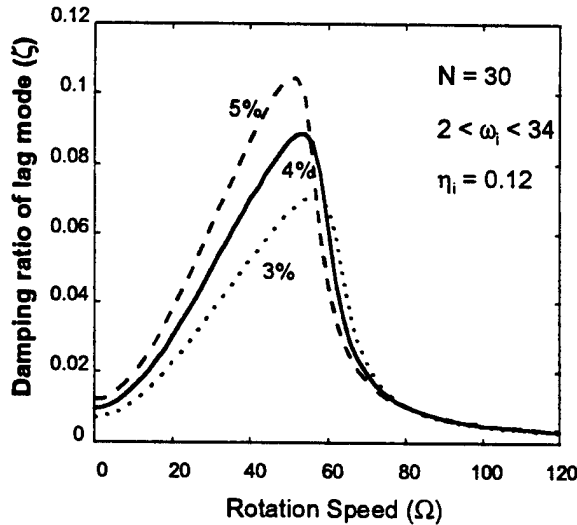


Figure 10 -- Damping Ratio vs. Rotation Speed

The damping ratio of the lag mode increases to a maximum value and then decreases and approaches a constant associated with the loss factor of the spring material as rotation speeds increase. This is due to the fact that the natural lag frequencies are no longer within the range of tuning frequencies of the absorber system. The effects of this can be seen more effectively in Figure 11.

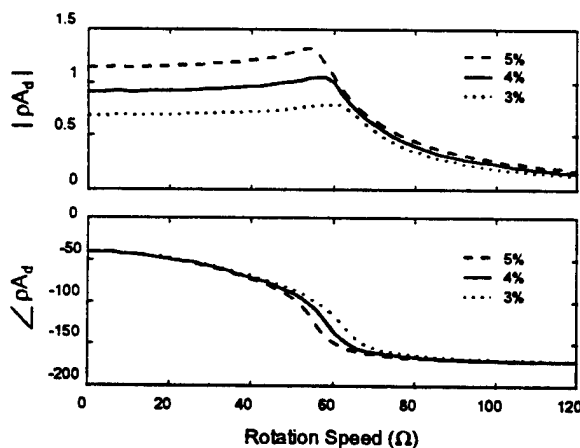


Figure 11 -- Effective Mass vs. Rotation Speed

Here it can be seen that for frequencies below the tuning frequency range of the absorber system, its

mass acts as simply real added mass. Then at higher frequencies, above the tuning range, the effective mass of the absorber system approaches a real value and acts like N parallel springs or stiffness since it is -180° out of phase. At both of these extremes the absorber system mass remains real and therefore no effective damping is provided to the system. Also it can be seen that there is a point where the phase of the effective mass passes through -90° which corresponds to viscous damping. The frequency at which this occurs is consistent with the peak damping seen in Figure 10.

Conceptual Design

A simple conceptual design has been devised to communicate a potential realization of the idea. Figure 12 shows multiple views of a partial section of the leading edge weight structure with absorbers incorporated in it. The idea is to create a mass surrounded by rubber that would be embedded into the leading edge weight structure in the form of plugs.

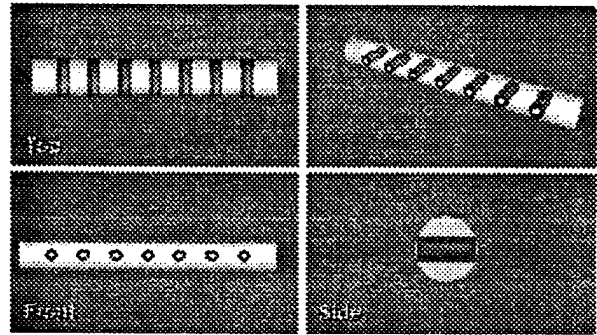


Figure 12 -- Conceptual Design of Absorber System

Conclusions

The use of multiple vibration absorbers, highly distributed both in space and in frequency, to provide lag damping was investigated. The inert mass of the leading edge weight structure could be made productive in damping of the fundamental lag mode of the rotor blade. The simulation results show that the distributed tuned vibration absorber system can potentially be very effective at providing damping in the blade lag motion. Through alteration of the various design variables the amount of damping produced can be changed. Using as little as 3% of the total blade mass (much less than that already used for the leading edge weights), with the appropriate absorber frequency band, this method could provide

damping comparable to or better than that provided by methods already in use or proposed.

Future Research

Future research could investigate at least the following attributes of the distributed tuned vibration absorber system:

- Physical considerations, such as whether the absorber could impact the inner cavity of the blade. This is critical because excessive motion of the absorber system cannot be tolerated within the blade.
- The effect of the absorber system and its motion on the center of gravity of the blade cross-section. This will determine any changes to the blade flap, lag and torsion couplings. Also, the impact of aerodynamics on the absorber system and the resulting consequences to the helicopter need to be investigated. The effects of absorber system motion on helicopter and blade stability also needs to be determined.
- Experiments to validate performance in conjunction with development of a method of effective implementation.

References

- 1) Tarzanin, F. J., Panda, B., "Development and Application of Nonlinear Elastomeric and Hydraulic Lag Damper Models", AIAA/ASME/ASCE/AHS Structures, Structural Dynamics, and Materials Conference, New Orleans, LA, April 1995
- 2) Smith, E. C., Beale, M., Govindswamy, K., Vascisnec, M., and Lesieutre, G. A., "Formulation, Validation, and Application of a Finite Element Model for Elastomeric Lag Dampers", Journal of the American Helicopter Society, Vol. 41, No.3, 1996
- 3) Nath, S., Wereley, N. M., "Active Constrained Layer Damping For Rotorcraft Flex Beams", AIAA/ASME/ASCE/AHS Structures, Structural Dynamics, and Materials Conference, New Orleans, LA, April 1997
- 4) Kamath, G. M., Wereley, N. M., "Distributed Damping of Rotorcraft Flexbeams Using Electrorheological Fluids", AIAA/ASME/ASCE/AHS Structures, Structural Dynamics, and Materials Conference, New Orleans, LA, April 1995
- 5) Taylor, Robert B., Teare, Paul A. "Helicopter Vibration Reduction with Pendulum Absorbers",

30th Annual National Forum of the American Helicopter Society, May 1974

- 6) Pierce, Alvin G., Hamouda, M-Nabil H., "Helicopter Vibration Suppression Using Simple Pendulum Absorbers on the Rotor Blade", American Helicopter Society National Specialists' Meeting on Helicopter Vibration, Hartford, Conn, Nov. 2-4, 1981
- 7) Zapfe, J. A., Lesieutre, G. A., "Broadband Vibration Damping in Beams Using Distributed Viscoelastic Tuned Mass Absorbers", AIAA/ASME/ASCE/AHS Structures, Structural Dynamics, and Materials Conference, Salt Lake City, UT, April 1996
- 8) Zapfe, J. A., Lesieutre, G. A., "Broadband Vibration Damping Using Highly Distributed Tuned Mass Absorbers", AIAA Journal, Vol. 35, No.4, 1997
- 9) Johnson, Wayne, *Helicopter Theory*, Dover Publications Inc., New York, 1980

APPENDIX 51

Can a coupling coefficient of a piezoelectric device be higher than those of its active material?

George A. Lesieutre,* Christopher L. Davis

Penn State University, Center for Acoustics and Vibration,
Aerospace Engineering Department, University Park, PA 16802

ABSTRACT

A coupling coefficient is a measure of the effectiveness with which a shape-changing material (or a device employing such a material) converts the energy in an imposed signal to useful mechanical energy. There are different kinds of material and device coupling coefficients, corresponding to different modes of excitation and response. Device coupling coefficients are properties of the device and, although related to the material coupling coefficients, are generally different from them. It is commonly held that a device coupling coefficient cannot be greater than some corresponding coupling coefficient of the active material used in the device. A class of devices was recently identified in which the apparent coupling coefficient can, in principle, approach 1.0, corresponding to perfect electromechanical energy conversion. The key feature of this class of devices is the use of destabilizing mechanical pre-loads to counter inherent stiffness. The approach is illustrated for a piezoelectric bimorph device: theory predicts a smooth increase of the apparent coupling coefficient with pre-load, approaching 1.0 at the buckling load. An experiment verified the trend of increasing coupling with pre-load. This approach provides a way to simultaneously increase both displacement and force, distinguishing it from alternatives such as motion amplification, and may allow transducer designers to achieve substantial performance gains for some actuator and sensor devices.

Keywords: Coupling coefficient, piezoelectric, energy transduction, transducer, sensor, actuator

1. INTRODUCTION

Many mechanical transducers employ shape-changing materials as an integral part of their construction. An example of a material exhibiting such behavior is a piezoelectric ceramic. In the case of actuators, such shape changes, or strains, are the result of the application of an imposed external signal, such as an electric field. Device performance depends intimately on the ability of these materials to convert energy from one form to another. One measure of the effectiveness with which a material or device converts the energy in an imposed signal to useful mechanical energy is the *coupling coefficient*.

One definition of a coupling coefficient is the following: the ratio of the energy converted to that imposed is equal to the square of the coupling coefficient, k . Thus, no material coupling coefficient can be greater than 1.0, as this represents the limit of 100% conversion of imposed energy to mechanical energy. In addition, as the result of the ability to impose signals in different ways, as well as the ability of a material to strain in different ways, any material has multiple coupling coefficients corresponding to different modes of excitation and response. The largest coupling coefficients for piezoelectric ceramic materials are on the order of 0.7, corresponding to energy conversion factors of about 50%. Considerable research has addressed the development of new material compositions that might exhibit higher electro-mechanical coupling.¹

Devices made using such active materials are also said to have coupling coefficients. These are properties of the device and, although related to the material coupling coefficients, are generally different from them. Various device coupling coefficients can also be defined, corresponding to specific modes of excitation and response. Accepted design guidelines suggest two ways to maximize device (and composite material) coupling coefficients: 1) use a material with high inherent coupling; and 2) configure the device so as to best use the available material coupling.^{2,3} Considerable research has addressed ways to exploit material coupling, resulting in devices such as the "moonie."⁴ It is commonly held that no device coupling coefficient can be greater than the largest coupling coefficient of the active material used in the device.

* G.A.L. (correspondence): Email: g-lesieutre@psu.edu; Telephone: 814-863-0103. Associate Professor.
C.L.D.: Email: cld103@psu.edu; Telephone: 814-865-9072. Ph.D. Candidate.

2. BACKGROUND: PIEZOELECTRIC COUPLING COEFFICIENTS

2.1 Piezoelectric Material Coupling

The behavior of piezoelectric materials involves coupled mechanical and electrical response. The constitutive equations of a linear piezoelectric material can be expressed in terms of various combination of mechanical and electrical quantities (stress or strain, electric field or electric displacement). In light of the popularity of the modern displacement-based finite element method, the constitutive equations used herein employ the strain and electric fields. (Strain is related to the gradient of the mechanical displacement field, while electric field is the gradient of the electric potential field.) In condensed matrix notation, the nine constitutive equations for a typical piezoelectric ceramic material are:

$$\begin{Bmatrix} T \\ D \end{Bmatrix} = \begin{bmatrix} c^E & -e^T \\ e & \epsilon^S \end{bmatrix} \begin{Bmatrix} S \\ E \end{Bmatrix} \quad (1)$$

where: T is the stress vector; S is the strain vector (6 components each);
 D is the electric displacement vector; E is the electric field vector (3 components each);
 c^E is a matrix of elastic coefficients (at constant electric field);
 e is a matrix of piezoelectric coefficients; and
 ϵ^S is a matrix of dielectric permittivities (at constant strain).

2.1.1 Simple Strain / Electric Field Patterns. In engineering analysis, materials may sometimes be assumed to experience a state in which only a single stress or strain component is non-zero, and in which only a single electric field or electric displacement component is non-zero. In that event, the nine constitutive equations may be reduced to two, so that the matrices of coefficients become scalars. The corresponding *single* coupling coefficient may be found from either:⁵

The difference between the open-circuit (constant electric displacement) stiffness (c^D) and the short circuit (constant electric field) stiffness (c^E):

$$k^2 = \frac{c^D - c^E}{c^D} = \frac{\left(c^E + \frac{e^2}{\epsilon^S}\right) - c^E}{\left(c^E + \frac{e^2}{\epsilon^S}\right)} = \frac{e^2}{(c^E \epsilon^S + e^2)} \quad (2)$$

The difference between the free (constant stress) permittivity (ϵ^T) and the blocked (constant strain) permittivity (ϵ^S):

$$k^2 = \frac{\epsilon^T - \epsilon^S}{\epsilon^T} = \frac{\left(\epsilon^S + \frac{e^2}{c^E}\right) - \epsilon^S}{\left(\epsilon^S + \frac{e^2}{c^E}\right)} = \frac{e^2}{(c^E \epsilon^S + e^2)} \quad (3)$$

2.1.2 Eigen Strain / Electric Field Patterns. Eigenanalysis of the constitutive equations for a typical piezoelectric ceramic material reveals that only 3 characteristic strain/electric field patterns exhibit electromechanical coupling.⁶ Because each stress / electric displacement pattern is related to the corresponding strain / electric field pattern by a scalar (the eigenvalue), individual patterns may be considered to be effectively one-dimensional; the total electromechanical system may then be considered as a set of parallel one-dimensional systems. When the conventional coordinate system is used ("3" the poling direction, and "1-2" the plane of isotropy),⁵ the three patterns which exhibit electromechanical coupling involve the three components of the electric field vector individually; the first two involve shears in planes normal to the plane of isotropy, and the third involves a combination of all three normal strains. For many materials, the coupling coefficient associated with each of these three eigen patterns is about 0.70.

2.1.3 Arbitrary Strain / Electric Field Patterns. An effective coupling coefficient may be defined for an arbitrary quasistatic electromechanical state of the material from energy considerations. For the selected form of the constitutive equations (block skew symmetric), the total energy density is the sum of the mechanical (strain) energy density and the electrical (dielectric) energy density:

$$U_{tot} = U_{mech} + U_{elec} \quad \text{where} \quad U_{mech} = \frac{1}{2} \{S\}^T [c^E] \{S\} \quad \text{and} \quad U_{elec} = \frac{1}{2} \{E\}^T [\epsilon^S] \{E\} \quad (4)$$

Although with this form of the constitutive equations there is no "mutual" energy density,⁷ a "one-way coupled" energy density may be defined as:

$$U_{coup} = \frac{1}{2} \{E\}^T [e] \{S\} = \frac{1}{2} \{S\}^T [e^T] \{E\} \quad (5)$$

With these definitions, an effective coupling coefficient for an arbitrary electromechanical state may be defined as:

$$k^2 = \frac{U_{coup}}{U_{tot}} = \frac{U_{coup}}{U_{mech} + U_{elec}} \quad (6)$$

Of course, this relation is most meaningful when the state considered corresponds to a quasistatic equilibrium attained as the result of some electromechanical loading process starting from zero initial conditions. Also, since any electromechanical state of the material can be expressed as a linear combination of the eigen patterns discussed in the preceding, the coupling coefficient associated with an arbitrary state cannot be greater than the largest eigen coupling coefficient.

When the electromechanical loading process corresponds to purely electrical or purely mechanical loading, special cases of Eq. 6 may be developed. In that case, the total energy is equal to the work done by the loading system, and the transduced energy is equal to the one-way coupled energy defined in Eq. 7.

For purely electrical loading, the coupling coefficient may be expressed as:

$$k^2 = \frac{U_{mech}}{W_{elec}} \quad \text{where} \quad W_{elec} = \frac{1}{2} \{D\}^T \{E\} \quad (7)$$

For purely mechanical loading, the coupling coefficient may be expressed as:

$$k^2 = \frac{U_{elec}}{W_{mech}} \quad \text{where} \quad W_{mech} = \frac{1}{2} \{T\}^T \{S\} \quad (8)$$

2.2 Piezoelectric Device Coupling

The stiffness of non-active elements tends to reduce *device* coupling coefficients relative to *material* coefficients. Definitions of coupling coefficients for piezoelectric devices must also recognize that the electromechanical response will generally be non-homogeneous within the device. Versions of any of the preceding energy-based definitions of material coupling coefficients (Eqs. 6, 7, 8) may be applied to devices, so long as the work and energy quantities are considered for the entire device (for example, energy densities must be integrated over the device volume). Further, if the electromechanical equations describing the device are expressed in terms of scalar stiffness and capacitance coefficients, methods analogous to the simple material coefficient method (Eqs. 2 (stiffness), and 3 (capacitance)) may also be used with success.

Piezoelectric devices are often used dynamically, to induce or to sense motion. In that case, a dynamic definition of coupling coefficient may be obtained for each combination of electrical leads and natural vibration modes, based on the difference between the open-circuit natural vibration frequency (ω^D) and the short circuit natural vibration frequency (ω^E):

$$k^2 = \frac{(\omega^D)^2 - (\omega^E)^2}{(\omega^D)^2} \quad (9)$$

Note that under static, homogeneous conditions, this reduces to Eq. 2.

3. CONCEPT: REDUCE DEVICE STIFFNESS WITH DESTABILIZING PRE-LOADS

Inspiration for a way to increase the effective coupling coefficient of a piezoelectric device may be obtained by close inspection of Eq. 2, reproduced here and discussed using "device" terms, rather than "material" terms.

$$k^2 = \frac{e^2}{(c^E \epsilon^S + e^2)}$$

If the stiffness (c^E) could be reduced without affecting the capacitance (ϵ^S) or the piezoelectric coupling (e), the coupling coefficient would be increased. Furthermore, as the stiffness approached zero, the coupling coefficient would approach unity.

Although it may be impossible to accomplish such stiffness reductions for real materials, it is possible for built-up devices. The field of elastic stability, perhaps most familiar to structural analysts in the fields of aerospace, civil and mechanical engineering, addresses the effects of various loads on the stability of structures.⁸ It is common to consider such destabilizing loads as decreasing structural stiffness. In fact, as the critical buckling load is approached, both the structural stiffness and the fundamental natural frequency of vibration approach zero.

Of course, when an external mechanical load acts on a structure or device, it may do mechanical work. This must be considered when defining the coupling coefficient for a device when such loads are present.

4. THEORY: FLEXURAL PIEZOELECTRIC DEVICE

4.1 Device Configuration and Assumptions

The concept for increasing device electromechanical coupling coefficients using destabilizing mechanical pre-loads is illustrated through consideration of a simple planar piezoelectric bimorph. Figure 1 shows a schematic of such a device, as well as the origin and orientation of the coordinate system. The device consists of a base beam made of a non-piezoelectric material, with thin pieces of piezoelectric material bonded to its upper and lower surfaces (or, directly to one another). In the most common realization, these pieces are monolithic piezoceramic and are poled in the direction normal to the plane of the beam ("3"). A bimorph operates in such a way that electrical excitation in the poling direction causes the beam to bend laterally. This is accomplished by driving the piezoceramics in opposition, extending one side and contracting the other.



Figure 1. A piezoelectric bimorph with a compressive axial load

For illustration, the device will be assumed to be simply supported, and modeled as a symmetric composite (multi-element) beam. Let cross-sections be identified by the longitudinal ("1") coordinate x , and let the lateral ("3") motion of the midplane be denoted $w(x)$. The following kinematic assumptions are made:

Transverse shear strains are negligible. Therefore, the longitudinal motion of a point in a cross-section, $u(x)$, is proportional to the bending rotation of the cross-section, and to the distance from the midplane, z . The deformation of the beam can be characterized fully by the longitudinal normal strain, S_{11} .

$$u(x, z) = -z \frac{\partial w}{\partial x} = -z w' \quad \text{and} \quad S_{11}(x, z) = \frac{\partial u}{\partial x} = -z w'' \quad (10, 11)$$

The beam is inextensible, that is, changes in the developed length of the midplane are negligible. The axial load can only do work when the beam bends and its two ends move closer together.

Since transverse shear strains are negligible, and neither E_1 nor E_2 is prescribed, the only electrical field of significance is E_3 . The electrical potential, Φ , is assumed to vary linearly through the thickness of the piezoelectric layers, h_p , but not at all along the length because the upper and lower surfaces are electroded (equipotential). The voltage, V , at the outer surfaces is the same, and zero at the inner surfaces.

$$E_3(z) = -\frac{\partial \Phi(z)}{\partial x} = \left\langle -\frac{V}{h_p} \quad \text{top}; \quad +\frac{V}{h_p} \quad \text{bottom} \right\rangle \quad (12)$$

Under the preceding conditions, the material constitutive equations reduce to the following one-dimensional form:

$$\begin{Bmatrix} T_{11} \\ D_3 \end{Bmatrix} = \begin{bmatrix} c^E & -e^T \\ e & \epsilon^S \end{bmatrix} \begin{Bmatrix} S_{11} \\ E_3 \end{Bmatrix} \quad (13)$$

The focus bimorph is characterized by the following geometric and material properties. Sample numerical values (SI units) are also shown for later use.

Base Beam (aluminum)

h_b	thickness	0.0010
b	width	0.0100
L	length	0.1000
c_b^E	Young's modulus	7.000e+10
ρ_b	density	2750

Piezoelectric Ceramic (PZT-5A; full set of material constants⁹)

h_p	thickness	0.0005
c_p^E	Young's modulus (constant electric field)	6.152e+10
e_p	piezoelectric coefficient	-10.48
ϵ_p^S	dielectric permittivity (constant strain)	1.330e-08
ρ_p	density	7250

(Note: Using Eq. 2, the material coupling coefficient, $k_{31} = 0.344$.)

Axial Load

P axial load (compression is positive)

4.2 Model and Governing Equations

The governing equations for this multi-layered piezoelectric beam may be found using the method of virtual work or Hamilton's Principle. Because the beam is assumed to be uniform and simply-supported, the fundamental vibration mode and the buckling mode are both half-sinusoids. Therefore, an assumed-modes method based on a such a shape function yields the exact solution for the first mode. The transverse deflection of the midplane is then given by:

$$w(x, t) = d(t) \sin\left(\frac{\pi x}{L}\right) \quad (14)$$

where $d(t)$ is the magnitude of the lateral deflection at the center of the beam. Application of the assumed modes method of analysis leads to the following two coupled equations:

$$\begin{bmatrix} m & 0 \\ 0 & 0 \end{bmatrix} \begin{Bmatrix} \ddot{d} \\ \ddot{V} \end{Bmatrix} + \begin{bmatrix} K^E - K_G & -p^T \\ p & C^S \end{bmatrix} \begin{Bmatrix} d \\ V \end{Bmatrix} = \begin{Bmatrix} 0 \\ Q \end{Bmatrix} \quad (15)$$

where d is the discrete displacement variable, V is the voltage across the device terminals, and Q is the charge imposed on the device. Note that direct mechanical forcing of lateral motion is omitted.

The device electromechanical coefficients are:

$$\text{mass} \quad m = b(\rho_b h_b + 2\rho_p h_p) \frac{L}{2} \quad (16a)$$

$$\text{stiffness} \quad K^E = b \left(c_b^E \frac{h_b^3}{12} + 2c_p^E \left(\frac{h_p^3}{12} + h_p \left(\frac{h_b + h_p}{2} \right)^2 \right) \right) \left(\frac{\pi}{L} \right)^4 \frac{L}{2} \quad (16b)$$

$$\text{capacitance} \quad C^S = 2\epsilon^s \frac{bL}{h_p} \quad (16c)$$

$$\text{piezoelectric coupling} \quad p = 2be(h_b + h_p) \left(\frac{\pi}{L} \right) \quad (16d)$$

$$\text{"geometric" stiffness} \quad K_G = P \left(\frac{\pi}{L} \right)^2 \frac{L}{2} \quad (16e)$$

Note that the work done by the axial pre-load is represented as the "geometric stiffness," and that its main effect is to reduce the effective lateral stiffness of the layered device. In fact, if the axial load P is made high enough, K_G will fully counteract K^E and the beam will be on the verge of instability. The corresponding value of P is P_{cr} , the critical load for buckling.

4.3 Coupling Coefficients of the Axially-Loaded Piezoelectric Bimorph

4.3.1 Without axial load. A first estimate of the device coupling coefficient may be obtained by multiplying the material coupling coefficient by the fraction of the stiffness associated with extension of the midplanes of the piezoelectric layers. For the sample numerical values used, this fraction is about 0.83. The coupling coefficient of the piezoelectric material used is 0.344. The resulting device coupling coefficient estimated in this manner is 0.286.

Additional estimates of the device coupling coefficient may be obtained by extending Eqs. 2 (stiffness change due to electrical boundary conditions) and 3 (capacitance change due to mechanical boundary conditions) to devices. For the sample numerical values used, a value of 0.288 is obtained. Use of Eq. 9 (change in natural vibration frequency due to electrical boundary conditions) yields the same result.

By doing electrical work on the device (imposing a charge, Q) and finding the equilibrium displacement/voltage state, Eq. 6 or 7 may also be used to obtain an estimate of the device coupling coefficient, with the same result, 0.288.

4.3.2 With axial load. The definitions of coupling coefficient used in the preceding must be modified to reflect the action of an external compressive load. Depending on the way the axial load is considered, both "apparent" and "proper" coupling coefficients may be defined.

"Apparent" coupling coefficient. Treating the axial load simply as a reduction of effective lateral stiffness of the device suggests the definition of an "effective" or "apparent" coupling coefficient. Eqs. 2 (stiffness) and 3 (capacitance) can be used with the simple modification of replacing K^E with the quantity $(K^E - K_G)$, the effective or net lateral stiffness. Eq. 9 (frequency) can be used directly. Clearly, as the load approaches the buckling load, the apparent coupling coefficient approaches 1.0.

An energy approach can be adopted to yield similar results. Consider the following definitions of energy- and work-related quantities:

$$W_{tot} = W_{elec} + W_{mech} \quad \text{where} \quad W_{elec} = \frac{1}{2} QV \quad \text{and} \quad W_{mech} = \frac{1}{2} K_G d^2 \quad (17)$$

$$U_{tot} = U_{elec} + U_{mech} \quad U_{elec} = \frac{1}{2} C^S V^2 \quad U_{mech} = \frac{1}{2} K^E d^2 \quad (18)$$

$$U_{coup} = \left| \frac{1}{2} p V d \right| \quad (19)$$

Clearly, Eq. 7 cannot be used directly as it could lead to coupling coefficients greater than 1.0. It might be reasonably modified, however, to omit the work done by the mechanical pre-load from the mechanical strain energy, as follows:

$$k_{app}^2 = \frac{U_{mech} - W_{mech}}{W_{elec}} \quad (20)$$

The numerator can be interpreted as that part of the mechanical energy stored that is due to the input of electrical energy, and Eq. 20 yields results consistent with the stiffness reduction approach. An alternate approach involves considering the ratio of the one-way coupled energy to the electrical work input:

$$k_{app}^2 = \frac{U_{coup}}{W_{elec}} \quad (21)$$

This approach, too, yields results consistent with the stiffness reduction approach.

"Proper" coupling coefficient. Although the "apparent" coupling coefficient appears to be a practical definition based on the interconversion of mechanical energy associated with lateral deformation and electrical energy, a "proper" coupling coefficient might be defined by treating the work done by the compressive axial pre-load as work, and not simply as a stiffness reduction. Such a definition would have the same general form as Eq. 6:

$$k_{proper}^2 = \frac{U_{coup}}{W_{tot}} = \frac{U_{coup}}{U_{tot}} = \frac{U_{coup}}{U_{mech} + U_{elec}} = \frac{U_{coup}}{W_{mech} + W_{elec}} \quad (22)$$

Figure 2 shows the theoretical relationship between the "apparent" and "proper" coupling coefficients for the piezoelectric bimorph and the axial pre-load. Two pairs of curves are shown: the lower pair corresponds to the nominal case of material coupling of 0.34, while the upper pair corresponds to material coupling of 0.70. In all cases, the device coupling coefficient increases initially as the load increases from zero. For both inherent material coupling values, the "apparent" coupling coefficient approaches 1.0 as the load approaches the buckling load, while the "proper" coupling coefficient attains a maximum value, then approaches 0.0 with increasing load. Even at modest pre-load levels, device coupling coefficients can increase substantially from their unloaded values, and can exceed the coupling coefficient of the active material used.

The destabilizing pre-load is observed to increase bimorph device coupling coefficients, by either definition. In practice, however, because the pre-load may be obtained by passive design, the "apparent" coupling coefficient may be a better measure of the useful coupling between mechanical and electrical signals.

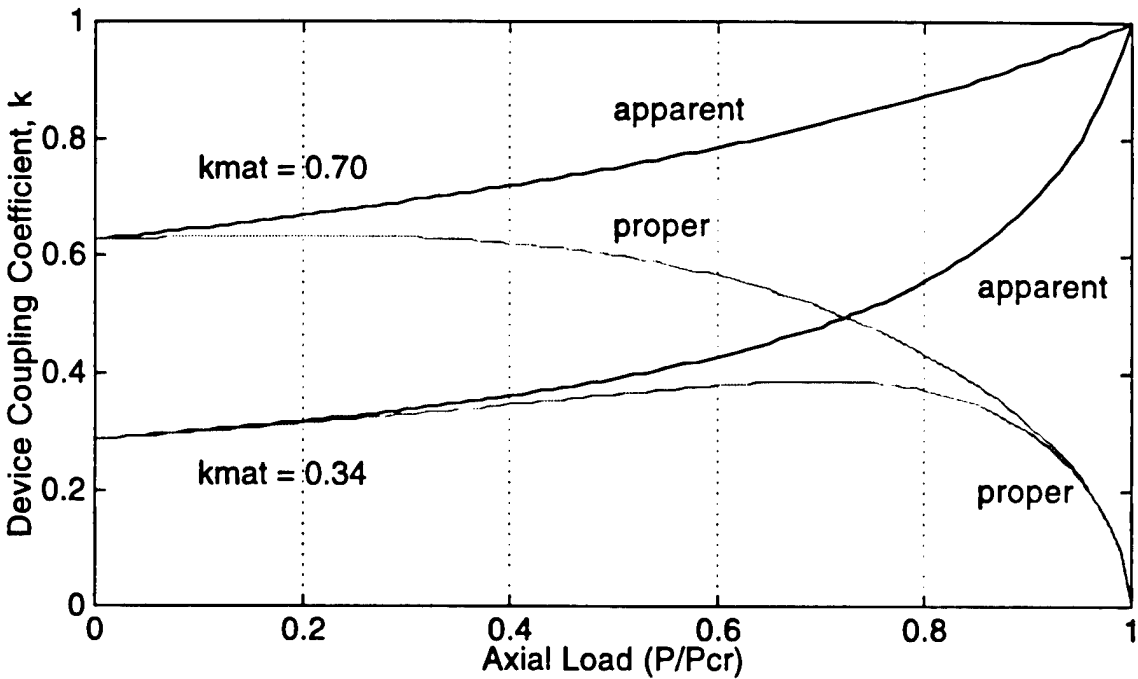


Figure 2. Variation of "apparent" and "proper" coupling coefficients with axial pre-load

5. EXPERIMENTAL

An experiment was performed to investigate the effect of a compressive axial pre-load on the apparent coupling coefficient of a piezoelectric bimorph. The experimental bimorph consisted of a built-up beam under clamped-clamped boundary conditions. As shown in Figure 3, the built-up beam comprised a brass base beam and two piezoelectric plate elements (Piezo Kinetics Incorporated PKI 500 Lead Zirconate Titanate).

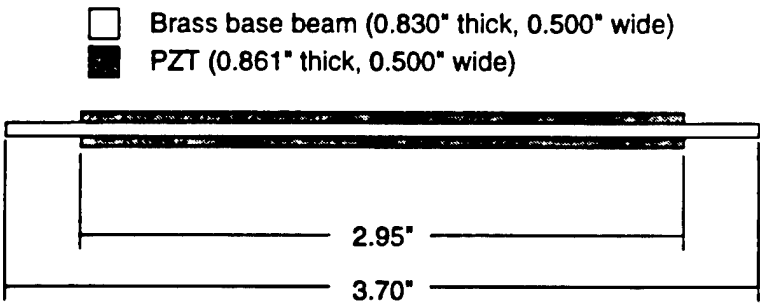


Figure 3. Piezoelectric bimorph specimen

Table 1 summarizes the material properties of the bimorph specimen. The PZT was bonded to the brass beam with Devcon 5 Minute® Epoxy. A small amount of conducting epoxy (Emerson & Cuming Eccobond Solder 56C mixed with Catalyst 9) was used on a tiny area of the bond surface to ensure electrical conduction of the PZT electrodes to the brass beam, which was used as an electrical terminal.

Table 1. Bimorph material and geometry

Material Property	Brass Base Beam	Lead Zirconate Titanate PKI 500
modulus [N/m ²]	105.0E+9	64.9E+9 *
density [kg/m ³]	8470	7600
gage length [mm]	75	75
width [mm]	12.7	12.7
thickness [mm]	0.8306	0.8611
coupling coefficient	--	0.34

* short-circuit modulus

Clamped-clamped boundary conditions were simulated by clamping the uncovered brass beam ends between two pieces of 0.375" x 0.750" x 2.500" aluminum bar stock, as shown in Figure 4. The ends of the brass base beam were made flush with the outside surfaces of the aluminum clamps and a small gap was left between the inside surface of the aluminum clamps and the PZT. This configuration ensured the axial load would only be applied to the brass base beam, thus avoiding direct axial loading of the attached PZT. Screws were used to hold the aluminum blocks in place and to prevent any rotation of the bimorph specimen at the clamp ends. Electrical leads were attached using a low temperature solder.

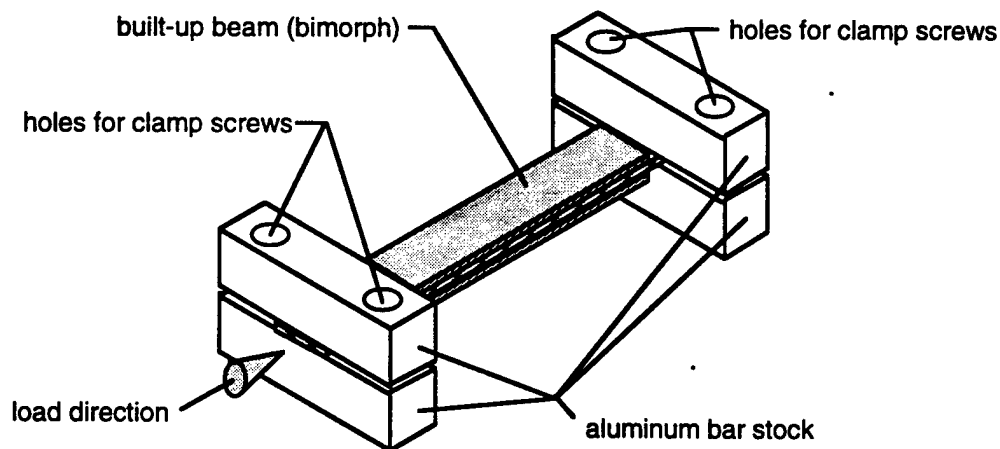


Figure 4. Simulated clamped-clamped bimorph test apparatus

The boundary conditions differed from those assumed in the preceding theoretical section because a clamped boundary was significantly easier to implement than a simply-supported condition. The clamped boundary in combination with piezoelectric elements that were nearly as long as the gage length of the base beam reduced the nominal coupling coefficient substantially.

The electrical impedance of the bimorph was determined experimentally by measuring the ratio of voltage to current (V/I) in a circuit including the bimorph. Figure 5 shows a schematic of the circuit used in the measurement. The resistor in the circuit, R , was much smaller than the impedance of the bimorph ($R \approx 1\Omega$). Thus, the current in the resistor (also the current in the bimorph) was proportional to and thus approximately equal to the voltage across the resistor. Because the voltage drop across the bimorph was much larger than the voltage drop across the resistor, the voltage across the bimorph was very nearly equal to the drive voltage.

The device electrical impedance was measured using a Hewlett Packard 3563A Control System Analyzer. The initial drive voltage used was a 1.5 V_{rms} periodic chirp signal from 0 to 1.6 kHz. Channel #1 of the signal analyzer measured the voltage across the resistor (proportional to the current in the bimorph), and channel #2 measured the total applied voltage (the voltage across the bimorph). The resulting complex frequency response measurement is proportional to the electrical impedance.

A low frequency zero was introduced as a result of the impedance-measuring approach. The frequency of the next zero (minimum value), f_z , corresponded to the short-circuit natural frequency of the bimorph, as V was very nearly zero. The frequency of the nearby pole (maximum value), f_p , corresponded to the open-circuit natural frequency of the bimorph, as I was very nearly zero. The apparent coupling coefficient was determined using Eq. 9.

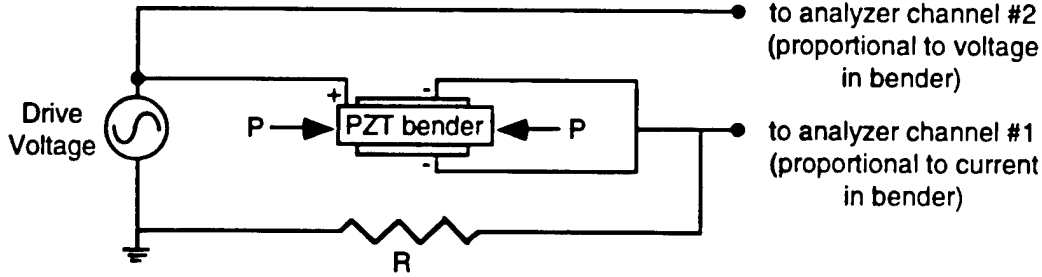


Figure 5. Schematic of bimorph electrical impedance measurement circuit

The ratio of the axial load to the critical load (P/P_{cr}) for a given data point was estimated from the change in short-circuit frequency, f_z (relative to its initial no-load value, f_{z0}), using the following relation:

$$P/P_{cr} = 1 - \left(\frac{f_z}{f_{z0}} \right)^2 \quad (23)$$

A compressive axial load was applied to the specimen using a large adjustable clamp, as shown in Figure 6.

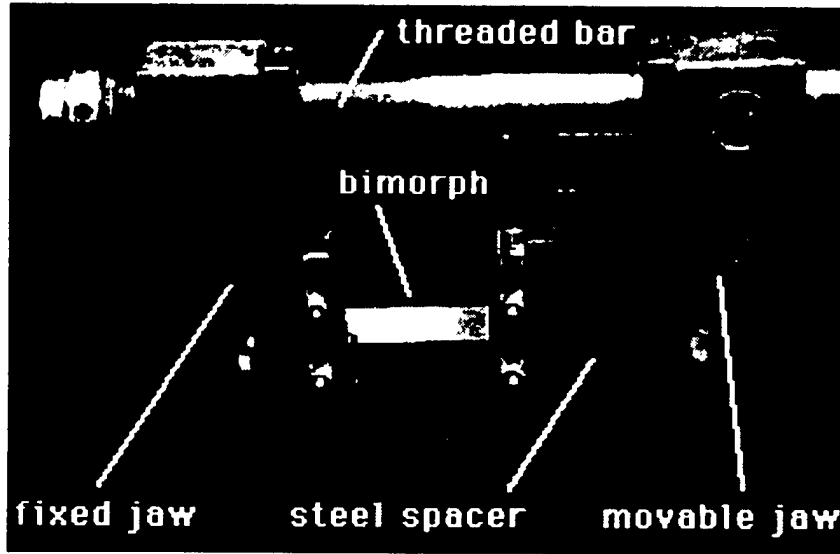


Figure 6. Experimental apparatus

Testing proceeded as follows: First, the bimorph was placed between the jaws of the adjustable clamp with just enough pressure to ensure that the aluminum bimorph clamps could not move axially or rotate. This was considered the no-load condition. A frequency response measurement of electrical impedance was made using a periodic chirp drive voltage signal between 0 and 1.6 kHz. Next, a swept sine measurement was made over a much smaller frequency range containing the zero and pole frequencies. A curve fit of the swept sine data yielded numerical estimates for the zero and pole frequencies.

After curve fitting the swept sine data, the load was increased slightly and the measurement process repeated. Figure 7 shows plots of device electrical impedance for two load cases, $P/P_{CR} = 0.35$ (solid line) and $P/P_{CR} = 0.50$ (dashed line). Note that both the short-circuit and open-circuit natural frequencies decrease as the load increases, but that the *relative* separation increases. This increasing separation corresponds to an increase in apparent coupling coefficient.

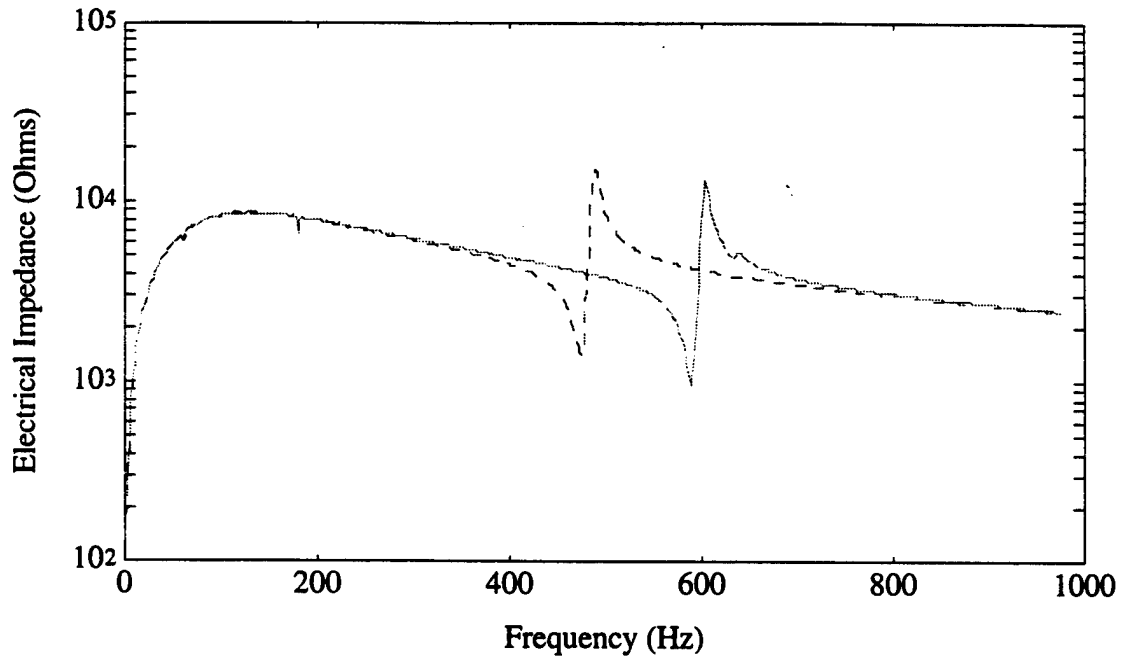


Figure 7. Experimental device electrical impedance measurements

Figure 8 shows the measured apparent device coupling coefficient as a function of axial load. The symbols indicate the measured data, while the solid line is a curve fit based on the model described in the preceding. In this curve fit, only the unloaded coupling coefficient was regarded as unknown. Note that the coupling coefficient increases substantially as the compressive pre-load increases. In addition, note the general agreement of the data with theory.

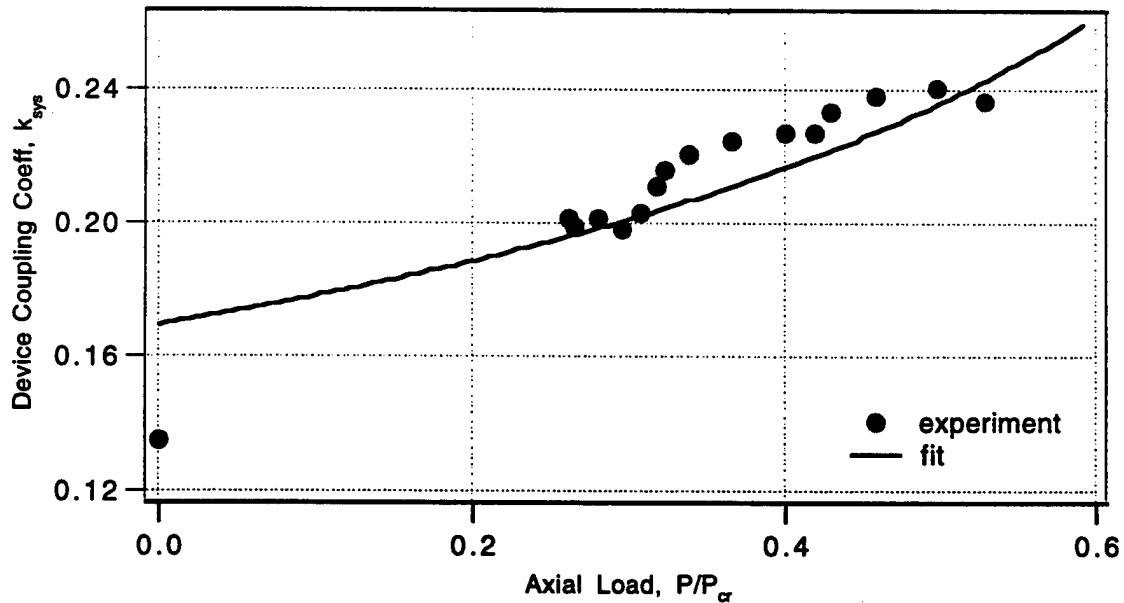


Figure 8. Measured device coupling coefficient as a function of axial pre-load

6. SUMMARY AND CONCLUSIONS

A class of devices was recently identified in which the apparent coupling coefficient can, in principle, approach 1.0, corresponding to perfect electromechanical energy conversion. The key feature of this class of devices is the use of destabilizing mechanical pre-loads to counter inherent stiffness. The approach was illustrated for a piezoelectric bimorph device: theory predicts a smooth increase of the apparent coupling coefficient with pre-load, approaching 1.0 at the buckling load. An experiment verified the trend of increasing coupling with pre-load.

From energy considerations two alternative device coupling coefficients were defined: an "apparent" coupling coefficient that treats the destabilizing pre-load as a reduction in stiffness; and a "proper" coupling coefficient that explicitly treats the pre-load as a source of mechanical work on the device. By either definition, device coupling coefficient increases initially as the pre-load increases from zero. As the load continues to increase towards the critical buckling load, the "apparent" coupling coefficient approaches 1.0, while the "proper" coupling coefficient attains a maximum value, then approaches 0.0. Even at modest pre-load levels, device coupling coefficients can increase substantially from their unloaded values, and can exceed the coupling coefficient of the active material used. In practice, because the pre-load may be obtained by passive design, the "apparent" coupling coefficient may be a better measure of the useful coupling between mechanical energy associated with transverse motion and electrical energy.

This approach provides a way to simultaneously increase both the operating displacement and force of a device, distinguishing it from alternatives such as motion amplification, and may allow transducer designers to achieve substantial performance gains for some kinds of actuator and sensor devices.

ACKNOWLEDGMENTS

This work was initially supported by PCB Piezotronics under a Phase II SBIR program from the NASA Langley Research Center (NAS1-20205), and later by the Office of Naval Research under the Acoustic Transduction MURI program (N00014-96-1-1173). Enlightening discussions with Dr. Jeff Dosch and Dr. Wallace Arden Smith are gratefully acknowledged.

REFERENCES

1. L. Eric Cross, *et al.*, *Piezoelectric and Electrostrictive Materials for Transducer Applications*, 1991 Annual Report, ONR Contract No. N00014-89-J-1689.
2. Wallace Arden Smith, "The key design principle for piezoelectric ceramic/polymer composites," *Recent Advances in Adaptive and Sensory Materials and Their Applications*, pp. 825-838, April 27-29, 1992.
3. Smith, Wallace Arden, "Maximal electromechanical coupling in piezoelectric ceramics—its effective exploitation in acoustic transducers," *Ferroelectrics* **134**, pp. 145-150, 1992.
4. R.E. Newnham, Q.C. Xu, and S. Yoshikawa, "Transformed Stress Direction Acoustic Transducer," U.S. Patent 4,999,819, 12 March 1991.
5. *IEEE Standard on Piezoelectricity*, ANSI / IEEE Std 176-1987, Institute of Electrical and Electronics Engineers, New York, 1988.
6. Baerwald, H. G., "Eigen coupling factors and principal components, the thermodynamic invariants of piezoelectricity," 1960 IRE International Convention Record, Part 6, pp. 205-211, 1960.
7. Wilson, O. B., *Introduction to theory and design of sonar transducers*, Peninsula, Los Altos, CA, 1988.
8. Brush, D. O., and B. O. Almroth, *Buckling of bars, plates, and shells*, McGraw-Hill, New York, 1975.
9. *Guide to modern piezoelectric ceramics*, Morgan Matroc Inc., Vernitron Division, Bedford, OH.

3-D Acoustic Intensity Probes

APPENDIX 52

Active control of axial-flow fan noise

Gerald C. Lauchle, John R. MacGillivray, and David C. Swanson

Penn State University, Graduate Program in Acoustics and Applied Research Laboratory, P.O. Box 30, State College, Pennsylvania 16804

(Received 14 February 1996; accepted for publication 19 July 1996)

Discrete-frequency axial-flow fan noise reduction using active noise control is described. The unique aspect of the current research is the use of the fan itself as the antinoise source in the active noise control scheme. This is achieved by driving the entire fan unit axially with an electrodynamic shaker which mechanically couples the solid surfaces of the fan to the acoustic medium. The fan unit is thus transformed into a crude loudspeaker. A near-field microphone serves as an error sensor, where transfer function measurements between the electrical input to the shaker and the electrical output of the microphone are found to be reasonably free of phase distortions and linear. A feedforward algorithm utilizing the output of a tachometer as a reference signal is used. The experimental apparatus is composed of a baffled fan unit in a free field. A small cylindrical flow obstruction is placed on the inlet side of the fan to enhance noise emissions at the blade-pass frequency and harmonics. The experiment successfully demonstrates the concept of active control of tonal fan noise using a shaken fan as the cancellation source. For the fan operating in a planar baffle, the fundamental blade-passage frequency sound-pressure level at the location of the error sensor is reduced by 20 dB, while the second and third harmonic levels are reduced by 15 and 8 dB, respectively. Placing a cabinet enclosure over the baffled fan did not affect these results significantly, and free-field sound power measurements indicate similar level reductions with the active control in operation. © 1997 Acoustical Society of America. [S0001-4966(97)00112-4]

PACS numbers: 43.50.Ed, 43.50.Ki, 43.28.Ra [GAD]

INTRODUCTION

Under the long-wavelength (relative to rotor diameter) constraints of compactness, a subsonic fan, either baffled or unbaffled, radiates acoustic energy because of both steady and unsteady aerodynamic forces generated by the rotating blades. For typical fans operating in air, the blades are usually assumed rigid. The steady forces on fan blades generate the thrust of the fan, but because they are rotating, they also create a steady-loading noise component. The mechanism for steady-loading noise (Gutin noise) is the time-dependent distance between the individual steady forces on the blades and the observer. This component radiates sound at the blade-passing frequency (BPF) given by the number of fan blades multiplied by the shaft speed. The predominant direction of radiation is 90° to the fan axis, where the time variation in distance between any given blade and a fixed observation point is maximum. This type of noise begins to dominate other fan noise mechanisms only under the conditions of very high blade tip speeds (very high subsonic and supersonic conditions) and clean inflow/outflow conditions.

Unsteady blade forces result when the blades pass through spatially nonuniform, time invariant flow fields. Such situations occur when the fan is operated close to obstructions that can disrupt an otherwise uniform inflow. As the blades pass through these regions, the magnitude and direction of the local velocity incident to the blade sections varies with circumferential position. This gives rise to a local blade section lift and drag force that varies periodically with time. Dipole sound is produced by these fluctuating forces at harmonics of the BPF. Peak sound pressure occurs along the axis of the fan for the lower harmonics. In addition to the

spatially nonuniform, time invariant flows, random flow variations due to turbulence and unsteady upstream conditions may also be present. These stochastic flow variations cause random blade forces which lead to a broadband component of sound radiation. The level of sound at the harmonics of the BPF, however, are usually many dBs above the broadband components. The BPF tones are therefore important to suppress (initially) in a fan noise reduction program.

There has been considerable interest and fundamental research on the use of active noise control (ANC) to reduce the level of discrete-frequency noise radiated from fans, blowers, and turbomachines. One of the first demonstrations of this technology was by Ffowcs Williams¹ on a British Gas Corp. gas turbine. Koopmann *et al.*² and Neise and Koopmann^{3,4} were able to actively control the tonal emissions from a centrifugal blower operating in a duct, while Mendat *et al.*⁵ achieved active attenuation of the random noise components as well. Felli *et al.*⁶ demonstrated active blower noise control in a duct while using the reciprocal characteristics of a loudspeaker to permit replacement of the more conventional microphone error sensor by a loudspeaker. Ducted propeller or blower ANC is relatively straightforward to accomplish for the plane-wave propagating pressure components due to their one-dimensional nature. To actively cancel higher-order duct modes requires an array of synchronously phased antinoise sources in the duct.^{3,4} Sutliff and Nagel⁷ have also made progress at doing this for a ducted propeller through use of a feedforward ANC algorithm that uses a rotor blade position sensor as a reference.

Studies of active noise control for fans situated in the

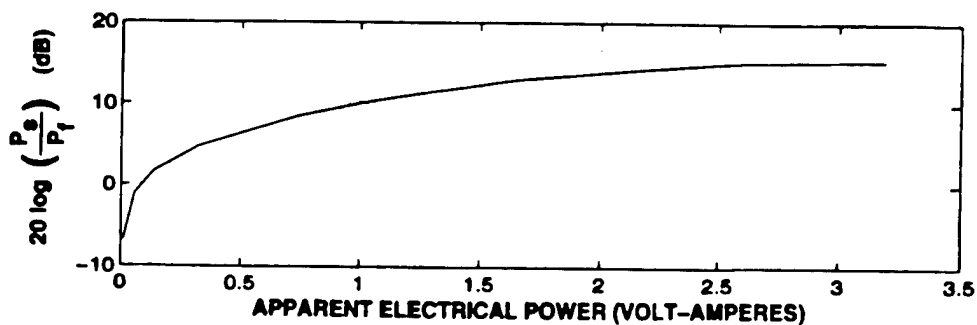


FIG. 1. On-axis far-field sound-pressure level from the shaken fan unit relative to the BPF tonal sound-pressure level radiated by the same fan in free-delivery operation. The independent variable is the apparent electrical power supplied to the mechanical shaker.

open field or in baffles are not numerous. Quinlan⁸ was successful in reducing the blade-passage tones of an axial-flow cooling fan mounted in a planar rigid baffle. Located next to the fan in the baffle was the antinoise loudspeaker. The baffle apparently tends to bring the fan directivity into axial symmetry and makes it more uniform. With the antinoise source and baffled (compact) fan noise source having similar directivities, global far-field noise reduction of 10 dB was achieved for the first two harmonics of the blade-passage frequency components.

The goal of the research presented in this paper is to investigate the use of the fan itself as an antinoise source in the active control of the tonal emissions from an acoustically compact, baffled, axial-flow fan. Chiu *et al.*⁹ used coherence function measurements between a small, fan-mounted force sensor and a far-field microphone to show that the radiation at the first several harmonics of the BPF was due entirely to the total integrated (over the plane of the rotor) unsteady rotor force. This result suggests that the appropriate antinoise actuator in ANC schemes for compact fans should be a mechanical shaker, or similar device that can generate controlled unsteady forces on the primary source. Furthermore, a shaken fan secondary source, if acoustically efficient, would be collocated with the primary aerodynamic fan noise sources which would be a significant advantage in global noise control where directivity issues are of concern. In the experiments described below, we use a small, commercially available electronic cooling fan as the primary fan noise source. It is mounted directly to an electrodynamic shaker and the entire assembly is mounted in a rigid planar baffle. A feedforward ANC algorithm is used to control the shaker so that global cancellation of the far-field tonal fan noise emissions is achieved. A tachometer provides the reference signal for the algorithm, which consists of a pulse for each blade passage, and a microphone is used to supply the error signal. A feasibility study is also described that provides information on the efficiency of a shaken fan as an acoustic radiator.

I. FEASIBILITY OF USING SHAKEN FAN AS ANTINOISE SOURCE

A basic issue that needs to be addressed in the determination of whether or not a particular fan unit can be successfully implemented in the proposed ANC scheme is whether the shaken fan unit produces substantial acoustic radiation for a reasonable power input to the shaker. Another issue to

be addressed is the fan noise directivity. It is desirable to have the directivity patterns of the primary and secondary sources identical. These issues are addressed experimentally for a given fan unit.

A. Shaken fan feasibility tests

Experiments involving shaker-induced radiation from the fan unit were conducted in the flow-through anechoic chamber¹⁰ located at the Applied Research Laboratory of Penn State University. A Nidec, 82-mm-diam plastic fan was fitted with an aluminum disk on the back of its frame, which allowed for connection to a Wilcoxon, Type F3 electromagnetic shaker via a stinger which was fabricated from stainless-steel rod. The stinger was aligned along the axis of fan rotation. The shaker/fan assembly was mounted to a rigid stand such that the fan axis was vertical. Tests were conducted with the stand isolated above the anechoic wedges; the fan was unbaffled. The effect of the fan flow field on the radiation from the shaken fan unit was investigated by simply operating the fan simultaneously with the shaker.

A B&K Type 4136 microphone (1/4-in.) was suspended 1 m above the fan blades on the inlet side; its signal was analyzed on an HP 35 665A spectrum analyzer. In order to calculate the apparent electrical power¹¹ consumed by the shaker, a voltmeter was placed in parallel and an ammeter in series with the electrical connections to the shaker. For certain tests the fan was swiveled 180° to reverse the direction of airflow.

The fan was shaken at 264 Hz which is its free-delivery fundamental BPF. Figure 1 shows the measured on-axis acoustic pressure (p_s) at 1 m as a function of the apparent electrical power supplied to the shaker. Here, the dB level is referenced to the on-axis acoustic pressure (p_f , also at 1 m) which is produced by the normal free-delivery operation of the fan at the BPF (while the shaker was off). It is seen that the shaken fan radiation matches the pressure amplitude generated by the aerodynamic fan noise mechanisms when approximately 0.1 W of apparent power is supplied to the shaker. Figure 1 also demonstrates that with a sufficient supply of electrical power, the acoustic pressure response from the shaken Nidec fan can produce much greater acoustic pressures than the fan in operation. These results suggest that the shaken fan can act as a crude loudspeaker and is hence capable of serving as the antinoise source in ANC applications.

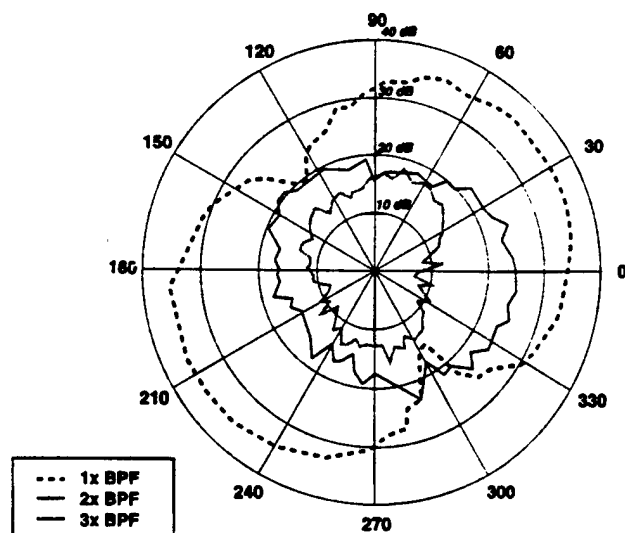


FIG. 2. Far-field directivity patterns for the unbaffled fan radiation at the first three harmonics of the BPF. The 90° axis corresponds to the fan axis on the inlet side.

Additional data of the type shown in Fig. 1 have been obtained for off-axis positions of the microphone, the fan, and shaker in operation at the same time, and again with the flow direction reversed.^{12,13} In all of these situations the shaken fan was found to create sufficient acoustic energy to warrant its use as an antinoise source. However, it was observed that when the flow from the fan was reversed and directed toward the microphone (which was 1-m away and uninfluenced by the flow), the shaken fan acoustic pressure amplitude was about 2 dB less than the case when the flow was away from the microphone. This is explained as a change in radiation impedance due to flow. An analysis by Muehleisen¹⁴ has predicted this level of change for the typical mean flow velocity of this fan.

B. Fan directivity characteristics

Unbaffled axial flow fan units are reported to produce skewed directivity patterns.⁸ A nonsymmetric fan directivity pattern would suggest that complicated ways of shaking the fan would be necessary in order to most effectively cancel the fan noise. Radiation patterns for the type of fan units considered here are measured under unbaffled and baffled conditions in order to obtain knowledge about the source type and to determine the effect of the baffle on the radiation pattern. All directivity patterns were measured at 1 m from the fan in the free field. A movable microphone boom provided measurements in increments of 5°. The unbaffled directivity patterns for the first three harmonics of the BPF of the Nidec fan are shown in Fig. 2. In order to obtain results which were repeatable within ± 1.5 dB, each data point required 300 spectral averages over a frequency bandwidth of 1.6 kHz. The sampling rate was 4096 Hz. It is clear from the results shown on this figure that the unbaffled fan has complicated directivity characteristics. The pattern for the first harmonic could be interpreted as dipolelike, but it is skewed off-axis by some 60°. The patterns for the second and third

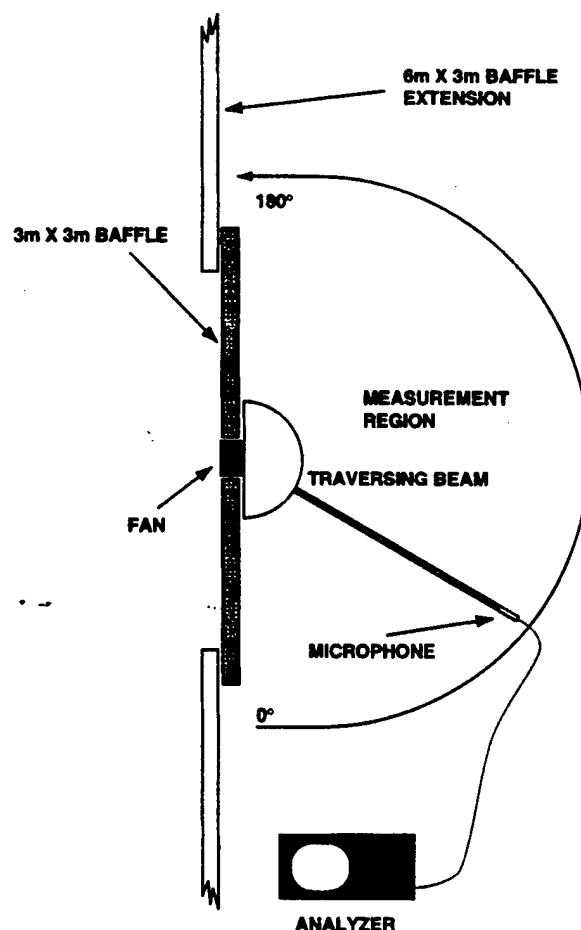


FIG. 3. Sketch of the experimental setup for measuring baffled fan directivity patterns.

harmonics cannot be interpreted in terms of simple dipole radiation patterns. These results are very consistent with those reported by Quinlan⁸ for a different but similar fan. The reason for the skewness is not known precisely, but it may be a result of asymmetries in the fan construction that result in peak aerodynamic forces being directed off-axis.

When the acoustically compact fan unit is shaken as described above, one would expect dipole directivity of the sound pressure with an on-axis peak. Placement of the fan in a baffle, such as that depicted schematically in Fig. 3, would transform the dipole source directivities into monopole directivities. Figure 4 shows the baffled fan directivity patterns measured on the inlet side of the fan. The patterns are clearly more uniform than in the unbaffled case, which is favorable from the ANC viewpoint. The directivity patterns on the outlet side of the fan were measured also¹³ and found to be nearly identical to those shown in Fig. 4. These experimental results confirm the findings of Quinlan.⁸ They indicate that baffled fan ANC should be simpler to achieve than unbaffled fan ANC when the secondary source is of the dipole type (loudspeaker or shaken fan unit) and located in the planar baffle containing the fan.

II. EXPERIMENTAL ACTIVE FAN NOISE CONTROL

An experiment is constructed to demonstrate reduction in tonal noise from an axial-flow fan in which the fan is

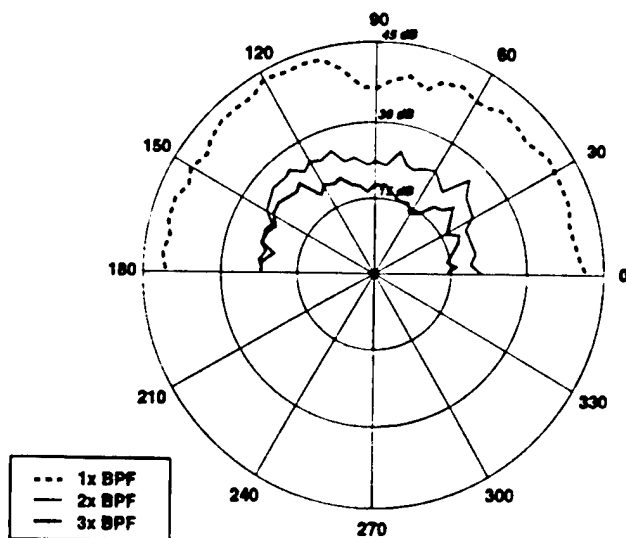


FIG. 4. Far-field directivity patterns for the baffled fan radiation from the inlet side at the first three harmonics of the BPF.

shaken to produce antisound. A Filtered-X control algorithm^{15,16} is implemented and responds only to the tonal components in the fan spectrum for this experiment. The Filtered-X algorithm is a feedforward algorithm that uses an independent reference signal related to the tones of the primary source. Because the tones of interest are the harmonics of the BPF, a simple optical-type tachometer is used for the reference.

A. Experimental setup

Elements of the Filtered-X active noise control experimental setup are shown schematically in Fig. 5. In this sys-

tem, the primary noise is the noise generated by the fan in operation and the secondary noise is the acoustic signal produced by the shaken fan. The error signal is the electrical output of a microphone placed on the inlet side of the fan unit, and an independent reference signal is provided by the optical tachometer. The optical sensor is placed above the fan and is sensitive to the passing of reflective strips located on the leading edge of each blade. The signal from the sensor is coherent at the BPF in addition to the higher harmonics because the voltage pulse is rectangular in shape; the Fourier transform of these periodic pulses produces a harmonic train. The optical sensor is insensitive to the motion of the axially shaken fan because the reflective strips, which the optical sensor monitors, pass orthogonally to the axis of the fan. An independent reference signal for the controller is therefore produced by the optical sensor.

The height of the error microphone above the fan unit was typically a fan diameter or more and was often moved to verify noise cancellation observations. The seven-bladed fan was mounted in a plywood baffle such that its inlet side was flush to the surface of the baffle. The gap between the fan housing and the baffle was 5 mm such that the housing was not in physical contact with the baffle. The fan was supported completely by the Wilcoxon shaker which was rigidly mounted to a platform located underneath the baffle. A small cylindrical rod was placed across the center of the fan at an axial distance of approximately $0.1R$ from the fan hub, where R is the fan blade tip radius. This distance is close enough to cause an increase in the tonal fan noise components due to the wake of the obstruction.¹⁷ Enhancement of the BPF tones by operating the fan in a time-invariant, non-uniform inflow field seems appropriate because most practical installations result in such an inflow. The experiment was

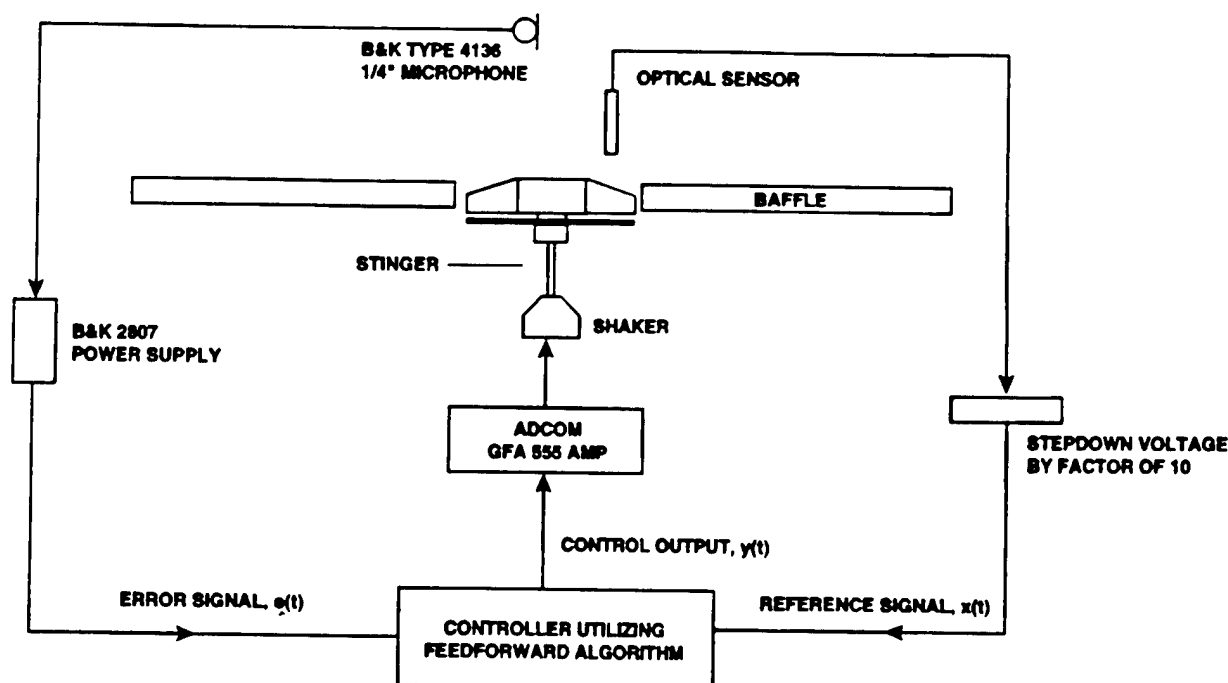


FIG. 5. Sketch of the experimental setup used to demonstrate active fan noise control.

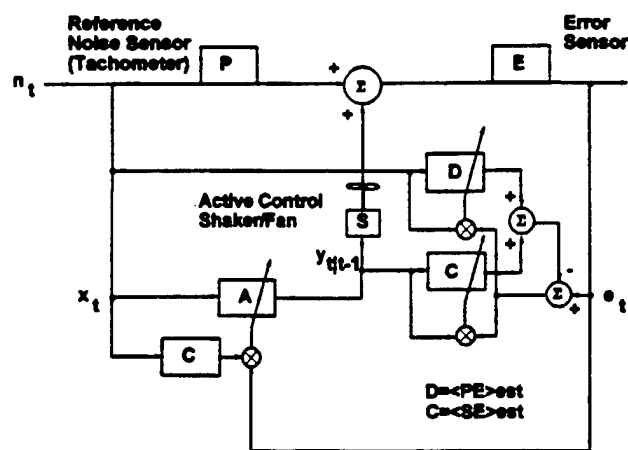


FIG. 6. Filtered-X adaptive noise cancellation block diagram used for axial fan noise reduction.

conducted in the anechoic chamber described in Sec. I A, with acoustic spectral analysis being performed using the same HP analyzer. Sound power measurements followed standard procedure.¹⁸

B. Control algorithm

Figure 6 presents a block diagram representing the signal processing and control for the active fan noise controller using a Filtered-X algorithm.¹⁵ The reference signal x_t is generated by the optical sensor described in Sec. II A. The Fourier transform of the reference signal pulse train reveals exactly the same harmonic frequencies as the tonal acoustic noise generated by the fan. The block P in Fig. 6 represents the transfer function relating the magnitude and phase of the reference signal pulse train to that for the acoustic noise at the fan location. The block S represents the transfer function for the shaker/fan assembly relating the electrical input $y_{t/t-1}$ to the acoustic response at the fan location. The block E represents the transfer function of the error sensor where the input is the acoustic noise in the near field of the fan, and the output is the electrical response of the microphone to this field. Clearly, if the adaptive control filter A adapts to a transfer function approximating $-P/S$, the vibrations of the shaker/fan assembly and the unsteady forces of the blades are superimposing in a way which suppresses the radiated acoustic tonal noise. This is because the reference signal only contains harmonics coherent with the tonal acoustic noise.

We chose a passive system identification strategy¹⁶ for the adaptive controller because we do not wish to risk increasing the broadband noise of the actively controlled fan. For the reference signal to be properly correlated to the error signal in the adaptive least-mean-square (LMS) algorithm for the controller A, we must filter x_t by the transfer function represented by the product SE, where the output is the electrical signal from the error microphone and the input is the electrical control signal to the shaker/fan assembly. The C adaptive block in Fig. 6 models the SE transfer function and the D adaptive block models the PE transfer function at the frequencies present in the reference signal x_t and the control output signal $y_{t/t-1}$. The notation $y_{t/t-1}$ depicts the fact that

the digital control signal at the shaker at time t was generated by the adaptive filter last updated at time $t-1$. This delay is important physically as it indicates an unavoidable linear phase component in the SE transfer function. If the filter model C has the proper phase response at the reference signal frequencies, the Filtered-X should converge without difficulty. It is necessary to update the three LMS filters D, C, and A in real time due to the changing transfer function responses in a real fan noise application.

To insure C has the correct phase, a second system identification filter D is used to model the forward PE. The sum of the outputs of the forward model D and error model C give a prediction of the error signal e_t . The difference between the true error signal from the microphone and the prediction of the error signal is used to update the two LMS filters used in the passive system identification. Its operation is self-correcting as long as a reference signal x_t and a control signal $y_{t/t-1}$ are present (i.e., both signals are nonzero). If the control output is low, then the error signal is dominated by the forward plant and D is a good match to PE, allowing C to model SE with the residual. Conversely, if the control output is exceedingly high, the error signal is dominated by the SE loop allowing C to closely model the error plant and D to model PE with the residual. If the error signal becomes quite small (the goal of the ANC system), all of the adaptive filters slow down and converge on the desired result. Passive on-line system identification is important to axial fan ANC because flow rates and the corresponding plant time delays are always changing and the addition of broadband noise is unacceptable. It is noted that SE is the transfer function defined as the response of the error sensor when a white noise input signal to the shaker amplifier is applied in the absence of a primary excitation signal. Figure 7 shows the magnitude and phase of this function determined experimentally. The linear phase response is expected for a simple delay path associated with acoustic propagation from the fan to the error sensor.

A numerical simulation of the operations depicted in Figs. 5 and 6 has been carried out.¹³ The results indicate that the algorithm of Fig. 6 operates only on causal, periodic signals. Discrete-frequency noise was thus canceled completely in the simulations. The simulation also included broadband random components of primary noise, but these were not canceled by the Filtered-X algorithm because they simply were not part of the tachometer reference signal. If a microphone reference sensor was used, rather than the tachometer, the broadband noise detected at the fan would very likely have low coherence with the far-field acoustic broadband noise due to localized turbulent flow noise at the reference position which would not be present at the far-field position. A method for suppressing local turbulent pressure fluctuations on a microphone in a flow field has recently been demonstrated,¹⁹ but was not used in the subject investigation.

For the active fan noise control experiments, the Filtered-X algorithm was programmed in C on a WE-DSP32C floating-point digital signal processing board which was installed in an IBM PC equipped with an Intel 486DX processor operating at 33 MHz with a Windows 3.1 real-time

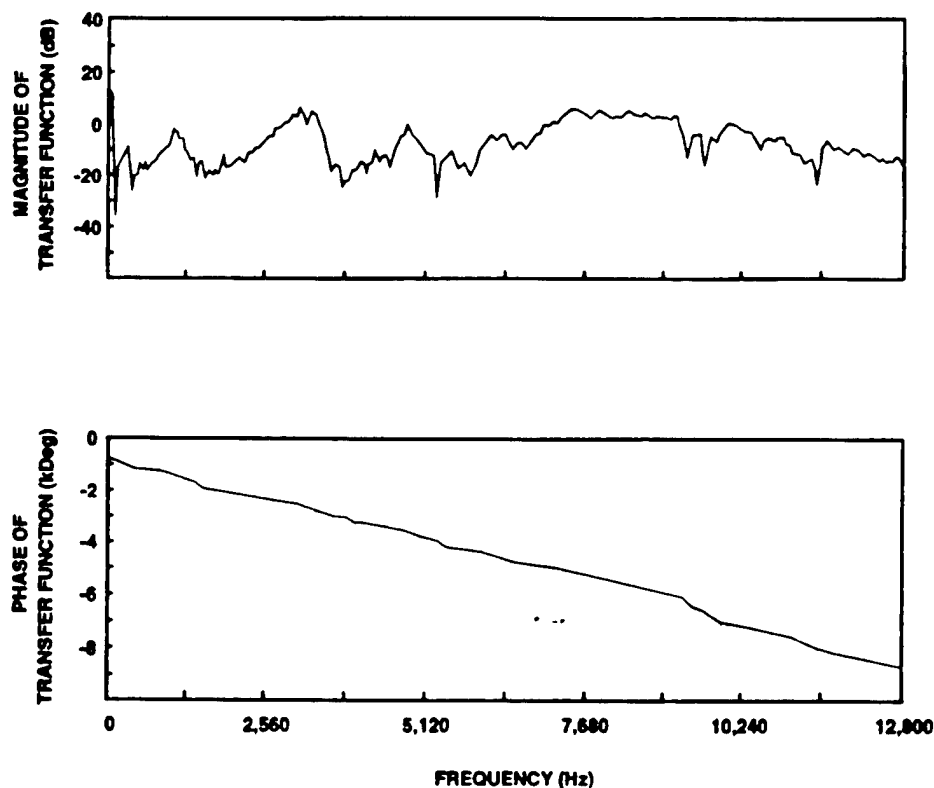


FIG. 7. Frequency response characteristics of the measured error path defined by the ratio of the Fourier transform of the input to the shaker-to-the Fourier transform of the microphone output.

user interface, also written in C. The sample rate of the controller was selected to be 2 kHz and 24 dB/octave low-pass filters were set at 900 Hz and placed at the pre-A/D and post-A/D stages of the digital signal processing board. Twenty taps (coefficients) with a step size of 0.0005 were selected for the adaptive control filter. Ten taps with a step size of 0.04 were selected for the error plant SE and ten taps with a step size of .05 were selected for the forward plant PE. On-line passive identification of the error plant (being the path representing the input to the shaker amplifier-to-the output of the error sensor) was executed in real time with the adaptive control. Using the largest step size for the D filter (in Fig. 6) modeling PE allows it to converge fastest, followed by C which models SE, and then finally the A adaptive filter, which converges to a transfer function approximating -P/S at the frequencies of the tachometer reference signal.

C. Results

Typical sound-pressure level spectra for the error sensor microphone with and without the controller on are presented in Fig. 8. The error microphone was situated approximately 19 cm above one edge of the fan frame on the inlet side. The amount of cancellation achieved at the third and higher harmonics of the BPF was found to be sensitive to the actual location of the error sensor. This is expected because the baffled fan directivity patterns become less uniform at higher harmonics of the BPF. Comparing the two spectra in Fig. 8 reveals a 20-dB reduction of the fundamental BPF tone, while the second and third harmonic levels are reduced by 15

and 8 dB, respectively. A frequency at approximately 980 Hz is also reduced. This component is related to the shaft rotation speed of 40.57 Hz and is perhaps due to a mechanical resonance of the fan unit. The fourth harmonic of the BPF at 1.136 kHz shows an 8-dB increase with the controller on. This is suspected to be due to aliasing because the low-pass filters used in the digital signal processing board were set at 900 Hz, the sampling Nyquist frequency was 1 kHz, and the 24 dB/octave filter roll-off may not be sufficient to prevent a residual component from entering the presented spectra.

The sound power radiated by the fan with and without the controller on was measured using a standard 12-point measurement procedure¹⁸ on the inlet side of the fan over the baffle. A hemispherical surface, 0.5 m in diameter was used. Figure 9 shows the reduction in sound power level (which is indicative of global noise reduction) with the controller on as a function of frequency. The sound power at the fundamental and second harmonic BPF tones is reduced by 13 dB and 8 dB, respectively.

The sound power level reduction is some 6 or 7 dB less than the reduction in sound-pressure level measured at the error microphone location. This observation can be explained from the directivity patterns presented in Fig. 10. These patterns were measured over the baffled fan on the inlet side at the BPF, with and without the controller on. The effect of the small cylinder placed in front of the fan is evident in the "control off" pattern when compared to the unobstructed case of Fig. 4. The obstruction causes an approximate 10-dB increase in sound-pressure level over most observation positions. Figure 10 reveals a null in the direc-

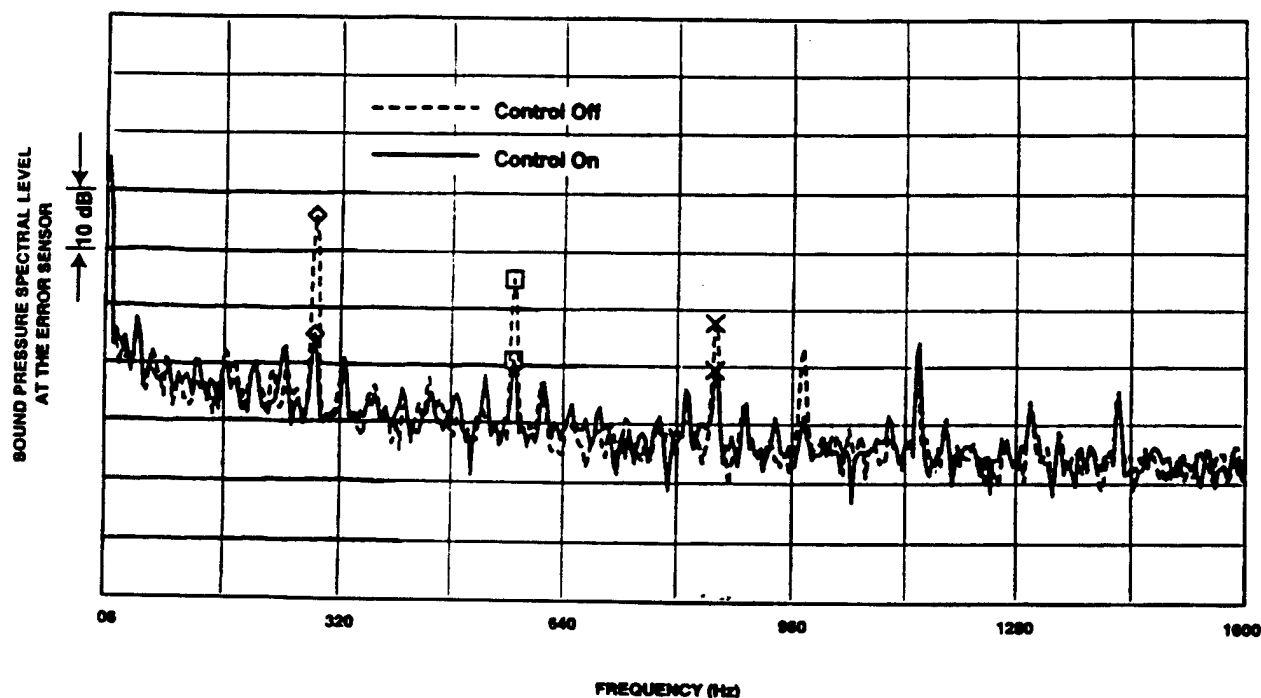


FIG. 8. Spectra of the fan sound-pressure level sensed at the error sensor position when the controller is on and off. A small cylindrical flow obstruction was placed near the fan inlet during these experiments, and the sensor is approximately 19 cm away from the edge of the fan frame, normal to the baffle.

tivity pattern along the fan axis when the control is in operation. This null clearly shows that the axial radiation is almost completely canceled by the applied axial force. Sound radiation reduction at 0° and 180° is of the order 10 dB. Obviously, these directions are less influenced by the secondary source because of its axial dipole characteristics. The error sensor was placed near the axis of the fan, so it was in the

null region of the "control on" directivity pattern. The sound-pressure reductions are very large in this region relative to all other angular positions. This is the apparent cause of the sound power reductions being less than the sound-pressure reductions.

Additional noise reduction measurements were performed with the error microphone located on the opposite

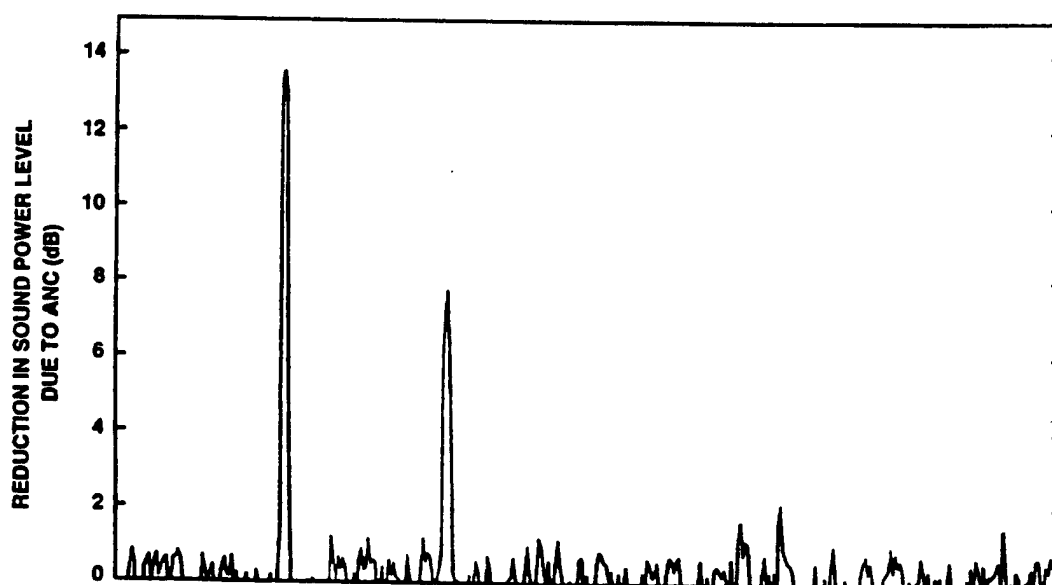


FIG. 9. Reduction in baffled axial-flow fan sound power level in dB as a function of frequency achieved using the active noise control procedures described in this paper.

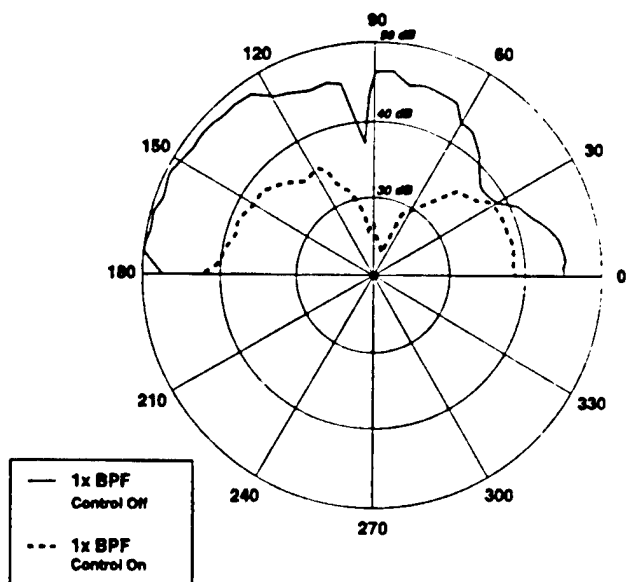


FIG. 10. Sound-pressure level directivity patterns measured for the baffled fan with the small flow obstruction in place, with and without the ANC in operation.

side of the baffle (outlet side) along with a remote microphone located anywhere from 0.4 to 1.0 m away from the fan.¹³ Again, the sound-pressure level at first two harmonics of the BPF was found to be reduced by 6 or more dB at the remote (and error) microphone positions. Sound power was not measured on this side of the baffle because of the proximity of the apparatus to the hard reflecting floor of the hemi-anechoic chamber.

As one last experiment to explore the potential applicability of the subject methodology, an empty desktop computer cabinet was placed on the planar baffle over the fan. In this arrangement, the fan pulled air into the cabinet. The air exited through the opposite side of the baffle. The error microphone was placed inside the cabinet approximately 10 cm away from the fan, and slightly off-axis. A remote microphone was positioned outside the cabinet 1 m away from the fan and 0.5 m above the baffle. Figure 11 shows the results for this experiment. The sound pressure level at the BPF is seen to be reduced by 21 dB at the external (remote) position, and by 26 dB at the internal (error microphone) position. Tone level reductions for the second harmonic are 10 and 17 dB, respectively. Sound power was not measured for the cabinet configuration, but is the subject of future applied research. The results of Fig. 11 suggest that the active noise control method employed in this study has the potential for success in a typical cooling fan application.

III. CONCLUSIONS

Although previously published research has shown that the tonal emissions from fans can be reduced through various active noise control strategies, the current research is the first to show that the fan itself, if shaken adaptively, can act as the antinnoise source. This is a very significant finding because the need for a separate, secondary source is eliminated. Un-

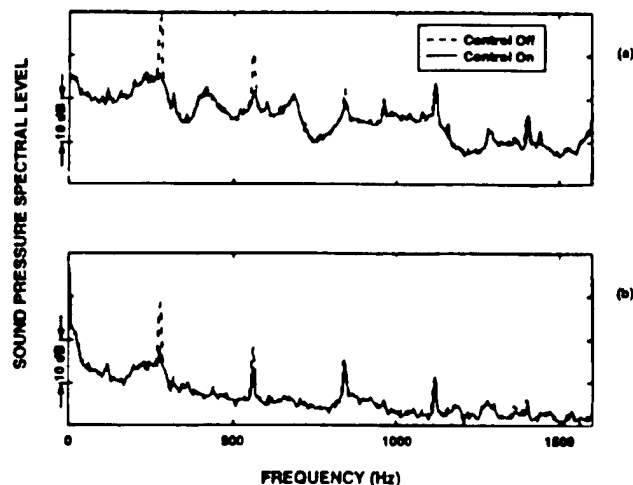


FIG. 11. Spectra of the sound pressure measured with and without the ANC in operation for the baffled fan operating inside a desktop computer cabinet: (a) the error sensor spectra measured inside the cabinet, and (b) the spectra measured at a remote location outside the cabinet.

der the conditions of aeroacoustic compactness, the shaken fan (the secondary source) is collocated with the primary fan noise source. This tightly coupled configuration produces the excellent global noise reduction reported, and also leads to the possibility of analog feedback control strategies. This may possibly permit random noise components of the fan noise radiation spectrum, in addition to the tonal components, to be reduced. With either feedback or feedforward control, and under the premise that unsteady forces are the mechanism of subsonic fan sound production, it would be a straightforward extension of the subject methodology to utilize an internal unsteady force sensor²⁰ as the error sensor. Future efforts also include shaking the rotor only as opposed to shaking the entire fan assembly as was done here. Other possible modifications include multiple shakers either on individual fan blades or located at fan frame mounting lugs to aid in high-frequency cancellation when the directivity characteristics are nonuniform, and when the aeroacoustic compactness assumption is no longer valid.

ACKNOWLEDGMENTS

This work has been supported by the IBM Corp. Shared University Research Program. Dr. David Yeager, project monitor. The continuous support of the Applied Research Laboratory at Penn State University is also gratefully acknowledged.

¹J. E. Ffowcs Williams, "The silent noise of a gas turbine," *Brit. Sci. News* 175, 9-12 (1981).

²G. H. Koopmann, W. Neise, and W. Chen, "Active noise control to reduce the blade tone noise of centrifugal fans," *J. Vib. Acoust. Stress Relia. Des.* 110, 377-383 (1988).

³W. Neise and G. H. Koopmann, "Active source cancellation of the blade tone fundamental and harmonics in centrifugal fans," *Proc. InterNoise 88*, Avignon, France (Noise Control Foundation, Poughkeepsie, NY, 1988), pp. 801-804.

⁴W. Neise and G. H. Koopmann, "Active sources in the cutoff of centrifugal suction fans to reduce the blade tones at higher-order duct mode frequencies," *J. Vib. Acoust.* 113, 123-131 (1991).

⁵D. P. Mendat, K. H. Eghtesadi, M. P. McLoughlin, D. G. Smith, and E.

- W. Ziegler, Jr., "Active control of centrifugal fan noise," Proc. Fan Noise, an International INCE Symposium, Senlis, France (Noise Control Foundation, Poughkeepsie, NY, 1992), pp. 455-462.
- ⁶M. Felli, F. Cotana, and L. Santaripa, "A loudspeaker sensor for active fan noise control: An experimental facility," Proc. Fan Noise, an International INCE Symposium, Senlis, France (Noise Control Foundation, Poughkeepsie, NY, 1992), pp. 471-474.
- ⁷D. L. Sutliff and R. T. Nagel, "Active control of far-field noise from a ducted propeller," AIAA J. 33, 231-236 (1995).
- ⁸D. A. Quinlan, "Application of active control to axial flow fans," Noise Control Eng. J. 39, 95-101 (1992).
- ⁹W.-S. Chiu, G. C. Lauchle, and D. E. Thompson, "Subsonic axial flow fan noise and unsteady rotor force," J. Acoust. Soc. Am. 85, 641-647 (1989).
- ¹⁰R. C. Marboe, G. C. Lauchle, and W. A. Kargus IV, "Quiet wall jet facility for basic aero/hydroacoustics research," in ASME Publication NCA Vol. 10, *Hydroacoustic Facilities, Instrumentation, and Experimental Techniques*, edited by T. M. Farabee and R. E. Arndt (ASME, New York, 1991), pp. 69-73.
- ¹¹W. H. Hayt and J. E. Kemmerly, *Engineering Circuit Analysis* (McGraw-Hill, New York, 1986), 4th ed., pp. 297-301.
- ¹²J. MacGillivray and G. C. Lauchle, "Active control of axial flow fan noise," Proc. Noise-Con 94, Fort Lauderdale, FL (Noise Control Foundation, Poughkeepsie, NY, 1994), pp. 71-76.
- ¹³J. R. McGillivray, "Active control of discrete-frequency noise from small subsonic fans," MS thesis, Penn State University, 1996.
- ¹⁴R. Muchleisen, "Reflection, radiation, and coupling of higher order modes at discontinuities in finite length rigid walled rectangular ducts," Ph.D. thesis, Penn State University, 1996.
- ¹⁵P. A. Nelson and S. J. Elliott, *Active Control of Sound* (Academic, San Diego, 1992), pp. 172-175, 195-198.
- ¹⁶S. D. Sommerfeldt and J. Tichy, "Active control of a two-stage vibration isolation mount," J. Acoust. Soc. Am. 88, 938-944 (1990).
- ¹⁷K. B. Washburn and G. C. Lauchle, "Inlet flow conditions and tonal sound radiation from a subsonic fan," Noise Control Eng. J. 31, 101-110 (1988).
- ¹⁸D. A. Bies and C. H. Hansen, *Engineering Noise Control* (Unwin Hyman, London, 1988), pp. 135-139.
- ¹⁹R. S. McGuinn, G. C. Lauchle, and D. C. Swanson, "A low flow-noise microphone for active noise control applications," AIAA J. (to be published).
- ²⁰An internally mounted fan unsteady force sensor has been developed, successfully evaluated, and reported in Ref. 9.

APPENDIX 53

Low Flow-Noise Microphone for Active Noise Control Applications

R. S. McGuinn,* G. C. Lauchle,[†] and D. C. Swanson[‡]
Pennsylvania State University, University Park, Pennsylvania 16802

A method that couples output from a hot-wire anemometer with that of a microphone to reduce flow-induced pseudonoise from the microphone signal was developed. In these experiments, a microphone and a hot-wire sensor were placed in a well-defined low-speed turbulent flow in a rectangular duct. Controlled acoustic noise, both random and time harmonic, was superimposed on the flow noise by placing a speaker source close to the entrance of the duct. Detailed studies of the coherence between the hot-wire and microphone signals in the presence of flow and acoustic noise indicated that the proper combination of the two signals could reduce the turbulence noise contamination in the microphone signal. Subsequent tests demonstrated that using an adaptive least-mean-square algorithm to filter the hot-wire signal before subtracting it from the microphone signal produced broadband flow noise attenuation on the order of 20 dB at frequencies below 100 Hz and spectra that approached those of the uncontaminated microphone signal. Moreover, the resulting "hot-mic" signal retains the acoustic pressure of interest, making it an ideal sensor for use in active noise control applications where the sensing or error microphone must be placed in a flowfield.

Nomenclature

c	= filtered hot-wire signal
d_h	= hydraulic diameter
$E\{\}$	= expectation operator
err	= error signal
f	= frequency, Hz
$\hat{G}_{xx}(f)$	= autospectral density estimate
H	= Fourier transform of h
h	= filter impulse response
M	= Fourier transform of m
m	= microphone signal
N	= number of filter coefficients
n_d	= number of ensemble averages
p	= pressure
u	= velocity
W	= Fourier transform of w
w	= hot-wire signal
x	= spatial direction
γ^2	= ordinary coherence function
ϵ_r	= random error
μ	= convergence coefficient, fluid viscosity
ρ	= fluid density

Introduction

MANY active noise control problems involve placing a sensing microphone, error microphone, or both in a flow. One such example is the active control of fan noise in an air conditioning duct. A microphone placed in a flow senses aerodynamic pressure fluctuations (pseudonoise) as well as acoustic pressure fluctuations. Because the microphone senses these fluctuations simultaneously, the active control system will try to cancel the flow-induced noise as well as the actual noise. However, the directly radiated noise due to turbulent pressure fluctuations is much smaller than the pseudonoise

imposed by them on a microphone, and the phase speeds of the two different types of pressure fluctuations are also considerably different. As a result, active cancellation of the flow noise is not accomplished. Instead, the level of the pseudo-pressure fluctuations imposes a limit below which active acoustic attenuation cannot be achieved.¹⁻³ Consequently, removing the flow noise from the microphone signal, with minimal loss of amplitude or phase information of the acoustic noise, is important for active noise control applications.

Methods for eliminating flow noise from a microphone signal include placement of an open-cell foam ball or a streamlined nose cone over the microphone diaphragm, incorporation of a bias error correction in the estimate of the pressure spectrum,⁴ or spatial averaging using data processing techniques such as the cross spectral density, correlation function, coherence function, or transfer function between two or more microphones spaced beyond the turbulence correlation length.⁵⁻⁸ The drawbacks of the preceding methods include, respectively, too much flow blockage, loss of phase information of the pressure, or too little turbulence suppression. These issues make them undesirable or useless for active noise control applications. Methods that do not result in loss of the pressure data include the use of transducers large enough to average out the turbulent fluctuations,⁹ transducer arrays,¹⁰ and sampling or slit tubes.¹¹⁻¹⁵ These techniques may result, however, in undesirable pressure attenuation, additional expense, or increased length (volume) requirements. Using a slit tube in conjunction with the microphone, a means of turbulence noise suppression currently used in some active noise control applications provides little or no flow noise attenuation for frequencies less than 70 Hz (Ref. 16) and requires a longer sensing length than typically desired.

Objective

The objective of this research is to remove flow noise from the microphone signal with minimal loss of phase or amplitude of the acoustic pressure signal of interest while maintaining minimum impact on sensor space requirements. In particular, the emphasis for flow noise reduction is placed on the frequency range $f < 100$ Hz. In this investigation flow noise attenuation is performed by combining the response of the microphone with a signal from a hot-wire sensor placed in the same flow. Although the purpose of this research is to devise a low flow-noise microphone that functions well under the restrictive requirements of the active noise control application, active noise control, per se, is not discussed in detail. In addition, no attempt is made to optimize the adaptive algorithms.

Received March 15, 1996; presented as Paper 96-1784 at the AIAA/CEAS 2nd Joint Aeroacoustics Conference, State College, PA, May 6-8, 1996; revision received Sept. 9, 1996; accepted for publication Sept. 20, 1996; also published in *AIAA Journal on Disc*, Volume 2, Number 2. Copyright © 1996 by the American Institute of Aeronautics and Astronautics, Inc. All rights reserved.

*Graduate Student, Department of Aerospace Engineering, Student Member AIAA.

[†]Professor of Acoustics, Graduate Program in Acoustics and Applied Research Laboratory, Member AIAA.

[‡]Professor of Acoustics, Graduate Program in Acoustics and Applied Research Laboratory.

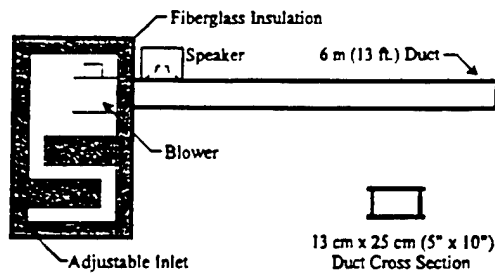


Fig. 1 Rectangular duct test facility.

Experimental Setup

Experiments were performed in a $0.25 \times 0.13 \times 4$ m ($0.8 \times 0.4 \times 13$ ft) rectangular duct, illustrated in Fig. 1, with airflow provided by a variable speed centrifugal blower. A hot-wire probe and a microphone were mounted on a support stand on the centerline at the exit of the duct where the flow conditions, mean velocity equal to 7 m/s (23 ft/s) and turbulence intensity of 10%, approximated those expected in a typical active noise control application. A signal generator provided a random or time-harmonic output that was amplified and used to drive a speaker mounted in the top section of the duct near the exit of the blower.

A single-sensor hot-wire probe 0.005 mm (0.0002 in.) in diameter with a sensing length of 1.5 mm (0.06 in.) was used to measure velocity. Acoustic measurements were obtained with a pinhole microphone¹⁷ consisting of a 12.7-mm (1/2-in.) free-field condenser microphone with a streamlined 0.8-mm (1/32-in.) inner diameter pinhole/tube nose cone instead of the standard protective grid. The pinhole nose cone provided a more streamlined surface than the standard protective grid and also greatly reduced the sensing area to better approximate a "point" measurement. The resonance frequency of the pinhole cavity was approximately 1200 Hz, above the frequencies of interest in this study.

Data were acquired using a fast Fourier transform analyzer and simultaneous time capture to a computer hard drive at a sampling rate of 2048 samples/s. Spectral analysis employed antialias filtering and a Hanning window. There is no bias error from spectra to spectra because the sampling rate and analysis bandwidth (2 Hz) remained the same for all samples. The random error, also the same for all cases, can be computed from¹⁸

$$\varepsilon_r[\hat{G}_{xx}(f)] = 1/\sqrt{n_d} \quad (1)$$

where the number of ensemble averages $n_d = 100$. Both the hot-wire and microphone spectral data were repeatable to within 1 dB for each condition tested, which is consistent with the estimated random error of 10%.

Results and Discussion

Coherence

The pressure-velocity relationship for low-speed incompressible flow can be derived by combining the divergence of the momentum equation with the continuity equation to yield Poisson's equation,¹⁹

$$\nabla^2 p = -\rho \frac{\partial^2 (u_i u_j)}{\partial x_i \partial x_j} \quad (2)$$

Solution of Eq. (2) reveals that pressure fluctuations at a given point result from an integration of weighted velocity fluctuations over all space.

A hot-wire sensor provides a measure of velocity fluctuations but it does so over only a small and finite length. In addition, a hot-wire signal is proportional to the square root of velocity.²⁰ For the low-speed, incompressible flow of interest here, we know from Euler's equation that velocity is proportional to the square root of pressure. The output from a hot-wire anemometer is therefore a nonlinear representation of the fourth root of the local aerodynamic pressure fluctuations. A microphone, on the other hand, provides a direct and linear measure of pressure.

To determine the feasibility of using a hot wire to provide an aerodynamic pressure signal that can be combined with a microphone signal, coherence measurements between the hot-wire signal and a

signal from a nearby microphone placed in the same flowfield have been carefully examined. The ordinary coherence function between the hot-wire signal $w(t)$ and the microphone signal $m(t)$ is defined as¹⁸

$$\gamma_{wm}^2(f) = \frac{|G_{wm}(f)|^2}{G_{ww}(f) \cdot G_{mm}(f)}, \quad 0 \leq \gamma_{wm}^2(f) \leq 1 \quad (3)$$

A high coherence, $\gamma_{wm}^2(f)$ near 1, between the two signals in the presence of flow implies that both sensors are responding to similar fluid dynamic fluctuations. In such a case, properly combining the hot-wire signal with the microphone signal may lead to a reduction in the flow noise response of the microphone.

A systematic study was performed to determine the optimum configuration of the hot-wire sensor and microphone to promote high coherence between them. We know from Eq. (2) that the fluctuating pressure at a point is the result of the integrated velocity fluctuations over a much larger volume. To reduce the measurement area of the microphone and thereby reduce the area of contributing velocity fluctuations, the standard protective grid of the microphone was replaced with a pinhole nose cone as shown in Fig. 2. The pinhole diameter was 0.8 mm (1/32 in., $d = 0.005d_h$), and the tube was 2.54 cm (1 in., $l = 0.15d_h$) long. The pinhole microphone¹⁷ exhibits a slight attenuation (~ 1 dB) of the pressure but still maintains a flat frequency response except at the cavity resonance frequency. For the pinhole size used here, a comparison calibration showed the resonance frequency to be at approximately 1200 Hz, which is above the frequencies of interest in this study and does not adversely affect the pressure measurements.

Variations in the placement of the pinhole microphone and the hot-wire sensor relative to the pinhole opening were tested. It was found that the highest coherence between the hot wire and microphone occurred when the pinhole microphone was aligned with the flow with the pinhole pointing in the upstream direction as shown in Fig. 2. In this manner, it will behave like a total head probe. The microphone vent removes the effect of the mean pressure, and the resulting pressure signal is representative of fluctuating pressures traveling in the freestream direction. It therefore responds more to streamwise velocity fluctuations and mean shear rather than normal velocity shear that is dominant when the microphone is mounted flush with the duct wall, normal to the flow. When the microphone is oriented in the streamwise direction, broadband flow noise measured by the microphone is approximately 5 dB higher than that measured with the microphone normal to the flow but in the same location. The objective of the research, on the other hand, is to reduce the flow noise inherent in the microphone signal. This increase in flow noise is an issue to be concerned with and is discussed in more detail later.

The hot-wire placement was determined after tests that included streamwise and spanwise orientation (both of which, by virtue of the fact that a single sensor was used, contain transverse velocities) as well as variations in location with respect to the pinhole opening. Highest coherence levels were obtained with the hot-wire sensor placed upstream of the centerline of the pinhole and oriented to measure the streamwise velocity component. The optimum configuration is shown in Fig. 2, where the hot-wire sensor is located 0.5 mm (0.02 in.) upstream of the center of the pinhole opening. This configuration is used for all measurements reported herein.

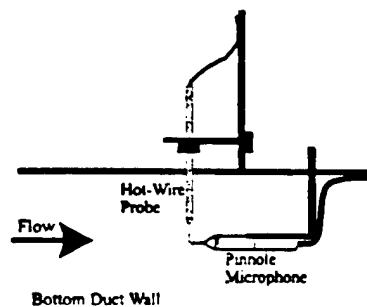


Fig. 2 Hot-wire and microphone placement in duct.

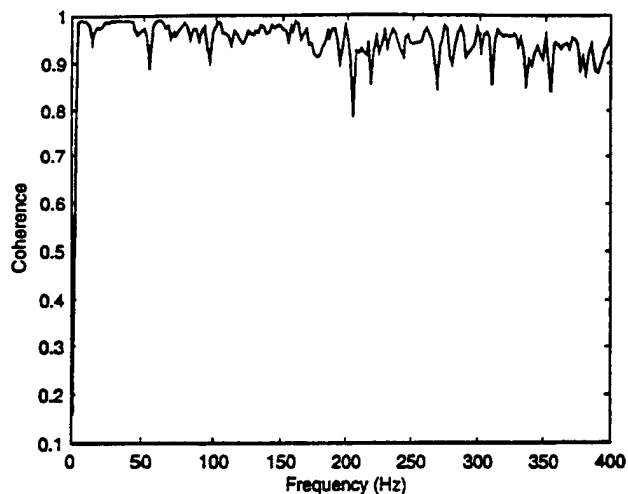


Fig. 3 Measured coherence function between hot-wire sensor and microphone in flow only.

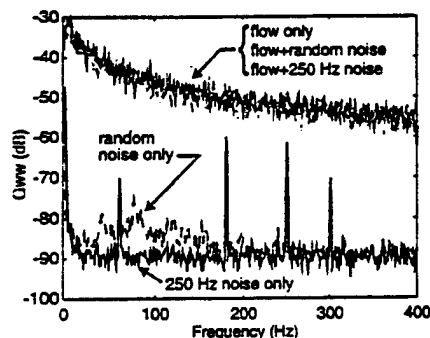


Fig. 4 Hot-wire autospectral densities.

Measurements were made to ensure that placing the hot wire just upstream of the pinhole opening of the microphone did not alter the microphone response. A comparison of the microphone response with and without the hot wire in front of the opening revealed that, for the frequency range of interest, the interference is negligible. It is expected that the hot wire does affect the microphone response at higher frequencies (the hot-wire vortex shedding frequency ~ 305 kHz based on a Strouhal number of 0.2 for cylinder vortex shedding).

The measured coherence function between the hot-wire and microphone signals when placed in the flow in the duct is shown in Fig. 3. The coherence levels are high, greater than 0.9 over the entire frequency range and approaching unity at frequencies below 100 Hz. These high levels indicate that combination of the two signals for removal of flow noise from the pressure signal is feasible.

Detailed studies of autospectral density of each sensor and the measured coherence function between them were performed with the sensors in the presence of both aerodynamic and acoustic excitation. Random and time-harmonic acoustic noise was introduced into the duct by the speaker located near the entrance of the duct (Fig. 1). The speaker output was adjusted so that the overall acoustic sound pressure level at the microphone in the duct without flow matched the overall sound pressure level perceived by the microphone placed in the same location in the duct with flow only (approximately 80 dB re: 20 μ Pa). The sinusoidal acoustic noise was generated by driving the speaker at 250 Hz. This frequency was chosen by virtue of the fact that it is below the plane wave cutoff frequency of the duct and therefore should be a plane wave disturbance. (The cut-on frequency of the first duct cross mode is approximately 650 Hz.) Furthermore, 250 Hz is not a harmonic of 60 Hz line noise.

The autospectral densities of the hot-wire and microphone responses are plotted in Figs. 4 and 5, respectively. In these and all subsequent plots, the dB scale is referenced to 1 V. The five curves in each plot represent each of the five test cases considered: flow

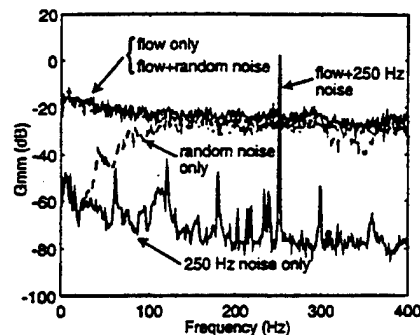


Fig. 5 Microphone autospectral densities.

only, flow + random acoustic noise (white noise), flow + 250 Hz time-harmonic acoustic noise, random noise only, and 250 Hz sine wave noise only. Reflections from the duct walls and higher-order duct modes are present but do not affect the intent or results of this study and, therefore, will not be discussed. Note that, although both the microphone and the hot-wire sensor were calibrated prior to the experiments, no calibrations were applied to the output from either sensor during these tests. This is because we are only interested in relative changes in the microphone signal due to the signal conditioning using the hot wire and least-mean-square (LMS) algorithm. Coherence functions never require calibrated signals because the calibration constant cancels in its definition [Eq. (3)]. Additionally, the raw voltages are important in the signal conditioning since it is these signals that are to be combined. The coherence measurements will therefore indicate whether the uncalibrated, nonlinear hot-wire signal, proportional to the fourth root of pressure, may be combined with a microphone signal, linearly proportional to the pressure, to remove the flow-induced noise.

In Fig. 4, it is clear from the collapse of the data for the first three cases that the hot-wire response is aerodynamically dominated in the presence of flow regardless of the speaker-generated noise. This effect is expected since the level of the acoustic noise, adjusted to give the same overall sound pressure level at the microphone as the flow-induced noise, produces fluctuating velocities that are much smaller (on the order of 50 times smaller) than those generated by the flow. It can also be seen by the spectrum levels that most of the flow energy is contained at the lower frequencies. In the absence of flow, the hot-wire response tends to be buried in the anemometry system noise.

The microphone responses plotted in Fig. 5 show that the microphone signal is highly contaminated by flow noise especially at frequencies below 100 Hz. The shape of the spectra for the cases in the presence of flow are almost identical to each other and to those of the hot-wire spectra for the same conditions (the plot scales are different). The addition of flow to the random noise does not significantly alter the spectrum from the random-noise-only spectrum above 100 Hz but causes a large increase in level below 100 Hz where most of the flow contamination is concentrated. A broadband increase of nearly 50 dB results from adding flow to the 250 Hz noise.

The data presented in Figs. 4 and 5 clearly illustrate the need for flow noise suppression for the microphone response, especially for frequencies below 100 Hz. The data also show that the hot wire does respond to acoustic excitation, but in the presence of flow the acoustic response is masked by the response to the aerodynamic effects.

To determine whether the signals from the two sensors may be combined to reduce flow noise, coherence function measurements between the hot-wire and microphone signals were studied for the same flow and acoustic conditions. The measured coherence function for the sensors placed in the duct with flow only was given in Fig. 3. Similar plots of the measured coherence functions for the other four cases are given in Figs. 6–9.

The coherence functions are almost identical for the cases with flow only (Fig. 3) and flow + 250 Hz acoustic noise (Fig. 6) with the exception of a decrease at 250 Hz. The similarity was expected since the hot-wire and microphone spectra for these conditions, too, were nearly identical. The drop in coherence at 250 Hz is due to the fact that the microphone response to the tone is strong but the

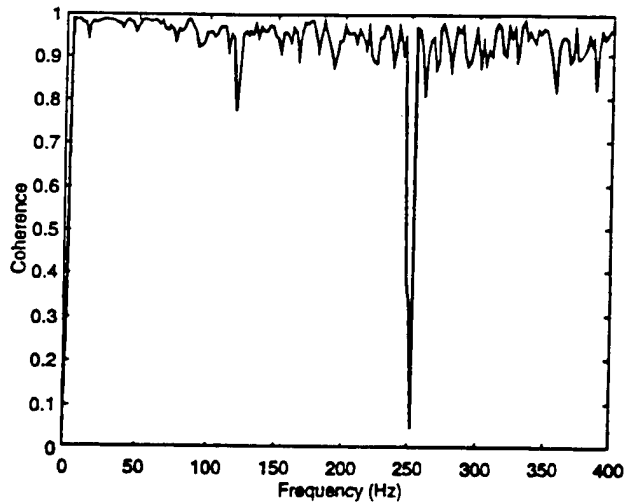


Fig. 6 Measured coherence function for flow + 250 Hz case.

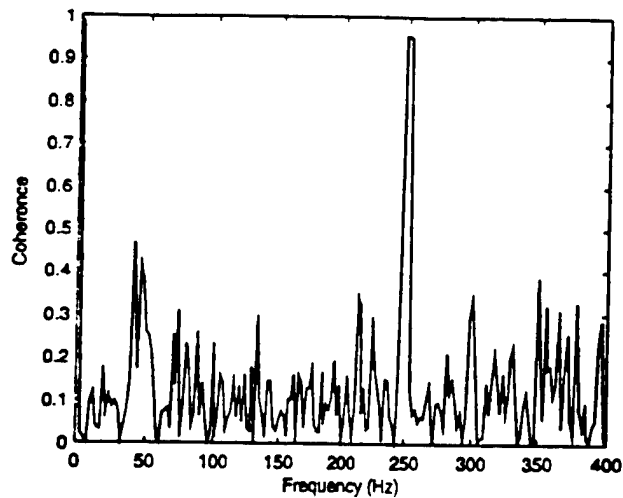


Fig. 9 Measured coherence function for 250 Hz only case.

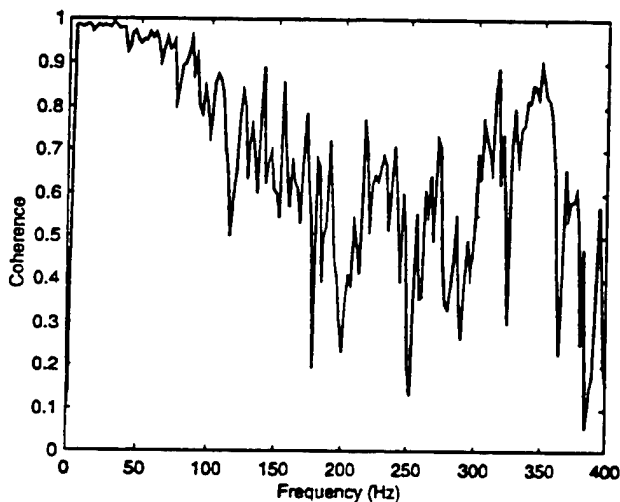


Fig. 7 Measured coherence function for flow + random noise case.

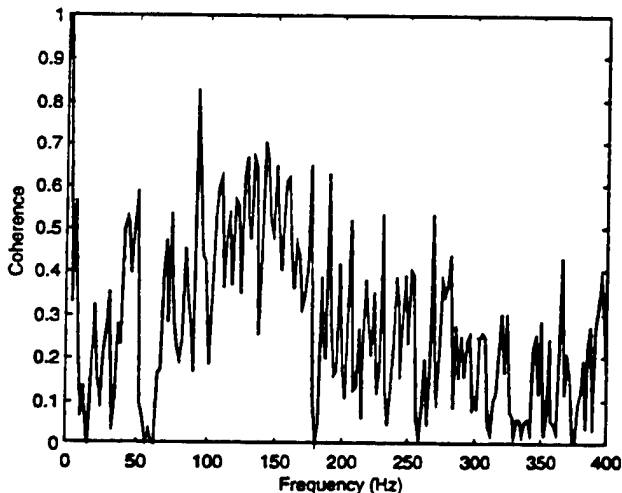


Fig. 8 Measured coherence function for random noise only case.

hot-wire response is still dominated by the aerodynamic velocities rather than the acoustic velocity fluctuations associated with the tone. The coherence measured with both flow and random noise (Fig. 7) is high for frequencies less than 100 Hz because most flow noise contamination occurs in this range, but drops off at higher frequencies. When only acoustic excitation is present (Figs. 8 and 9) the coherence levels are much lower than in the presence of flow with the exception of the 250 Hz tone.

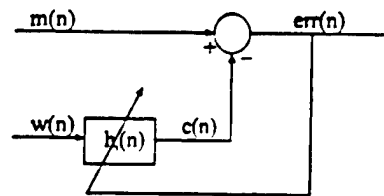


Fig. 10 Schematic representation of the hot mic.

Note that the coherence levels are generally high in the presence of flow, especially where desired at frequencies below 100 Hz, and that the levels are significantly lower in the absence of flow. This effect is desirable because we want to combine the signals to remove the effects of flow (pseudonoise) from the microphone signal but leave the acoustic pressure signal (in this case, the random or 250 Hz noise) unaltered. Since the fluid dynamic response of the two sensors is coherent but the acoustic response is not, a proper combination of the two signals should result in attenuation or elimination of the (coherent) fluid dynamic contribution from the signals.

Flow Noise Reduction

Flow noise reduction was achieved by adaptively filtering the hot-wire signal and then subtracting it from the microphone signal. This combination was performed with the 10 second time-capture data using an LMS algorithm, and for the sake of brevity, the filtered hot-wire/microphone signal combination, which performs as a single sensor, will be referred to as a "hot mic." The schematic for the hot-mic is given in Fig. 10. No attempt has been made to optimize the adaptive algorithm or the convergence speed, and as in the coherence measurements, no calibration is applied to either the hot-wire or microphone signal.

In this algorithm, the digitized hot-wire signal $w(n)$ is passed through the adaptive filter $h_i(n)$ and then subtracted from the microphone signal $m(n)$ to produce an error signal $err(n)$. The output of the filter $c(n)$ should be that part of the hot-wire signal that is coherent with the microphone signal, i.e., the noise caused by turbulence pressure fluctuations. The subtraction of $c(n)$ from $m(n)$ will then produce an output proportional to the acoustic pressure fluctuations with the pseudonoise component removed.

The i -filter coefficients were updated using an LMS algorithm,

$$h_i(n+1) = h_i(n) + 2\mu w(n)err(n) \quad (4)$$

In all cases, the convergence coefficient was set at $\frac{1}{10}$ of its maximum value, μ_{max} , which was determined from the following stability criterion:

$$\mu_{max} = \frac{1}{N \cdot E\{w^2(n)\}} \quad (5)$$

The filter coefficients were initially set according to

$$H(f) = M(f)/W(f) \quad (6)$$

where $M(f)$ and $W(f)$ are the Fourier transforms of the microphone and hot-wire responses, respectively. The impulse response was then obtained by taking the inverse Fourier transform of $H(f)$ and truncating it to the desired number of filter coefficients. The number of points used for the Fourier transforms was varied, and, as expected, the greater the number of points, the better the filter approximated the optimal transfer function between the hot-wire sensor and microphone. For the sake of brevity, however, variations in the n -point Fourier transforms will not be discussed further. Only those performed with 1024 points are included in this paper.

In the hot-mic algorithm, the first 1024 points of the hot-wire and microphone data records were used to calculate the initial filter coefficients as discussed earlier. The remaining data points were then treated as real-time data to which the algorithm adapted. After the 10-s sample was processed, the hot-mic output (the error signal), which ideally contains acoustic pressure information with the flow-induced pseudonoise removed, was compared with the microphone spectra with and without flow contamination. Figure 11 is a plot of this comparison for the case of random noise. In this plot, the solid line represents the spectrum of the hot-mic signal, the dashed line represents the microphone signal in the presence of random noise without flow contamination, and the dotted line shows the microphone response to the random noise in the presence of flow.

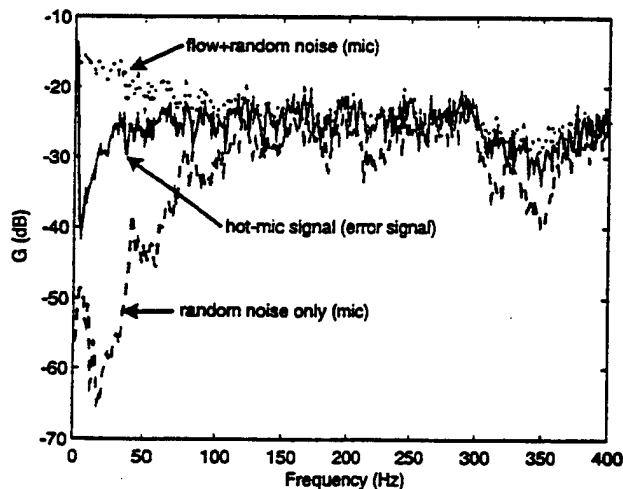


Fig. 11 Autospectral densities of microphone and error signals, random noise, four coefficients, $\mu = 0.1$.

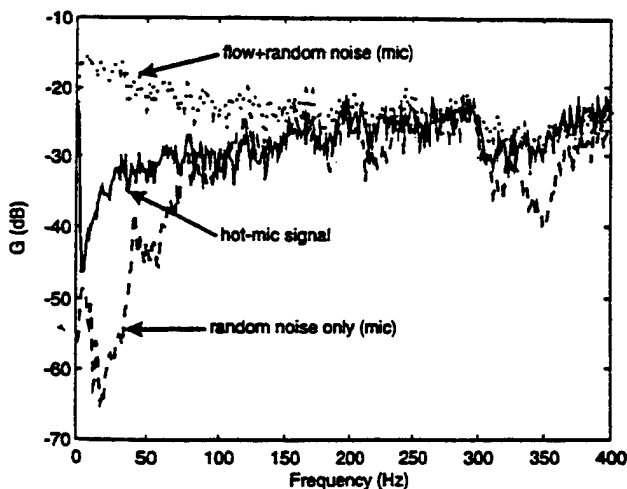


Fig. 12 Autospectral densities of microphone and error signals, random noise, 16 coefficients, $\mu = 0.025$.

The desired result is for the spectrum of the hot-mic signal to approach that of the microphone signal in the absence of flow. It can be seen from Fig. 11 that the hot-mic signal does indeed approach that of the uncontaminated microphone signal, resulting in a flow noise attenuation of greater than 15 dB at below 100 Hz and better spectral approximation to the uncontaminated microphone signal out to 400 Hz.

By increasing the number of filter coefficients, the approximation of the error signal to the uncontaminated microphone increases. Figure 12 shows the same spectral comparison with 16 filter coefficients. Flow noise attenuation is increased an additional 5–10 dB at frequencies below 100 Hz without losing the pressure information at the higher frequencies. A point will be reached, in this case with approximately 100 filter coefficients, where the slow convergence of the LMS algorithm cannot keep up with the coefficient update, especially since the coherence between the hot-wire and microphone signals decreases as frequency increases. The important result, however, is that flow noise attenuation in the pressure signal of 20 dB or more and a better spectral approximation to the uncontaminated pressure signal is possible with very few filter coefficients and a simple LMS adaptive algorithm. Moreover, the flow noise reduction is sufficient to overcome the increase caused by streamwise orientation of the microphone.

The same type of comparison was also made with the 250 Hz noise superimposed on the flow. Figures 13 and 14 illustrate how low-frequency as well as higher-frequency turbulence suppression was attained with just 4 and 16 filter coefficients, respectively. Moreover,

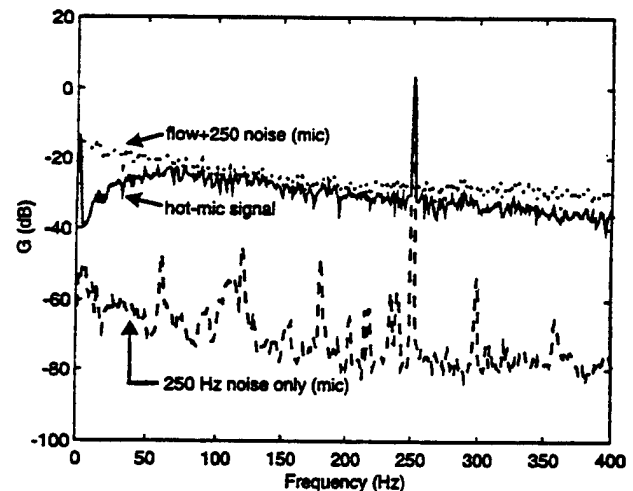


Fig. 13 Autospectral densities of microphone and error signals, 250 Hz noise, four coefficients, $\mu = 0.1$.

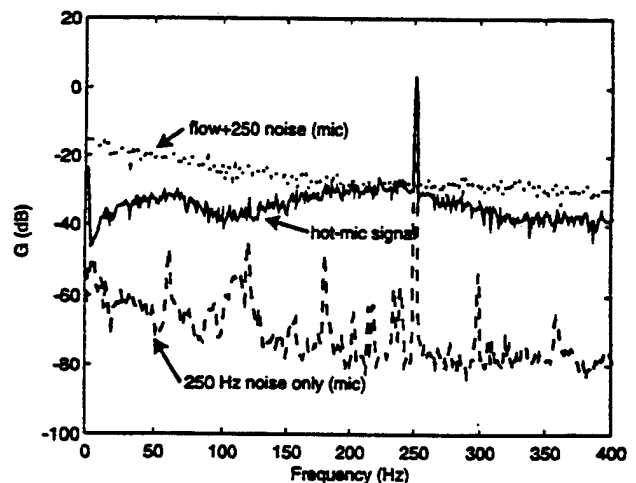


Fig. 14 Autospectral densities of microphone and error signals, 250 Hz noise, 16 coefficients, $\mu = 0.025$.

the flow noise suppression was performed without reducing the level of the acoustic pressure fluctuations at 250 Hz.

Conclusions

A hot-wire and a microphone signal may be combined to suppress turbulence-induced pseudonoise from the microphone signal without losing the acoustic pressure signal. Measured coherence levels between a raw hot-wire signal and the signal from a pinhole microphone located 0.5 mm downstream of the hot-wire sensor were high over a wide frequency range in the presence of flow but low in the absence of flow, indicating that the two signals could be combined to remove the coherent (flow-induced) part. Adaptively filtering the hot-wire signal using an LMS algorithm before subtracting it from the flow-contaminated microphone signal results in the hot-mic output that more closely resembles that of the uncontaminated microphone signal. Flow noise suppression on the order of 20 dB is attained at frequencies below 100 Hz. In addition, attenuations of more than 10 dB may be observed at higher frequencies. Furthermore, the resulting hot-mic signal retains the acoustic pressure information of interest, making the hot-mic an ideal sensor for use in active noise control applications where the sensing or error microphone must be placed in a flowfield.

Acknowledgments

The authors would like to acknowledge Bill Patrick and the United Technologies Research Center for the sponsorship of this work.

References

- ¹LaFontaine, R. F., and Shepherd, I. C., "An Experimental Study of a Broadband Active Attenuator for Cancellation of Random Noise in Ducts," *Journal of Sound and Vibration*, Vol. 91, No. 3, 1983, pp. 351-362.
- ²Nakamura, A., Sugiyama, A., Tanaka, T., and Matsumoto, R., "Experimental Investigation for Detection of Sound-Pressure Level by a Microphone in an Airstream," *Journal of the Acoustical Society of America*, Vol. 50, No. 1, 1971, pp. 40-46.
- ³Shepherd, I. C., LaFontaine, R. F., and Cabelli, A., "Active Attenuation in Turbulent Flow Ducts," *Proceedings of Inter-Noise 84 Conference* (Honolulu, HI), Noise Control Foundation, New York, 1984, pp. 497-502.
- ⁴Lauchle, G. C., "Effect of Turbulent Boundary Layer Flow on Measurement of Acoustic Pressure and Intensity," *Noise Control Engineering Journal*, Vol. 23, No. 2, 1984, pp. 52-59.
- ⁵Munro, K. H., and Ingard, U. K., "On Acoustic Intensity Measurements in the Presence of Mean Flow," *Journal of the Acoustical Society of America*, Vol. 65, No. 6, 1979, pp. 1402-1409.
- ⁶Chung, J. Y., "Rejection of Flow Noise Using a Coherence Function Method," *Journal of the Acoustical Society of America*, Vol. 62, No. 2, 1977, pp. 388-395.
- ⁷Alfredson, R. J., and Loh, M., "The Multiple Coherence Method for Reducing Flow Noise on Microphones," *Proceedings of Inter-Noise 91 Conference*, Australian Acoustical Society, Sydney, Australia, 1991, pp. 1117-1120.
- ⁸Chung, J. Y., and Blaser, D. A., "Transfer Function Method of Measuring Acoustic Intensity in a Duct System with Flow," *Journal of the Acoustical Society of America*, Vol. 68, No. 6, 1980, pp. 1570-1577.
- ⁹Corcos, G. M., "Resolution of Pressure in Turbulence," *Journal of the Acoustical Society of America*, Vol. 35, No. 2, 1963, pp. 192-199.
- ¹⁰Shepherd, I. C., LaFontaine, R. F., and Cabelli, A., "The Influence of Turbulent Pressure Fluctuations on an Active Attenuator in a Flow Duct," *Journal of Sound and Vibration*, Vol. 130, No. 1, 1989, pp. 125-135.
- ¹¹Nakamura, A., Matsumoto, R., Sugiyama, A., and Tanaka, T., "Some Investigations on Output Level of Microphones in Air Streams," *Journal of the Acoustical Society of America*, Vol. 46, No. 6, 1969, pp. 1391-1396.
- ¹²Crocker, M. J., Cohen, R., and Wang, J. S., "Recent Development in the Design of Turbulent Microphone Windscreens for In-Duct Fan Sound Power Measurements," *Proceedings of Inter-Noise 73 Conference* (Copenhagen, Denmark), Inst. of Noise Control Engineering, New York, 1973, pp. 594-598.
- ¹³Wang, J. S., and Crocker, M. J., "Tubular Windscreen Design for Microphones for In-Duct Fan Sound Power Measurements," *Journal of the Acoustical Society of America*, Vol. 55, No. 3, 1974, pp. 568-575.
- ¹⁴Neise, W., "Theoretical and Experimental Investigation of Microphone Probes for In-Duct Fan Sound Power Measurements," *Journal of Sound and Vibration*, Vol. 39, No. 3, 1974, pp. 371-400.
- ¹⁵Shepherd, I. C., and LaFontaine, R. F., "Microphone Screens for Acoustic Measurements in Turbulent Flows," *Journal of Sound and Vibration*, Vol. 111, No. 1, 1986, pp. 153-165.
- ¹⁶Anon., *Condenser Microphones and Microphone Preamplifiers for Acoustic Measurements: Data Handbook*, Brüel and Kjaer, Copenhagen, Denmark, 1982.
- ¹⁷Blake, W. K., "Turbulent Boundary-Layer Wall-Pressure Fluctuations on Smooth and Rough Walls," *Journal of Fluid Mechanics*, Vol. 44, Pt. 4, 1970, pp. 637-660.
- ¹⁸Bendat, J. S., and Piersol, A. G., *Random Data: Analysis and Measurement Procedures*, 2nd ed., Wiley, New York, 1986, pp. 137 and 285.
- ¹⁹Willmarth, W. W., "Pressure Fluctuations Beneath Turbulent Boundary Layers," *Annual Review of Fluid Mechanics*, Vol. 7, 1975, pp. 13-38.
- ²⁰Kovaszny, L. S. C., "Hot Wire Method," *Physical Measurements in Gas Dynamics and Combustion*, Vol. 9, Art. F2, Princeton Univ. Press, Princeton, NJ, 1954, pp. 219-276.

APPENDIX 54

LOW FLOW-NOISE PRESSURE MEASUREMENTS USING A "HOT-MIC"

R. S. McGuinn

Associate Research Engineer, United Technologies Research Center
411 Silver Lane, East Hartford, CT 06108
and

G. C. Lauchle and D. C. Swanson

Graduate Program in Acoustics and Applied Research Laboratory
The Pennsylvania State University, University Park, PA 16802**Abstract**

Real-time attenuation of flow-induced pseudo noise from the pressure signal of a microphone placed in a flowfield was performed by coupling an uncalibrated hot-wire signal with that of the microphone (the combination is called a "hot-mic"). A pinhole microphone and a hot-wire sensor located just upstream of the pinhole opening were placed in a well-defined, low-speed turbulent flow in a rectangular duct. Controlled acoustic noise, both random and time-harmonic, was superimposed on the flow noise by a speaker source located near the entrance of the duct. Experiments indicated that significant flow-noise attenuation is achievable in real time by adaptively filtering the hot-wire signal using a least-mean-square algorithm before subtracting it from the microphone signal. The resulting hot-mic signal retains the acoustic pressure information of interest. Moreover, it was shown that the measured coherence between two hot-mics in the presence of flow is higher than the measured coherence between two identically placed microphones. These results indicate that the hot-mics would make better acoustic pressure sensors for use in active noise control applications where the sensing and/or error microphone must be placed in a low-speed, turbulent flowfield.

Nomenclature

c	= filtered hot-wire signal
d_h	= hydraulic diameter
E	= Fourier transform of e
$E\{\}$	= expectation operator

e	= error signal
err	= error signal
f	= frequency
G_{xx}	= autospectral density of x
G_{xy}	= cross spectral density function between x and y
γ_{xy}^2	= ordinary coherence function between x and y
H	= Fourier transform of h
h	= filter impulse response
M	= Fourier transform of m
m	= microphone signal
n	= discrete time variable, noise signal
N	= number of filter coefficients
S	= Fourier transform of s
s	= sensing microphone signal
W	= Fourier transform of w
w	= hot-wire signal
μ	= convergence coefficient

Introduction

There are many instances when it is desirable to measure acoustic pressure in the presence of flow. These include in-situ and laboratory measurements as well as many active noise control (ANC) problems. One such ANC application of current interest is the control of fan noise in a ventilation system.

A microphone placed in flow cannot distinguish aerodynamic pressure fluctuations from acoustic pressure fluctuations even when the two are independent and uncorrelated with each other. If the flowfield is turbulent, the microphone signal is contaminated by the turbulence-induced pseudo noise. When turbulence is sufficiently high, the acoustic pressure of interest can be completely masked by the flow noise.

In many ANC applications, a sensing and/or error microphone may be located in a flowfield to

provide acoustic input to the control system. Based upon the noise sensed by the microphones, the controller will send a signal to a speaker where a canceling noise is introduced. If the microphone is contaminated by flow-induced pseudo noise, the control system will try to cancel the pseudo noise as well as the acoustic noise. Since the acoustic and pseudo pressure fluctuations are not correlated with each other and since the pseudo noise imposed on the microphone is much greater than what it actually radiates to the far-field, the flow noise is not canceled. Instead, the level of turbulence-induced pseudo noise imposes a limit below which the acoustic noise may not be actively attenuated.^{1,2,3} Consequently, it is important that the pseudo-noise component be removed from the microphone signal. Moreover, it is desirable that this noise be reduced without removing any of the acoustic pressure information.

One method of flow-noise reduction involves the placement of foam, streamlined nosecones, or turbulence screens (such as a porous or slit tube^{4,5}) over the diaphragm of the microphone. This type of treatment is often bulky or long and provides little or no flow-noise attenuation at frequencies below 100 Hz.⁹ Spatially averaging out the turbulence pressure fluctuations by using an array of microphones can be expensive and requires use of a sufficient volume over which to average.¹⁰ Data processing techniques such as taking the cross spectrum between two microphones to remove the pseudo noise result in a loss of the phase information of the acoustic pressure signal, making the technique useless for active noise control.¹¹⁻¹⁴

A previous investigation¹⁵ showed that flow-noise attenuation was possible by combining an uncalibrated hot-wire signal with a microphone signal using a least-mean-square algorithm. The significance of the *uncalibrated* hot wire lies in the fact that the hot-wire does not have to be calibrated or linearized (the hot-wire signal is nonlinearly proportional to velocity fluctuations¹⁶). Despite the fact that the hot-wire signal provides a nonlinear measure of the turbulence-induced pressure fluctuations, it can be combined with the linear response of a microphone to pressure fluctuations for reduction of the pseudo noise.

The results discussed in the previous work were obtained by post processing time-series data. Although the data showed that the hot-mic can be used to remove low frequency flow noise from the microphone signal, the time-capture-post-analysis method is impractical if the technique is to be applied to active noise control. To be useful, the hot-mic

algorithm must be performed "in real time" so that the control system can process the signal and introduce a canceling noise signal to the speaker.

Objective

The objective of this research was to verify that pseudo noise inherent in a microphone placed in flow could be reduced in real-time by using a hot-mic. In addition, it was desired to determine whether the hot-mic would provide a better acoustic pressure signal than a streamlined microphone for active noise control applications where the microphone must be placed in flow. To do so, it is necessary to show that the hot-mic provides a less contaminated signal than a microphone with a nosecone designed for use in a turbulent flowfield, especially at frequencies below 100 Hz.

Experimental Setup

Experiments were performed in a 0.25 x 0.13 x 4 m (0.8 x 0.4 x 13 ft.) rectangular duct illustrated in Figure 1. A variable speed centrifugal blower provides the air flow. The flow in the duct was characterized using hot-wire anemometry at six cross-sections corresponding to $x/L = 0.11, 0.26, 0.42, 0.57, 0.72$, and 0.88 , where x is measured from the exit of the blower and $L = 4$ m (13 ft.) is the duct length. The six cross-sections are denoted, sequentially, as Locations 1 through 6, with Location 1 nearest the blower at $x/L = 0.11$. The flow measurements at these locations included mean velocities, turbulence intensities, and turbulence scales in both the streamwise and transverse directions.

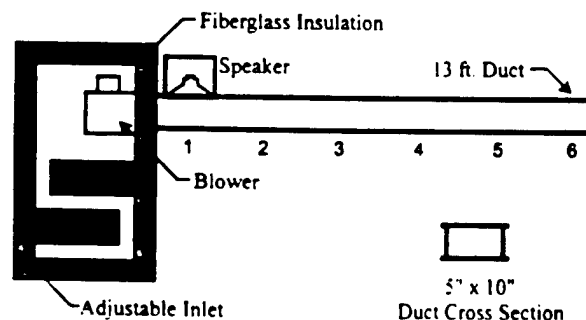


Figure 1: Rectangular duct test facility.

Two uncalibrated single-sensor hot wires with 0.005 mm (0.0002 in.) diameters and sensing lengths of 1.5 mm (0.06 in.) were used for the velocity measurements. The hot-wire sensors were operated with a constant-temperature anemometer and had frequency responses of approximately 50 kHz. Two 1.3 cm (1/2 in.) free-field condenser microphones with streamlined pinhole nosecones were used to reduce the sensing area. The pinhole¹⁷ diameters were 0.8 mm (1/32 in.) and 0.16 mm (1/16 in.), respectively. The corresponding resonance frequencies due to the pinhole cavities were determined by comparison calibration to be approximately 1200 Hz and 1400 Hz, respectively. The pinhole microphone response in both cases was flat (within 1 dB) from approximately 6 Hz to 1000 Hz.

For each hot-mic, the hot-wire probe and the pinhole microphone were placed as shown in Figure 2. The pinhole microphone is aligned with the centerline of the duct with the pinhole pointing in the upstream direction. The hot-wire sensor is located 0.5 mm (0.02 in.) upstream of the pinhole opening. This arrangement was in order to provide the greatest coherence between the hot-wire and microphone signals in the presence of flow.¹⁸ Measurements verified that the placement of the hot wire upstream of the pinhole opening did not affect the microphone response in the frequency range considered (the hot-wire vortex shedding frequency is approximately 305 kHz based on a Strouhal number of 0.2 for cylinder vortex shedding).

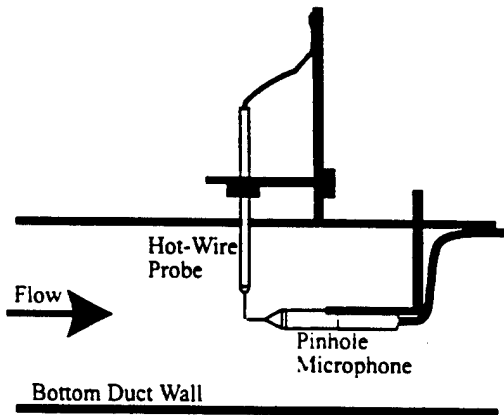


Figure 2: Streamwise placement of pinhole microphone and hot-wire probe.

The hot-mic algorithm is shown schematically in Figure 3. The digitized hot-wire signal, $w(n)$, is

passed through an adaptive digital filter with i coefficients, $h_i(n)$, and then subtracted from the microphone signal, $m(n)$, to produce an error signal, $err(n)$. The output of the filter, $c(n)$, is that part of the hot-wire signal which is coherent with the microphone signal, i.e. the noise caused by turbulence pressure fluctuations. The subtraction of $c(n)$ from $m(n)$ produces an output proportional to the acoustic pressure fluctuations with the pseudo noise component removed. In other words, the error signal is decorrelated from the hot-wire signal. If the hot-wire signal contains only flow information, the error signal contains only acoustic pressure information.

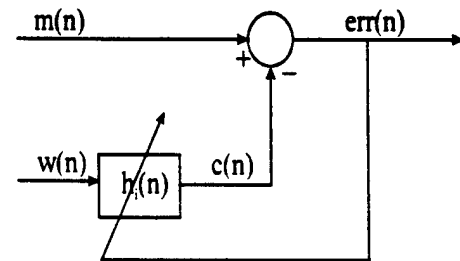


Figure 3: Schematic representation of hot-mic.

The filter coefficients were updated using an LMS algorithm given in Equation 1,¹⁹

$$h_i(n+1) = h_i(n) + 2\mu \cdot err(n) \cdot w(n-i). \quad (1)$$

All hot-mic measurements were made using 16 filter coefficients and a convergence coefficient, μ , set at 1/50 of its maximum value. The maximum convergence coefficient, μ_{max} , was determined from the following stability criterion:¹⁹

$$\mu_{max} < \frac{1}{N \cdot E\{w^2(n)\}}, \quad (2)$$

where N is the number of filter coefficients and $E\{\}$ is the expectation operator. The number of filter coefficients and the value of the convergence coefficient were determined in prior work^{15,18} to provide flow-noise attenuation at frequencies below 100 Hz where other methods are inadequate.

For the real-time measurements, the signals from the two sensors (hot wire and microphone) of the hot-mic probe were processed by a DSP floating-point

digital signal processing board via two high speed analog I/O channels on the board. The board was resident in a personal computer with a 90 MHz processor. The analog inputs and outputs were filtered with 4th-order low-pass filters with cut-off frequencies of 612 Hz. The hot-mic algorithm was programmed onto the board in C. A Windows-based interface, also programmed in C, was used to set the sampling rate (3000 samples/sec) and filter parameters and to control the operation of the hot-mic algorithm. The hot-mic output was then passed through the analog output on the DSP board to a fast Fourier transform analyzer for spectral analysis. Each spectrum was sampled at 2048 samples/second and averaged 100 times. The bandwidth was 2 Hz. The bias error from spectrum to spectrum is zero since the sampling rate and bandwidth were not changed. The random error estimate of 10% is also the same for all cases. Both the hot-wire and microphone spectral data were repeatable to within 1 dB which is consistent with the estimated random error. A block diagram of the setup is shown in Figure 4

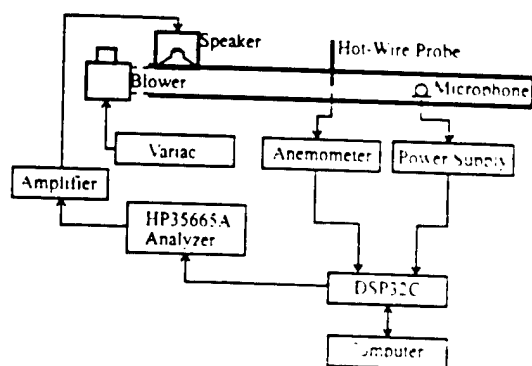


Figure 4: Block diagram of experimental setup for real-time hot-mic operation.

Results and Discussion

Real-time Hot-Mic Results

Real-time data were obtained with the hot-mic at Locations 2 through 6 in the duct. The speaker was placed at Location 1. Results from Locations 2 and 6 are emphasized since they represent the extremes of flow and acoustic variations. The results from Locations 3, 4, and 5 follow the trends established by the presented data.

Plots showing a comparison between the hot-mic signal and the microphone signals for random noise with and without flow are given in Figures 5 (a) and (b) for duct locations 2 and 6, respectively. Each plot shows the autospectrum of the microphone signal measured in the presence of both random noise and flow, the uncontaminated microphone autospectrum (measured in the presence of the acoustic random noise only), and the hot-mic autospectrum.

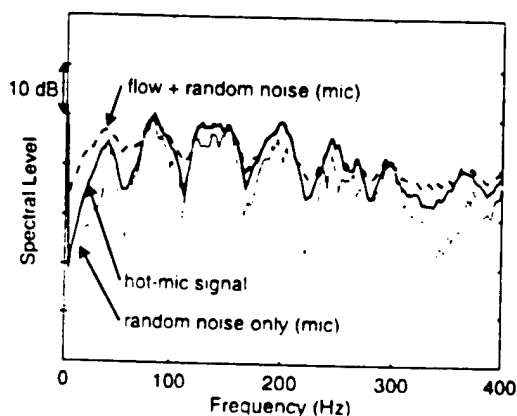


Figure 5 (a): Real-time hot-mic and microphone autospectral densities at Location 2, $\mu=0.005$.

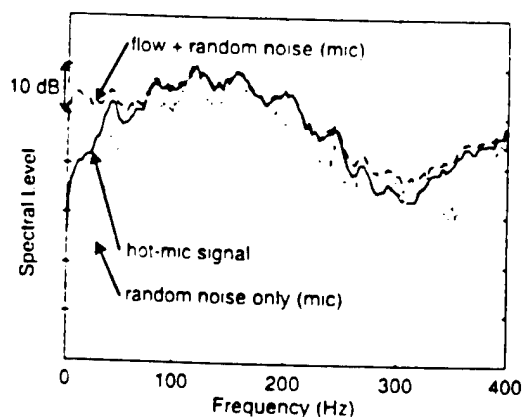


Figure 5 (b): Real-time hot-mic and microphone autospectral densities at Location 6, $\mu=0.005$.

At all locations, flow-noise attenuation is achieved and is generally confined to frequencies below 100 Hz. The difference in the two cases presented here (Location 2 and Location 6) is that the

The objective of this research was to develop a sensor that minimizes the turbulence-induced flow noise, the main contributor to the measurement noise of the ANC system described above. It is known from the previous section that flow noise attenuation is possible with the hot-mic, especially at frequencies below 100 Hz. If the coherence between two hot-mics is measured and compared to the coherence measured between two microphones under the same flow and acoustic conditions, it is expected that the hot-mic coherence will be higher.

The coherence measurements between the two hot-mics and between the two microphones of the hot-mics were performed in succession under identical flow conditions. For these tests, the 1/32 in. pinhole microphone was used for the upstream measurements and the 1/16 in. pinhole microphone was used for the downstream measurements. (It was necessary to use the two different pinhole sizes because they were the two nosecones available for this research.) Flow-noise attenuation with the larger diameter hot-mic is slightly less than that possible with the smaller diameter hot-mic due to the increased microphone sensing area. However, a 5-10 dB reduction in flow noise at low frequencies is achievable with the larger hot-mic.¹⁸ Therefore the coherence tests still provide a good measure of whether the hot-mic sensor gives a better signal than a microphone for active noise control in a flow.

A comparison of the microphone/microphone coherence and the hot-mic/hot-mic coherence measured in flow and with acoustic random noise is shown in Figure 7. The sensors were positioned at Location 2 ($x/L = 0.26$) and Location 4 ($x/L = 0.57$). (The separation distance between them is $\Delta x/L = 0.31$.) It can be seen that the coherence between the two hot-mics is higher than the coherence between the two microphones. In addition, the increase in coherence occurs over the entire frequency range. This result was not clearly predicted by the spectral comparisons. As expected, the greatest increase in coherence occurs at $f < 100$ Hz since it is this region that contains the most flow-noise contamination and it is in this region where most of the flow-noise attenuation occurs. Note that there is no appreciable change in coherence function values for $f < 20$ Hz. Figure 5(b) shows hot-mic flow-noise attenuation of 20 dB for $f \leq 20$ Hz, but the spectral levels are still 10 dB above the uncontaminated microphone signal. For this reason, no increase in coherence is seen with the hot-mics for $f < 20$ Hz.

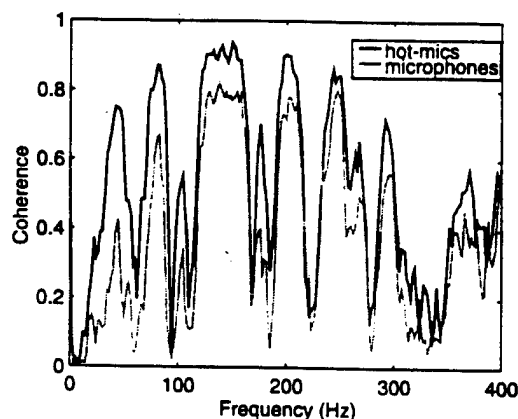


Figure 7: Coherence between sensors at Locations 2 and 4, respectively, in flow + random acoustic noise.

A similar comparison is shown in Figure 8 for the sensors positioned at Locations 2 and 6 ($\Delta x/L = 0.62$), and Figure 9 for the sensors positioned at Locations 3 and 4 ($\Delta x/L = 0.15$). As in the case for $\Delta x/L = 0.31$, an increase in coherence with the hot-mics occurs over nearly the entire frequency range. Note that, even though the upstream sensors are in the presence of evanescent waves (recall Figure 2) and higher turbulence intensities, the increase in coherence with the hot-mics is as good if not better than at the other locations. Since the hot-wire is not adversely affected by higher-order duct modes or evanescent waves, it appears that these disturbances serve only to limit the upper bound of the hot-mic/hot-mic coherence.¹⁸

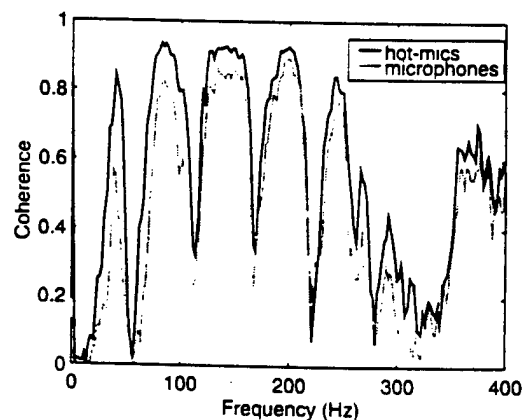


Figure 8: Coherence between sensors at Locations 2 and 6, respectively, in flow + random acoustic noise.

spectral content differs at each duct location as a result of standing and evanescent waves. In addition, the flow noise is greater at Location 2 (close to the blower) due to higher turbulence levels. The acoustic signal-to-flow noise ratio is less at Location 2 ($S/N_2 = 0.9$) than at Location 6 ($S/N_6 = 1$). Identical scales in each plot of Figure 5 allow the increase in flow noise at low frequency perceived by the microphone with upstream location to be seen. There is no undesired acoustic noise attenuation at any location.

These results are in agreement with post-processed time-series data obtained.¹⁹ They verify that real-time flow noise attenuation can be achieved using a hot-mic.

Hot-Mic vs. Microphone Coherence Results

To determine if the hot-mic would provide a good measurement of the acoustic pressure signal for use in an ANC application, we consider an active noise control system for the minimization of plane acoustic waves in a duct as shown in Figure 6. In this simple system, the sensing microphone measures the unwanted sound, sends the signal through the filter which adjusts the signal and sends it to the speaker for noise cancellation. The error microphone measures any residual noise. This signal is used to adjust the controller filter coefficients so that the error is minimized, for example, using an LMS algorithm.

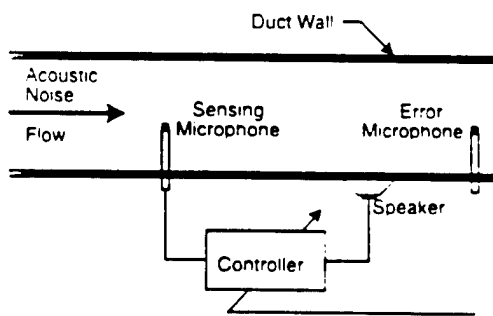


Figure 6: Schematic of adaptive ANC system for the minimization of plane acoustic waves in a duct.

By measuring the coherence between the sensing and error microphones in the duct *without* control, the maximum effectiveness of a control system can be estimated. Recall that the ordinary coherence

function between sensing microphone signal, $s(t)$, and an error signal, $e(t)$, is defined as²⁰

$$\gamma_{se}^2(f) = \frac{|G_{se}(f)|^2}{G_{ss}(f) \cdot G_{ee}(f)}, \quad 0 \leq \gamma_{se}^2(f) \leq 1, \quad (3)$$

where $G_{se}(f)$ is the cross-spectral density function between $s(t)$ and $e(t)$ and $G_{ss}(f)$ and $G_{ee}(f)$ are the autospectral density functions of $s(t)$ and $e(t)$, respectively. Assume that the sensing and error signals are correlated and that $e(t)$ is a linear combination of $x(t)$ and an extraneous, uncorrelated noise, $n(t)$. Here, $x(t)$ represents the error signal that might be ideally predicted from the sensing microphone signal in the absence of any noise.

The error signal may be expressed as

$$e(t) = x(t) + n(t), \quad (4)$$

so that its autospectrum is

$$G_{ee}(f) = G_{xx}(f) + G_{nn}(f), \quad (5)$$

where

$$G_{xx}(f) = |H(f)|^2 G_{ss}(f), \quad (6)$$

and

$$H(f) = \frac{G_{se}(f)}{G_{ss}(f)}. \quad (7)$$

The coherent output power spectrum is the acoustic spectrum at the sensing microphone as measured by the error microphone with the linear correlated effects due to $n(t)$ removed. It is given by:

$$G_{xx}(f) = \gamma_{se}^2 G_{ee}(f). \quad (8)$$

It follows that

$$G_{nn}(f) = (1 - \gamma_{se}^2) G_{ee}, \quad (9)$$

which suggests that the coherence function may be used to predict the effectiveness of the ANC system. For example, if the coherence between the two signals is 0.9, then a 10 dB noise reduction is possible with a perfect control system. Factors which contribute to a decrease in the coherence between two signals includes non-linearities in the system, measurement noise, and, in a duct, the presence of evanescent modes.^{20,21}

Acknowledgments

The authors would like to acknowledge Dr. Bill Patrick and the United Technologies Research Center for sponsoring this work.

References

- ¹LaFontaine, R.F. and Shepherd, I.C., "An Experimental Study of a Broadband Active Attenuator for Cancellation of Random Noise in Ducts," *Journal of Sound and Vibration*, **91**(3), 351-3362, 1983.
- ²Nakamura, A., Sugiyama, A., Tanaka, T., and Matsumoto, R., "Experimental Investigation for Detection of Sound-Pressure Level by a Microphone in an Airstream," *Journal of the Acoustical Society of America*, **50**, 40-46, 1971.
- ³Shepherd, I.C., LaFontaine, R.F., and Cabelli, A., "Active Attenuation in Turbulent Flow Ducts," *Inter-Noise 84 Proceedings*, 497-502, 1984.
- ⁴Nakamura, A., Matsumoto, R., Sugiyama, A., and Tanaka, T., "Some Investigations on Output Level of Microphones in Air Streams," *Journal of the Acoustical Society of America*, **46**(6), 1391-1396, 1969.
- ⁵Crocker, M.J., Cohen, R., and Wang, J.S., "Recent Development in the Design of Turbulent Microphone Windscreens for In-Duct Fan Sound Power Measurements," *Inter-Noise 73 Proceedings*, 594-598, 1973.
- ⁶Wang, J.S. and Crocker, M.J., "Tubular Windscreen Design for Microphones for In-Duct Fan Sound Power Measurements," *Journal of the Acoustical Society of America*, **55**(3), 568-575, 1974.
- ⁷Neise, W., "Theoretical and Experimental Investigation of Microphone Probes for In-Duct Fan Sound Power Measurements," *Journal of Sound and Vibration*, **39**(3), 371-400, 1974.
- ⁸Shepherd, I.C. and LaFontaine, R.F., "Microphone Screens for Acoustic Measurements in Turbulent Flows," *Journal of Sound and Vibration*, **111**(1), 153-165, 1986.
- ⁹Bruel & Kjaer Condenser Microphones and Microphone Preamplifiers for Acoustic Measurements: Data Handbook, Sept., 1982.
- ¹⁰Shepherd, I.C., LaFontaine, R.F., and Cabelli, A., "The Influence of Turbulent Pressure Fluctuations on an Active Attenuator in a Flow Duct," *Journal of Sound and Vibration*, **130**(1), 125-135, 1989.
- ¹¹Munro, K.H. and Ingard, U.K., "On Acoustic Intensity Measurements in the Presence of Mean Flow," *Journal of the Acoustical Society of America*, **65**(6), 1402-1409, 1979.
- ¹²Chung, J.Y., "Rejection of Flow Noise Using a Coherence Function Method," *Journal of the Acoustical Society of America*, **62**(2), 388-395, 1977.
- ¹³Alfredson, R.J. and Loh, M., "The Multiple Coherence Method for Reducing Flow Noise on Microphones," *Inter-Noise 91 Proceedings*, 1117-1120, 1991.
- ¹⁴Chung, J.Y. and Blaser, D.A., "Transfer Function Method of Measuring Acoustic Intensity in a Duct System With Flow," *Journal of the Acoustical Society of America*, **68**(6), 1570-1577, 1980.
- ¹⁵McGuinn, R.S., Lauchle, G.C., and Swanson, D.C., "Low Flow-Noise Microphone for Active Noise Control Applications," *AIAA Journal*, **35**(1), 29-34, 1997.
- ¹⁶Kovaszny, L. S. C., "Hot Wire Method," Physical Measurements in Gas Dynamics and Combustion, Vol. IX, Art. F2, Princeton University Press, Princeton, NJ, pp. 219-276, 1954.
- ¹⁷Blake, W.K., "Turbulent Boundary-Layer Wall-Pressure Fluctuations on Smooth and Rough Walls," *Journal of Fluid Mechanics*, **44**(4), 637-660, 1970.
- ¹⁸McGuinn, R.S., "On the Development of a Hot-Mic: A Low Flow-Noise Pressure Sensor for Use in Active Noise Control," Ph.D. thesis, The Pennsylvania State University, 1996.
- ¹⁹Nelson, P. A. and Elliott, S. J., Active Control of Sound, Academic Press Limited, London, 1992, pp. 113-115.
- ²⁰Bendat, J. S. and Piersol, A. G., Random Data: Analysis and Measurement Procedures, 2nd Edition, John Wiley & Sons, Inc., New York, p. 137, 1986.
- ²¹Tichy, J. and Warnaka, G. E., "Effect of Evanescent Waves on the Active Attenuation of Sound in Ducts," *Proceedings of Inter-Noise 83*, 435-438, 1983.

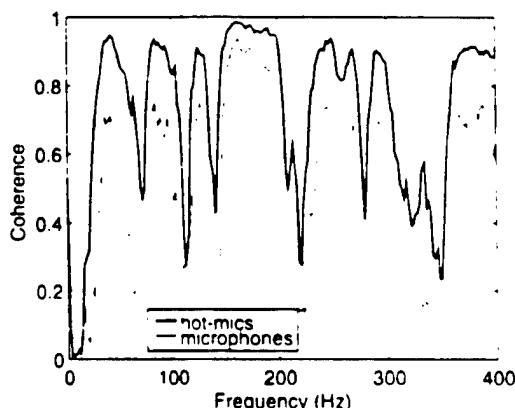


Figure 9: Coherence between sensors at Locations 3 and 4, respectively, in flow + random acoustic noise.

Increases in coherence using hot-mics compared to coherence using microphones only were also seen with 250 Hz acoustic tone cases. A plot showing this behavior is given in Figure 10 for the sensors placed at Locations 2 and 4 ($\Delta x/L = 0.31$). Here, the hot-mic coherence is higher than the microphone coherence at frequencies below 200 Hz. At frequencies greater than 250 Hz, there is no difference between the two types of sensors.

Since the 250 Hz tone is, theoretically, the only acoustic disturbance introduced to the duct (with the exception of the motor noise), it is important to describe the high coherence seen at low frequencies in Figure 10. Standing waves are present in the duct due to the open end termination. The first four modal frequencies of the standing waves are 43, 86, 129, and 172 Hz.¹⁸ These modes are excited by the broadband motor blower noise of the facility and it can be seen in Figure 10 (as well as in most other figures) that the microphone and the hot-mic signals are coherent at these frequencies. Coherence between the hot-mics is greater at these frequencies than it is for the microphones. Therefore, the hot-mics, in reducing the flow-induced noise, allow the acoustic characteristics of the blower and duct, as well as those generated by the speaker, to be unmasked.

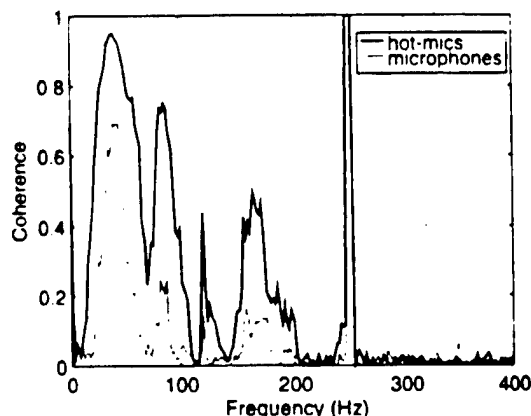


Figure 10: Coherence between sensors at Locations 3 and 4, respectively, in flow + 250 Hz acoustic tone.

Conclusions

The results obtained in this work demonstrate that real-time attenuation of pseudo-noise contained in a microphone signal is possible using a hot-mic. The combination of the uncalibrated hot-wire signal with the microphone signal using an LMS algorithm reduced the pseudo noise in the microphone signal by approximately 10 dB at frequencies below 100 Hz. Flow noise attenuation was also achieved at higher frequencies. In all cases, the pseudo noise reduction was achieved without loss of the acoustic pressure signal.

In comparing the hot-mic response with microphone response under the same conditions, it was found that the measured coherence function between two hot-mics was significantly greater than the measured coherence between two identically placed microphones in the duct with flow. Higher coherence between the hot-mics occurred over the entire frequency range. It was also found that the hot-mics, in reducing the flow-induced noise, allow the acoustic characteristics of the blower and duct, as well as those generated by the speaker, to be unmasked. The results demonstrated here suggest that the hot-mics would provide better reference and error signals for an ANC system which requires acoustic pressure sensing in the presence of flow.

APPENDIX 55

Designing a Virtual Sound-Level Meter in LabVIEW

by Dean E. Capone, Research Assistant, and Gerald C. Lauchle, Professor of Acoustics, Penn State University; Graduate Program in Acoustics and Applied Research Laboratory.

The Challenge: Creating a virtual sound-level meter for distribution with an accredited CD-ROM-based education course in acoustics.

The Solution: Using flexible signal generation and processing tools in LabVIEW to create an interactive virtual instrument with all the functionality of a commercial sound-level meter.

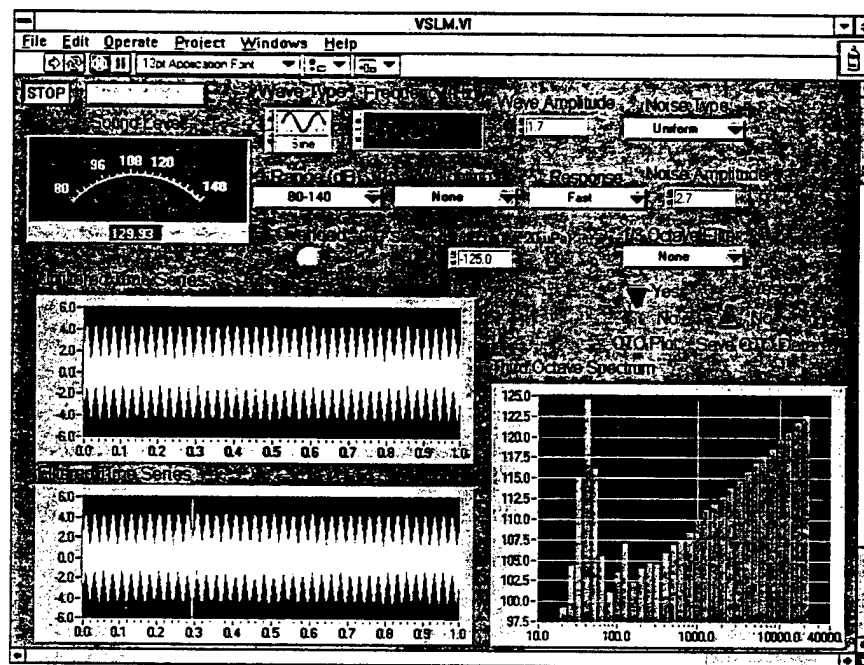
Background

A program funded by the Alfred P. Sloan Foundation began in December 1995 as a joint effort among the Pennsylvania State University's Graduate Program in Acoustics, the Center for Academic Computing, and the Office of Continuing & Distance Education to develop a cohort-based asynchronous Certificate Program in Acoustics. One goal of this project was to create a model for engaging distant students in a multi-course learning community. Another goal was to test the model through an Acoustics

We selected LabVIEW for our examples because of its readily available signal generation and processing tools, its easy-to-create simulated virtual instruments, and its ease of use for the novice operators.

Certificate Program in Noise Control Engineering delivered nationally using CD-ROM, Netscape Navigator™, and First Class™ technologies.

Seven faculty members are assembling materials and lectures for this course, to provide participating students with enough information to confidently take and pass a professional exam in noise control



User interface of the interactive virtual sound-level meter.

engineering, such as that offered by the Institute of Noise Control Engineering. We designed the lectures to cover basic and advanced acoustics as well as acoustical data collection and processing, in addition to specific application areas such as modal analysis, structural acoustics, flow-generated noise, room acoustics, and statistical energy methods. We are assembling and distributing via CD-ROM, hands-on examples using LabVIEW and MATLAB[®] to illustrate the concepts presented.

To augment many of the course lectures, we designed a series of virtual instruments so students would have an opportunity to obtain hands-on experience with typical instrumentation used professionally in noise control engineering. We chose LabVIEW for our examples because of its readily available signal generation and processing tools, its easy-to-create simulated virtual instruments, and its ease of use for novice operators. We are now designing specific instruments for each phase of the instructional process.

Virtual Sound-Level Meter

Unit 4 of the first course (there are a total of five courses) introduces the basic principles of performing sound and vibration measurements. As part of this unit, we designed a virtual sound-level meter to illustrate the concepts of basic noise measurements and the use of these measurements in computing quantities such as noise reduction or insertion loss. The primary function of a sound-level meter is to condition and measure an incoming acoustic signal in accordance with standards defined in the ANSI specification, then to display the measured sound pressure level (SPL). The starting point for the meter design was ANSI standards S1.4, Specification for Sound-Level Meters, and S1.11, Specification for Octave-Band and Fractional-Octave-Band Analog and Digital Filters. Although we designed the sound-level meter around the appropriate ANSI Standards, our primary design goal was to use the virtual instruments (VI) as an interactive learning tool.

We began our design efforts by focusing on the noise control concepts



Professor Gerald Lauchle and Dean Capone evaluate their LabVIEW virtual sound-level meter.

we wanted to illustrate with the virtual sound-level meter. Originally, we planned to import data files of various noise sources, such as those arising from traffic, factory machinery, or aircraft. Then the student could perform analysis on these recorded sounds using the sound-level meter. After further study of the signal generation tools provided with LabVIEW, we decided that it could easily generate the time-series data. The instructor could direct the student-user to specify the frequency and magnitude of a number of deterministic signals, such as sine waves, square waves, and sawtooth waves that are combined linearly with uniformly or Gaussian distributed random noise of a user-selected magnitude. Because the resultant raw time series is displayed on the front panel of the VI, students could visualize the signal created.

The signal conditioning consists of microphone frequency weighting as to produce A, B, or C frequency-weighted sound-levels. Of course, no weighting (called linear) is also an option. You can also pass these weighted signals through individual one-third octave

filters with center frequencies covering the entire audible range. You determine the time averaging characteristics of the frequency-weighted signal of the sound-level meter by one of three settings – fast, slow, or impulse. You can also use the meter to capture the mean-square pressure magnitude level (or equivalent sound-level, or Leq), the peak level, or the minimum level. All of these features are implemented in the virtual sound-level meter. The

Using the modular programming inherent in LabVIEW, we can easily modify the sound-level meter to accept input data from other sources.

student can apply various weightings and one-third octave filters and observe the effects in two ways. First, the conditioned time series is displayed below the original time series to illustrate the effect in the time domain. Second, as the cursor tracks across the conditioned time series, the student can observe the real-time SPL on both analog and digital

meters. Once the scan is completed, at the users discretion, you can display the one-third octave level as a function of frequency. You can also store these calculated values as a two column ASCII file, frequency versus level, for comparison to later results. Similarly, students can easily observe the effects of meter response time on the results for signals of various characters by repeating the analysis with a different meter response, for example, fast versus slow.

Conclusions

Using the analysis tools available in LabVIEW, we have constructed a software-only virtual sound-level meter to illustrate some of the basic measurements used in noise control engineering. With this virtual instrument, students can perform subjective, visual comparison of various data types, while displaying objective, calculated quantities, such as filtered and/or weighted sound pressure levels. This VI has all of the same features as real instruments produced commercially. With the LabVIEW signal-generation tools, students can easily generate and analyze repeatable time-series data. Using the modular programming inherent in LabVIEW, we can easily modify the sound-level meter to accept input data from other sources. Future projects may involve reading previously recorded data from an existing file or using an A/D board inside of the computer to perform real-time sound-level measurements. With these options, students can analyze acoustic signals, whatever their field of interest.

For more information, contact Gerald Lauchle or Dean Capone at Penn State University, Applied Research Lab, P.O.Box 30, State College, PA 16804, tel (814) 863-9893 (Capone), tel (814) 863-7145 (Lauchle), fax (814) 863-3287 (either), e-mail dec@wt.arl.psu.edu (Capone).

